Limb-darkening Measurements on Exoplanet Host Stars and the Sun

Dissertation
zur Erlangung des Doktorgrades
des Fachbereichs Physik
der Universität Hamburg

vorgelegt von
Holger Matthias Müller
aus Hamburg

Hamburg
2015

Gutachter der Dissertation:	Prof. Dr. Jürgen H. M. M. Schmitt Prof. Dr. Stefan Dreizler
Gutachter der Disputation:	Prof. Dr. Peter H. Hauschildt Prof. Dr. Robi Banerjee
Datum der Disputation:	15.07.2016
Vorsitzender des Prüfungsausschusses:	Dr. Robert Baade
Vorsitzender des Promotionsausschusses:	Prof. Dr. Peter H. Hauschildt
Dekan der MIN-Fakultät:	Prof. Dr. Heinrich Graener

Zusammenfassung

Nach der Entdeckung der ersten Planeten, die um sonnenähnliche Sterne kreisen, ist die Untersuchung dieser Exoplaneten zu einem neuen Feld in der Astronomie geworden, das sich steigender Beliebtheit erfreut. Die Suche nach neuen Welten mit der Hoffnung letztlich einen Planeten ähnlich der Erde zu entdecken treibt die Entwicklung neuer Instrumente an. Einige dieser sind Weltraumteleskope wie *Kepler*, die Photometrie von Transit-Ereignissen mit bemerkenswerter Genauigkeit liefern. Dies machte es möglich mehr als tausend neue Exoplaneten zu entdecken; mehrere tausend Kandidaten müssen nun noch bestätigt werden.

Die Untersuchung von Transits offenbart nicht nur Eigenschaften der Planeten, sondern bietet auch die Möglichkeit Eigenschaften ihrer Zentralsterne zu untersuchen. Während des Transits wird die Helligkeitsverteilung der Sternoberfläche abgetastet. Dies beinhaltet Aktivitätsindikatoren wie Flecken und Fackeln, aber auch die *Randverdunkelung*. Letzteres ist ein geometrischer Effekt und hängt von Eigenschaften der Photosphäre ab, wie z.B. der Effektivtemperatur. Bei der Modellierung von Transits in schlechter Datenqualität muss die Randverdunkelung aus Modellatmosphären angenommen werden. Allerdings ist es bisher nicht geklärt, ob diese Vorhersagen realistisch sind. Der Vergleich zwischen gemessenen und vorhergesagten Randverdunkelungen ist eines der Hauptziele dieser Arbeit.

Für die Untersuchung der Randverdunkelung nutze ich *Kepler* Photometrie von 48 Hauptreihensternen verschiedener Effektivtemperaturen. Diese Objekte werden von Planeten bedeckt, was zu typischen Lichtkurven führt. Im Gegensatz zur Verwendung von Randverdunkelungsvorhersagen für die Modellierung dieser Transits, erlaubt die hohe Datenqualität eine direkte Messung zusammen mit den übrigen Transitparametern. Diese Messungen sind die präzisesten in der Geschichte der Randverdunkelungsforschung entfernter Sterne.

Die Vorhersage der Randverdunkelung erfordert genaue Kenntnis der stellaren Parameter, z.B. Effektivtemperatur und Oberflächengravitation. Diese Größen können aus Spektren abgeleitet werden. Ich verwende hochaufgelöste VLT/UVES Spektren von zwei Sternen (ε Eridani und CoRoT-2A) zur Demonstration der Bestimmung dieser Größen mit Hilfe eines Programms, das auf synthetischen Spektren beruht. Der Vergleich dieser Parameter mit denen aus der Literatur offenbart wie verlässlich diese Methode ist um die erhaltenen Parameter zur Erstellung von Modellintensitäten zu verwenden. Die präzisesten verfügbaren Messungen der Randverdunkelung – die der Sonne – eignen sich ausgezeichnet zum Vergleich mit solchen Vorhersagen. Ich präsentiere einen direkten Vergleich und führe eine Skalierung der Modellintensitäten ein, die systematische Abweichungen reduziert.

Die bisherige Verwendung von Randverdunkelungsgesetzen in Transitmodellen ist zu einem gewissen Grad willkürlich. Deshalb entwickle ich einen numerischen Transitalgorithmus, der Randintensitäten direkt aus den Modellatmosphären verwendet. Dies eröffnet neue Möglichkeiten der Transiterzeugung, wie z.B. in beliebigen Wellenlängen oder Filtern. Darüber hinaus können beliebige Planetenformen und Bilder von der Sonne verwendet werden.

Abstract

After the discovery of the first planets orbiting solar-like stars at the end of the last century, the study of these exoplanets has become a new field in astronomy with increasing popularity. The search for new worlds with the hope to discover a planet similar to the Earth drives the development of new instruments. Some of these are space-based observatories like *Kepler* which offer photometry of transit events with a remarkable precision. These modern instruments made it feasible to discover more than a thousand new exoplanets; several thousands of planetary candidates are yet to be confirmed.

The study of transit light curves not only reveals properties of the planets, but also provides the opportunity to investigate properties of their host stars. During its transit the planet probes the star's surface brightness distribution. This includes activity indicators like spots and faculae, as well as the *limb darkening*. The latter is a line-of-sight effect and depends on properties of the photosphere, like the effective temperature. In the case of modeling transits with poor photometric quality the limb darkening has to be assumed based on model atmospheres, which have already proven their accuracy in spectral synthesis. However, whether these model predictions are realistic or not is not conclusively answered. The comparison between measured and predicted limb darkening is one of the main goals of this thesis.

For the study of the limb darkening I use *Kepler*'s high precision photometry of 48 main-sequence stars with different effective temperatures. These objects are eclipsed by orbiting planets causing typical transit signatures in the light curves. In contrast to the use of limb-darkening predictions in modeling these transits, the high quality of the data allows to measure the limb darkening together with the remaining transit parameters. These measurements are the most precise in the history of limb-darkening studies on stars other than the Sun.

For the prediction of limb darkening a precise knowledge of stellar parameters, e.g., the effective temperature and the surface gravity, is required. These parameters can be deduced from spectroscopic data using line-ratio measurements or synthetic spectra. I use high resolution VLT/UVES spectra of two well studied planet host stars (ε Eridani and CoRoT-2A) to present the determination of these parameters using a software tool based on spectral synthesis. The comparison of the parameters to those found in the literature reveals how reliable the used method is for synthesizing model limb intensities based on the resulting parameters. The most precise limb-darkening measurements available – those of our Sun – are well suited to compare them to such limb-darkening predictions. I present a direct comparison and introduce a rescaling of the model limb intensities that reduces systematic differences.

The current usage of limb-darkening laws in transit modeling is at least to some degree arbitrary. Therefore, I employ numerical methods to develop a highly efficient transit algorithm which is capable of directly using limb intensities from model atmospheres. Using this method opens up new possibilities for transit modeling, like simulating transits in any wavelength or filter band. Moreover arbitrary shapes of the planet and images of the Sun can be used as input.

Contents

List of Figures

*References of these figures are listed in the bibliography and they are cited under every image. All remaining figures are produced by the thesis author.

List of Tables

1 Introduction

Studies of other stars than the Sun are by nature more difficult since these objects are too far away to be resolved in observations. Although there are a few exceptions where the surface can directly be resolved using interferometry (e.g., Haubois et al., 2009) or Doppler imaging (e.g., Nesvacil et al., 2012), the information on the majority of stars can only be taken indirectly from the light which reaches us. We know that this light is powered by nuclear fusion deep inside the stars. However, the light that we can observe originates from the outermost part of the stars called the *stellar atmosphere*. Stellar characteristics like age, spectral class, and conclusions about their interior are driven by studies of the light coming from this region.

1.1 Stellar atmospheres

The stellar atmosphere contains hot gas and plasma and can be characterized by the temperature and the density as a function of height. As illustrated by Fig. 1.1, the temperature and density structure of the Sun's atmosphere allows dividing it into different layers. These layers are named (from bottom to the top) as *photosphere*, *chromosphere*, and *corona*. The corona – the largest part of the stellar atmosphere – can reach an extent of several stellar radii, depending on the state of magnetic activity. Certainly, only very little optical light is coming from this region of the atmosphere. For instance, the Sun's corona is only visible during solar eclipses or when a coronograph is used. The temperature of the coronal plasma is higher than one million degree, while the heating mechanisms are still not fully understood. At the bottom of the corona we find the transition region to the upper chromosphere, which is identified by a steep decrease in temperature down to the chromosphere, together with a rapid increase of the density. The position and the structure of this transition region is still under debate and depends on the magnetic activity causing coronal loops or holes. The thickness of the chromosphere itself is therefore also varying, but typically in the range of about 2500 km; compared to the size of the corona, this is not even one percent. The photosphere is the smallest part of the atmosphere. As visible in Fig. 1.1, the Sun's photosphere is only about 500 km thick. On stars other than the Sun its thickness can differ depending on the surface gravity, the temperature, and the composition of the hot gas (metallicity). The photosphere is also often called the stellar surface in visible light, because it is the region where the star becomes optically thick. Stellar spots and the granulation can be found here. Although this is the smallest region of the atmosphere, most of the observed light is coming from this layer. This includes the optical spectral absorption lines and the continuum, while in contrast most emission lines originate in the chromosphere. Due to the low amount of light, the other layers

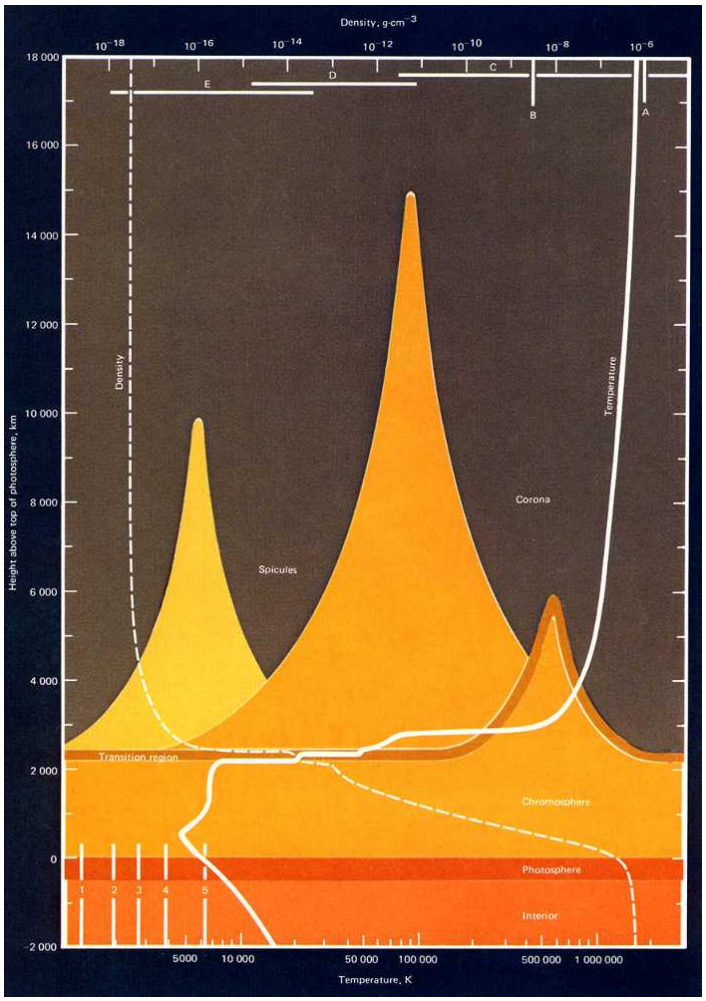

© [Eddy, 1979]

Figure 1.1: Temperature and density structure of the Sun's atmosphere. The height is measured from the top of the photosphere. Different parts of the atmosphere are *labeled*. For comparison some temperature and density regions are marked: *Numbered lines* (lower left corner) give the melting point of gold (1) and iron (2), and the boiling point of silver (3). The temperatures of an acetylene welding flame and an iron welding arc are marked with (4) and (5). *Lettered lines* (top) indicate the densities of the Earth's atmosphere at hight of 50 km (A) and 90 km (B), a mechanical vacuum pump (C), diffusion pump (D), and an ion pump (E). Information taken from picture reference.

of stellar atmospheres are much more difficult to study on stars further away than the Sun. Only with great technical effort using space-based X-ray observatories it is, e.g., possible to study stellar coronae. Nevertheless, today it is even possible to study the stellar interior. For instance, the region right below the photosphere sometimes called the sub-photosphere (e.g., Gray, 1976), which takes part in spot creation and evolution. These measurements are carried out using the techniques of helioseismology (e.g., Komm et al., 2013), which require high temporal resolution and an outstanding photometric precision.

Beside measurements another important part of modern stellar astrophysics is the simulation of their atmospheres. These simulations are, e.g., based on the absorption and transmission of light in hot gas or plasma. On the one hand, the theory is used to simulate the physics in stars to reproduce observations and, on the other hand, the theory also predicts observables which then could be proved by measurements. The first stellar model atmosphere was created by

McCrea (1931) who used a numerical integration to get the total number of neutral atoms and the electron pressure at a given optical depth. This made it possible to predict a more precise absorption than before, namely not only for hydrogen but also including other elements. Since then the numerical simulations got more and more complex and computationally demanding, which now require super computers with hundreds or even thousands of CPUs. Over the decades many model atmosphere codes were developed, e.g. PANDORA (Avrett & Loeser, 1992), MULTI (Carlsson, 1992), ATLAS (Kurucz, 2005), and PHOENIX (Hauschildt & Baron, 2010) just to mention some of them. These codes lead, e.g., to very precise model predictions and reproductions of observed stellar spectra. Therefore, they make important contributions to the further understanding of convection, radiation, and spectral line formation in the atmospheres of stars.

Both, observations and simulations of stellar atmospheres are irreplaceable astrophysical tools. Only their combination provides a fundamental understanding about stars and their development. The study of stars also helps us to understand the nature and processes of our own Sun. This thesis is mainly based on the analyses of light coming from the photosphere, except for a few examples to be found in Chapter 6. This includes spectral observations and photometry of transiting exoplanets. The spectral analysis is then carried out to determine fundamental stellar parameters, like their effective temperatures, by using synthetic spectra generated from model atmospheres. The photometric data is analyzed by transit modeling to measure the surface brightness distribution of these stars and to compare these results to predictions given by model atmospheres. Therefore, this work can give new insights to the quality and precision of the most recent available stellar model atmospheres.

1.1.1 The origin of stellar limb darkening

When observing the Sun in visual wavelengths one can see a decrease in brightness from disk center toward the limb (Fig. 1.2). Additionally, the limb of the Sun appears more red when compared to the center. These phenomena are summarized as *limb darkening* and can easily be observed using small telescopes or even by eye when using filters. In earlier days of astronomy the solar limb darkening was not known and even Galilei and also Huygens were of the opinion that the Sun has a homogeneous brightness distribution. The German Jesuit priest Christoph Scheiner, who lived at the time of Galilei, seems to be the first who found the Sun to be dimmer at the limb (G. Müller, 1897). However, the first quantitative measurements were made in the middle of the 18^{th} century by Pierre Bouguer. He determined the normalized intensity at 0.75 solar radii away from the center to about 73 % (Bouguer, 1760). Ghacornac (1859) then was the first who found that disk center and limb are different in color, which was later quantitatively measured by Vogel (1877) using spectroscopic observations. Naturally, there are much more astronomers who provided pioneering observations of the brightness distribution of the solar disk who I am not going to mention here. Instead, I recommend the book of G. Müller (1897) where one can find a short historical introduction about the observations and methods used to determine the solar brightness distribution across the disk.

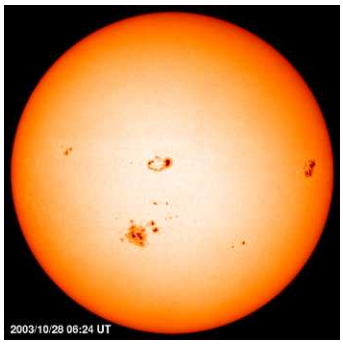

© [ESA & NASA, 2003]

Figure 1.2: Colorized image of the solar photosphere. The limb darkening is clearly visible as well as prominent spot groups. The limb appears also more red compared to the center.

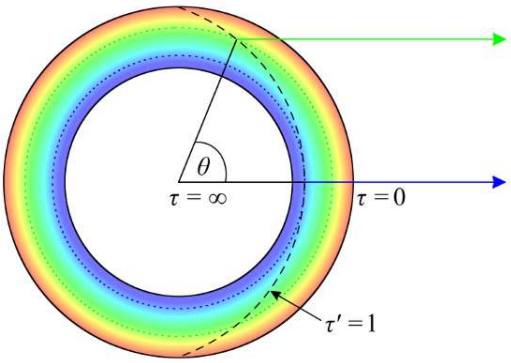

Figure 1.3: The reason of limb darkening. *Colored ring* represents the photosphere with hot (*blue*) and cool layers (*red*). *Dashed curve* indicates unit optical depth in direction of the line-of-sight. See also, e.g., Gray (1976, Fig. 9.2).

The knowledge about the fact that the Sun is not only a simple glaring sphere but rather surrounded by an atmosphere is essential for the understanding of limb darkening. We have seen in Fig. 1.1 that the photosphere is the lowest part of the Sun's atmosphere and it is the origin of the visible light and actually of the limb darkening. Like the Earth's atmosphere, the photosphere shows *extinction* that means it scatters light and also absorbs a certain amount of it. Therefore, the *optical depth* $\tau_\nu = \int_a^b \kappa_\nu \rho \, \mathrm{d}x$ is introduced. κ_ν is the frequency dependent absorption coefficient and ρ the density of the material. The optical depth describes the fraction of radiation that is scattered or absorbed on a path a to b. In other words τ_ν is a measure of transparency for a given frequency ν of the light. For values of $\tau_\nu \gg 1$ we say the atmosphere is optically thick and the mean free path of the photons is smaller than their wavelength. For $\tau_\nu \ll 1$ the atmosphere is optically thin and the mean free path of the photons is larger than the wavelength. An optical depth of $\tau_\nu = 1$ reduces the intensity of the radiation to $1/\mathrm{e}$. In the scheme of radiative transfer theory it is appropriate to use the optical depth as a measure of the geometrical depth in stellar atmospheres. At the stellar surface the optical depth is zero and in the center of the star it is infinity. The change of emergent intensity I_ν with optical depth is then given by

$$\frac{\mathrm{d}I_\nu}{\mathrm{d}\tau_\nu} = I_\nu - S_\nu \,, \tag{1.1}$$

which is a basic form of the *radiative transfer equation*. S_ν is called the *continuum source function* that describes the ratio of emission and absorption. However, Eq. 1.1 describes only the change of intensity perpendicular to the surface along the τ_ν-axis. As indicated by Fig. 1.3 this is only appropriate for light coming from disk center. For other disk positions the light seen by an observer has an exit angle θ with respect to the surface normal. Equation 1.1 is intuitively adapted to account for that angle and the radiative transfer equation then reads

$$\cos(\theta)\frac{\mathrm{d}I_\nu}{\mathrm{d}\tau_\nu} = I_\nu - S_\nu \,. \tag{1.2}$$

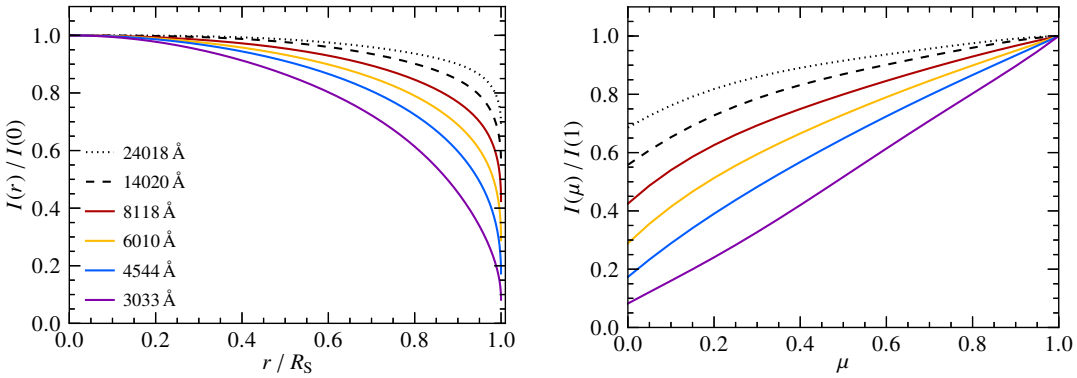

Figure 1.4: Solar limb darkening in different wavelengths (*labels*). Data taken from Pierce & Slaughter (1977) and Pierce et al. (1977), and plotted against the radial disk coordinate r (*left*) and using the limb angle μ (*right*). All profiles are individually normalized to corresponding disk center intensities.

For $\theta = 90°$ an observer looks parallel to a photospheric element with constant τ_ν and sees no change in intensity. This would be the case for a position at the disk limb. For disk center ($\theta = 0°$) this equation becomes the same as Eq. 1.1. The integrated form of Eq. 1.2 yields

$$I_\nu(0,\theta) = \int_0^\infty S_\nu \, \mathrm{e}^{-\tau_\nu \, \sec(\theta)} \sec(\theta) \, \mathrm{d}\tau_\nu \,, \tag{1.3}$$

which is the emergent intensity at the surface (e.g., Gray, 1976). The exponential factor is the extinction which scales with $-\tau_\nu \sec(\theta)$. We see that the intensity is massively influenced by that angle dependent extinction, since the secant reaches infinity for $\theta = 90°$. Consequently, the optical depth in the direction of the line of sight

$$\tau'_\nu = \tau_\nu \sec(\theta) \,, \tag{1.4}$$

reaches unity much earlier than the radial optical depth τ_ν. This is illustrated by the dashed line in Fig. 1.3. This hypothetical $\tau'_\nu = 1$ surface moves upward closer to the stellar surface for increasing θ. This means that an observer looks at higher photospheric layers at the limb than compared to the center. Due to the outward decreasing source function higher photospheric layers are less bright and also cooler which is in the end the reason for the limb darkening.

Since Bouguer (1760) the solar limb darkening has been measured with increasing accuracy. One of the most precise measurements of the last century is shown in Fig. 1.4. The measurements were made for a wide wavelength range covering optical and infrared spectral regimes. It is easily visible that the brightness decreases toward the disk limb ($r/R_S = 1$) and that this darkening is more pronounced for shorter wavelengths. The stronger extinction in short wavelengths together with the lower temperature at higher photospheric layers is the reason for the color dependence of the limb darkening. Therefore, measuring the limb darkening can also be used to determine the temperature structure of the photosphere.

Table 1.1: Summary of the most common limb-darkening laws.

Name	Equation	Reference
linear	$I(\mu)/I(1) = 1 - u(1-\mu)$	Schwarzschild (1906)
parabolic [a)]	$I(\mu)/I(1) = 1 - a(1-\mu) - b(1-\mu^2)$	Chalonge & Kourganoff (1946)
quadratic [b)]	$I(\mu)/I(1) = 1 - u_1(1-\mu) - u_2(1-\mu)^2$	Kopal (1950)
3-term log.	$I(\mu)/I(1) = 1 + \sum_{k=1}^{3} c_k \ln(\mu)^k$	Sykes (1953)
cubic	$I(\mu)/I(1) = 1 - v(1-\mu) - v'(1-\mu)^3$	van't Veer (1960)
logarithmic [c)]	$I(\mu)/I(1) = 1 - A(1-\mu) - B\mu\log(\mu)$	Klinglesmith & Sobieski (1970)
P_5	$I(\mu)/I(1) = \sum_{n=0}^{5} A_n \mu^n$	Pierce & Slaughter (1977)
square root	$I(\mu)/I(1) = 1 - c(1-\mu) - d(1-\sqrt{\mu})$	Diaz-Cordoves & Gimenez (1992)
nonlinear	$I(\mu)/I(1) = 1 - \sum_{k=1}^{4} a_k(1-\mu^{k/2})$	Claret (2000)
exponential	$I(\mu)/I(1) = 1 - g(1-\mu) - h(1-\mathrm{e}^{\mu})^{-1}$	Claret & Hauschildt (2003)
3 para. nonlin.	$I(\mu)/I(1) = 1 - \sum_{k=2}^{4} c_k(1-\mu^{k/2})$	Sing et al. (2009)

Notes: [a)] Original form: $A + B\mu + C\mu^2$, with $A = 1 - a - b$. [b)] Many authors refer to Kopal (1950) as the inventor of this law, but it seems to me that *his* presented equation is a different form of the parabolic law. The earliest source I can confirm for the quadratic law is van't Veer (1960, Eq. 18 a). [c)] The authors used a logarithm to the base 10, several others the $\ln(\mu)$, e.g. Orosz & Hauschildt (2000) and Claret (2000). Using the LDCs from the authors to create the limb profiles verifies this statement.

Because of the secant in Eq. 1.3 the measurement of the intensity close to the limb is difficult. The brightness drops off rapidly and for accurate measurements one has to acquire more points at the limb region. For a clearer illustration of the extreme limb regions it is appropriate to choose a different coordinate to express the disk position. When assuming $\tau'_\nu = 1$ we can directly infer from Eq. 1.4 that

$$\tau_\nu = \cos(\theta) \equiv \mu\,. \tag{1.5}$$

The μ-value is used as an abbreviation and often called the *limb angle*. At disk center is $\mu = 1$ and at the limb we find $\mu = 0$. Due to the nonlinear nature of μ, regions close to the limb are stretched as can be seen in the right panel of Fig. 1.4. This μ-axis is commonly used in limb-darkening studies and has, eventually, a physical meaning. Furthermore, the geometry of the problem (Fig. 1.3) allows us to express μ as a function of the radial coordinate, namely

$$\mu = \sqrt{1 - r^2} = \cos[\sin^{-1}(r)]\,, \tag{1.6}$$

which offers the opportunity to easily transform μ into the radial coordinate r and vice versa.

The empirical limb darkening as shown in Fig. 1.4 is usually approximated by a function of μ. Such a function is, e.g., used when modeling photometric time series data of eclipsing binaries. The simplest limb darkening description used for that purpose is a linear function. However, we have seen in Fig. 1.4 that the limb darkening is not linear and shows at most wavelengths a significant curvature. Hence, functions with higher orders are needed for appropriate intensity descriptions. I summarize in Table 1.1 some of the commonly used limb-darkening parameterizations proposed over the years. Of course there exist more

limb-darkening descriptions not mentioned here, like Barban et al. (2003) who presents a generalization of the cubic equation. However, all of these equations are only approximations to the real intensity distributions, although they are called *limb-darkening laws*. The diversity of the available laws implies that one is still uncertain about the correct description of stellar intensity distributions. In this regard, Neckel (2003) stated that among all laws the fifth order polynomial, P_5, is the best description of the solar intensity distribution available.

All limb-darkening laws share the characteristic that they need a certain number of coefficients, which are called *limb-darkening coefficients* (LDCs). In contrast to the simple linear law, e.g., the quadratic law introduces a second coefficient that causes a curvature, which leads to a much better description of the limb darkening. When looking at the derivatives

$$\frac{\mathrm{d}I}{\mathrm{d}\mu} = u_1 + 2u_2(1-\mu)\,, \tag{1.7}$$

$$\frac{\mathrm{d}^2I}{\mathrm{d}\mu^2} = -2u_2\,, \tag{1.8}$$

we can see that the curvature is only adjusted by u_2 while the gradient is influenced by both coefficients. However, the influence of u_2 is changing with the limb angle and it is more pronounced for positions close to the limb. To achieve a darkening the coefficients can only be adjusted in a certain range. As already shown by Kipping (2013) one can give physical constraints on the values of u_1 and u_2 by applying the assumptions that the intensity and the gradient have to be always positive. Together with the derivatives he shows that

$$u_1 + u_2 < 1\,, \qquad u_1 + 2u_2 > 0\,, \qquad u_1 > 0\,. \tag{1.9}$$

The strength of the limb darkening can, however, be estimated by calculating the integral of the quadratic limb-darkening law

$$\int_0^1 I\,\mathrm{d}\mu = 1 - \frac{u_1}{2} - \frac{u_2}{3}\,. \tag{1.10}$$

Low values of this integral indicate strong limb darkening which is mainly caused by a high value of u_1. If we look at cooler photospheric layers, e.g., using a red filter or observing through interstellar dust causing extinction, we will see weaker limb darkening but with a stronger curvature toward the stellar limb (cf. Fig. 1.4). Translated into limb-darkening coefficients, when using the quadratic law, one would see smaller values for u_1 und larger values for u_2, compared to hotter photometric layers where the limb darkening is stronger and also more linear. I will show later on that this quadratic law is quite accurate and a good choice, e.g., in transit modeling.

The limb-darkening coefficients are the base of all reasoning in modeling of the limb darkening and in general they are unknown. To measure the limb darkening and to acquire the coefficients by fitting, we have to observe the intensity distribution across the stellar disk. Due to the

distances it is a challenging task to directly measure the limb darkening on other stars than the Sun. Therefore, most techniques available are only indirect methods where the information about the stellar surface is drawn from light curves. For instance, a second object passes the line of sight blocking light coming from specific parts of the stellar surface. This is given in the case of eclipsing binaries (e.g., Claret, 2008) or planetary transits (e.g., Knutson et al., 2007), which are the most common methods to acquire limb-darkening information. A more elaborate technique is the observation of microlensing events (Zub et al., 2011). Thereby light from different parts of the stellar surface are magnified by a foreground moving gravitational lens. However, these events are quite rare and provide only a limited precision. A method to directly measure the surface brightness distribution is optical interferometry. This method tries to image the stellar surface, which is only feasible for close stars with large radii. Using this method, Haubois et al. (2009) present the determination of the limb darkening over a few surface elements of Betelgeuse. In principle, it is also possible to determine the limb darkening from the shape of spectral lines, which appears as an additional broadening as mentioned by Frisch (1975). However, other broadening mechanisms (see Chapter 2) have to be known in detail to use this method.

I showed above that limb darkening is the visible result of the outward changing source function $S_\nu(\tau)$. To find the source function is not a trivial task and part of radiation transport theory and, therefore, part of stellar model atmospheres. Consequently, there exists no exact analytical solution for describing the limb darkening. In the next subsection I will present some approximations developed by several authors.

1.1.2 Theoretical approach to the limb darkening

Karl Schwarzschild introduced the concept of *radiative equilibrium* (Schwarzschild, 1906), which should occur in an atmosphere where the exchange of energy is dominated by radiation. Before this groundbreaking idea, it was believed that the Sun's atmosphere is in adiabatic equilibrium, which means energy is mainly transported by convection. In his work he showed that the radiation F into one direction can be written as

$$F(i) = \frac{A_0}{2}(1 + 2\cos i)\,, \qquad F(0) = \frac{3A_0}{2}\,, \tag{1.11}$$

with i describing the angle between the direction of the radiation and the surface normal. The underlying geometry is the same like demonstrated in Fig. 1.3. Thus, this equation can be interpreted as a prediction of the brightness distribution on the solar disk, with $F(0)$ being the radiation seen at disk center. Normalized by the disk center radiation this yields a theoretically introduced limb-darkening law of the form

$$\frac{F(i)}{F(0)} = \frac{1}{3} + \frac{2}{3}\cos i = 1 - \frac{2}{3} + \frac{2}{3}\cos i = 1 - \frac{2}{3}(1 - \mu)\,. \tag{1.12}$$

This is in fact a linear description of the limb-darkening, with a constant coefficient ($u = 2/3$). Compared to measurements, Eq. 1.12 was the best approach available in these days, which

Schwarzschild commented as an empirical justification of the concept of radiative equilibrium. Consequently, the Sun's atmosphere is not in adiabatic equilibrium, which shows by theory an normalized intensity distribution equal to $\cos i$.

An even more precise approximation of the radiation field in the solar atmosphere was developed by Arthur Eddington (Eddington, 1926, § 226). He assumed that the intensity could be split into an inward and an outward component, which both are constant at any optical depth. This leads to an emergent intensity of

$$I_{\mathrm{E}}(\mu) = \frac{3}{4\pi}\sigma T_{\mathrm{eff}}^4 \left(\mu + \frac{2}{3}\right), \tag{1.13}$$

see, e.g., Hubeny & Mihalas (2014, p. 571) for more details. Is this solution again normalized by the disk center intensity, then the constants vanish and we get

$$\frac{I_{\mathrm{E}}(\mu)}{I_{\mathrm{E}}(1)} = \frac{3}{5}\left(\mu + \frac{2}{3}\right) = 1 - \frac{3}{5}(1-\mu)\,. \tag{1.14}$$

This is again a linear limb-darkening description, but with a smaller coefficient than found in Eq. 1.12. Hence, this relation yields a slightly weaker limb-darkening prediction. Nevertheless, as mentioned before in Section 1.1.1 the actual limb darkening is by no means linear. As a consequence we need more accurate approximations, which can be obtained by introducing the Λ-operator. This operator is essential to approximate the angle averaged intensity

$$J = \frac{1}{4\pi}\int_{4\pi} I \,\mathrm{d}\omega\,, \tag{1.15}$$

for a given source function S. We write

$$J(\tau) \equiv \Lambda_\tau[S(t)] = \Lambda_\tau[J(t)], \qquad \text{with} \qquad \Lambda_\tau[f(t)] \equiv \frac{1}{2}\int_0^\infty f(t)\, E_1(|t-\tau|)\,\mathrm{d}t. \tag{1.16}$$

In this scheme we have to make an initial guess of the source function and derive then the integral shown in Eq. 1.16. The result is then again used as an initial value to calculate the integral again. This process is called Λ-iteration and repeated until $J(\tau)$ converges. For simplicity we now only perform one Λ-iteration, using Eq. 1.13 from the Eddington approximation together with Eq. 1.15, as an initial value. This leads to a mean intensity over which we integrate analogous to Eq. 1.3 to get the emergent intensity. The normalized result is not as short as the previous examples and written as

$$\frac{I_{\mathrm{E}}^1(\mu)}{I_{\mathrm{E}}^1(1)} = \frac{\frac{7}{12} + \frac{1}{2}\mu + (\frac{1}{3}\mu + \frac{1}{2}\mu^2)\ln([1+\mu]/\mu)}{\frac{13}{12} + \frac{5}{6}\ln(2)}\,. \tag{1.17}$$

This equation is obviously not strictly linear anymore and predicts a normalized intensity of 0.35 at the limb. This value is about 13 % lower than achieved from the simple Eddington

approximation, but only 5 % higher than provided by Schwarzschild's approach. This is caused by a weak curvature provided by this prediction found close to the limb. In contrast to the intensities at the limb, the deviation from the Eddington distribution is negligibly small for most μ-values. Thus, Eq. 1.17 provides only a bit stronger limb darkening than Eq. 1.14. For more details about the presented limb-darkening approximation and the used Λ-iteration method, see Hubeny & Mihalas (2014).

Beyond these examples of approximations, there exist an exact solution of the problem predicting the emergent intensity, provided by Eberhard Hopf (Hopf, 1934, § 25). His solution is fairly complicated and available in different forms. Here I present the form

$$\mathcal{H}(\mu) = \frac{1}{\sqrt{1+\mu}} \exp\left[\frac{1}{\pi}\int_0^{\pi/2} \frac{\theta \tan^{-1}(\mu \tan\theta)}{1-\theta\cot\theta}\,\mathrm{d}\theta\right], \tag{1.18}$$

given in Hubeny & Mihalas (2014, Eq. 17.35), and leave it unnormalized for the purpose of clarity. The value of the disk-center intensity $\mathcal{H}(1)$ to be used as normalization constant is ≈ 2.91. For $\mu = 0$ this equation predicts a normalized intensity of 0.34, which is compared to the previous example again an indication for a slightly stronger limb-darkening prediction. The shape of the distribution is comparable with the one achieved when using Eq. 1.17 and it is hard to distinguish between them for $\mu > 0.3$. For a comparison of the shapes of all mentioned limb-darkening predictions I put them together in Fig. B.1.

The presented Equations 1.12, 1.14, 1.17 and 1.18 are solutions for a planar gray atmosphere in local thermodynamic equilibrium. This means that the geometry and the equations are only one-dimensional, the opacity is independent of wavelength, and the gradients of the physical conditions of the material are small in observed time scales. This is obviously a simplified assumption of the Sun's atmosphere. The assumed unrealistic opacity also implies that the limb darkening should not show any color dependence. Moreover, the absence of spectral lines in this theory is a great simplification. We know that millions of spectral lines have a crucial influence on the atmosphere's opacity, which is called *line blanketing*. Therefore, the actual limb darkening is also dependent on the presence of spectral lines and could only be predicted when accounting for them. Including, e.g., spectral lines and wavelength dependent opacities require numerical methods, which is actually one reason why we rely on model atmosphere codes to predict the limb darkening.

1.1.3 Influence of stellar parameters on the limb darkening

I showed in the above subsections that limb darkening is an inherent property of the photosphere. Consequently, we expect a connection between the characteristics of the photosphere, like chemical composition or temperature, and the limb darkening. To examine the parameter space and the influence on the limb darkening it is appropriate to use a grid of model atmospheres and, e.g., to study the changes of the limb darkening coefficients for one specific law. Claret (2000) already presented such analysis of the coefficients for the nonlinear limb-darkening law.

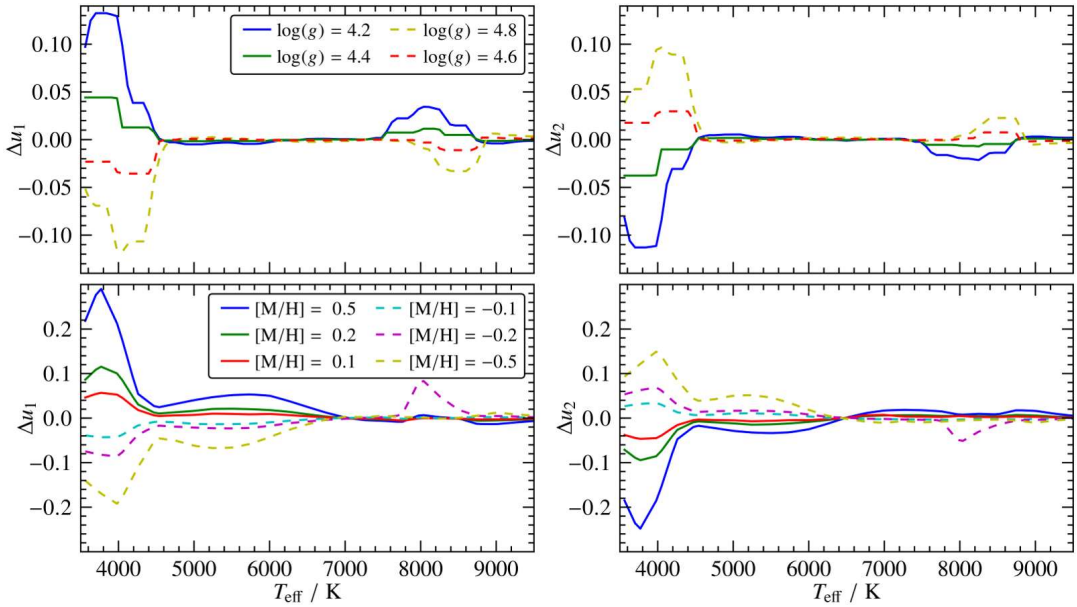

Figure 1.5: Influence of the surface gravity (*top*) and the metallicity (*bottom*) on the quadratic limb-darkening coefficients. The curves show differences between coefficients determined with different values for $\log g$ and [M/H] (*labels*) and predictions for $\log(g) = 4.5$ and [M/H] = 0.0. The models are based on ATLAS atmospheres in Johnson-V band. See text for details and Fig. B.2 for the effect of the microturbulence.

I will concentrate on the quadratic law because it plays a major role in this thesis and we will see that it is accurate enough for most applications.

For the analysis I used limb-darkening coefficients provided by Claret & Bloemen (2011) based on ATLAS model atmospheres. This multi-dimensional grid of coefficients depends on the effective temperature, the surface gravity, the microturbulent velocity, and the metallicity. To get the coefficients for one specific set of stellar parameters, I linearly interpolated on that grid. In Fig. 1.5 I show the effect of $\log g$ and [M/H] on the quadratic coefficients for a reasonable effective temperature range. Shown are the differences, e.g., between u_1 determined for $\log(g) = 4.5$ and [M/H] = 0.0, and values of u_1 determined for higher and lower values of these parameters. This is almost the same approach I showed in Müller et al. (2013, Sect. A) where I used the *Kepler* bandpass. However, this time I show the limb-darkening dependence as seen in a Johnson-V filter, change the sign of the differences for a more intuitive interpretation of the results, and present u_2. One can clearly see that the influence of the varied parameters is temperature dependent. There exists a temperature range (≈ 4500 K to ≈ 7500 K) where almost no influence of $\log(g)$ is visible. In contrast, for stars cooler than ≈ 4500 K we see a strong sensitivity on $\log(g)$. If we look at the bottom panels of Fig. 1.5 we see that the metallicity has a stronger effect on the limb darkening and also for a wider temperature range. However, I chose rather extreme values for the metallicity, since according to Casagrande et al. (2011) the metallicities of most stars in the solar neighborhood lie in the interval of

[M/H] = ±0.2. For such metallicities the coefficients show only a change of ±0.02 at 5500 K and, therefore, the metallicity behaves similar like $\log(g)$ and is only important for cooler stars. The microturbulent velocity does not show a clear temperature dependence like $\log(g)$ or [M/H] and has only a weak influence on the limb darkening at all (see, Fig. B.2). For the chosen temperature range the deviation from the coefficients determined with $\xi = 2.0\,\mathrm{km\,s^{-1}}$ never exceeds ±0.015 for both coefficients.

As already stated above, the presented curves are generated for a Johnson-V filter band. If we would repeat this analysis in different spectral bands we would see slightly different sensitivities of the limb darkening on the presented parameters. Like the limb darkening that becomes weaker when observed in red light also the influence of the discussed parameters becomes weaker in, e.g., a Johnson-I filter. In the case of $\log(g) = 4.5$ the peak value of the difference in u_1 is only ±0.09. For a metallicity of [M/H] = 0.5 the peak value is below ±0.2. The situation changes if we consider a Johnson-U filter. Compared to the curves in Fig. 1.5 the influence of $\log(g)$ is not stronger but also significant for temperatures of about 5000 K. For higher temperatures $\log(g)$ introduces a similar behavior to the coefficients like the metallicities in Fig. 1.5 with a maximum difference of both coefficients of ±0.02. If we consider the influence of the metallicity in this filter band, we see that the significant peaks around 4000 K are gone. However, the limb darkening now seems to be slightly more sensitive to [M/H] around 6000 K when compared to Fig. 1.5 and shows a peak difference of about ±0.04 for [M/H] = ±0.2.

From the presented analysis we can infer that higher surface gravities and lower metallicities both lead to weaker limb darkening. On the one hand, the circumstance that the limb darkening depends on fundamental stellar parameters makes it necessary to have a reasonable estimate of these parameters, before one can rely on predicted limb darkening for modeling. On the other hand, we are able to learn something about the fundamental parameters of stars by studying their limb darkening (see Neilson & Lester, 2012). Figure 1.5 allows us to estimate the sensitivity of the limb darkening on these stellar parameters. The dependence of the limb darkening on the effective temperature is not shown here. However, it will be part of some figures in Chapter 4 and can be summarize as it is stronger for cool stars and decreases with temperature.

1.2 Extrasolar planets

During the last few decades the observations and studies of planets orbiting other stars than the Sun have become a popular field in astronomy. Especially in the last five to ten years this development was mainly driven by space-based missions (CoRoT and *Kepler*) searching for undiscovered transiting extrasolar planets. The determination of the physical parameters of these exoplanets, such as their temperatures, radii, and densities, is only possible with a precise knowledge of the parameters of their parent stars. These stellar parameters are mainly deduced using spectroscopic observations, partially introduced later on in Chapter 2. However,

exoplanets can be for their part a new tool to study properties of stars, like the center-to-limb brightness distribution, which also includes spots and faculae.

In the following subsections I will give a brief introduction to the discovery of the first exoplanets and the most important detection methods. At least some of these methods are influenced by the center-to-limb brightness distribution of their host stars. For instance, the transit method on which I will concentrate in this thesis. In Section 1.3 I will then discuss the transit method in more detail.

1.2.1 First planet detections and their definition

The ancient astronomers had to rely on their eyes for observations, thus they were limited to bright celestial bodies. This included the Sun, the Moon, comets, bright stars and objects which we know as our solar system *planets*. Originally, depending on their movements at the sky these objects were all classified as either stars or planets. The latter term has its origin in the early Greek astronomy where they invented the word πλανητης (*planetes*), which means "wandering star". The development of the first small telescopes and the concept of the heliocentrism gave rise to a more modern definition of planets being objects orbiting the Sun. Further progress in the instrumentation made it feasible to discover much fainter planets than before. This concerns Uranus (1781, W. Herschel), Neptune (1846, J. G. Galle), and – almost 85 years later – Pluto (1930, C. Tombaugh), which was previously predicted by distortions of the orbits of Uranus and Neptune (Unsöld & Bascheck, 2005). After that more and more so-called trans-neptunian objects (TNOs) were found. It is believed that most of them are still undiscovered and that at least some of them could be even more massive than Pluto. Therefore, the International Astronomical Union (IAU) invented a new class of planets, which should include all "planet-like" solar system bodies historically not counted as planets, such as Ceres and all TNOs. This new class is called *dwarf planets* and to be distinguished from the classical planets according to the following characteristics (IAU, 2006):

- A *planet* is a celestial body, which a) orbit's around the Sun, b) accreted enough mass to be in hydrostatic equilibrium (almost round shape), and c) has cleared the neighborhood of its orbit from smaller bodies.

- A *dwarf planet* is a celestial body, that a) same as planet, b) same as planet, c) has not cleared the neighborhood of its solar orbit, and d) is not a satellite.

- *Small solar-system bodies* are all other objects that are neither a planet nor a dwarf planet, except satellites, also orbiting the Sun.

According to this definition Pluto lost its planetary status and was from now on counted as a dwarf planet. This IAU resolution is controversial not least because Pluto is not a planet anymore, but also because there were a few more or different characteristics proposed (Basri & M. E. Brown, 2006), e.g., taking their formation or mass into account. In the end, the found

consensus solves the immediate problem of an increasing number of solar system planets caused by new discoveries of TNOs.

Since the development of the telescope and the motivation of the Copernican model, the only known planets were those of our own solar system, divided into the inner, small and rocky planets (Mercury, Venus, Earth and Mars), and the outer gas giants (Jupiter, Saturn, Uranus and Neptune). In the year 1992 things changed due to the discovery of a planetary system orbiting a neutron star (Wolszczan & Frail, 1992). This neutron star was detected two years before by Aleksander Wolszczan as a millisecond radio pulsar with a pulse period of 6.2 ms. The authors found periodicities in the pulse period, which they attribute to at least two orbiting planets with 2.8 M_{Earth} and 3.5 M_{Earth}. The remarkable idea is that the planets have formed after the super-nova explosion. This assertion is also provided by their relatively small distances from the pulsar of about 0.5 AU and 0.4 AU. At these distances they should not have survived even the red-supergiant phase of their host star. Nevertheless, this was the first distinct detection of planets outside of our solar systems. However, there was already a claimed exoplanet detection in 1989, but rejected because it was believed that this object is a *brown dwarf*. These objects are too light to start hydrogen core fusion, but they are heavy enough to start deuterium or lithium fusion. The limit for this kind of energy production is in the range of $13 - 75\ M_{\text{Jup}}$, where the lower value defines the border at which deuterium burning can occur. More recent observations indicate that the object discovered in 1989 could actually be a real planet with a mass just below the deuterium burning limit (Kane et al., 2011). Beyond this revised planet detection, the first most unambiguous detection of a extrasolar planet was reported by Mayor & Queloz (1995). They measured a periodic velocity shift of 51 Pegasi in the direction of the line of sight caused by the orbiting planet. With at most 2 M_{Jup} and an orbital period of 4.2 days this planet was for a long time the first known exoplanet orbiting a solar-like star.

The discovery of more exoplanets and planetary systems will help to answer important questions about our own solar system, like how it was formed and how unique the structure is. In the end it will also help to answer the most challenging question: do habitable exoplanets comparable to the Earth exist?

1.2.2 Detection methods

There are several different methods for the detection of exoplanets that are continuously improved by new instrumentation. Almost all of them are *indirect* methods, so that the planet is not resolved in observations. Only by analyzing the light coming from the stars and searching for periodicities, we are able to draw conclusions about the existence of low-mass objects orbiting these stars. I will give here a short introduction into some important detection techniques and comment on their advantages or disadvantages. For a more general introduction I recommend the work of Perryman (2014), who provides an excellent overview of all detection methods.

Direct imaging

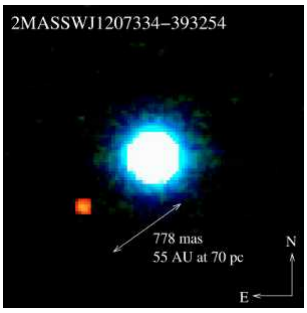

© [Chauvin et al., 2004]

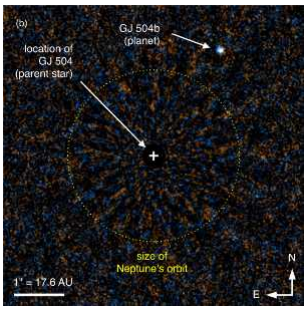

© [Kuzuhara et al., 2013]

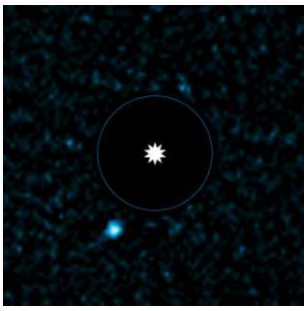

© [ESO/J. Rameau, 2013]

Figure 1.6: Three exoplanets detected by direct imaging. *Left*: First direct imaging planet 2M1207 b *red* and its host (a Brown Dwarf) *blue*. *Center*: GJ 504 b *small dot* at the upper right. Its host star is removed by image processing. *Right*: HD 95086 b *blue dot* at the lower left. Host star also removed by image processing. Position indicated by the *white symbol*. The blue line marks size of Neptune's orbit.

Direct imaging is the most intuitive detection method of exoplanets. The basic idea is to take an image of the planet on its orbit around the star. This is not to be understand as catching a resolved image of the planets surface, but rather the reflected star light or its own emission. The instrumental requirements for this method are very high. For instance the telescopes are operated using adaptive optics to reduce effects caused by the Earth atmosphere or tiny coronographs placed into the optical path to reduce the light coming from the host star. The required resolution of these instruments, to separate stellar and planetary point-spread-functions, can be determined by using the definition of the *parallax*

$$\sin \varpi = \frac{a}{d}. \tag{1.19}$$

If the distance d is given in parsec and the semimajor axis a of a hypothetical planet in astronomical units, then ϖ is measured in arcseconds. Using this relation we estimate that the angular distance between Jupiter's orbit and the Sun would be $0.17''$, when seen from a distance of 30 pc. Actually, the Very Large Telescope (VLT) is able to provide a resolution of typically $0.05''$/px using adaptive optics[1]. However, the resolution is not the only problem to solve. The more challenging part is to deal with the brightness contrast between star and planet. In optical wavelengths Jupiter is 10^9 times fainter than the Sun, while in the infrared this ratio is only 10^4. This is caused by Jupiter's self radiation that exceeds the reflected Sun light in the infrared. Therefore, this detection method is biased toward young and still hot planets, with large semimajor axes[2] of the order of $10^2 - 10^3$ AU. Unfortunately, the masses of such planets are hard to determine and normally estimated with evolution models. These masses have large uncertainties and in some cases detected objects turned out to be brown dwarfs.

[1] http://www.eso.org/sci/facilities/paranal/instruments/naco/overview.html
[2] http://exoplanet.eu

Radial velocity

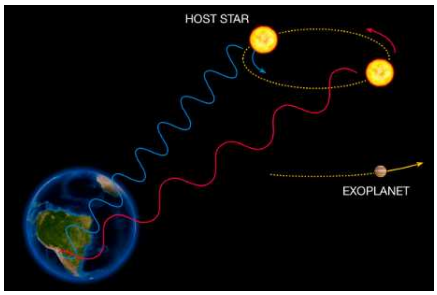

© [ESO, 2007]

Figure 1.7: Illustration of the radial velocity method. The planet and its host star are orbiting around their barycenter. This leads to a back and forth movement measurable as a Doppler shift of the star's light. *Blue* waves indicate blue shifted light when the star moves toward the observer, while *red* waves are measured when the stars moves in the opposite direction.

A totally different method is the *radial velocity* method. In contrast to direct imaging, this method does no try to detect planets by taking images. For the observations we need high resolution spectrographs to analyze the velocity component of the presumed host stars that is parallel to the line of sight. If a planet orbits a star, both bodies orbit around their center of mass. If the orbital plane is not oriented face-on, we will be able to measure a periodic change in the star's radial velocity. Therefore, this method belongs to the group of the indirect planet detection methods, since we only measure the influence of one or more orbiting masses on the host star. This is actually a spectral line shift caused by the Doppler effect written as

$$\frac{\Delta\lambda}{\lambda} = \frac{v}{c}\sin i = \frac{1}{c}\frac{2\pi r_S}{P}\sin i\,. \tag{1.20}$$

Due to the unknown inclination angle i of the orbital plane, the measured velocity is just a lower limit of the actual stellar motion induced by the orbiting planet. With the orbital period P and Kepler's third law, we can calculate the semimajor axis a of the planet's orbit, if we assume that the mass of the host star is known from stellar models. The distance of the star from the center of mass r_S is given by

$$r_S = a\,\frac{M_P}{M_S + M_P}\,, \tag{1.21}$$

which allows us to estimate the planetary mass. This mass is obviously again only a lower limit, because the value of $\sin i$ remains unknown. If we take Jupiter as an example, the Sun shows a radial velocity shift of at most $12.5\,\mathrm{m\,s^{-1}}$, when an observer would look edge-on to Jupiter's orbit. The major problem would be to observe the whole orbit, since Jupiter's orbit lasts almost twelve years. Therefore, this method is well suited for close-in planets with short orbital periods and massive planets or light stars which cause large radial velocity amplitudes. Additionally, to achieve enough signal-to-noise in the spectral observations, bright stars are preferred, as well as inactive stars with many spectral lines. Today's instrumentation is able to detect radial velocity shifts of at least $50\,\mathrm{cm\,s^{-1}}$. However, stellar intrinsic oscillations can cause velocity shifts on the same order and, therefore, the limitations of this method are not given by instrumentation (Mayor et al., 2003).

Planetary transits

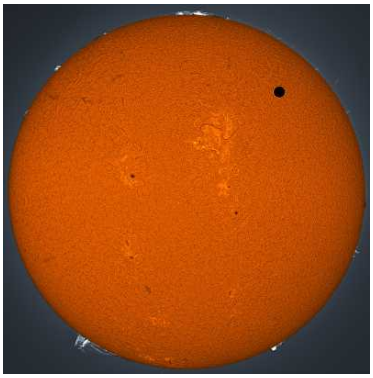

© [Hetlage, 2012]

Figure 1.8: Colorized H_α image of the Sun during the Venus transit 2012. The Venus is visible as the *black dot* at the upper right part.

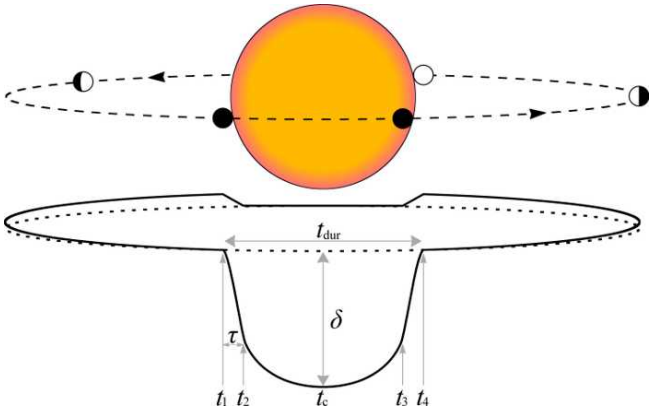

Figure 1.9: Illustration of a transit event. *Dashed* curve marks the planetary orbit, while the *solid* curve below shows the measured phase-dependent flux. The *dotted* curve represents the stellar flux without reflected light from the planet. Figure inspired by Winn (2009, Fig. 1).

A detection method of still increasing popularity is the observation of planetary transit light curves. During the last years this method was especially driven by the two space-based observatories CoRoT and *Kepler*. These instruments perform photometric observations to monitor the brightnesses of stars. If an orbiting planet eclipses its host star, the planetary disk blocks a part of the stellar light and the measured stellar flux is decreased by that amount. The relative flux change depends on the stellar surface area, which is covered during the eclipse, and can simply be expressed by the squared ratio of the involved radii,

$$\frac{\Delta\mathcal{F}}{\mathcal{F}} \approx \left(\frac{R_\mathrm{P}}{R_\mathrm{S}}\right)^2 . \tag{1.22}$$

This value is an approximation and only correct when limb darkening is negligible. Otherwise more light would be blocked at disk center and the transit depth, δ, increases. In Fig. 1.9 I present a typical transit event together with its light curve. During its orbit the planet shows phases because the planet reflects stellar light from its day-side into the direction of the line of sight. This reflected light contributes to the total flux measured from the system. This contribution is increasing until the planet starts to disappear behind the star which leads to a secondary transit.

The idea to search for periodic dimming of stars to detect exoplanets is quite obvious. Therefore, it is not easy to find out who first proposed this method. Otto von Struve mentioned in a proposal for radial velocity measurements (Struve, 1952) that it might be possible to observe eclipses of planet-like bodies. However, he concluded that radial velocity measurements would be more accurate when using the available instrumentation in these days. Almost 20 years later

Rosenblatt (1971) presented an additional detection method based on the color dependence of the stellar limb darkening. Due to the fact that the limb darkening is stronger in the blue than in the red light, the star appears slightly more blue when the planet is at the limb, blocking mostly red light. This effect vanishes while the planet moves toward the center of the stellar disk and becomes again pronounced when approaching the opposite limb. Borucki & Summers (1984) picked up the idea of searching for planetary transits and presented an estimate of the needed observing time and instrumentation. Nevertheless, no detection of a planetary transit was announced in these days. It took additional 16 years until the first detection of a transiting exoplanet was reported by Charbonneau et al. (2000).

As indicated by Eq. 1.22, this method is biased toward small stars and big planets, because the ratio R_P/R_S then maximizes. As an example Jupiter would cause a relative flux change of 1 % when it is eclipsing the Sun. For the Earth this value is of course much smaller. In that case we are searching for a transit with a depth of only 0.08 ‰. When we are looking at smaller stars, e.g., M-dwarfs, the detection of small planets becomes much more feasible caused by the much deeper transit signal. In contrast, transit detections in front of giant stars with, e.g., 1 AU radius are challenging, because the hypothetical transit depth would be $2.3 \cdot 10^{-7}$ for a Jupiter-size planet or even $1.6 \cdot 10^{-9}$ for an Earth-size planet. This is still beyond the precision of modern, even space-based photometry. Another also important fact is the dependence of the radii on the wavelength in which the objects are observed. Equation 1.22 is then written as

$$p^2 = \left(\frac{R_P(\lambda)}{R_S(\lambda)}\right)^2 \approx \delta. \tag{1.23}$$

If we think about the Earth seen in visual wavelengths, in which the atmosphere has a high transparency, the limb of the Earth is simply given by the surface. In X-rays, where the optical thickness of the Earth's atmosphere is quite high, the radius is larger by about 100 km. For other planets this effect could be more pronounced depending on their atmospheres, causing a deeper transit signal.

The obvious disadvantage of this detection method is that the orbital plane has to be oriented close to edge-on. Otherwise there is no eclipse detectable by the observer. This is in contrast to the radial velocity method where in principle all inclination angles between almost 0° and 90° would cause a Doppler shift. The inclination window at which an observer would be able to detect a planetary transit is related to the planet's semimajor axis a. For convenience the so called system *impact parameter*

$$b = \frac{a}{R_S}\cos i \approx 1 - \sqrt{\delta}\frac{t_{dur}}{\tau} \tag{1.24}$$

is introduced by many authors, e.g., Winn (2009). The value τ denotes the transit ingress duration until the full planetary disk is in front of the star. For all values of b between zero and one a planetary eclipse is observable (Fig. 1.10).

The limiting values for the inclination are then calculated by

$$i_{limit} = \cos^{-1}\left(\frac{\pm 1 R_S}{a}\right). \tag{1.25}$$

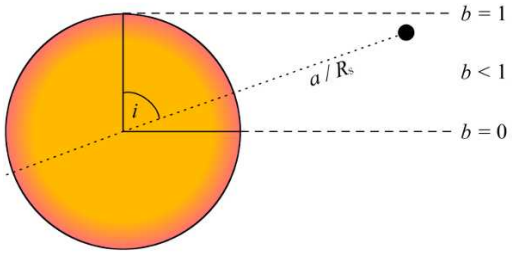

Figure 1.10: Schematic illustration of the impact parameter. The observer looks from the right onto the inclined orbital plane (*dotted line*). *Dashed lines* indicate the limiting impact parameters for transit observations.

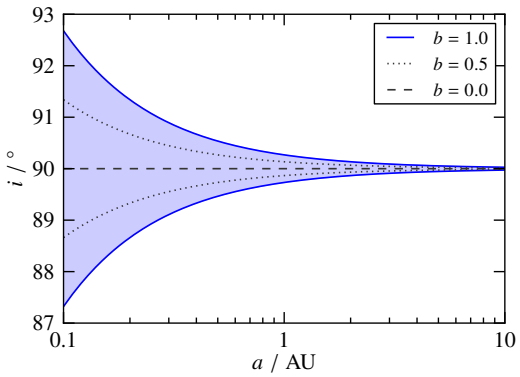

Figure 1.11: Allowed inclination angles expecting a visible stellar eclipse as a function of semi-major axis a (*blue area*). Lines for some impact parameters b are also given (*blue* and *gray lines*).

In this simplified solution I assumed $R_P \ll R_S$ and grazing transits are omitted. Figure 1.11 visualizes this equation and we can see that the inclination range at which we can observe transits rapidly decreases with a. This illustrates that the probability to detect a transiting planet which is far away from its host star is significantly lower than for close-in planets. The actual transit probability, P_{tr}, is just the ratio R_S/a (e.g., Winn, 2010). It follows that the transit probability of a planet orbiting at 1 AU around a solar-like star is about 0.5 %. This value is based on the assumption that the orientations of the orbital planes ($\cos i$) are uniformly distributed and that all stars actually have such planets.

1.3 Modeling of planetary transits

The analysis of transit light curves will be the major part of the presented thesis. Therefore, I will go into some more details about the transit parameters and how they are determined. There are a few parameters that in principle can be determined from the light curve without the prior knowledge of a transit model. This includes the transit depth δ, the time of first transit center t_0, and the transit duration t_{dur}. If there are more than one transit observed, we can also determine the orbital period P_{orb}. Except for δ, we can, e.g., use a linear regression of the transit flanks to determine all mentioned parameters.

In Fig. 1.12 I present simulated transits for different color bands. It is visible that the different strength of limb darkening leads to different transit shapes. For stronger limb darkening the transit is deeper since a larger fraction of the stellar light is blocked at disk center compared to the case with weaker limb darkening. Thus, the transit shape is massively influenced by the limb darkening. On the one hand, this means that further parameters deduced from the light curve are influenced by the stellar intensity distribution. Especially δ is not directly

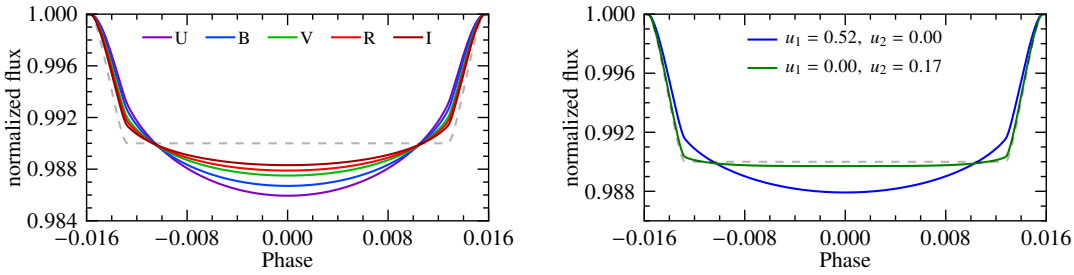

Figure 1.12: *Left*: Model transit light curves in different Johnson filter bands (*labels*). I used quadratic limb-darkening coefficients obtained by a fit to a PHOENIX atmosphere (Table A.9, "μ-rescaled"). *Right*: Model transits for different sets of quadratic coefficients (*labels*). The *dashed* curve represents a transit without limb darkening. Parameters used: $p = 0.1$, $i = 90°$, $a/R_S = 11.2$, $P_{Orb} = 4.32$ d. See also Knutson et al. (2007) for different bandpasses.

related to p anymore, as it would be the case when no limb darkening is present. Consequently, one has to account for limb darkening in transit modeling by relying on laws (Table 1.1) and the corresponding coefficients. On the other hand, the planet acts as a probe and transit light curves can be used to study structures of stellar atmospheres including the real limb darkening of other stars than the Sun. Therefore, planetary transits can be used to compare real measurements of the limb darkening to theoretical predictions.

For a precise transit study we need an analytical light curve formulation such as provided by Pál (2008). Actually there already exist easy to use codes for creating transit light curves. For my thesis I use the `occultquad`[3] and `occultnl` routines (Mandel & Agol, 2002) that provide transit models with linear, quadratic, and nonlinear limb darkening. The code is provided in `FORTRAN`, which results in faster computation times compared to other implementations. The major input parameter for these routines is the time-dependent sky-projected distance z of the two bodies. It can be shown that for circular orbits z can be written as

$$z(t)^2 = a^2 \left[\cos^2(i)\cos^2(\omega t) + \sin^2(\omega t)\right], \tag{1.26}$$

where ωt is the phase angle φ ($\varphi = 0°$ in transit center). The remaining input parameters are the radii ratio and the limb-darkening coefficients. Therefore, this code can be used to determine p, i, a, and the corresponding limb-darkening coefficients u_1 and u_2, e.g., by using a χ^2 minimization algorithm. The time of the transit center t_c and the orbital period P_{orb} have to be known for the modeling. As mentioned at the beginning of this section, they can be determined by using model independent methods. Consequently, they can be set as fixed parameters in transit modeling.

By using simple geometry it can be shown that the transit duration is given by

$$t_{dur} = \cos^{-1}\left[\frac{1}{\sin(i)}\sqrt{1 - \left(\frac{1+p}{a}\right)^2}\right] \cdot \frac{P_{orb}}{\pi}, \tag{1.27}$$

[3] `http://www.astro.washington.edu/users/agol/`

with the semimajor axis a measured in stellar radii. The transit ingress or egress duration, τ, can now also simply be determined by using the relation

$$2\tau = t_{\mathrm{dur}} - t_{\mathrm{on}}\,, \tag{1.28}$$

where t_{on} denotes the duration in which the full planetary disk is in front of the star. This value can be calculated by simply exchanging the $1 + p$ by $1 - p$ in Eq. 1.27. Now we are able to analytically determine all transit times ($t_1 \ldots t_4$).

For simulations, which I will present later on, it is sometimes of special interest to add some noise to the model. If we assume Poisson noise, the final simulation should be defined by

$$\mathcal{F}_{\mathrm{sim}}(t_i) = \mathcal{F}_{\mathrm{mod}}(t_i) + N(t_i|\sigma) \cdot \sqrt{\mathcal{F}_{\mathrm{mod}}(t_i)}\,, \tag{1.29}$$

where $N(t_i|\sigma)$ is the normally distributed noise vector with zero mean and standard deviation σ. By using this equation, we account for decreasing absolute errors during the transit, caused by the decreasing flux. The scatter of the simulation is now time-dependent as it is the case in real data (see Section 4.4). Therefore, this equation is indispensable for realistic simulations.

1.3.1 Markov chain Monte Carlo sampling

I presented in the previous subsection the used routine and minimum set of parameters for transit modeling (p, i, a). These parameters are highly correlated due to the complexity of the transit model. For instance, the transit duration as defined by Eq. 1.27 depends on these three parameters. Therefore, each of these parameters influences at least the width of a transit. By introducing limb darkening as a free model parameter the problem becomes even more complex. Depending on the chosen parametrization of the limb darkening the model gets additional parameters further increasing the degrees of freedom. Under these circumstances it is possible that a minimization algorithm gets stuck in a local minimum, leading to incorrect or even unphysical results. A Markov chain Monte Carlo method (MCMC) can deal with these problems and additionally yields a reliable error estimate of the correlated parameters. The MCMC method is based on Bayesian statistics and, therefore, I will give a brief introduction to that field and to the MCMC sampling approach I used. For a detailed introduction into Bayesian statistics I recommend, e.g., Bernardo (2003) or Loredo (1992) with an astrophysical context.

The most fundamental equation in Bayesian statistics is

$$P(A|B) = \frac{P(B|A)P(A)}{P(B)} = \frac{P(B|A)P(A)}{P(B|A)P(A) + P(B|\bar{A})P(\bar{A})}\,, \tag{1.30}$$

called *Bayes' theorem*. In this scheme A and B are events of a statistical process. $P(A|B)$ is the probability that event A becomes true given that B is true. For instance, the observed statistical process is tossing a dice, where one could define A to be the event when the result is an even number and B the result is bigger than two. $\bar{A}$ is the complement of A, that means event $\bar{A}$ is

true if the result is an odd number. This equation can be used in various statistical contexts, e.g., to evaluate the reliability of a medical test for diseases (see e.g., Niemi, 2013).

For the task of parameter estimation, e.g., in transit modeling we can use Bayes' theorem and write

$$p(\boldsymbol{x}|D) = \frac{p(D|\boldsymbol{x})p(\boldsymbol{x})}{p(D)} = \frac{p(D|\boldsymbol{x})p(\boldsymbol{x})}{\int p(D|\boldsymbol{x})p(\boldsymbol{x})\,\mathrm{d}\boldsymbol{x}}\,. \tag{1.31}$$

Note that I rewrote the capital P from Eq. 1.30 to a small p, now denoting probability distributions. Instead of the introduced events A and B, we now consider a parameter vector $\boldsymbol{x}$ that corresponds to some model function that we use to describe our observed data D. The left part of this equation, $p(\boldsymbol{x}|D)$, reads as the probability distribution of the parameters given the data and is called the *posterior* probability distribution. The determination of the posterior is essential for the estimation of the parameters and their uncertainties. The factor $p(D|\boldsymbol{x})$ is called the *likelihood*. In the case of measurements d_i with errors σ_i that are normally distributed, the logarithm of the likelihood can be written as

$$\ln(p(D|\boldsymbol{x})) = \sum_i \left(-\ln(2\pi\sigma_i^2) - \frac{(d_i - m(\boldsymbol{x}, t_i))^2}{2\sigma_i^2} \right) = C - \frac{1}{2}\chi^2. \tag{1.32}$$

In transit modeling we search for a set of transit parameters $\boldsymbol{x}$ that maximizes the likelihood. This is achieved if the error-weighted quadratic difference between model m_i and data becomes as small as possible. Under the chosen conditions for Eq. 1.32 this would be identical to a χ^2 minimization. The second factor in the numerator of Eq. 1.31, $p(\boldsymbol{x})$, is the *prior* probability distribution. This distribution holds information about the parameters known prior to the measurement, e.g., if one parameter is determined from a different experiment or known to be always positive, like the semimajor axis. In the case of my transit modeling, I will always use a *uniform prior* which means that all values in a certain interval between a lower and an upper limit have the same probability. The denominator, $p(D)$, is the probability distribution of the data itself called *prior predictive*. It gives the distribution of our observed data before we actually started the observation.

As mentioned above, for the parameter estimation we have to determine the posterior. This is in most cases not a trivial task and depends also on the complexity of the proposed model function. Note that in the case of transit modeling the posterior is a multidimensional probability density function. This function has to be integrated to get the individual *marginal probability* distributions of the parameters:

$$p(x_j|D) = \int_V p(\boldsymbol{x}|D) \prod_{i \neq j} \mathrm{d}x_i\,. \tag{1.33}$$

Instead of an analytical integration we can use numerical methods in particular sampling from the posterior using a Monte Carlo approach. However, a basic Monte Carlo algorithm which samples the whole parameter space by generating random variables is not very efficient. Therefore, we need a Monte Carlo technique which creates the samples in a different way. A

common approach is to use an algorithm which generates a sequence of random variables that are created by a random walk with some certain starting point. This sequence of samples is then called a *Markov Chain*. Obviously, there is no improvement by using a simple random walk since it would sample the whole parameters space like before. The process generating the Markov Chain has to be adapted so that the samples follow the posterior probability distribution. It is reasonable to achieve more steps where the posterior distribution is high and fewer where it is low. This is provided by the *Metropolis-Hastings algorithm* (Metropolis et al., 1953) which introduces a *proposal* distribution, $q(z_{i+1}|z_i)$, for the next step. A typical distribution is the Gaussian distribution and holds the probability of jumping to point z_{i+1} given the point z_i. Clearly, the choice of the proposal distribution has an influence on the convergence of the algorithm which could require a much higher number of performed samples. To account for this issue the *adaptive Metropolis-Hastings algorithm* (Haario et al., 2001) was introduced. In this algorithm the proposal distribution is updated after every accepted step of the sampler. This has the advantage that the step size varies during the sampling based on the cumulatively determined covariance.

For my work I used the `PyMC` (Patil et al., 2010) MCMC algorithm included in the `PyAstronomy`[4] that provides both, the adaptive and non-adaptive Metropolis-Hastings algorithm. However, after some tests I decided to use only the adaptive algorithm for my analyses. In Fig. 1.13 I present the accepted proposals of the sampling from the posterior of one of my studied objects (see Chapter 4). The marginal distributions of the parameters can now simply be determined by plotting the accepted parameter samples as histograms. The mean values of the individual marginal probability distributions yield – in the case of Gaussian distributions and uniform priors – the set of parameters that maximizes the likelihood. Consequently, these are the expected values of the parameters.

The final and probably most important step is the determination of reliable estimates of the parameter uncertainties. Given the marginal distributions we are able to obtain *credibility intervals* from them. Such an interval covers a defined portion of the marginal distribution, e.g., 95 %. If we consider one of our used model parameters, x_i, the covered portion calculates as

$$\int_a^b p(x_i|D)\ \mathrm{d}x_i = 0.95\,. \tag{1.34}$$

The integration limits are commonly chosen in a way so that the interval between a and b covers the highest portions of the marginal probability distribution. This interval is then called the *highest probability-density* credibility interval.

In addition to the parameter estimates and their credibility intervals we can directly infer information about the parameter correlations. The point clouds in Fig. 1.13 illustrate that for the used example all parameters are correlated with each other. This means, if one parameter is changed all others react on this change. We can also see that six out of ten parameter

[4] provided by Stefan Czesla on `https://github.com/sczesla/PyAstronomy`

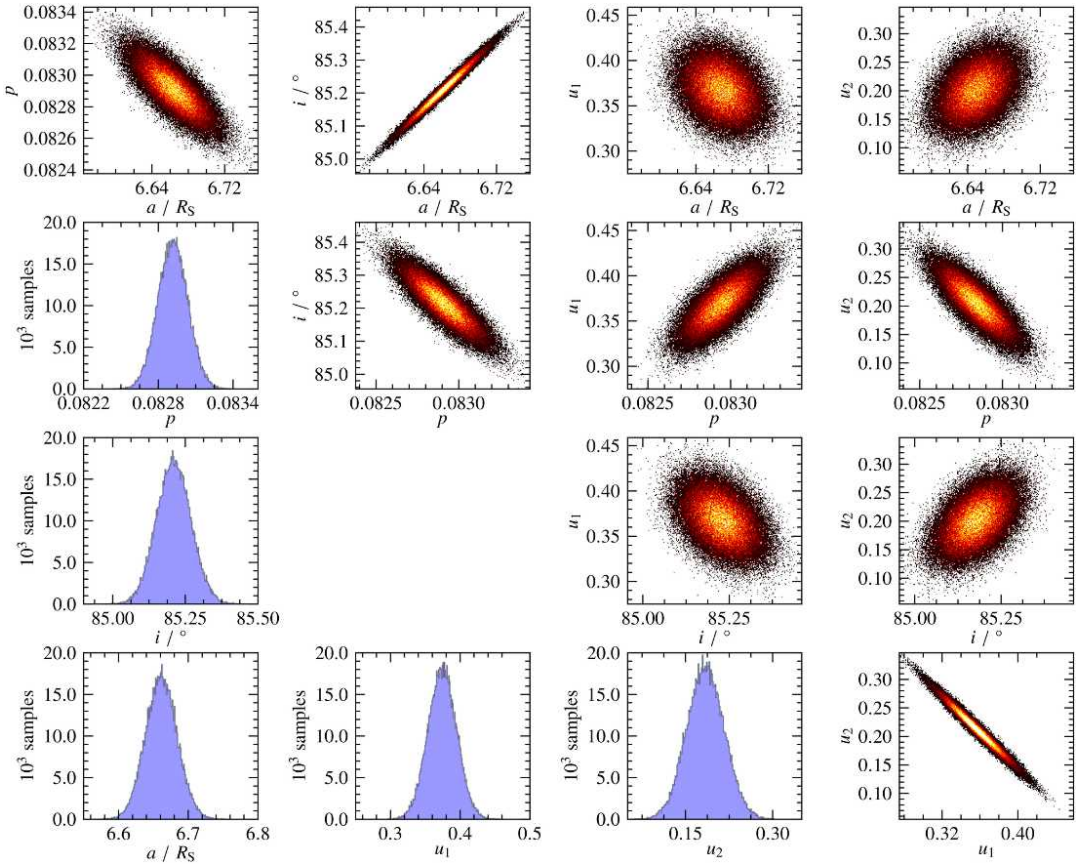

Figure 1.13: Point clouds and histograms of 10^6 accepted MCMC samples for the five modeled transit parameters (p, i, a/R_S, u_1, and u_2) using the light curve of *Kepler*-7b. The point density is color coded and can be estimated by the given histograms (200 bins).

combinations show an anti-correlation. As a prominent example, u_2 always decreases when u_1 is increased (Fig. 1.13, panel in the lower right corner). This can be interpreted as a decrease in the curvature of the limb profile when the slope is increased and vice versa. For an analytical approach to the correlation of u_1 and u_2, see Müller et al. (2013, Sect. B.4).

1.3.2 Impact of the data quality on fit results

As in almost all scientific measurements the data quality is defined by the signal strength compared to the statistical and instrumental noise, which is then often defined as a ratio between these values and called the signal-to-noise ratio S/N. Nevertheless, for transit studies this value is not very descriptive. For a specific photometric signal-to-noise the transit signature of a Jupiter-like planet could be well resolved while an Earth-sized planet could be hidden in the noise. Therefore, it is meaningful to take the transit event as the signal of interest,

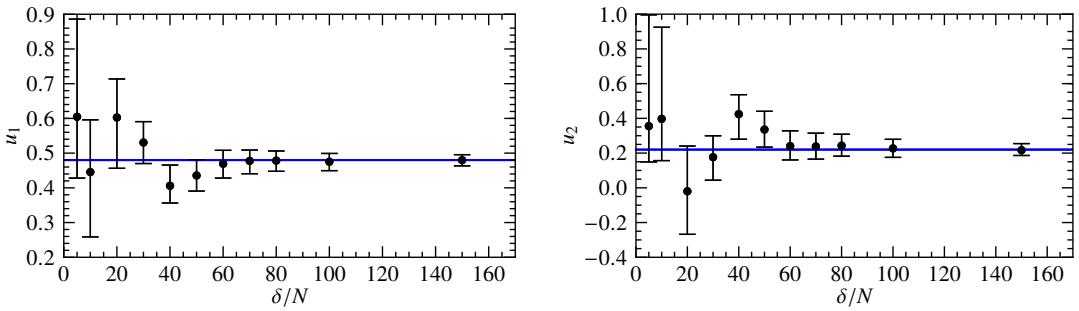

Figure 1.14: Estimation of the needed transit signal-to-noise ratio (δ/N) for fitting the quadratic limb darkening. *Dots*: fitted quadratic LDCs of simulated transits with different δ/N values. *Blue lines* indicate the values used for synthesizing the transits ($u_1 = 0.48$, $u_2 = 0.22$). The remaining orbital parameters were chosen as $p = 0.105$, $i = 88°$, $a = 11.2\,R_S$, which lead to a transit duration of about 3 hours. The error bars correspond to 68 % credibility intervals.

not the continuum level. For this approach we need to know the transit depth δ, which can be approximated by p^2. As already outlined for Eq. 1.23 this value is correct when no limb darkening is given. For all other cases I prefer to measure the depth in the transit center to get a more precise value and to be independent of transit models including the orbital inclination. Interpreting the transit depth as the signal we end up with a *transit signal-to-noise ratio*, which I denote as δ/N.

For the measurement of the stellar limb-darkening using transit light curves, we have to know which transit signal-to-noise is sufficient to achieve significant results. To give a reasonable assumption I simulated individual transit light curves for different planet sizes (1.02 R_{Jup}, 1.32 R_{Jup}, 1 R_{Earth}) and added normally distributed noise (Eq. 1.29). The noise was different for each planet size, but corresponds to δ/N values in the range from 5 to 150 for each planet size. These light curves were then fitted with respect to five transit parameters, namely the semimajor axis a/R_S, the inclination i, the planet-to-star radii ratio p, and two limb-darkening coefficients using the quadratic limb-darkening law. In addition I used an MCMC sampling algorithm (Section 1.3.1) to perform 10^5 iterations and discarding a burn-in of 10 000. The most probable parameters are then given by the mean values of the parameter traces. The resulting limb-darkening coefficients for the transits simulated using a planet radius of 1.02 R_{Jup} are presented in Fig. 1.14. As expected, the transit depth compared to the noise has a crucial influence on the measurement of the limb-darkening coefficients. Although we can see that almost all of these fit results are consistent with the values used for the simulations within their error bars, we should aim for results where the mean value of the parameter traces lies close to them. Therefore, my simulations show that one would need a transit signal-to-noise ratio of at least 60 to achieve credible results when only a *single* transit light curve is observed. For this planet size (1.02 R_{Jup}) this can be translated into a photometric signal-to-noise ratio of about 5000. This value is today still unreached by most ground-based instruments. The results for the other chosen planet sizes are quite comparable and shown in Fig. B.3, but they are plotted against the photometric signal-to-noise ratio.

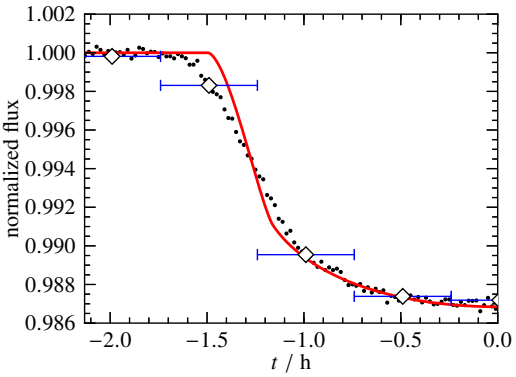

Figure 1.15: Effect on the transit shape, induced by long integration times. *Black dots* represent 25 phase folded transits, while the *white diamonds* show only one of these. The integration time (30 minutes) is indicated by horizontal *error bars*. The transit model with infinite time resolution is given as a *red* curve. Only the first half of the transit is shown. See also Kipping (2010, Fig. 1) for a trapezoid light curve.

Another important aspect of the data quality is the time resolution of the light curve. This time resolution is, e.g., defined by the integration time needed to reach a satisfying signal-to-noise ratio. For faint host stars or poor instrumentation this time interval is longer than for bright objects and good instruments. Variability which occurs during one exposure is not resolved by the measurement and included in one single data point. This data point can be understood as a mean value of the flux during the given integration time. In the case of the popular space telescopes CoRoT and *Kepler* these integration times are in the order of seconds. Unfortunately, these satellites have a limited data transfer rate, which makes it necessary to combine multiple exposures into a single one before sending them to Earth. This procedure is known as *binning* (or *re-binning*) and also frequently performed to reduce the visible noise in light curves or other kinds of data. However, this re-binning should *always* be avoided because there is no gain in information although the noise is reduced. In fact the opposite is the case: information is destroyed.

In the case of transit data the re-binning of the light curve has a crucial influence on the transit shape. This can easily be understood when looking at Fig. 1.15 where I compare 25 simulated and phase folded transits to the corresponding initial model. Before phase folding the synthetic data was binned down from one to thirty minutes. Obviously, this causes the transit ingress to occur significantly earlier than given by the model. The reason for this is that the binned data points are mean values of the flux in a time interval of thirty minutes, which is illustrated by the data points shown with horizontal error bars. Thus, the information of the actual transit start is smeared out and the whole transit shape is deformed. However, someone could argue that it might be a better idea to phase fold the transits first and perform the rebinning afterwards, e.g., to one minute. But this is in fact not recommend since the bin time is almost never a multiple of the orbital period. This leads to a different number of data points contributing to new individual bins and to systematic effects like red noise (Section 4.4).

For the purpose of transit modeling and acquiring precise limb-darkening measurements it is important to know whether data binning influences the resulting parameter estimates. It is obvious that a light curve with a crude time resolution contains less information than compared to one with short time binning. Therefore, we cannot expect a fit of the transit parameters to lead to the correct values. To provide an estimate on the size of the expected discrepancies

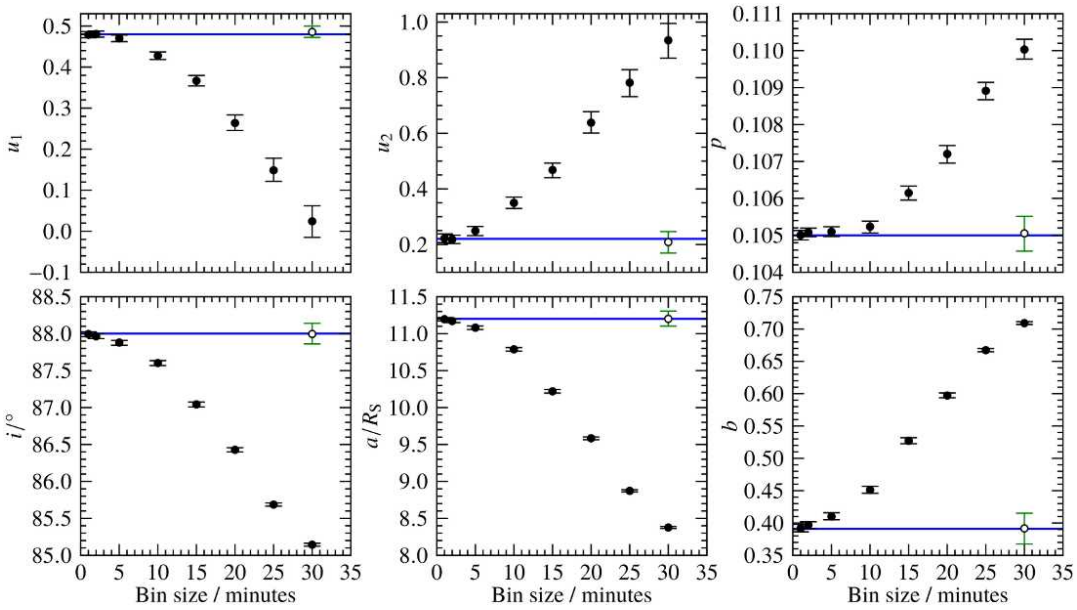

Figure 1.16: Fit results of simulated transit data, which was binned according to typical integration times. *Blue horizontal lines* indicate the parameter values used for the simulated transits. *Empty circles* show the best fit solutions for an overbinned model taking into account the finite integration time. The impact parameter b is deduced from the results of the inclination and the semimajor axis. The error bars mark the 95 % credibility intervals. Signal strength: $S/N = 10\,000$, $\delta/N \approx 130$.

between real and fitted transit parameters, I simulated transit light curves with different bin sizes and fitted the five transit parameters p, i, a, u_1, and u_2. These values were then again used for 10^5 MCMC iterations. The results of the sampling are shown in Fig. 1.16. We can clearly see that for bin sizes larger than two minutes the best-fit parameters substantially deviate from the values used for the simulations (blue lines). In general one would tend to measure larger planet-to-star radii ratios, more inclined orbits, but smaller semimajor axes with increasing bin sizes. Most notably, the fit results of the limb-darkening coefficients u_1 and u_2 reach their physical limits at a bin size of about 30 minutes. This behavior of the parameter fits is quite impressive and indeed relevant for transit analyses. The reason for this is that the transit model used for the fitting approach has by definition an infinite time resolution (or in other words it is unbinned), but it is only evaluated at points in time of the binned data. Kipping (2010) showed in his work "Binning is sinning" that it is necessary to evaluate the model function at a significantly smaller bin size to obtain correct planetary parameters in the case of long integration times. Such an *overbinned* model is then rebinned to the larger bin size of the data and used for the fitting process. This would mean that the model is now binned in the same way like the observed data. Using this approach, I gathered the resulting fit values shown as empty circles in Fig. 1.16. These values almost perfectly coincide with the initial model parameters, even in the case of the longest integration time of 30 minutes. This method is thus essential to achieve correct fit values, especially in the case of long cadence data obtained by the *Kepler*

mission, where the resulting time binning is 30 minutes. Unfortunately, this procedure leads to substantially longer computation times (factor of 16 for the presented simulations) and bigger uncertainties when compared to an analysis of unbinned data.

The effects of binned data are of course not limited to time resolved measurements and, e.g., also important for spectral data. It is everywhere of interest where a steep flux decrease or increase occurs, which is then smeared out in time (or wavelength) by the binning. Thus, the influence becomes most problematic for short ingress and egress durations found together with short transit durations. For comparison, the transit duration of my presented simulations (Figs. 1.15 and 1.16) is almost three hours which is a value often found in real data or even shorter for hot Jupiters. Although I showed that it is possible to achieve correct fit parameters using an overbinned fit model as proposed by Kipping (2010), I recommend to use photometry with integration times not larger than two minutes for transit durations of three hours or shorter. Otherwise, the fitted parameters are incorrect. The situation is even more complex if the integration time is changed during the transit observation, e.g. due to changing weather conditions. In that case the fit model has to be adapted to that circumstance. Furthermore, depending on the photometric signal-to-noise or the δ/N value, the resulting uncertainties of the fit parameters could be unsatisfactory when an overbinned fit model is used.

1.3.3 Which limb-darkening law should be used?

Due to the diversity of the available limb-darkening laws we have to face the question, which law we should use for our analysis. In many cases the decision is influenced by the complexity of the used model function or the data quality. Many authors tend to use the "simple" two parameter laws instead of more complicated descriptions. Even in some cases we still find the linear law in use, e.g., in Doppler imaging (e.g., Nesvacil et al., 2012), although it is often considered to be inadequate and outdated (see Claret (2000) and references there). The question arises how to decide which law is poor, which is excellent, and do we actually need laws with at least four coefficients or are two enough. Some authors argue that a limb-darkening law is declared to be good when it fits the model intensity distribution best. Therefore, some of these laws were intentionally invented to reduce the residuals between them and intensities obtained from model atmospheres. It seems that today's primary purpose of most of these laws is to be a good approximation of the model intensities and not of the real center-to-limb variation of stars. Unfortunately, only a few limb-darkening functions were explicitly developed to describe real observational data, like the polynomials given by Pierce & Slaughter (1977) or Neckel & Labs (1994). These laws are the only ones to which we can refer if we ask for "the correct" limb-darkening function. Obviously, such precise and direct measurements of the limb darkening are nowadays only available for the Sun. In most other cases we have to rely on indirect methods like transit studies. In this subsection I will present an analysis that should simplify the decision which limb-darkening law we should use in transit analysis. The prior assumption to be made is if transits using the individual laws do not differ much, then fits to real observational data using these laws do not differ much either.

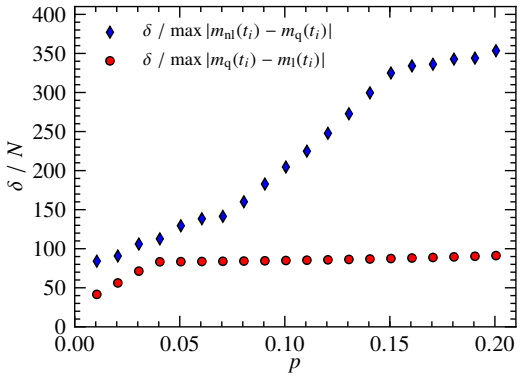

Figure 1.17: Minimum transit signal-to-noise ratio (δ/N) needed to detect residuals between transits with different limb-darkening laws as a function of the planet-to-star radii ratio. The labels show which model transits are compared. *Red* dots indicate comparison of transits with linear and quadratic limb darkening, while the *blue* symbols result from transits with quadratic and nonlinear descriptions.

For a given set of transit parameters the choice of different limb-darkening functions will result in slightly different transit shapes. If the differences are larger than the noise, we constitute that these differences are significant. In that case we expect that transit fits would yield different results depending on the used limb-darkening law, caused by the high correlation between the limb darkening and the remaining transit parameters. To estimate to which extent the results actually differ and which level of photometric noise is needed to distinguish between different limb-darkening laws, I present simulations. I used the four parametric nonlinear limb-darkening law (Claret, 2000) and created transit light curves for different planet-to-star radii ratios, p, with one minute cadence. I denote this transit model as $m_{\rm nl}$. The orbital inclination and the semimajor axis were set to 88.5° and 11.2 $a/R_{\rm s}$, respectively. This procedure is repeated with the same parameters using the linear and quadratic limb-darkening laws, resulting in the models $m_{\rm l}$ and $m_{\rm q}$. The limb-darkening coefficients were taken from Claret & Bloemen (2011) for $T_{\rm eff} = 5800\,{\rm K}$ and $\log g = 4.5$ in a Johnson-V filter using a PHOENIX atmosphere. The residuals between these three transit models are now only caused by their differing limb-darkening descriptions. The maximum of these residuals defines an upper limit of the noise at which we would just be able to detect differences induced by the chosen limb-darkening law. In Fig. 1.17 I present the transit depth, δ, divided by the maximum of the absolute value of the residuals occurring between transits using the nonlinear and the quadratic law ($m_{\rm nl}(t_i) - m_{\rm q}(t_i)$), as well as the quadratic and the linear law ($m_{\rm q}(t_i) - m_{\rm l}(t_i)$). The individual points could be interpreted as the minimum transit-signal-to noise (δ/N) needed to detect residuals at a 1 σ level between transits created with the particular limb-darkening laws. If we look at the red dots we can say that for values of δ/N below that points the residuals between a transit using the linear law and one using the quadratic law are hidden in the noise and, therefore, not significant. The same is the case for the residuals between the transits with nonlinear and quadratic laws but at a significantly higher transit signal-to-noise level (blue diamonds). The additional information that we can draw from Fig. 1.17 is that for small planets the effect of a poor limb-darkening description is seen at smaller δ/N than it is the case for larger planets. Therefore, the choice of the limb-darkening model is more important for small planets. This is actually what we expect since a small planet acts as a more precise probe of the stellar surface in contrast to a larger one.

Table 1.2: Fit results of a simulated transit using different limb-darkening laws.

Model	p	$i/^\circ$	a/R_S	LDCs [a)]	χ^2/ν
nonlinear	0.10000	88.50	11.20	$a_1,...,a_4$	
linear fixed	$0.09978^{+0.00006}_{-0.00006}$	$88.52^{+0.03}_{-0.03}$	$11.20^{+0.02}_{-0.02}$	$u = 0.6838$	3.79
quad. fixed	$0.09989^{+0.00005}_{-0.00005}$	$88.54^{+0.03}_{-0.03}$	$11.21^{+0.02}_{-0.02}$	$u_1 = 0.5624$, $u_2 = 0.1627$	1.16
linear free	$0.10069^{+0.00006}_{-0.00006}$	$88.32^{+0.02}_{-0.03}$	$11.12^{+0.02}_{-0.02}$	$0.6437^{+0.0014}_{-0.0013}$	1.20
quad. free	$0.10003^{+0.00009}_{-0.00011}$	$88.51^{+0.04}_{-0.04}$	$11.21^{+0.03}_{-0.02}$	$0.5996^{+0.0050}_{-0.0046}$, $0.0982^{+0.0096}_{-0.0115}$	0.92

Notes: The first row shows the input values of the synthetic transit, which should be reproduced by the model fits. [a)] In the cases where the limb-darkening coefficients are fixed they are taken from Claret & Bloemen (2011), for $T_{\rm eff} = 5800\,$K, $\log g = 4.5$ in Johnson-V filter using a PHOENIX atmosphere. Errors are deduced from a MCMC sampling (68.5 % highest probability density).

In the example presented above I compared transit models with the same parameters and fixed limb-darkening coefficients. This approach is useful to estimate the occurring residuals between these transits, only caused by the different limb-darkening laws. However, this is not very close to the actual problem. In real observational data at least the parameters p, i, and a would be fitted during transit modeling. This results in smaller residuals but also different transit parameters depending on the limb-darkening law. How these fitted parameters differ from the correct values can be estimated by transit modeling. My investigation relies on the synthetic transit created with the nonlinear law with $p = 0.1$ and added Gaussian noise to achieve a δ/N of 400. As we can see in Fig. 1.17 this value is twice as high as required to see residuals between the quadratic and nonlinear law. Therefore, we expect clear residuals and different transit parameters after the modeling. This transit was then fitted using a transit model with the linear and the quadratic law, first using fixed limb-darkening coefficients and then leaving them free. In Table 1.2 we find the results of this fitting procedure. Overall the fitted parameters do not differ much from the correct values, however, we can identify some characteristics. In the case of the linear limb darkening we see that the resulting parameters differ more from the correct values when the limb-darkening coefficient was also allowed to vary during the fit. Especially the inclination and the semimajor axis are significantly smaller. If the quadratic limb darkening is used, the parameters show a better match when the limb-darkening is fitted together with the other parameters. Additionally, the reduced χ^2 value offers valuable clues to the accuracy of the used model. The linear limb darkening is inadequate and leads to residuals, especially present when the coefficient is fixed to the predicted value. The inaccuracy of the linear law is also shown in the work by Raetz et al. (2014), where a fit of transits of TrES-2b leads to clear residuals. In contrast, Table 1.2 reveals that the quadratic limb darkening results in a much better fit, even when the coefficients are set to the predicted values. In the case where the quadratic limb darkening is fitted together with the transit parameters, we end up with an excellent fit expressed by an optimal χ^2/ν. This result is essential, because the chosen δ/N value is high enough that there would be

significant residuals. However, after a fit of all parameters the residuals are gone and the transit parameters were only slightly adjusted, namely p by 0.3 ‰, the inclination by 0.1 ‰, and the semimajor axis by 0.9 ‰.

Based on the shown results I conclude that it is reasonable to use the quadratic limb-darkening law in transit modeling. For a given transit signal-to-noise of 400 – this is equivalent to a noise level of $3 \cdot 10^{-5}$ together with $p = 0.1$ (cf. Table A.6) – higher orders of the limb-darkening description are *not* necessary. The occurring deviances of the parameters using the quadratic law compared to when using the nonlinear law are below the one permil level and smaller than the parameter uncertainties. Especially for observations with lower photometric accuracy, e.g. ground-based observations, the quadratic limb-darkening law offers a sufficient precision.

1.4 Thesis outline

We have seen in the foregoing sections that a detailed knowledge of the stellar limb darkening is indispensable for the study of various kinds of measurements in photometric and spectroscopic data. The treatment of the problem as a theoretically predictable phenomenon has been established in all fields where limb darkening plays a crucial role. The investigator relies on limb-darkening "laws", which are only approximations to the actual intensity distribution. The coefficients of these "laws" can only in a few exceptions be determined by using high quality observations. Thus, in most cases the coefficients are determined by fitting model atmospheres, which are on their own again only approximations to real stellar atmospheres. Whether these coefficients and laws are valid or not is still unknown. Consequently, the study of the limb darkening in a greater sample of stars could provide an empirical basis to answer that question.

The intention of this thesis is to provide a consistent analysis of the limb darkening in a greater sample of stars, starting with the determination of the needed stellar parameters. The major part of my work is therefore devoted to planetary transit studies and the determination of the limb darkening from these light curves. The results improve our knowledge about the validity of the limb-darkening coefficients, their laws, and about the underlying model atmospheres.

This thesis is divided into eight chapters, which in principle could be read independently. The only exception could be Chapter 4, which should be read after reading my publication (Müller et al., 2013). However, if chapters are read individually, I assume a prior knowledge of transit light curves, their main parameters and modeling, the orbit geometry of transiting exoplanets, and about the *Kepler* space mission.

Following the introduction presented in Chapter 1, Chapter 2 deals with spectroscopic observations partly obtained by myself and the analysis of the spectra. The main focus is set on the determination of the fundamental stellar parameters like the effective temperature, the surface gravity, and element abundances by using synthetic spectra based on model atmospheres. This is the first step to give an estimate of the star's limb darkening. As a side

effect we will see how accurate the spectral synthesizing based on model atmospheres is today. In Chapter 3 I introduce the *Kepler* space telescope, because a major part of my thesis is based on the analysis of data coming from this instrument. This includes an overview of the instrumental layout, a mission overview, and its capabilities to detect small earth-sized planets. This might be of interest for those who are not familiar with this instrument and its data acquisition. This chapter is followed by Chapter 4 in which I present my limb-darkening studies of high-quality transit light curves obtained by the *Kepler* space mission. They lead to the most precise measurements available of the limb-darkening of other stars than the Sun, published in the journal Astronomy & Astrophysics. In this chapter I also give some supplementary information not found in my publication (Müller et al., 2013). Chapter 5 is dedicated to a comparison of the precisely measured limb darkening of the Sun and predictions from model atmospheres. This will also allow to discuss the accuracy of the common fits to the limb intensities of model atmospheres and to introduce an alternative fit approach. In Chapter 6 I introduce an efficient numerical code to synthesize transit light curves independent of any limb-darkening "law" by directly taking disk intensities from model atmospheres. To show the capabilities of my code I present some simulations including transit light curves in different wavelength regimes with the Sun as a host star. Chapter 7 provides an overview of my contributions to refereed scientific journal articles. This also includes a complete version of my accepted first author publication *High-precision stellar limb-darkening measurements* (Müller et al., 2013). Finally, I close with Chapter 8 where I summarize my work. Each chapter is treated individually with a short outline about the methodology followed by my found results. At the end of this thesis I provide appendices with tables and figures.

2 Spectral Observations and Analyses

We have seen in Section 1.1.3 that the stellar limb darkening depends on several stellar parameters, such as the effective temperature. The knowledge of these parameters is thus indispensable for modeling transit light curves. The determination of these parameters requires additional data, at least in different color bands. This allows us to determine the B-V color index and, hence, an estimate of the effective temperature. For more precise analyses one preferably acquires spectroscopic observations. Together with line analysis methods and spectral synthesis using model atmospheres, it becomes possible to determine a whole bunch of stellar parameters with sufficient precision.

In this chapter I present own spectroscopic and photometric observations of a planet hosting star as well as the inspection of high-resolution spectra with a widely used software tool. First, the emphasis is set on the instrumentation and the observation method. For the selected object all transit parameters are well known from space-based observations and the limb darkening remains as the parameter of interest. I will show the resulting photometry and comment on occurred problems. In the case of the spectral analysis I will concentrate on the determination of the stellar parameters, like $T_{\rm eff}$ and $\log g$. The main purpose of this part will be to test the capabilities of the used software. In the end I will compare the resulting stellar parameters to values found in the literature.

2.1 Spectro-photometry of the CoRoT-2 system

CoRoT-2A (Alonso et al., 2008), a very active planet host star, was discovered by the CoRoT space telescope. The optical light curve shows remarkable spot induced variabilities, modulated by the stellar rotation (Fig. 2.1). Additionally, the light curve shows sharp dips that are caused by the occultation of the stellar disk by the transiting hot Jovian planet CoRoT-2b. Due to the amazing light curve with its periodic oscillations, CoRoT-2A is often referred to as the prototype of a new class of active stars. The great advantage of this system is the transiting planet that offers the opportunity to study the active host star in a totally new way. During its occultation the planet probes a well defined path on the stellar surface, thus features like spots and faculae can be resolved from transit light curves. The reconstruction of such surface features is also called planetary eclipse mapping (e.g., Huber et al., 2009).

The center-to-limb intensity distribution is an important input parameter of transit modeling. As shown in Section 1.3, it has its major influence on the transit shape and on the central depth. If the disk intensity distribution is distorted by spots or faculae, then transit light curves will

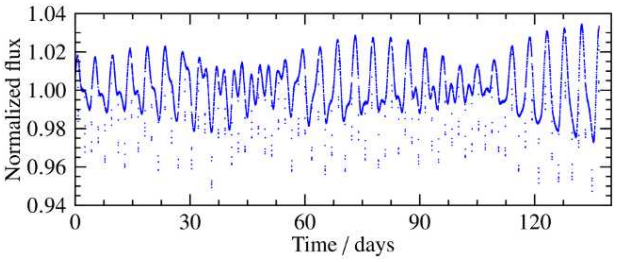

Figure 2.1: Light curve of CoRoT-2A normalized to its median value. The data was rebinned to half an hour. Dots below the light curve indicate planet eclipses. Data obtained by CoRoT.

reflect these features. If dark areas are transited by the planet, the disk-integrated intensity rises and causes bumps in the transit (e.g., Wolter et al., 2009). In the case of bright areas occulted by the planet, we observe additional dips in the transit. In contrast, if neither spots nor faculae are occulted during eclipses, although they are present beyond the transit path, the total transit depth varies according to the activity of the host star. Therefore, also not occulted active regions directly influence the size estimates of the planet (Czesla et al., 2009). However, in this case we are not able to learn something about the physical properties of these surface structures, which is conversely possible when they are transited. The size of a bump (or dip) in such a transit depends on the spatial dimensions of the underlying spot and the temperature contrast between spot and photosphere. Having spectral or at least multi color data of these regions would open up the possibility to directly measure the temperature of such features on other stars than the Sun. CoRoT-2A is a well suited target for that purpose, because a significant number of observed transits show spot induced perturbations. Even if no active regions are sampled by the planetary disk, the limb darkening of this young and active star could differ significantly from rather inactive stars with a comparable effective temperature like the Sun. In both cases transit observations provide a promising opportunity to study the wavelength-dependent center-to-limb intensity distribution on this young and active star.

2.1.1 Used instrumentation and observations

The following analysis is based on data obtained by Uwe Wolter and myself in June 2009 during my diploma thesis. For our observations we used the Potsdam Multi Aperture Spectrophotometer (PMAS) (Roth et al., 2005) mounted at the 3.5 m telescope at the Calar Alto Observatory, Almeria, Spain. The instrument was set up in PPak mode (Kelz et al., 2006). PPak is an integral field unit (IFU) for PMAS. It consists of 331 science fibers with a round shape arranged in a hexagon (Fig. 2.2). The instrument covers a field of view of $74'' \times 64''$ with a filling factor of the sky area of 60 %. Each fiber has a diameter of $2.7''$, with a small gap between them of about $0.9''$. The fibers are then fed into a grating spectrograph, providing a spectrum for each fiber corresponding to different positions on the sky. The spectrograph can be equipped with different gratings to change the wavelength resolution to up to $R \approx 8000$. We used a low-resolution grating (300 lines per mm) to cover the whole optical wavelength regime (here 4815 Å to 8050 Å). The acquired resolution was $R \approx 1800$, which should be enough to measure the center to limb intensity distribution in B, V, and R band.

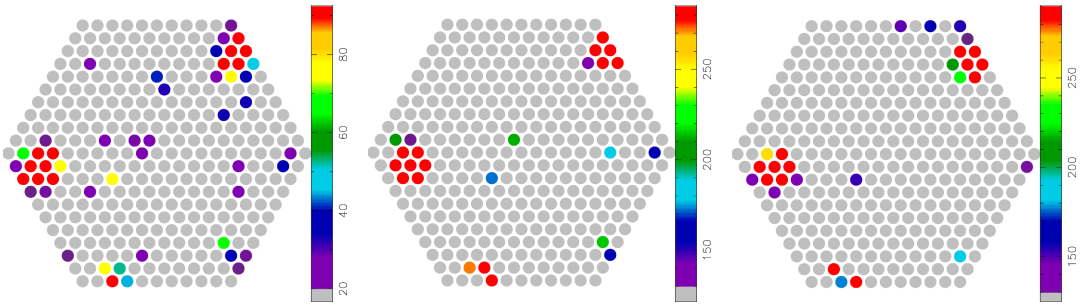

Figure 2.2: PPak raw images of our target field. Acquired counts (× 100) are color coded. The exposures were taken for three slightly different sky positions (dithering). The positions were changed according to the offsets $(\Delta\alpha,\Delta\delta) = \{(1.56'',0.78''),(0.0'',-1.56''),(-1.56'',0.78'')\}$. Images are produced during a quick-look reduction with E3D (see text for details).

The observations were carried out in two nights[1] with good weather conditions. Only at the beginning of the second observing night we had to close the dome due to clouds and high humidity. In both nights we had moderate atmospheric seeing between 1.1″ and 1.4″. It was planed to observe CoRoT-2b during a transit and simultaneously take photometric and spectroscopic data. To obtain a suitable photometric calibration a second star had to be placed into the field of view that is sufficiently bright. The only object close enough is USNO-B1.0 0913-00447626 (m_R = 11.4 mag) that is slightly brighter in R band than CoRoT-2A (m_R = 12.2 mag). Because of the relatively large angular distance between these two stars (52″) it was necessary to place both of them close to the edges of PPak's hexagonal field of view. Unfortunately, a rotation of the instrument around the optical axis, to achieve a better positioning of the targets, is not possible.

For the observations we chose an integration time of 300 s for the first night and 200 s during the second night. Given the expected transit duration of about 7900 s we would have been able to hypothetically catch about 26 and 39 data points during the transit event. These estimates are however slightly optimistic, because I neglected time overheads, e.g. caused by the CCD readout. For this instrument the readout time is on the order of 100 s, which is relatively high. However, this was in the end not the only reason that reduced the time resolution of the observations. The instrument expert and night astronomer Sebastian Sánchez highly recommended to perform the observations in "dither mode". In this mode the telescope pointing is manually shifted after every exposure. The resulting pointing pattern is a triangle which should account for systematic flux losses between the PPak fibers. Consequently, three individual exposures were then combined into one, leading to an effective time resolution of ≈ 1200 s per data point for the first night. Due to the shorter integration time during the second night, the achieved time resolution is slightly better with ≈ 900 s per data point. In Fig. 2.2 I show the images of the three individual exposures. One can clearly see both stars in the field of view and the slightly different positions caused by the changing telescope orientations. Beside the dithering, we had to make exposures for the wavelength calibration.

[1] 21.06.2009 and 28.06.2009. Dates denote the starting night.

For that purpose we used ThAr and HgHe lamps. Those emission lines are used to determine the individual dispersion of each fiber. The calibration exposures had to be repeated almost every hour because the dispersion is dependent on the fiber orientation and therefore on the telescope's pointing. These calibration exposures again reduced the final time resolution by about 150 s per hour. At the end of each observing night we took spectra of a spectroscopic standard star (HR 7596 and G 24-9[2]) to be able to perform an absolute flux calibration. Finally, we were able to acquire 21 spectra in the first night and 22 in the second night, then combined to 6 and 7 data points, respectively.

2.1.2 Data analyses and results

The data reduction of spectra obtained with an IFU is a whole thesis on its own and, therefore, not described in detail here. Although the reduction is carried out with a partially automated reduction software called R3D (Sánchez, 2006), some of the steps have to be done manually. This includes the correction for different start and end points of each fiber spectrum on the CCD. This behavior leads to CCD images curved perpendicular to the dispersion axis (see Kelz et al., 2006, Fig. 14). I had to define by eye some nodes used for a polynomial fit, which is used to correct the shifts of all fiber spectra. Another important step is the correction of the non-linear dispersion of the spectrograph using the ThAg and HgHe emission lines. Like before, the reduction software needs some manual interaction, by defining nodes for a polynomial fit. In both cases the orders of the polynomials are defined arbitrarily by the investigator. In fact, this step should be repeated for different orders of the polynomials and, depending on the goodness of the fits, the order should be set to the one that provides the best solution. All recorded files have to be treated in this way, which makes the reduction really time-consuming. In addition to the mentioned steps I had to perform a cosmic removal, which is also not implemented in the reduction software. Therefore, I wrote a script that calculates the ratio of two individual CCD images and determines the sliding pixel difference (line by line) of this ratio image. The sliding difference is compared to the median value in 150 preceding differences. If the difference exceeds the median by 15 % the pixel value is replaced by normal noise (Fig. B.4). Of course, there exist different or even much better methods to remove cosmics, but in this early stage of my PhD thesis and with respect to the final outcome of this analysis, my described method is absolutely sufficient.

After the reduction of all data files I continued by using the analysis software E3D (Sánchez, 2004). This software is specially designed to analyze IFU spectra and is able to generate data cubes out of the observations. A data cube has two spatial dimensions (the image of the sky) and one dimension for the spectral information. Hence, one slice from this cube represents a sky image in one specific wavelength. Also important for my observations is the ability to combine three images resulting from the mentioned dithering to one final cube. One resulting image slice is shown in the left panel of Fig. 2.3. The target star CoRoT-2A and the photometric

[2] It turned out that G 24-9 is an eclipsing binary system. An absolute calibration was not performed anyway.

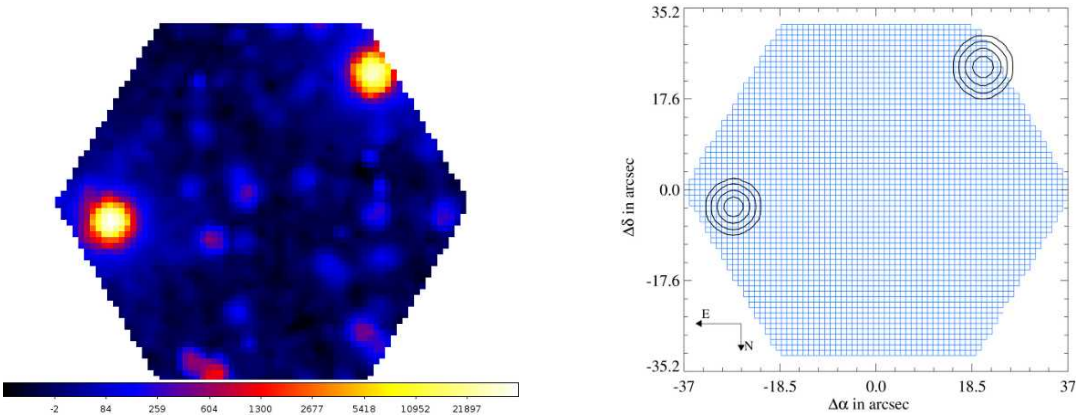

Figure 2.3: PPak's field of view after combining three dithered images. *Left*: Science image with CoRoT-2A in the upper right corner and USNO-B1.0[...] at the middle left. Counts are color coded in logarithmic scale. *Right*: Pixel map with reconstructed point-spread functions. The contour levels mark 0.15, 1.0, 10 and 45 % of the respective maximum flux.

calibrator are now better visible compared to Fig. 2.2. Again, each pixel of this image delivers a whole low resolution spectrum.

Having these final cubes I am in principle able to obtain wavelength-resolved relative photometry of CoRoT-2A. Therefore, I can choose any arbitrary wavelength point in the observed range to study CoRoT-2b transits. However, as already visible in Fig. 2.3, CoRoT-2A was placed too close to the edge of the field of view that caused a non-negligible flux loss during observation. The angular distance between CoRoT-2A and the photometric calibrator made it impossible to solve this problem. To estimate the flux loss I modeled the instrumental point spread function (PSF) with a two dimensional Gaussian, which also allows for elliptical shapes (Fig. 2.3, right panel). I found a time- and color-dependent flux loss of the order of a few percent. As a consequence, the accuracy required for a detailed spectro-photometric analysis of less than one percent is not provided. Also conspicuous is the changing shape of the PSF when looking at different final data cubes. Sometimes the shape of CoRoT-2A is significantly elongated toward PPak's edge. This behavior could suggest pointing inaccuracies of the telescope on scales relevant for observations of point sources. Thus, it can happen that the position of the stars on the fibers is not the same for one specific dither position. Indeed, an inspection of the fits-headers yield a mean pointing inaccuracy of 0.7″ during the dithering. Therefore, the modeling of the flux loss at the edge of the field of view is not sufficient to reconstruct the stellar flux.

Despite the mentioned problems, I used the six final data cubes of the first night and the seven of the second night to apply a simple aperture photometry of CoRoT-2A. I selected 94 pixels in a rectangular shape around CoRoT-2A and summed up all pixel values. This value was then divided by the corresponding value of the photometric calibrator (130 pixels) which led to a ratio of roughly 0.7. The resulting light curves of both nights are shown in Fig. 2.4. I chose

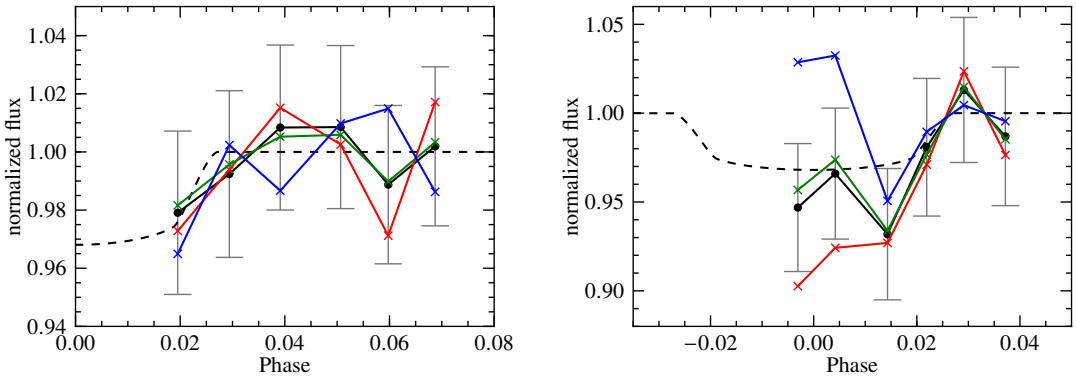

Figure 2.4: Normalized PPak light curves of CoRoT-2A in four color bands (*red*: 6975 Å - 8050 Å, *green*: 5895 Å - 6975 Å, *blue*: 4815 Å - 5895 Å, *black*: 4815 Å - 8050 Å). The error bars indicate the 1σ uncertainties of the black dots, others are not shown for clarity. *Dashed lines*: Transit model of CoRoT-2b. *Left*: First observing night, detrended by linear fit. *Right*: Second observing night, last data point left out. See text for details.

three different wavelength regions (see caption) in which I simply summed up the light. As usual the light curves had to be normalized by the out-of-transit flux level. In the first night we were only able to catch one data point inside the transit and five after the eclipse. Therefore, I used a simple linear fit to the last five data points, to remove a decreasing trend and to normalize the light curve. This was repeated for each of the chosen wavelength regions. In the second night we were only able to acquire two usable data points outside of the transit. Thus, I used the mean of these points to normalize the light curve. Due to the lack of measurements before both transits the normalization and detrending is unreliable. I present for interest the first light curve without the applied detrending and the second together with the left out last data point in Fig. B.6. The errors of the data points are determined by assuming a Poisson statistic. The relatively large uncertainties and the scatter of the data points are striking for both nights. Unfortunately, the presumably visible lower flux during the transit events in Fig. 2.4 is not significant. Especially for the second night where the light curves obtained in the blue and the red light show contrary trends during the transit.

The obtained light curves are quite unsatisfactory. Due to the crude time resolution, the high amount of flux loss at the edge, and the pointing errors of the telescope, I was neither able to study the wavelength dependent limb darkening nor photospheric features like spots. We were not able to achieve the time resolution required for this kind of analysis (see Section 1.3.2). The time consuming dithering and the calibration exposures make the used instrument inadequate for our intended purpose. It was originally designed to study extended objects such as galaxies or clusters and not for photometry of point sources. Although it turned out that the observations were insufficient to reach our planned goals, the data presented in Fig. 2.4 can give hints which photometric precision and time resolution could be reached by this instrument. In the end, the observations and the analysis could be understood as a kind of a feasibility study, especially because we were the first who tried to observe a transit light curve using an IFU.

2.2 Spectral analyses of two planet hosting stars

Spectral observations are important for the determination of various stellar characteristics, for instance the spectral class. Among others we use stellar spectra to measure fundamental photospheric properties like the effective temperature or the radial velocity. The determination of the effective temperature from a spectrum can e.g. be carried out by the measurement of line equivalent widths. Sousa et al. (2010) present an empirical relation between ratios of some specific equivalent widths and the effective temperature of 451 stars. The preferred spectral lines are those of iron and its first ionization state (Fe I, Fe II). The measurement of the equivalent widths ratios of Fe I to Fe II has the advantage that iron shows plenty of spectral lines distributed over the whole optical wavelength range and beyond. The high number of lines makes this analysis statistically significant and independent of cosmics or instrumental issues.

In contrast to the measurement of line equivalent widths, we can also obtain the stellar parameters by directly fitting synthetic spectra to the observed data. For my investigations I used the spectroscopic analysis tool *Spectroscopy Made Easy* (SME) (Valenti & Piskunov, 1996), which uses this approach. It relies on a line list from the VALD project[3] (Piskunov et al., 1995) and on a grid of model atmospheres. I used the preset Kurucz model atmosphere grid, but in principle other atmospheres could be used if the file formats would be changed to an SME-readable form.

In the following, I present the determination of stellar parameters using high resolution spectra. These spectra belong to two planet host stars (ε Eridani[4] and CoRoT-2A[5]) and were obtained by our group using the VLT UVES instrument. The resulting stellar parameters will be compared to values found in the literature to give a general assessment of the accuracy of the used software. According to Section 1.1.3, the limb darkening is influenced by stellar parameters, especially by the effective temperature. Therefore, an easy and also precise method to determine these parameters is of great interest to model low signal-to-noise transit light curves when using limb-darkening predictions. In the case of CoRoT-2A the results of the parameter fits and the comparison to other methods are published in cooperation with S. Schröter (Schröter et al., 2011).

2.2.1 Using SME to determine stellar parameters

The spectral analysis tool SME is able to determine a whole bunch of stellar parameters from an observed spectrum by minimizing the χ^2 between data and model. For convenience the available parameters can be divided into three groups. First, the *global* parameters that have an influence on all absorption lines, second, the *line* parameters which influence individual lines,

[3] VALD2 http://vald.astro.univie.ac.at/~vald/php/vald.php, used in this thesis, VALD3 http://vald.astro.uu.se also includes some molecular lines.
[4] Program ID: 383.D-1002(A), PI: Wolter (Nov. 2009)
[5] Program ID: 385.D-0426(A), PI: Wolter (Jun. 2010), Observer: Huber

and last the individual element *abundances*. The parameters that belong to the second group are the absorption oscillator strength $\log(gf)$ and the van-der-Waals damping γ_6. These should only be fitted if the focus lies on some specific lines or elements. Especially for improving the accuracy of the abundance measurements, the oscillator strengths of the corresponding lines should be calibrated by using a solar spectrum[6]. Nevertheless, such a detailed investigation should only be carried out after the determination of the global parameters. These parameters are $T_{\rm eff}$, $\log g$, [M/H], the microturbulence ξ, the macroturbulence ζ, the projected rotation velocity of the star $v \sin i$, and a global γ_6 factor. Before I present the fit results of these parameters when using the mentioned high resolution spectra I will comment on a few steps which have to be done to achieve proper stellar parameters. The general usage of SME is explained in the available handbook (Valenti et al., 2012), and therefore not explained in detail here. However, in the following we will also see some implemented features and how SME has to be operated.

First of all, the observed spectrum has to be normalized before it is read into the software. Although, SME is able to handle data that is given in absolute flux units, I recommend this step to achieve most reliable results. If a simple detrending after the normalization process is still needed, SME can also perform a linear fit to the continuum on its own. When no further detrending or normalization is necessary, we have to determine the spectral resolution ($\lambda/\Delta\lambda$) of the data. This is absolutely necessary especially for low resolution spectra. Similar as the bin time for transit light curves (see Fig. 1.15), the limited spectral resolution broadens the absorption lines. Consequently, the SME software has to account for this circumstance in the spectral modeling to achieve correct fit values. In fact SME generates a highly resolved synthetic spectrum, which is broadened by convolution with a Gaussian corresponding to the given spectral resolution of the data. The minimization process is then performed between this broadened spectrum and the data. This approach is quite similar to the overbinned fit model used in transit modeling. After assigning the spectral resolution we can proceed with the object's radial velocity ($v_{\rm rad}$). It causes a relative Doppler shift of the spectrum with respect to the observer, thus, $v_{\rm rad}$ has to be known otherwise the spectral synthesis of SME would not fit the data anyway. There exist different methods how to determine $v_{\rm rad}$, e.g. using cross-correlation, but it is also possible to use SME. In this case SME fits a synthetic spectrum to the data by applying a Doppler shift. For this fit we have to guess values for the global parameters. Actually, it is not necessary to be close to the correct values of the star, though it is more important to keep the broadening of the lines equal or below that found in the data. In this way SME is able to find a global match of the line center positions.

After we have performed the three initial steps explained above we can in principle start a global fit leaving all the associated parameters free. This is, however, not recommended due to correlations between the parameters. It would be more appropriate if we could perform a fit of only one of these parameters. Therefore, we select spectral lines which are mainly sensitive to only one or at least weakly sensitive to the remaining parameters. For the estimation of $T_{\rm eff}$ we e.g. use the H_α and H_β lines. Their line wings are primarily sensitive to the effective

[6] Piskunov, private communication

temperature (e.g., Fuhrmann, 2004) and only slightly influenced by the other parameters like $\log g$. When using the Balmer lines we have to leave out the line cores during the fitting approach, because they are affected by chromospheric emission. After that fit we can set $T_{\rm eff}$ to the value achieved and fix it for all further modeling. For the surface gravity we proceed in a similar way. We select the Na D lines, which show a clear sensitivity to $\log g$ (e.g., Gray, 1976) and perform a fit of $\log g$ with SME keeping all other parameters fixed. It is important to first achieve a proper effective temperature before fitting for the gravity, since the Na D lines are also known to be significantly affected by $T_{\rm eff}$. By the determination of $T_{\rm eff}$ and $\log g$, we reduced the number of parameters to be fitted to five, which are finally fitted together. The introduced steps, first fitting $T_{\rm eff}$ followed by $\log g$ and finally a fit of the remaining parameters, should be the normal approach when modeling observed data using SME.

As an interesting byproduct, SME can also be used to generate synthetic spectra. Depending on the line list used, the resulting spectrum consists of only one element or a full set of all available elements together with some molecular lines. Furthermore, these spectra could be synthesized for almost any parameter combinations. I used this feature to create a grid of almost 80 synthetic spectra in the range of 5500 Å to 9000 Å. For the initial parameter set I used arbitrary values: $T_{\rm eff} = 5500\,\mathrm{K}$, $\log g = 4.44$, $\xi = 1.1\,\mathrm{km\,s^{-1}}$, $\zeta = 0.0\,\mathrm{km\,s^{-1}}$, $v \sin i = 2.0\,\mathrm{km\,s^{-1}}$, and [M/H] = 0.0. For each following parameter set of the grid I varied one specific parameter and kept the remaining fixed to the initial values. The resulting grid is excellent to see the effects of e.g. the effective temperature or the surface gravity on the spectrum and to find absorption lines sensitive to specific parameters. In Fig. 2.5 I show five different spectral lines of my SME grid for which these effects are well pronounced. As we can see, the influence of the effective temperature on the H_α line profile is clearly visible for the chosen temperature range. For each increased temperature (400 K per step) the line becomes deeper and the wings extend further. The width of the line core also increases with $T_{\rm eff}$. At 4000 K the influence is limited to ±5 Å away from the line center, while at 6000 K the continuum is suppressed in a range of about ±50 Å. The surface gravity has a similar effect on the Na D lines. The line wings are significantly pressure broadened, but there is almost no change in line depth. In contrast to $T_{\rm eff}$ and $\log g$ the Doppler broadening caused by the $v \sin i$ has the same influence on all lines. The upper right panel of Fig. 2.5 illustrates the broadening and decreasing of the line depth for typical velocities. At high velocities spectral lines which are located close to each other are merged and cannot be individually resolved anymore. Two further broadening mechanisms are the micro- and macroturbulences. In the concept of the microturbulence the size of the turbulent cells is smaller than the mean-free photon path. Photons emitted in one cell can reach another cell and will be absorbed there. Due to the relative velocities between these cells, a photon emitted in the line core is then absorbed at a Doppler shifted wavelength, e.g. in the line wing. Thus the microturbulence ξ broadens the line and increases the equivalent width. In the case of macroturbulence ζ the turbulent cells are larger than the mean-free photon path. The photons are emitted and absorbed in the same cell. The velocities relative to the observer are now relevant. Consequently, the macroturbulence broadens the line together with a constant equivalent width. For weak spectral lines both turbulences are not distinguishable, which should be illustrated by the small Mo I line in the

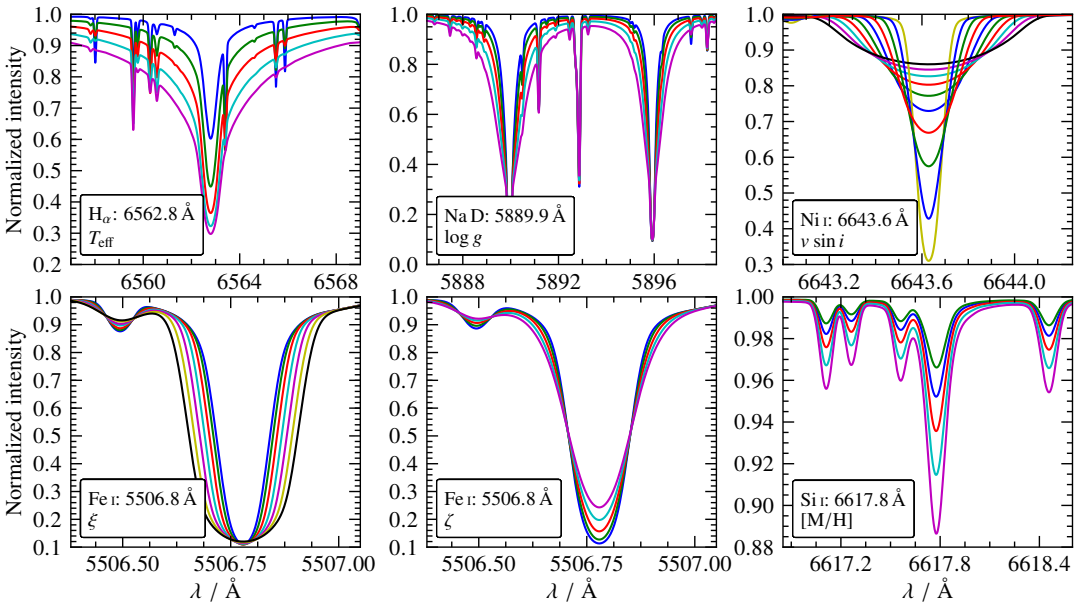

Figure 2.5: Synthetic absorption lines generated with SME for different stellar parameters. The center wavelengths, the designations, and each varied parameter are given in the *labels*. $T_{\rm eff}$: 4000 – 6000 K, $\log g$: 3.0 – 5.0, $v \sin i$: 2 – 20 km s^{-1}, ξ: 0.2 – 3.0 km s^{-1}, ζ: 0.25 – 5.0 km s^{-1}, [M/H]: −0.3 – 0.3.

upper left corner of these panels. The influence of the metallicity on the spectral lines is shown in the bottom right panel of Fig. 2.5. Higher metallicities lead to stronger lines, which can easily be seen by an increasing depth and an almost constant line width. This means that the line equivalent widths increase with metallicity due to a higher number of absorbers in the line of sight, which is the concept of the curve of growth.

Another interesting feature of SME is the option to define a set of limb angles μ, for which the spectrum is synthesized. By default the number of different μ-values is set to seven, but it is possible to define an arbitrary number or even only one single limb angle. The synthesis for different μ-values is important, since limb darkening occurs as an additional line broadening mechanism with rather U-shaped lines at the limb and more V-shaped at disk center (e.g. Frisch, 1975). Beside the normalized intensities SME also provides the specific intensities for the generated spectrum. Therefore, it is possible to get the specific intensities for individual μ-values. I used SME to generate model spectra at 15 individual limb angles between 0.0001 and 1.0 together with solar values for the global parameters. The resulting spectra were then convolved with Johnson-R and -V filter functions. To determine the intensity for each μ-value I calculated the sum of the filter-convolved specific intensities. Finally, these are normalized by the disk-center value ($\mu = 1.0$) and visualized in Fig. 2.6. The shown limb intensity profiles could in principle be used to determine limb-darkening coefficients in any photometric pass band. However, a by eye inspection reveals that these profiles are not compatible with any model limb darkening available in Claret & Bloemen (2011) or Claret et al. (2013), especially for the Sun. The curvature is too strong, which leads to an overestimation of the intensities for

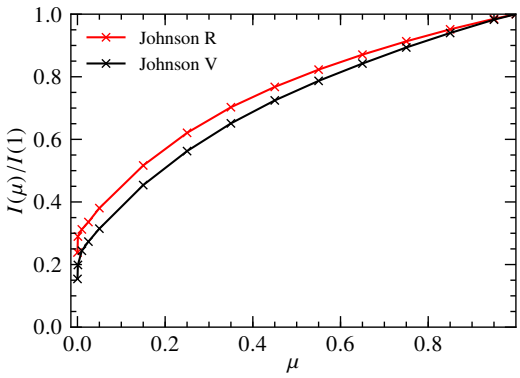

Figure 2.6: Limb darkening simulated with SME. The limb intensity profiles shown are generated for two Johnson filters (*labels*). The limb angle μ was varied between 0.0001 and 1.0 (*crosses*). For each limb angle a spectrum was synthesized. See text for details.

almost all μ-values. A fit of these profiles in the range of $\mu = 0.01$ to 1.0 leads to quadratic limb-darkening coefficients of $u_1 = 0.16$ and $u_2 = 0.52$ for Johnson-R, and $u_1 = 0.25$ and $u_2 = 0.50$ for the Johnson-V filter. Due to the curvature the values for u_2 are quite high and consequently u_1 is small. Such a combination cannot be found in the mentioned publications, neither for solar-like parameters nor in more extreme temperature regimes.

2.2.2 Fit results for ε Eridani and CoRoT-2A

After the introduction of the usage and capabilities of SME above, I now present the analysis of real data. For that purpose I use the observations of the two planet hosts ε Eridani and CoRoT-2A mentioned above. To follow the introduction I started with the normalization of the spectra using the class `ContiInteractive` from the `PyAstronomy`. This class allows estimating the continuum manually by defining a set of points in an interactive plot window. The decision where to set these points is supported by a highly resolved synthetic spectrum. The usage of this tool is easy and the spectra are well normalized and rectified. Hence, I can now determine the spectral resolution ($\lambda/\Delta\lambda$) of both observations, which I carry out by fitting a Voigt profile to telluric lines. For both objects I chose five different, deep, and distinct telluric lines in the region 6900 Å to 7300 Å (see Table A.3). The full width at half maximum (FWHM) of the fitted Voigt profiles is then taken as $\Delta\lambda$. The mean spectral resolution calculated from these five individual lines is 55 248 ± 2587 in the case of ε Eridani, and 65 832 ± 2540 for the CoRoT-2A spectrum.

In contrast to the approach mentioned in the previous subsection, I started with a global parameter fit instead of individual fits for $T_{\rm eff}$ and $\log g$ using the H_α and Na D lines. In this way we will see whether the results significantly deviate from the individual line fits and if it is worth to make these additional steps. To reduce the number of free parameters I fixed the macroturbulence ζ in the case of ε Eridani to 1.3 km s^{-1}. This value is found according to Saar & Osten (1997), who give a relation between spectral index and ζ. They also show that the macroturbulence is higher for active stars. CoRoT-2A is known to be highly active and, therefore, I chose the value determined by Valenti & Fischer (2005a), (Eq. 1). Their equation provides an upper limit of the macroturbulence, which leads to 3.1 km s^{-1} for CoRoT-2A.

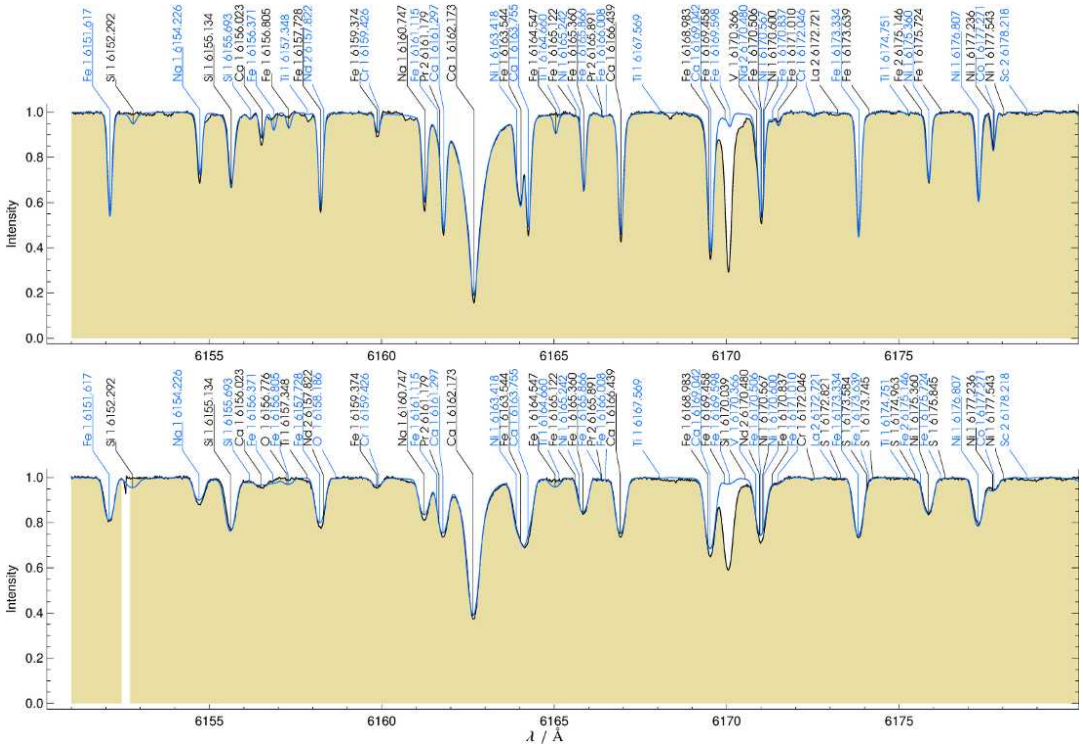

Figure 2.7: Comparison of observed (*black*) and best-fit synthetic spectra (*blue*) of ε Eridani (*top*) and CoRoT-2A (*bottom*). The region around Ca I at 6162.2 Å is shown. Most lines are labeled, only a few weak lines are not included. Shaded areas mark spectral regions used for the optimization process, while white areas are neglected. Graphs produced with SME.

According to their work the macroturbulence is mostly correlated to the line broadening caused by the stellar rotation and that is why they fixed $v \sin i$ to zero for their investigations. For my global fit I leave $v \sin i$ as a free fit parameter, but additionally fixed the van-der-Waals damping constant γ_6 to 1.0. My simulations showed that in the range between 1.0 and 2.5, which is reasonable for iron lines, this value has only marginal effects on all spectral lines. The remaining number of parameters for a global fit were now reduced to five. For these I set common initial values: $T_{\rm eff} = 5500\,\mathrm{K}$, $\log g = 4.5$, $v \sin i = 2.5\,\mathrm{km\,s^{-1}}$, $\xi = 1.5\,\mathrm{km\,s^{-1}}$, and [M/H] = 0.0. The stellar rotation velocity of CoRoT-2A is obviously higher than my chosen initial value and so I estimated $11.25\,\mathrm{km\,s^{-1}}$ by using the visible major variability of 4.5 days (see Fig. 2.1). For both spectra I marked regions with strong telluric contamination to be left out during the optimization process.

The results of this global fit are shown in Fig. 2.7 and in Table 2.1 in the case of ε Eridani and in Table 2.2 for CoRoT-2A. For the plot in Fig. 2.7 I arbitrarily chose a spectral region near the Ca I line at 6162.2 Å. The agreement between the synthetic best-fit model and the observed data is amazingly good for both stars. Most notably the region close to the mentioned Ca I line, which has broad line wings with additional absorption lines located there, is also

Table 2.1: Stellar parameters of ε Eridani.

Source	$T_{\rm eff}$ / K	$\log g$	$v \sin i$ / km s^{-1}	ξ / km s^{-1}	ζ / km s^{-1}	[M/H]
SME global fit [a)]	5084 ± 44	4.68 ± 0.06	2.42 ± 0.50	1.39	1.3 fixed	-0.09
SME H_α, Na D [a)]	5066 ± 89	4.51 ± 0.06	2.79	1.34	1.3 fixed	-0.07
Valenti [b)]	5146	4.57	2.40			0.00
Gonzales [c)]	5032 ± 48	4.30	2.50	0.60		-0.01
Tsantaki [d)]	5049 ± 48	4.45 ± 0.09		0.83 ± 0.10		-0.15

Notes: Comparison of SME's best-fit stellar parameters to values found in the literature. [a)] This work, [b)] Valenti & Fischer (2005b), [c)] Gonzalez et al. (2010), [d)] Tsantaki et al. (2013).

well reproduced by the model. The wavelength region shown is a good example for the whole spectral range available. This means that we find well looking matches between model and data everywhere in the spectrum, but also lines which are not reproduced by the model, and lines which are predicted by the model but not present in the data. For instance, the Si I line (6152.3 Å) at the left of Fig. 2.7 or Fe I line (6164.5 Å) close to the middle of the image are both predicted by the model but not visible in the data. The opposite is the case for the strong Fe I line at 6169.6 Å. This line is present in the spectra of both objects, with almost the same strength, but totally underestimated by the model. Both phenomena – line strengths overestimated or underestimated by theory – are probably caused by incorrect oscillator strengths provided by the line list. The overall agreement between model and data is good after the optimization and the major difference between these two observations is the broadening of the lines caused by different stellar rotation velocities. In the case of CoRoT-2A this causes some lines to be blended by neighbors, e.g. visible in the right line wing of the mentioned Ca I line. Nevertheless, this region is also well reproduced by the model. The resulting parameters of this global fit are listed in the mentioned tables. Unfortunately, the determination of parameter errors is not implemented in SME. For the global fit I thus used the statistical errors provided by Valenti & Fischer (2005a). Compared to the other values found in the literature my global fit parameters of ε Eridani are quite reasonable. For the effective temperature my result is in agreement to the literature values when 2σ intervals are assumed. In contrast to the others, my global fit leads to a significantly higher surface gravity. The $v \sin i$ values are all in an interval of ± 400 m s^{-1}, that is smaller than the assumed uncertainty. My fit also yields a sub-solar metallicity, as most of the other values publically available. It seems that the precision of a simple global parameter fit is sufficient to determine the stellar parameters. Nevertheless, we should have a look at fit results when first the individual line fits are carried out to determine $T_{\rm eff}$ and $\log g$ separately. As already mentioned above, I will use the H_α line to estimate the effective temperature and the Na D lines to determine the surface gravity. For the H_α line fit it is important to include enough surrounding "continuum", because of the broad line wings. This way we increase the sensitivity of the fit. In the case of ε Eridani I selected an interval from 6550 Å to 6580 Å. For the Na D lines the selection for the fit is rather similar. Both wavelength ranges are shown in Fig. 2.8 together with the best-fit models. The H_α line profile

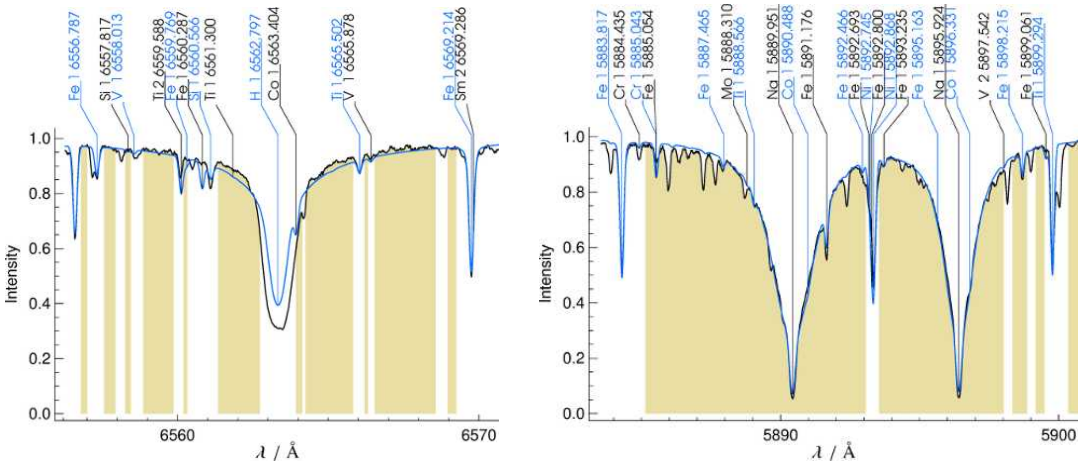

Figure 2.8: Comparison of observed (*black*) and best-fit synthetic spectra (*blue*) of ε Eridani. *Left*: H_α region for the determination of $T_{\rm eff}$. *Right*: Na D lines to measure $\log g$. White areas are neglected during the optimization process.

is not perfectly reproduced by the model, especially the line core. However, a perfect fit of the H_α line is not to be expected when only using LTE models. More important is an agreement between model and data further away from the line core, which is reasonably good in the presented case. The Na D lines show in contrast a really good agreement between model and data. The values for $T_{\rm eff}$ and $\log g$ are now a little bit lower than for the global fit, but still compatible with the other values listed in Table 2.1. The given 1σ errors are determined over the χ^2 statistics and now twice as high for $T_{\rm eff}$. The remaining parameters $v \sin i$, ξ, and [M/H] are fitted after setting the temperature and the gravity to the values found in the individual fits. ξ and [M/H] show no appreciable difference. The $v \sin i$ has increased but only in the range of the uncertainty of the value achieved by the global fit. It is only conspicuous that I found higher values for the microturbulence than the given values from the literature. For the remaining parameters there are no significant discrepancies between the values found in the literature and when SME was used. Conclusively, in the case of ε Eridani it is reasonable to perform a global parameter fit. The additional effort of the individual fits for the effective temperature and the surface gravity seems to be not necessary.

The discussion of the values achieved for CoRoT-2A can be found in Schröter et al. (2011) and, therefore, is not reviewed in detail here. Nevertheless, we can see in Table 2.2 that the estimates of the effective temperature show a larger scatter as it is the case for ε Eridani. The values span a range of 150 K in contrast to 114 K. This range is 32 % larger than found for ε Eridani, most probably caused by CoRoT-2A's activity. If we look at the metallicity, we see positive and negative values, while we only found negative values in the case of ε Eridani. Between minimum and maximum metallicity we see a range of 0.13, which is almost the same as in Table 2.1. The discrepancy of the microturbulences seen in the case of ε Eridani is not present for CoRoT-2A. All presented values are more or less in the 1σ range given by Ammler-von Eiff et al. (2009). Therefore, it can be assumed that it was not a systematic

Table 2.2: Stellar parameters of CoRoT-2A.

Source	$T_{\rm eff}$ / K	$\log g$	$v \sin i$ / km s^{-1}	ξ / km s^{-1}	ζ / km s^{-1}	[M/H]
SME global fit [a)]	5475 ± 44	4.62 ± 0.06	10.79 ± 0.50	1.52	3.1 fixed	-0.06
SME H_α, Na D [a)]	5510 ± 90	4.53 ± 0.18	10.78	1.47	3.1 fixed	0.00
Bouchy [b)]	5625 ± 120	4.30 ± 0.20	11.25 ± 0.45			0.00
Ammler [c)]	5608 ± 37	4.71 ± 0.20		1.49 ± 0.04		0.07
Torres [d)]	5575 ± 66	4.51 ± 0.04	10.30 ± 0.90			-0.04

Notes: Comparison of the resulting SME stellar parameters and values found in the literature. [a)] This work, published in Schröter et al. (2011), [b)] Bouchy et al. (2008), [c)] Ammler-von Eiff et al. (2009), [d)] Torres et al. (2012).

behavior of SME to overestimated ξ of ε Eridani. If we look at the results obtained by the individual fits for $T_{\rm eff}$ and $\log g$ we see that they also do not differ significantly from the global fit, as it was the case before for ε Eridani.

We have seen in the foregoing examples that the software tool SME is able to determine stellar parameters, which are comparable with values determined with other methods of spectral analyses. In the end this is not necessarily surprising, because SME is e.g. already used for the determination of stellar parameters of Kepler targets (Batalha et al., 2013) and today widely used in astronomy. The resulting parameters are thus well suited to help estimating the limb darkening from theoretical models or tables. Furthermore, I showed that the differences of the parameters determined with a global parameter fit or after a individual fit for $T_{\rm eff}$ and $\log g$ are not significant. Therefore, a simple global fit – where all important parameters are set free at the same time – is enough for determining the stellar parameters. This makes SME a handy tool to easily determine the fundamental stellar parameters with reasonable accuracy.

3 The *Kepler* Space Mission

The *Kepler* space telescope is a project developed by the American space agency NASA. It was especially designed for the search for earth-sized planets near or in the habitable zone of solar-like stars (cf. Borucki et al., 2010). The mission is named after the German astronomer Johannes Kepler ($\star$ 1571, † 1630), who invented fundamental celestial laws by analyzing precise position measurements of Mars made by Tycho Brahe. Today his laws are known as the three Kepler-laws which describe the orbital motion of the solar system bodies with great accuracy (e.g. Unsöld & Bascheck, 2005; NASA, 2009), of course neglecting small relativistic effects known nowadays. Kepler was the first who found that the planets move on *elliptical* paths around the Sun, which was also a proof for a heliocentric solar system. His landmarking laws can obviously be applied to other stellar systems far away from ours and, therefore, it is a tribute to name this NASA mission after him.

3.1 Instrumental layout

To search for new exoplanets the *Kepler* telescope looks for periodic dimming of the emitted light of stars in the field of view which is also often referred to as transit method (Section 1.2.2). To achieve such transit data *Kepler* measures simultaneously the brightness of a greater number of stars over a long period. This is necessary to account for the transit probability (also discussed in Section 1.2.2) and for long lasting orbital periods to accumulate a representative number of transiting exoplanets.

The *Kepler* space telescope (Fig. 3.1) is a *Schmidt*-type telescope used as a photometer with a primary mirror which has a diameter of 1.4 m. The aperture has a diameter of 0.95 m The overall length is 4.7 m and it has a total diameter of 2.7 m. The main camera is placed in the focal plane of the primary focus (Fig. 3.2). This camera is build as a CCD array of 42 individual CCDs with a resolution of 2200×1024 pixels each. The quantum efficiency curve lies in the optical regime and reaches its maximum of $\approx 85\,\%$ at $\lambda \approx 600$ nm. The total spectral response of the photometer is slightly shifted to the blue, since it is a combination of all optical components, e.g. the transmissivity of the Schmidt-corrector and the reflectivity of the primary mirror. The maximum spectral response of 73 % is located at $\lambda \approx 590$ nm. The photometer provides a bandpass between 440 nm and 830 nm at FWHM[1]. The whole array is cooled down to −85 °C reducing the dark current to less than 1 $e^{-}px^{-1}s^{-1}$ making it completely negligible compared to stray- and zodiacal light which is on the order of 10^2 $e^{-}px^{-1}s^{-1}$. The

[1] Full width at half maximum

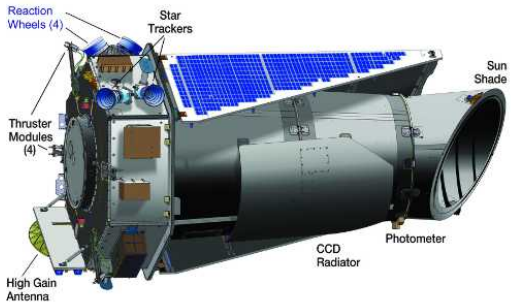

© [NASA & Ball Aerospace, 2008]

Figure 3.1: Overview of important elements of the *Kepler* flight segment. The lens tube contains the *Kepler* photometer while the hexagonal structure is the spacecraft. (Minor modifications applied).

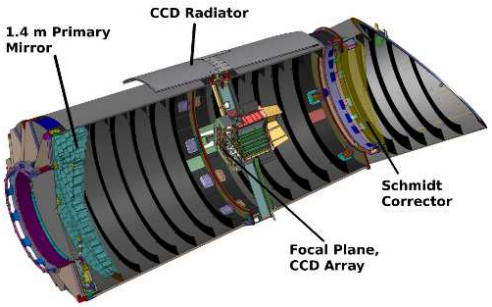

© [NASA, 2006]

Figure 3.2: Cross-section of the *Kepler* photometer. The lens tube is strengthened by graphite rings (*black*). (Labels added by thesis author according to NASA (2005)).

total field-of-view achieved by this camera is about 115 square degrees. This covers almost 0.3 % of the whole sky in which stars with a visual magnitudes between 9 and 15 were planed to be observed. In the end also stars with visual magnitudes down to $\approx 5.5^{\mathrm{m}}$ and up to $\approx 20^{\mathrm{m}}$ were observed. The resulting guidance accuracy of the spacecraft is better than $0.009''$ which is much better than the given pixel scale of $3.98''$. This accuracy is achieved by two star trackers (see Fig. 3.1) in combination with four small additional CCDs located in the corners of the main CCD array. Roll and pointing movements are performed by small thrusters and four reaction wheels (also Fig. 3.1). The advantage of reaction wheels in contrast to thrusters is obvious; they do not need any propellant and work only with electric power provided by the solar modules to induce gyroscopic forces. (Cf. NASA, 2009; Van Cleve & Caldwell, 2009; Bryson et al., 2010a).

The data acquisition and the total number of observed stars are limited by the bandwidth of the telemetry downlink to Earth and by the applied amount of onboard data storage. In general all 42 CCDs are read out every 6.54 s after an exposure time of 6.02 s, which results in over 13 000 shots per day. This would produce a tremendous amount of data. To restrain this problem only a selection of target pixels is stored instead of the full images, whereas the amount of target pixels depends on brightness of the target objects. The average aperture size is 85 pixels, however, overexposed targets can also be scientifically used by applying a saturation model to all involved pixels, including adjacent pixels contaminated by charge bleeding (Van Cleve & Caldwell, 2009). All data is then added up into observations with almost 30 minutes bin time and named as *Long Cadence* (LC) data. This approach makes it possible to acquire nearly continuous observations of more than 160 000 stars at the same time. For measurements where high temporal resolution is needed, e.g. the search for transit timing variations or in my case limb-darkening analyses, the data of at most 512 targets can be added into observations of one minute bin time then called *Short Cadence* (SC) data. In this mode nine integrations are combined into one time bin. Beside the target pixels it is

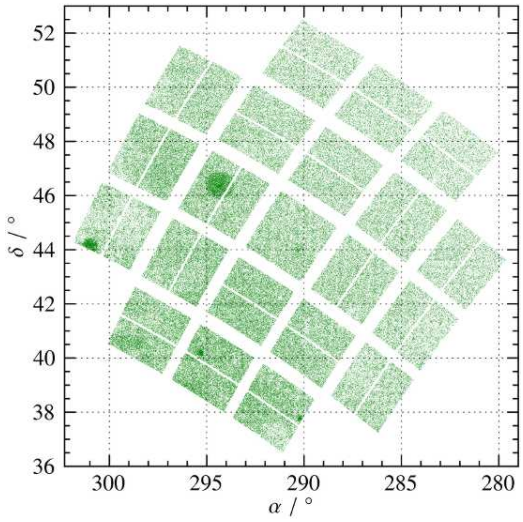

Figure 3.3: *Kepler*'s field-of-view and CCD array. Each point represents a target star observed by *Kepler*, 207 607 in total. Separations between the 40 CCDs are clearly visible, only between the two centered CCDs the gap is filled up due to clock-wise quarterly rolls. Dark areas represent higher density of selected target stars.

necessary to store sets of background and reference pixels. The background pixels (378 kpx in total) are used to remove zodiacal light and two-dimensional instrumental artifacts, while 96 000 pixels are collected as reference pixels to examine the health status of the CCDs and readout electronics. The are downloaded every four days. In contrast to the amount of background and reference pixels only 43 520 pixels are available for targets observed in SC mode. This clearly illustrates the importance of the background and reference pixels to achieve scientifically usable data. (Cf. Van Cleve & Caldwell, 2009; Borucki et al., 2010; Bryson et al., 2010a).

In Fig. 3.3 I show all stars observed with *Kepler* through the whole main mission life time (Section 3.2). Each point represents a set of celestial coordinates read out from the headers of the corresponding FITS files. This illustration visualizes *Kepler*'s field-of-view and the layout of the CCD array. Visible narrow and broad separations are caused by gaps between the CCDs. This makes it possible to simply identify the 42 individual CCDs, although the narrow gap of the two centered CCDs is filled up with stars. This is due to *Kepler*'s 90° clock-wise rotation around the optical axis performed every three months (see Section 3.2). Dark areas correspond to a higher spatial density of selected stars which not necessarily translates into the real spatial density of stars at the sky. Usually there are more stars in a given region than selected by the *Kepler* team, e.g. this is supported by the "dark spot" at $\delta \approx 46.5°$ with a diameter of nearly one degree. There is indeed the open star cluster NGC 6811 located, but it has only a diameter of less than a half minor tickmark. A similar selection pattern was applied to the positions of the open star cluster NGC 6866 ($\alpha = 301°$, $\delta = 44.2°$) and to the two open star clusters slightly hard to identify in this figure NGC 6791 ($\alpha = 290.2°$, $\delta = 37.7°$) and NGC 6819 ($\alpha = 295.3°$, $\delta = 40.2°$). Overall *Kepler* gathered light curves of 207 607 stars of which 5328 are observed additionally in SC mode. Note that the slightly curved structure visible in Fig. 3.3 results from the coordinate transformation of Cartesian-CCD coordinates to celestial coordinates and not from the convex shape of the focal plane needed for a Schmidt-telescope.

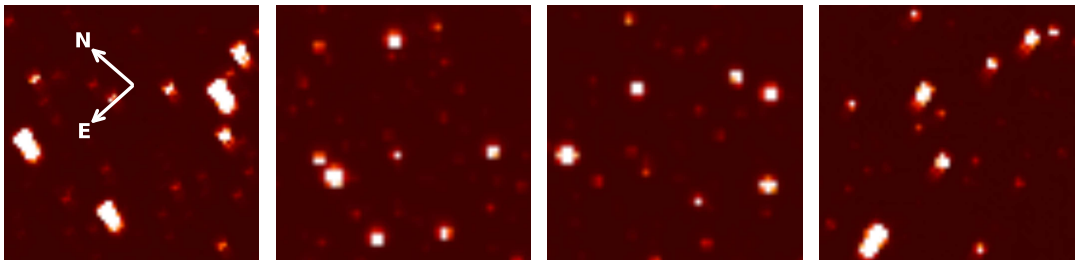

Figure 3.4: Details of *Kepler* full frame images of four different CCD channels (*left to right:* 56, 41, 43 and 15). Stars are visible as bright dots. All images have almost the same orientation towards the celestial coordinates (*white arrows*).

The FITS files themselves are publically available through the NASA Mikulski Archive for Space Telescopes (MAST[2]). In addition to the light curve data, so called *Kepler* full frame images (FFI) are also available, providing CCD images of the target field. Each CCD is thereby divided into two *channels* consecutively numbered (see Fig. B.9). To investigate the performance of this implementation of a Schmidt-telescope, I selected FFI channels from the center and from the edges of the focal plane and plotted arbitrary details of the target field (Fig. 3.4). Starting to count from the left, the second and third image show circular stars. The left and the right image show deformed, elongated stars. This is remarkable, since the images in the middle are gathered from near the center of the focal plane, while both outer images are selected from near its edge. Actually the elongation increases in radial direction and shows an alignment towards the center of the focal plane. That implies for the left image the elongation to be parallel to the declination axis and in the right image parallel to the right-ascension axis (cf. Fig. B.9), which is almost the case. Such a behavior of the point-spread-function (PSF) hints at *coma*, an aberration typical for wide field-of-views but normally corrected when using a Schmidt-telescope. Of course, without further knowledge of the instrumentation this can be only an assumption since there are several possible sources of this deformation under discussion. For a deeper look into the behavior of the PSF or the pixel response function I recommend the work of Bryson et al. (2010b).

It is worth to mention that the region close to *Kepler*'s target field has already been observed by a Schmidt-telescope. In the year 1931 Bernhard Schmidt himself made one of his first observations with his new invented *coma-free* telescope (Schmidt, 1938). In Fig. 3.5 I present a digital copy of the original 55×170 mm photographic plate, stored in the large plate archive of Hamburg Observatory[3]. The field of view is 15° in diameter, and all stars are sharp round dots, also far away from the center of the focal plane! Although, the *Kepler* field is not included in this image (it is located above the upper edge), it is an exciting coincidence. Because 78 years later, a small telescope is orbiting the Sun, the *first* using Schmidt's groundbreaking concept in space, searching for exoplanets close to this observation.

[2] http://archive.stsci.edu/kepler/; renamed after Barbara A. Mikulski. Old name was Multimission Archive at the Space Telescope Science Institute.

[3] http://plate-archive.hs.uni-hamburg.de/index.php/en/, D. Groote, private communication.

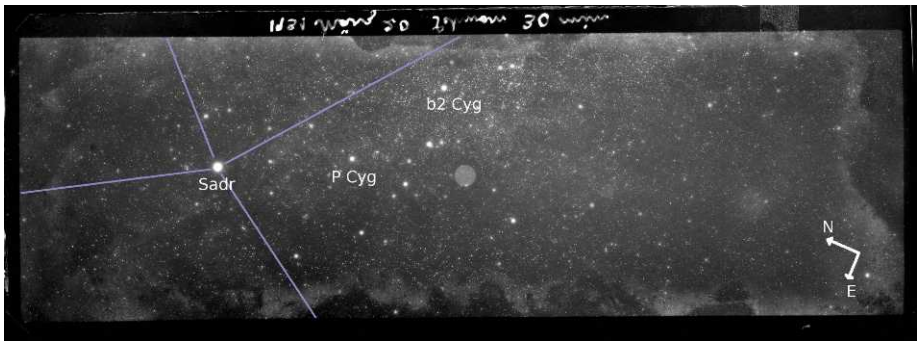

Figure 3.5: Original photographic plate of the Cygnus region, observed by B. Schmidt in 1931 with his new *coma-free* telescope. This image is rotated around the horizontal axis. The *lines* indicate the Cygnus constellation (labels and lines added by thesis author). Text on the plate: "1931 März 20 Schwan 30 min".

3.2 Mission timeline and overview

The *Kepler* mission can be divided into three main phases: launch, commissioning, and science operations. Ahead of these, the star field was selected by fulfilling the constraints to be continuously observable through the whole mission and to be star rich. A continuously observable star field means in this sense, that the line of sight is never blocked by any solar system body. Obviously, the Earth, the Sun and the Moon are the most problematical ones due to their large apparent diameter and their contribution to stray light. Therefore, the remaining directions for this mission lie significantly above or below the ecliptic. Finally, the region near the constellations Cygnus and Lyra in the northern sky was selected since it has slightly more stars than the field in the southern sky, and additionally all ground-based telescopes available for follow-up programs are located on the northern hemisphere. Another important task performed before the launch was the classification of the stars in this field. This time-consuming photometric observations were carried out during a five year program using ground-based telescopes providing different color bands. The gathered results of this program, e.g. effective temperatures, surface gravities, metallicities and apparent magnitudes of more than $13 \cdot 10^6$ stars were summarized in the *Kepler Input Catalog* (KIC) (T. M. Brown et al., 2011). Most of them ($11.4 \cdot 10^6$) lie in the region of the chosen target field near Cygnus and Lyra (boundaries of Fig. 3.3), whereby $4.5 \cdot 10^6$ of these are imaged onto the CCD array. The remaining $1.6 \cdot 10^6$ stars are spread over different areas of the sky. The key aim of this program was to distinguish between dwarf and giant stars as well to remove giants from the target list (Borucki et al., 2010). The resulting transit signal would be too weak for *Kepler* to find Earth-sized planets (see Section 3.3). Nevertheless, there are giants in the target list so long as the found stellar parameters are reliable, e.g. the effective temperature and $\log g$ are believed to be credible within ±200 K and ±0.4, respectively (T. M. Brown et al., 2011).

The launch of the Delta II rocket carrying the *Kepler* telescope was on March 7, 2009 at 03:49:57 UTC (March 6, 2009 10:49:57 p.m. EST (NASA, 2013a)), 400 years after the

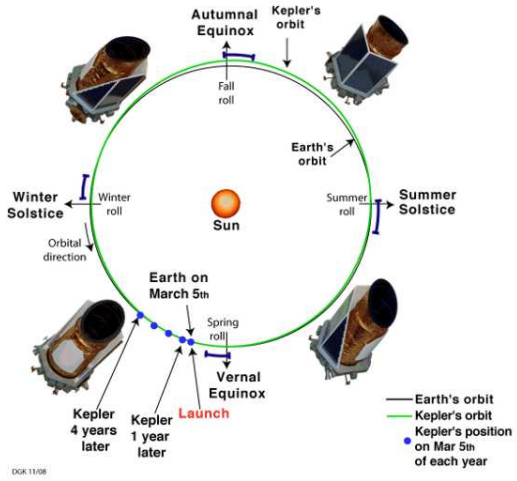

© [NASA & DGK, 2008]

Figure 3.6: Schematic of *Kepler*'s heliocentric orbit, trailing the Earth. View from ecliptic north pole.

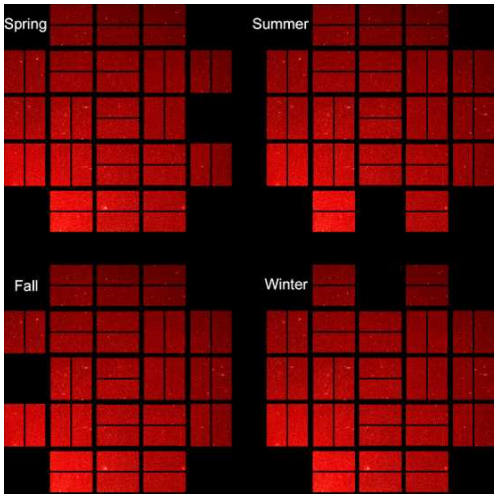

© [NASA, 2010]

Figure 3.7: Depiction of 90° clock-wise rotations of *Kepler*'s focal plane during the seasons. Two defective CCDs sensors indicate the new orientation.

publication of Johannes Kepler's book *Astronomia Nova, 1609* (Kepler & Caspar, 1929) in which he presented his first two laws of planetary motion. The spacecraft was brought to an orbit following the Earth on it's way around the Sun (Fig. 3.6), since the premise of a never blocked field-of-view to acquire continuous observations is then efficiently achieved. At this orbit the influence of the magnetic field and gravitational potential of the Earth is very small, which would otherwise lead to torques on the spacecraft hampering accurate pointing. The orbital speed of *Kepler* is a little bit slower then the Earth's speed so the spacecraft needs 371 days for a complete orbit around the Sun leading to a slowly increasing distance to Earth. Due to this heliocentric orbit geometry, *Kepler* needs to perform 90° rolls around the optical axis almost every three month to keep Sunlight on the solar panels. After such a quarterly roll, each target star is than observed by a different CCD. This leads to different flux count rates measured from the same objects probably caused by different CCD sensitivities.

The *Kepler* mission was designed for three and a half years of science operations after a commissioning phase of 60 days with the possibility to extend the mission until 2016. The first observation of the target field was announced on April 16th 2009. Since then *Kepler* spend over 1600[4] days in space, of which 1425 where used for observations, divided into quarters from 0 to 17. In January 2010, during quarter four, two CCDs were broken, whereby 5 % of the field-of-view were lost; but by reason of the quarterly rolls always a different portion of the target field is not observed by these CCDs as indicated by Fig. 3.7. Therefore, some objects have periodic quarterly gaps in their light curves, e.g. TrES-2b (O'Donovan et al.,

[4] As of September 2013

2006) which is the first detected transiting exoplanet in the *Kepler* field. From then on *Kepler*'s focal plane comprised 40 individual CCD detectors, operating well for all remaining quarters. Unfortunately, this was not the only failure *Kepler* had to deal with. In July 2012 one of the four reaction wheels failed, which are used for fine pointing movements of the spacecraft (see Fig. 3.1). In principle these reaction wheels can induce torques to the three spacial axes of the spacecraft. By the time the anomaly occurred, large pointing jitter affected the observations, thus six days of science data were lost. After several tests the *Kepler*-team decided to deactivate the corrupted wheel #2, since the spacecraft remained fully operational with only three of them. In contrast to other satellites in an earth-near orbit, *Kepler*'s distance to Earth is too large to provide a service mission. Consequently, a failure of one or more of the three remaining reaction wheels would lead to the inability of an accurate pointing, and therefore, to the end of *Kepler*'s search for transiting planets. After almost ten months of observations with only three functional reaction wheels, the spacecraft was found in thruster-controlled self-protecting mode to stabilize it's attitude. This was already an evidence for another reaction wheel to fail. However, the reason for the safe mode was yet unknown and the *Kepler* team was able to transition the spacecraft from thruster-control into reaction wheel control, continuing the data acquisition. Only a few days later on May 14, 2013, the spacecraft was found in a dramatic situation. *Kepler* was rotating around the axis perpendicular to the optical axis, the solar panels always oriented towards the Sun. Thus, the telemetry and communication link was periodically interrupted, since the high gain antenna (see Fig. 3.1) was rotationally induced not permanently directed to Earth anymore. The ground team was able to stop the rotation using *Kepler*'s thrusters. It shall be deemed pretty sure that a failure of the bearing of reaction wheel #4 caused *Kepler* to be in this critical situation. After months of testing the engineers were not able to transition the spacecraft back to reaction wheel control. Therefore, *Kepler* lost its initial pointing stability necessary to search for planets in the designated target field. However, the *Kepler* team made a call for scientific white papers to determine astrophysical studies to be carried out in the spacecraft's current condition. This led to the "K2 mission" (Howell et al., 2014) with lower pointing accuracy observing different parts of the sky. (Cf. NASA, 2013b).

Despite the sudden mission ending at the beginning of quarter 17, *Kepler* was already able to complete its planed prime mission of 3.5 years of nearly continuous observations of the same target field in November 2012. Of the four years of extended mission only nine months were achieved. Nevertheless, it can be referred to the *Kepler* mission as a complete success, not only by reason of 4696 planetary candidates and 1030 confirmed new transiting exoplanets (NASA, 2013c), but also due to the excellent and never before reached photometric precision. One Earth-sized planetary candidate was detected in the habitable zone (PHL, 2013), but one has to keep in mind that Earth-sized is not to be confused with Earth-like (see Section 1.2). *Kepler* also yields data for the study of asteroseismology (e.g., Doğan et al., 2013), which render it possible to examine the interior of stars. The end of the *Kepler* mission does not imply the end of new insights and discoveries provided by this mission, since there is enough data gathered to constitute the basis for many years of analysis. In particular one has to be curious about further confirmations of the large number of planetary candidates, then accomplished by follow-up programs, maybe finding a potentially habitable planet.

3.3 Detection capabilities

In the previous sections I introduced the main characteristics of the *Kepler* instrument, but I did not comment on the acquired data quality and the resulting detection capability. The signal-to-noise ratio of a given data set is one of the most important properties of an astronomical instrument. This value is in principle easy to determine and holds the information how significant a measured signal is compared to the noise. Therefore, the signal-to-noise ratio is a descriptive value, which in the case of the *Kepler* mission says something about the instrument's ability to find small, rocky planets. For my further investigations I will often use the inverse of this value, which is also known as the photometric precision, and comparable to the expected transit depth.

According to Eq. 1.22 the transit depth of an earth-sized planet eclipsing in front of a solar-like star is 0.08 ‰. This is the order of precision we are aiming at. Since the transit center is the deepest part of a transit light curve, we should be able to detect at least this dip. In fact, we better need a photometric precision of $4 \cdot 10^{-5}$ otherwise the transit dip would be hidden in the noise and, therefore, statistically not significant. To estimate *Kepler*'s detection capabilities I will in the following determine the signal-to-noise ratio of a reasonable number of light curves and in the end I will give a short comparison between the two landmarking space-based planetary transit searchers: CoRoT and *Kepler*.

3.3.1 Photometric quality

The easiest way to demonstrate the accuracy of *Kepler*'s photometry is to compare its light curves to ground-based photometry. I have access to photometric observations carried out at Hamburg Observatory (Fig. 3.8, left panel) of one of the *Kepler* targets: TrES-2b (O'Donovan et al., 2006). The direct comparison of these observations clearly illustrates the awesome performance of *Kepler*'s photometer. The Hamburg Oskar Lühning Telescope (OLT) and *Kepler* are about the same size and the bin times of these observations are 56 s and 59 s, respectively. To quantify the difference in photometric quality, I determined the noise level as a simple standard deviation in parts of the light curve surrounding the transit. For the OLT light curve I get $3.1 \cdot 10^{-3}$ and for this *Kepler* transit I get $2.4 \cdot 10^{-4}$. This is a factor of 13 higher signal-to-noise provided by *Kepler*. The poorer signal-to-noise provided by the OLT is mainly caused by the Earth's atmosphere, nicely illustrating the advantage of space-based observations. Additionally, we also have to keep in mind that the shown example is only *one* observed transit light curve, with its original time binning of one minute. But *Kepler* observed a few hundred transits of this object in the same quality. This obviously further increases the photometric precision provided by *Kepler*, e.g. if these transits are phase-folded and rebinned.

Besides this astonishing example, *Kepler* successfully gathered many light curves of transiting exoplanets (see Table 3.2). Therefore, it is reasonable to study the signal-to-noise of a greater number of objects. Hence, I chose objects which should be interesting for my work, which

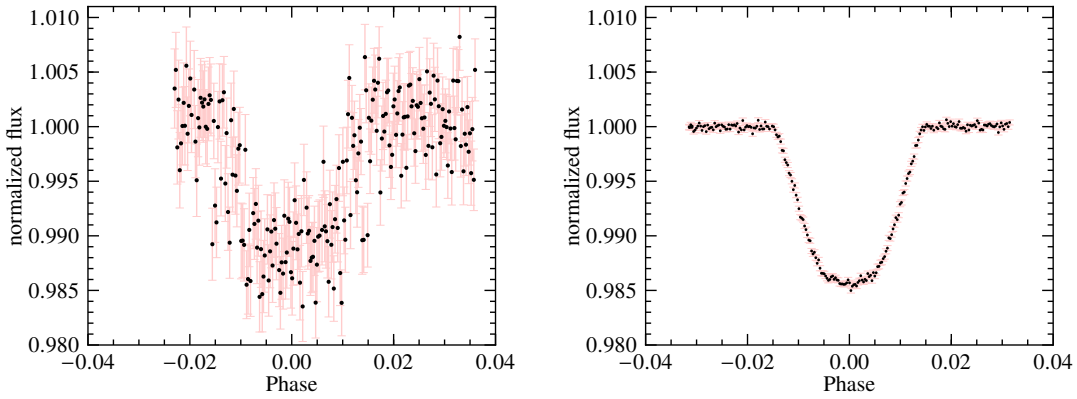

Figure 3.8: A single transit light curve of TrES-2b, plotted in phase. Flux is normalized to continuum level. Transit observed with the Hamburg 1.2 m Oskar Lühning Telescope (OLT) (*left*) and spaced-based with *Kepler* (*right*). OLT observations carried out by D. Mislis.

means objects announced as planetary candidates (STScI, 2012), and determined the signal-to-noise. Obviously, the signal-to-noise is a function of the apparent magnitude of the host star. For an easy overview I plot the determined signal-to-noise values against the *Kepler* magnitude in Fig. 3.9. We can see a clear decrease in the signal-to-noise value with increasing magnitude, which is not surprising. More interesting is that most objects used here show a signal-to-noise of smaller than 2000. This means that the photometric precision of these objects is not high enough to detect a transiting earth in front of a solar-like star, since we would need at least 12 500. However, we know that *Kepler* observed significantly more than one transit event per object, which allows us to calculate a cumulative signal-to-noise given as

$$(S/N)_\mathrm{c} = \sqrt{N_\mathrm{T}} \cdot \sigma_\mathrm{Ph}^{-1}\,, \tag{3.1}$$

or its inverse what I call *cumulative detection limit*. The parameter N_T denotes the number of detected transits. If we assume that N_T is, e.g. 200, which is a reasonable value for objects with an orbital period of, say, 7 days, we end up with $3.5 \cdot 10^{-5}$ and, therefore, an Earth-sized planet could be detected. In contrast, the detection of Earth-sized planets in the habitable zone around a solar-like star is not possible, since *Kepler* would only have recorded up to 4 transits, which leads to a cumulative detection limit of $2.4 \cdot 10^{-4}$ (or a signal-to-noise ratio of "only" 4000). In conclusion, the determined signal-to-noise values shown in Fig. 3.9 are important for short lived signatures like spots probably only present in one transit. If there are more transits available, we can also use this figure to give an assumption of the total detection limit. In the end, *Kepler* found 7 nearly Earth-sized planetary candidates in the habitable zone around their stars, and 233 nearly Earth-sized planets in total (Fig. B.5). These numbers are the best proof of the data quality provided by *Kepler*. For more information about the detection statistics, I recommend Borucki et al., 2011.

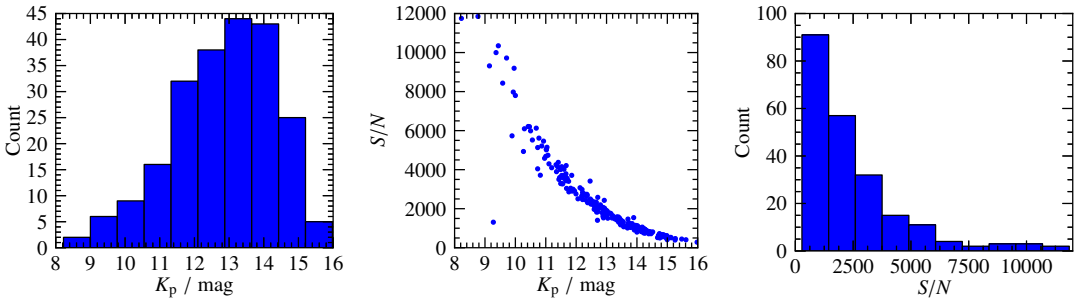

Figure 3.9: Data quality of *Kepler* short cadence planetary candidates. From *left* to *right*: Frequency distribution of the apparent magnitude of *Kepler* planetary candidate host stars, instrumental performance in the sense of signal-to-noise ratio as a function of apparent magnitude, and frequency of high quality light curves.

3.3.2 Comparison of CoRoT and *Kepler*

The CoRoT space telescope (Baglin & COROT Team, 1998) was launched two years before *Kepler* and also designed to search for planetary transits. It was the first space-based program to search for exoplanets. The mission was also announced as a search for Earth-size planets (e.g., Deleuil et al., 1997) and, therefore, a direct comparison of these two instruments is obvious.

Both missions differ in instrumental characteristics as well as in the chosen orbit geometry. In contrast to *Kepler* the CoRoT satellite was launched into a polar Earth orbit. For that reason it was necessary that the spacecraft performs a 180° rotation every half year, otherwise the Sun would move into the field-of-view. After such a rotation CoRoT was then observing in the opposite direction. Consequently, the CoRoT mission has two different target fields, one in the direction of the galactic center, both observed for almost 150 days. The most eye-catching differences between both instruments are on the one hand the diameters of the main mirrors and on the other hand the number of used CCD cameras. For instance, the effective light-gathering surface area of CoRoT's main mirror is 12.4 times smaller than *Kepler*'s. I summarize the most important instrumental differences in Table 3.1.

The diverse instrumental characteristics inherently bare differing detection capabilities for planetary transit light curves. Also the fact that CoRoT was *only* able to observe the same target field for 150 days implies, that the detection of transiting planets with long lasting orbital periods (e.g., $\geq$ 1 year) was quite improbable and only feasible by chance. In addition, CoRoT has a significantly smaller field-of-view, which indirectly forces the CoRoT ground team to change the target field after every semiannual rotation, to increase the total number of observed stars and, therefore to increase the number of detected exoplanets. These points were clear advantages of *Kepler*, which was able to observe the same target field for the whole mission life time. To get an impression of the performance of both telescopes I contrast among others the discovered exoplanets in Table 3.2, which clearly demonstrates that *Kepler* is preeminent.

Table 3.1: Comparison of the instruments CoRoT and *Kepler*.

	CoRoT	*Kepler*
Mirror-⌀	27 cm	95 cm (140 cm Schmidt)
FOV	0.0012 sr	0.0352 sr
Pixel-scale	2.32″	3.98″
Camera [a)]	2 CCDs	42 CCDs
Cadence	32 s / 512 s	59 s / 1766 s
S/N [b)]	670	2700

Notes: Informations are taken from Auvergne et al. (2009) in the case of CoRoT and Van Cleve & Caldwell (2009) for *Kepler* values. [a)] The CoRoT camera box is equipped with 4 CCDs of which two were used for asteroseismology. [b)] S/N calculations are based on a 12 mag star (CoRoT-2b). For *Kepler*'s value see Section 3.3.1.

We have to keep in mind that the number of confirmed planets could be biased by a more intense follow-up program in the case of *Kepler* planetary candidates.

Table 3.2: Comparison of planet detections made by CoRoT and *Kepler*.

	CoRoT	*Kepler*
Days Observed	2136 [a)]	1425 [d)]
Planetary Candidates	530 [b)]	4696 [e)]
Confirmed Planets	32 [c)]	1030 [e)]
Detection Rate	0.2 d^{-1}	3.3 d^{-1}
Confirmation Rate	5.5 a^{-1}	264 a^{-1}

Notes: The detection- and confirmation rates are estimated using the number of observed days, which are in the case of CoRoT slightly overestimated, since these are the mission days. For *Kepler* this number is simply determined using observational data. [a)] CNES (2013), [b)] Moutou et al. (2013), [c)] DLR (2013), [d)] Table A.2, [e)] NASA (2013c).

Nevertheless, the CoRoT mission was groundbreaking and set new benchmarks in the sense of high quality photometry together with its high time resolution. The nearly continuous light curves with a duration of about 150 days made it possible to get new insights into transiting exoplanets, stellar activity, and star spots of planet hosters (e.g., Huber et al., 2009, 2010). The *Kepler* telescope was the more modern one with lower photometric noise, larger field-of-view ($\approx$ 29 times lager than CoRoT's), and all CCDs dedicated for the planetary transit search. Therefore, *Kepler* represents another milestone in optical photometry.

4 Measuring LD using *Kepler* Data

As already outlined in Section 1.3, transit light curves can be a great tool to measure the limb darkening of other stars than our own Sun. However, the data quality needs to meet some special requirements, like low photometric noise and high time resolution, because the limb darkening can only be determined from the light curve together with the remaining transit parameters p, i, and a. Due to strong correlations, these parameters tend to show relatively large uncertainties, especially if the mentioned requirements are not fulfilled. The *Kepler* space telescope introduced before, offers an outstanding opportunity to acquire light curves with high signal-to-noise ratios and in many cases also with high time resolution. Since the satellite was specially designed for the detection of transit like events, the publicly available data holds a remarkable number of transiting exoplanets, well suited for high precision transit studies.

In the following sections I present the analyses and the results of my selected *Kepler* targets. My main focus is set on the measurements of the limb-darkening coefficients (LDCs) for the linear and the quadratic limb-darkening law, which I then compare to theoretical predictions. These predictions are taken from tables provided by Claret & Bloemen (2011) based on 1D plane-parallel PHOENIX and ATLAS model atmospheres. In the case of my short cadence target sample I also take quadratic LDCs into account, which are provided by Claret et al. (2013). These are determined from spherically symmetric PHOENIX model atmospheres, using the *quasi-spherical* approach (see Claret & Hauschildt, 2003, or Section 5.1.4). I interpolated linearly on the given tables to get theoretical LDCs which I use for my comparisons. In the case where the measured LDCs are shown in figures, the predictions originate from model atmospheres with a surface gravity of $\log(g) = 4.5$, solar metallicity [M/H] = 0.0, and micro-turbulent velocity $\xi = 2.0\,\mathrm{km\,s^{-1}}$.

In Section 4.1 I comment on the selection of suitable objects, the applied data preparation, and the necessary transit normalization. Section 4.2 provides the results of my first target sample which was observed in long cadence (LC) mode, while Section 4.3 is related to the results obtained from modeling of short cadence (SC) data, which are mainly discussed in my paper (Müller et al., 2013). Therefore, this section is to be understood as a supplement to my published work. In Section 4.4 I present details of my analysis of time-correlated noise in the short cadence target sample and discuss different white noise predictions.

4.1 Selection of suitable targets and data priming

4.1.1 Object selection

For the *Kepler* mission all light curves, which are publicly available, can be obtained from the NASA Mikulski Archive for Space Telescopes. The data releases are divided into *Kepler* quarters (Q0-Q17, Table A.2), where new quarters are released after several months of data analysis by NASA scientists. If a planetary candidate was detected, all important system parameters, like $T_{\rm eff}$ or signal-to-noise values (see Borucki et al., 2011, Table 2 and Chap. 4), were added to the publicly released *Kepler* Planetary Candidates list (KPCL) (STScI, 2012), on which my work is based. Today, this list is not updated anymore and all planet candidates can be found in the *Kepler* objects of interest (KOI) table in the NASA Exoplanet Archive (NASA, 2014).

At the beginning of my transit studies there were slightly more than 1200 planetary candidates discovered in the quarters Q0 to Q3, but only a limited number of these objects (≈60) were observed in short cadence mode. According to their photometric signal-to-noise ratio, all objects get an especially defined value describing the "total S/N of all transits detected" (Borucki et al., 2011), which can be found in the KPCL. This value is deemed to be the transit's significance, because it is determined over all detected and phase folded transits and using the transit depth as signal. Borucki et al. (2011) simply divide the transit depth by the photometric noise σ and then multiply it with the square root of the total number of transit data points $N_{\rm p}$. To distinguish between this value and the simple photometric signal-to-noise, I denote the total signal-to-noise ratio of all transits detected as *SNR* like found in the KPCL. Following my simulations (Section 1.3.2, $\delta/N \approx 60$, $N_{\rm p} = 180$) and an inspection of some objects, a *SNR* value of higher than 1000 turned out to be reasonable for fitting the limb darkening. Unfortunately, only four[1] candidates observed in SC had a $SNR > 1000$ and only one additional object is found if $SNR > 500$ is considered. In the LC sample 18 objects fulfilled the first and 7 the second criterion. This circumstance was the reason why I first chose the best 25 objects observed in LC mode.

After the release of new *Kepler* quarters, it became possible to look for further suitable objects in the SC data sample. Over the mission life time the number of discovered planet candidates increased to 2321 (Q0-Q6). Now there were 322 planetary candidates observed in SC mode. In the data of the first seven *Kepler* quarters I found 26 planetary candidate target stars with $SNR \geq 1000$. These objects constitute my *high signal-to-noise target sample* discussed in my paper (Müller et al. (2013), see Chapter 7).

During my analysis it turned out that it would be interesting to study objects with high transit impact parameters ($b \geq 0.8$) like TrES-2b. Objects, which exhibit such a system property, would show a systematic behavior of the determined LDCs, like previously outlined by Howarth (2011). Therefore, analyzing such objects would be a good opportunity to verify his

[1] TrES-2b, KIC 9631995, Kepler-12b, KIC 9631995 and Kepler-13b

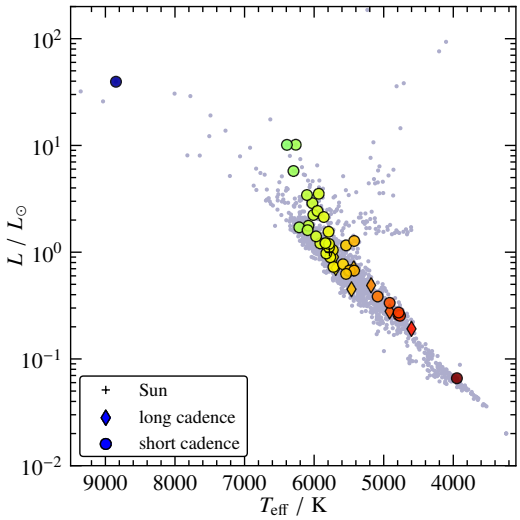

Figure 4.1: Hertzsprung-Russel diagram of 2312 planetary candidate host stars. The luminosity is calculated using the stellar radii and effective temperatures given in the KPCL, normalized by the luminosity of the Sun. The *colored symbols* indicate my selected *Kepler* target stars (colors are related to $T_{\rm eff}$). Eight *diamonds* mark objects only available in long cadence mode. Objects available in short and long cadence are marked as *circles*.

predictions empirically. To get a reasonable number of objects I had to select objects with a $SNR \geq 150$, which led to twelve additional target stars.

In the end, I selected and analyzed 46 different *Kepler* planetary candidates, which are listed in Table 4.1. I analyzed seventeen of them in both SC and LC mode, while 21 are unique to my SC sample. This sample shows stars spanning a wide range of effective temperatures, but most objects are clearly found in the regime between 5500 K and 6500 K, which makes them at least in the sense of effective temperature comparable to our Sun. Furthermore, a comparison with all planetary candidates in a Hertzsprung-Russel diagram (Fig. 4.1) shows that these objects are in their hydrogen burning phase on the main sequence. The effective temperature, which is the most important parameter for my limb-darkening studies, is determined with an accuracy of about ±200 K or better. For a description of how the fundamental stellar parameters are determined see Batalha et al. (2013) and Appendix A of Müller et al. (2013). Out of this selection, 25 objects have been confirmed as real exoplanets as of 26.03.2015. Due to the excellent preselection the false positive rate among the planetary candidates is believed to be small, in the order of 10 % (Fressin et al., 2013).

4.1.2 Transit normalization

After my selection process I had to normalize and detrend the transit light curves of all objects. This procedure is necessary because, on the one hand, the light curves can be influenced by intrinsic flux trends such as caused by spots and, on the other hand, by some instrumental peculiarities like residuals left by the reduction process which are visible as jumps and exponential decays. Both intrinsic and instrumental variabilities can be relevant on transit time scales. For that purpose I performed a second order polynomial fit to the continuum surrounding every single transit light curve. All transit data points were simply divided by this polynomial function. A linear fit is clearly insufficient to remove the mentioned variabilities,

Table 4.1: My selected *Kepler* target stars ordered by increasing $T_{\rm eff}$.

Identifier	$T_{\rm eff}$/K	log g	Identifier	$T_{\rm eff}$/K	log g	Identifier	$T_{\rm eff}$/K	log g
Kepler-45b [a)]	3948	4.72	Kepler-19b	5541	4.53	Kepler-412b [a)]	5912	4.44
3749365	4601	4.66	Kepler-41b [a)]	5585	4.49	Kepler-7b [a)]	5934	4.04
HAT-P-11b	4766	4.59	3935914	5690	4.49	8684730	5952	4.19
Kepler-94b	4786	4.49	9166862	5714	4.50	Kepler-422b [a)]	5972	4.41
11391018	4787	4.58	Kepler-423b [a)]	5722	4.55	Kepler-12b [a)]	6011	4.23
5084942	4915	4.55	Kepler-77b [a)]	5731	4.45	Kepler-8b	6025	4.11
Kepler-428b	4915	4.63	7849854	5734	4.45	Kepler-43b [a)]	6082	4.37
Kepler-425b [a)]	5087	4.59	7023960	5768	4.50	3762468	6094	4.41
9115800	5181	4.47	Kepler-15b [a)]	5786	4.42	Kepler-25c	6103	4.07
12105051	5425	4.50	Kepler-17b	5787	4.45	10019708 [a)]	6214	4.41
5771719	5425	4.21	Kepler-68b	5793	4.28	HAT-P-7b	6264	3.79
11414511	5431	4.43	TrES-2b [a)]	5814	4.38	Kepler-5b	6297	3.99
8544996	5463	4.61	12019440 [a)]	5826	4.49	3861595	6391	3.81
8845026	5490	4.49	Kepler-6b	5826	4.42	Kepler-13b [a)]	8848	3.94
BOKS-1b [a)]	5504	4.54	8456679	5838	4.42			
6849046 [a)]	5541	4.32	8554498	5861	4.19			

Notes: Objects given in *black* constitute my short cadence sample (Section 4.3); results published in Müller et al. (2013). Objects given in *gray* were exclusively analyzed in LC mode (Section 4.2). Objects marked by [a)] were analyzed in both cadence modes. $T_{\rm eff}$ and $\log(g)$ are taken from the mentioned KPCL. Unconfirmed planets are identified by their KIC numbers.

which leads to prominent residuals. Caused by the additional degrees of freedom, higher order polynomials tend to be instable or in extreme cases start fitting the noise. Therefore, a second order polynomial seems to be the best choice under the given circumstances.

The important question, which now arises is, how well are all transits normalized? Of course, due to the enormous amount of more than 3000 individual transit light curves in my sample, it is almost impossible to create a normalization algorithm which can handle all occurring variations of different shape-distorting effects, at least not in a reasonable time frame. Thus, there remains a number of normalized transits, which exhibit abnormal distortions clearly visible during a by eye inspection of some objects. So I had to find a solution to increase the quality of my set of normalized transit light curves by *not* refining the normalization process. Therefore, I invented a filter algorithm for poorly normalized transit light curves, which allows me to automatically discard individual transits. The basic idea is to apply three linear fits to the continuum parts after normalization. The gradients of these fits should be close to zero, in the case of a well normalized transit. The first fit is applied to both continuum parts, left and right beside each transit. This fit should depict whether there is a global trend left on the transit time scales. The second and the third fit include the left and the right continuum parts individually. They are needed, if the transit passes the first fit, but shows remaining curvature in the continuum. This method introduces two parameters, which are the gradient thresholds

of the linear fits. In practice, I had to determine these thresholds by testing. Good results were achieved, if all transits showed a gradient of the first fit lower than $1.5 \cdot 10^{-7}$ d^{-1}, and lower than $1.5 \cdot 10^{-3}$ d^{-1} for the two latter fits. However, it was necessary to manually discard some transits, namely in the case where the transits are well normalized, but significantly distorted by starspot crossings, like it is the case in the transits of HAT-P-11b (see Sanchis-Ojeda & Winn, 2011). Overall, the automatic procedure performed quite well, and together with the manual method only 9 % of all transits were discarded.

To further increase the data quality and to get reliable reduced χ^2 values, I removed outliers inside the transit light curves. Outlier removal during the transit occultation is complicated, since the real transit depth and shape is normally not known beforehand. To get rid of some insistent outliers I used a sliding median filter with a window size of 10 minutes and rejected all points detected at a 4σ level or higher. I assured that the number of deleted data points is small compared to the number of transit data points (< 5 %).

In the case of outliers, which cannot be attributed to the statistical population of the signal of the host star, the determination of the standard deviation itself is influenced by these outliers. To identify such outliers and to determine a reliable σ value, I used the *median absolute deviation* (*MAD*) within the selected continuum parts and set 0.6745^{-1} *MAD* as 1σ error (Hampel, 1974). This method delivers a robust estimator of the standard deviation, comparable to a Gaussian-fit to a histogram of the residuals. Both methods are weighted by the number of data points, like the median, while in contrast the mean and the normal standard deviation are weighted by the actual flux values and, therefore, more susceptible to outliers.

For further details about my data handling, the normalization process and a complete list of discarded transits, see Section 2 and Table B.1 of Müller et al. (2013). All data I used for this part of my work was processed by *Kepler*'s photometric analysis pipeline (releases 4 to 7; see data release notes[2] for more information). This pipeline has been changed during different data releases. In the most recent data release (23) a few transits are deleted by default and not available anymore, such as transits 19 and 26 of TrES-2b, which were previously detected by my filter algorithm.

4.2 Long cadence data

My first approach to indirectly measure the stellar limb darkening using planetary transit light curves was based on *Kepler* long cadence data. As outlined in Section 1.3.2, the crude time resolution of the LC data makes it necessary to use an *overbinned* fit model, since the shape of the sampled transit light curves is systematically broadened, which has already been shown using *Kepler* data for TrES-2b by Gilliland et al. (2010). It is obvious that transits which have a crude time binning hold less information on the host star's disk compared to data with high time resolution. The overbinning procedure, which is definitely needed to model

[2] http://archive.stsci.edu/kepler/release_notes/, visited in April 2014.

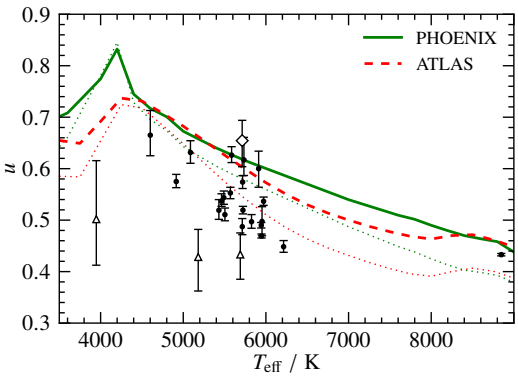

Figure 4.2: MCMC results of the LDC using a linear limb-darkening law. *Colored lines*: model predictions by PHOENIX (*green*), ATLAS (*red*). *Dotted lines*: LDCs assigned from flux conserving fit method, see text for details. The error bars mark 68.3 % HPD. The *diamond* symbol indicates object with highest impact parameter in this selection (TrES-2b). *Triangles*: conspicuous objects, discussed in text.

data with time binning longer than one to two minutes, is a really time consuming part of the transit modeling, especially in the case of data containing many transit light curves. I used an overbinning factor of 30, leading to a transit model being evaluated at one minute bin time, and then rebinned down to the 30 minutes bin time of the *Kepler* LC data. I expected that the resulting uncertainties would be rather large, which is the reason why I started fitting the limb darkening using the linear law

$$\frac{I(\mu)}{I(1)} = 1 - u(1-\mu)\,, \tag{4.1}$$

which introduces only one additional fit parameter, the linear coefficient u. This is the simplest approach to the limb darkening among the equations introduced in Table 1.1. If this would not lead to credible results, then it would not make any sense to use further, more complicated limb-darkening descriptions for this kind of data.

The orbital period $P_{\rm orb}$ and the transit center time t_0 are needed for transit modeling and they are given in the KPCL. However, I had reasons to suspect that they are not as precise as required for my investigations, because they led to characteristic residuals if the transits were shown phase folded, and they were not updated with the release of new *Kepler* quarters. Therefore, I first fitted $P_{\rm orb}$ and t_0 using a downhill simplex algorithm setting all other parameters to the values found in the KPCL. After that I started the transit modeling with four free parameters: the planet-to-star radii ratio p, the inclination angle i, the semi major axis $a/R_{\rm S}$, and the linear limb-darkening coefficient u.

For all my transit investigations I used the Fortran `occultquad` routine (Mandel & Agol, 2002). To obtain a linear limb darkening the quadratic LDC is set to zero. After fitting the parameters, using again a downhill simplex algorithm, I used an MCMC sampling algorithm (see Section 1.3.1), performing 10^6 iterations. I interpreted the mean values of the parameter traces as the expectation values of the parameters together with their 68.3 % highest probability-density (HPD) intervals as a reliable 1σ estimate.

I present the resulting linear LDCs of my sampling approach in Fig. 4.2 together with the predicted LDCs of Claret & Bloemen (2011) for ATLAS and PHOENIX atmospheres. The *dotted* lines represent LDCs obtained by a *flux conserving* fit method forcing the integrated flux

under Eq. 4.1 to be equal to that determined from the model atmosphere (Claret, 2000). There is a remarkable difference visible between the LDCs obtained by this method and a normal least squares (LS) fit to the intensity distribution of the atmospheres, especially pronounced for increasing effective temperatures. This means that the LS method underestimates the overall emitted stellar flux, resulting in stronger prediction of the limb darkening (I will discuss this effect later on in Chapter 5). For now, we concentrate on the predictions determined by the LS method (*solid* and *dashed* lines).

We can clearly see that only four or five objects are consistent with the model predictions. Three of these lie directly on the PHOENIX values, the fourth object is TrES-2b (*diamond* symbol), and the fifth object is the second coolest in this sample, barely consistent with the predictions. All other objects, as those showing quite small error bars, lie clearly below the predicted LDCs. Considering now the predictions made by the flux conserving method, I found six objects consistent with these predictions, but the majority of objects still lie below theory. At this point I can state that the predicted LDCs for the linear law are inconsistent with my measurements.

To quantify the difference between models and measurements, I first have to discuss some of the objects which should not be considered. The three objects marked with *triangles*, with significantly weaker limb darkening in comparison to the others, and TrES-2b should be neglected due to their high impact parameter causing the measured limb darkening to be unreliable (see Section 6.5, and Müller et al. (2013)). Starting with the coolest of these objects (Kepler-45b), the obtained LDC is not necessarily incompatible with theory, because in this temperature regime the LDCs strongly depend on the $\log(g)$ and the stellar metallicity (Section 1.1.3). This object is also available in short cadence data and will be discussed there (Section 4.3). The other two objects (KIC 9115800, KIC 3935914) cannot be explained in the same way, but their light curves show stellar variability most likely induced by starspots. The influence of starspots on the determination of the limb darkening is beyond the scope of my work, but in principle all objects of this sample with larger uncertainties except TrES-2b show spot induced rotational modulations in

The median values of the residuals between measurements and predictions lead to deviations of $\Delta u_{\mathrm{P}} = -0.10$ and $\Delta u_{\mathrm{A}} = -0.08$ in the case of the least-square fit method for PHOENIX and ATLAS, respectively. If the flux conserving method is considered, the deviations are to be found as $\Delta u'_{\mathrm{P}} = -0.06$ and $\Delta u'_{\mathrm{A}} = -0.03$. In general, the predictions of the flux conserving fit method are not preferred, since they lead to significantly poorer fits to the intensity distribution of the model atmospheres (see Claret, 2000). However, in the demonstrated case (Fig. 4.2) these theoretical LDCs would be the better choice for transit modeling or other kinds of data where a linear limb-darkening prediction is used (e.g. Ohta et al., 2005). It is also noteworthy that the objects with the smallest error bars seem to follow the global trend of the predictions (weaker limb darkening with increasing temperature).

As a next step, I decided to repeat the fitting and MCMC sampling approach, this time setting also the quadratic coefficient u_2 free, since the uncertainties of most of the objects in Fig. 4.2

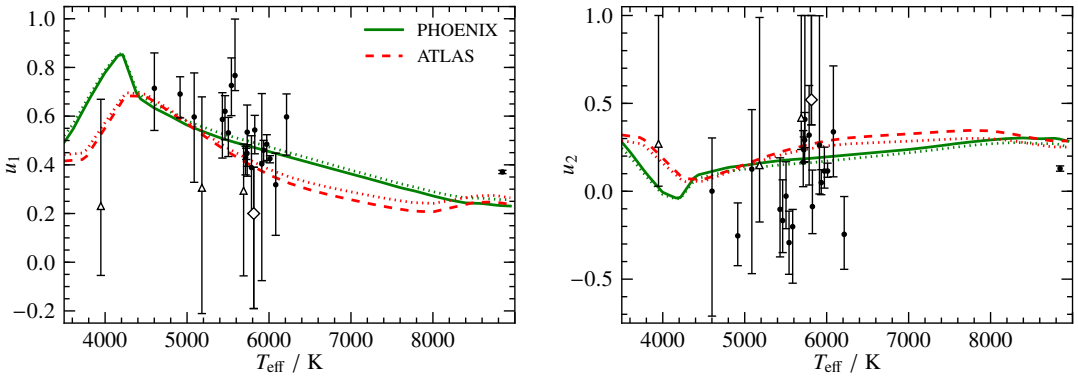

Figure 4.3: Fit results of the quadratic LDCs for my long cadence target sample (see Table 4.1). *Left*: linear coefficient u_1, *right*: quadratic coefficient u_2. *Green solid* lines: predictions based on PHOENIX, *red dashed* lines based on ATLAS atmospheres. *Diamond* indicates TrES-2b. *Triangles* mark same objects as in Fig. 4.2. 68.3 % HPD error margins.

are promisingly small. Now, the limb-darkening law

$$\frac{I(\mu)}{I(1)} = 1 - u_1(1-\mu) - u_2(1-\mu)^2\,, \tag{4.2}$$

has two coefficients (u_1, u_2) and, therefore, the number of fitted transit parameters increases to five. The measured LDCs for this sample are shown in Fig. 4.3. Unfortunately, the uncertainties of the coefficients are large, which is not unexpected due to the additional degree of freedom and the strong correlation between u_1 and u_2. In comparison to Fig. 4.2, where only one limb-darkening parameter was fitted, the error bars are now more than twice as large. Nevertheless, I found five objects with small error bars, four in the region around 6000 K (Kepler-423b, Kepler-7b, Kepler-422b, Kepler-12b), and the fifth is the hottest host star in my sample (Kepler-13b). These objects are also available in my short cadence sample and therefore discussed there. It is notable that nine objects with small to moderate error bars lie significantly below both predictions of the quadratic coefficient u_2. The median value of the quadratic coefficient of these objects is -0.18 ± 0.05, which translates into an offset from the used PHOENIX prediction of $\Delta u_2 = -0.36 \pm 0.05$. In contrast, there are only three objects which lie significantly above u_1. All other objects are consistent with at least one of the model atmospheres, caused by their large errors. All measured coefficients and transit parameters of this sample can be found in Table A.5. Due to the large uncertainties caused by the insufficient time resolution, I omit a further discussion about the question which model atmosphere should be preferred in transit modeling. To give more significant results with smaller error margins, I had to wait for the release of new *Kepler* light curves, including high signal-to-noise short cadence measurements.

4.3 Short cadence data

After the release of new *Kepler* quarters, I was able to find suitable short cadence targets for fitting the limb-darkening. Due to the higher time resolution, the transit light curves contain more spatial information on the stellar disks and, therefore, the fit results of the limb darkening are expected to be more reliable. The results of my short cadence target sample are mainly discussed in my paper (Müller et al., 2013), so I will only summarize the results here and give some further details not included in the paper.

The analysis of the short cadence data was carried out like outlined for the long cadence data. In detail, this means I started with a normalization and detrending of all transits, a proper fit of t_0 and $P_{\rm orb}$, an outlier removal, and a downhill simplex fit of all transit parameters. I continued with a Markov chain Monte Carlo approach to sample the parameter space using the best-fit values determined before as start parameters. Additionally, I carried out an analysis searching for *red noise*, i.e. time correlated noise in the data. Because of the complexity of this topic, I will discuss this analysis in a separate section (Section 4.4).

In Fig. 4.4, I present phase folded transit light curves of three objects together with my best-fit models. I chose these objects according to their transit signal-to-noise ratio (δ/N) to show

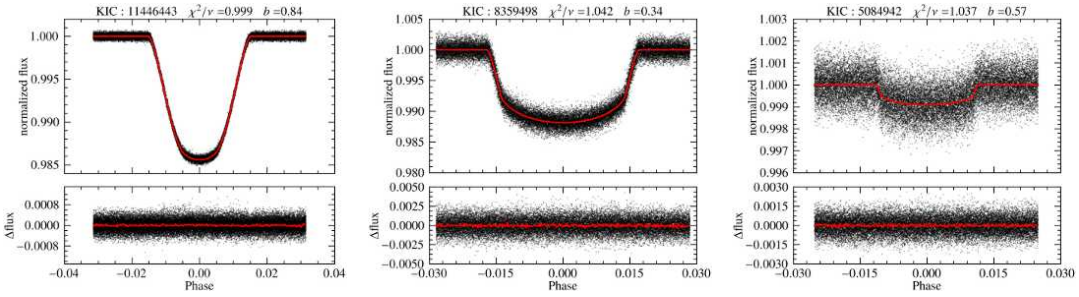

Figure 4.4: Examples of phase folded transit light curves of my short cadence target sample, together with my best-fit models (*red* lines). *Bottom* panels show the residuals and the residuals rebinned to one minute bin time in *red*. For additional information I give the KIC identifier, the reduced-χ^2 value, and the system impact parameter at the top of the images. Revised figure of Müller et al. (2013, Fig. B.2).

the whole range of transit-event significance found in my sample. In the left panel we see the transit of TrES-2b, which has the highest ratio of transit depth to photometric noise (60.6) in the whole *Kepler* sample. The middle panel of this figure shows the transit light curve of Kepler-77b which is an example of objects with intermediate δ/N values (12.2), while in the right panel the observed transits are only slightly deeper than the photometric noise (1.4). Although the transit signal of the last object shown is really weak compared to the noise, we have to keep in mind that the whole light curve consists of 114 recorded transit events, which increases the significance by $\sqrt{N_{\rm T}}$ and, therefore, it is possible to measure the orbital parameters and the limb darkening with reasonable accuracy. I summarize the δ/N values together with the total photometric precision for all objects in my short cadence sample in

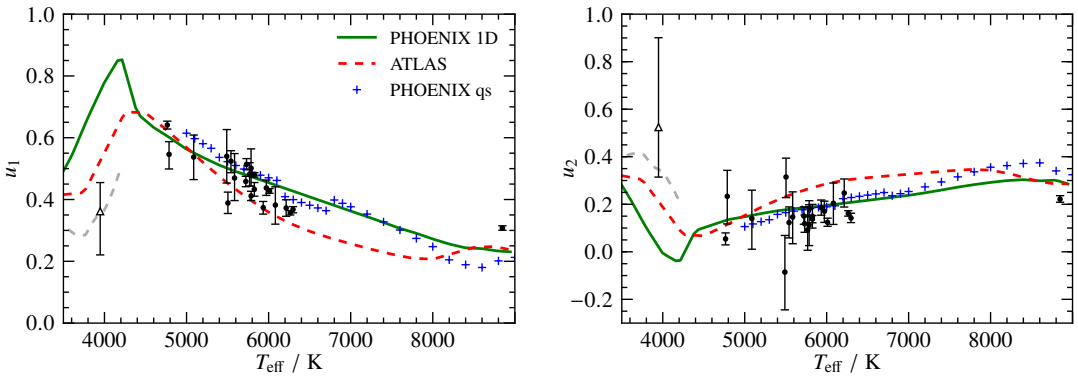

Figure 4.5: Fit results of the quadratic LDCs for my short cadence target sample (see Table 4.1). *Left*: linear coefficient u_1, *right*: quadratic coefficient u_2. Model predictions are drawn as lines and crosses (*labels*, see text for references). *Triangle* marks the M-dwarf in my sample, shown together with ATLAS model prediction for $\log g = 5.0$ (*gray dashed* lines). Objects with $b > 0.7$ are removed from this plot, but included in Fig. 4.7.

Table A.6. As a measure for the goodness of the fit I determined the reduced χ^2 values, where the degrees of freedom are defined by $\nu = n - f - 1$. The number of data points is given by n and f is the number of fitted parameters (u_1, u_2, p, i, a), i.e. five. I found that for all of my objects χ^2/ν is close to one, which is a clear indication that the fits are really good. To confirm the precision of the fits, I show the residuals after subtracting the best-fit models in the bottom panels of Fig. 4.4. Furthermore, I rebinned these residuals down to one minute bin time. Even after rebinning, there are no systematics visible. At this point we have to remember that according to Section 1.3.2 the rebinning of the data before fitting the parameters is *not* recommended. There is no gain in information if the light curve would be rebinned, in fact information is destroyed. However, after the determination of all parameters the rebinning can be helpful, e.g. for illustrating the residuals.

The results of my transit modeling are summarized in Table 3 of Müller et al. (2013). There we can find measured limb-darkening coefficients including the 1σ error estimates, as well as the predicted PHOENIX coefficients. For the following discussion, I plot again the measured coefficients together with the model predictions of PHOENIX and ATLAS (Fig. 4.5), but this time also including more recent predictions (Claret et al., 2013). All predictions coming from the flux-conserving fit method are neglected. Compared to Fig. 4.3, the limb-darkening measurements show an amazing precision. Nevertheless, as already outlined in my publication, there were some objects which have remarkably large error bars and a clear deviation from the predictions. According to my analysis, their systematic behavior can be attributed to their high system impact parameters, on which I will comment in the next subsection. Therefore, I removed these three objects[3] from this figure. I further identified only one remaining object which is an "outlier" in both u_1 and u_2. This object is a K-dwarf according to the given effective temperature of only ≈ 4000 K. As we know from Section 1.1.3, the limb darkening is very

[3] TrES-2b, Kepler-412b, Kepler-8b

sensitive to, e.g., the surface gravity $\log g$ in this temperature regime. Thus, the theoretical predictions used here ($\log g = 4.5$) are a bad choice for this object, and I additionally present the ATLAS predictions for higher surface gravity ($\log g = 5.0$, common for late K-dwarfs) in that figure. This shows that this object is no outlier and also consistent with theory.

One of my major results is that the measured coefficients show deviations from the theories. Although I found that the measurements of the linear coefficient u_1 show partially good agreement with one of the models at a time, my results show that on average the measured coefficients deviate from both predictions, u_1 and u_2. I measured this deviance in the temperature range 5300 K to 6500 K, where most objects of my sample are located, by calculating the median values of the residuals after subtracting the individual model values. The resulting differences are summarized in Table 4.2. Looking at Δu_1 we see that my found values lie below

Table 4.2: Measured mean deviations from model predictions.

Model	Δu_1	Δu_2
PHOENIX 1D [a)]	-0.05 ± 0.01	-0.03 ± 0.01
ATLAS [a)]	$+0.04 \pm 0.01$	-0.10 ± 0.01
PHOENIX qs [b)]	-0.03 ± 0.01	-0.04 ± 0.01

Notes: Differences are calculated for the fitting results of my high signal-to-noise target sample ($b < 0.7$, Fig. 4.5), in the temperature range 5300 K to 6500 K. [a)] Claret & Bloemen (2011), [b)] quasi-spherical (qs) predictions Claret et al. (2013).

the PHOENIX 1D predictions and almost the same amount above the ATLAS values. This result also proves what we can see in Fig. 4.5 where the measurements seem to sample the gap between the model predictions. In contrast, Δu_2 shows a different behavior. The measurements lie clearly below both model predictions. Therefore, the predictions given for u_2 are in both cases significantly too high, which is also visible in the right panel of Fig. 4.5, but in any case the ATLAS predictions are far too high. The quasi-spherical predictions are slightly closer to the results of u_1 compared to PHOENIX 1D and ATLAS, but slightly further away in u_2 than PHOENIX 1D. A calculation of χ^2 yields that $\chi^2_{\mathrm{P\,1D}}$ is four times smaller than χ^2_{A} in the case of u_2 predictions. For both coefficients I find that $\chi^2_{\mathrm{P\,1D}}$ is still a factor of 1.4 smaller than χ^2_{A}. This leads to the conclusion that at least for these objects, together with this specific photometric passband, the PHOENIX prediction is the better choice for transit modeling.

Besides the obtained differences of my measurements to the model predictions, it would also be interesting to compare the underlying limb intensities and to see the actual effect on the transit profile. For clarity I decided to select the results of objects found in a sharp solar-like temperature range (5750 K to 5850 K), where I found five objects (see Müller et al., 2013, Table 1). According to the accuracy of the given effective temperatures (±200 K), these objects have virtually the same temperatures and should be comparable to the Sun. The limb-intensity profiles of these objects are slightly different, as visible as a gray area in the left panel of Fig. 4.6. Additionally, I show the limb profiles predicted for this temperature range by ATLAS,

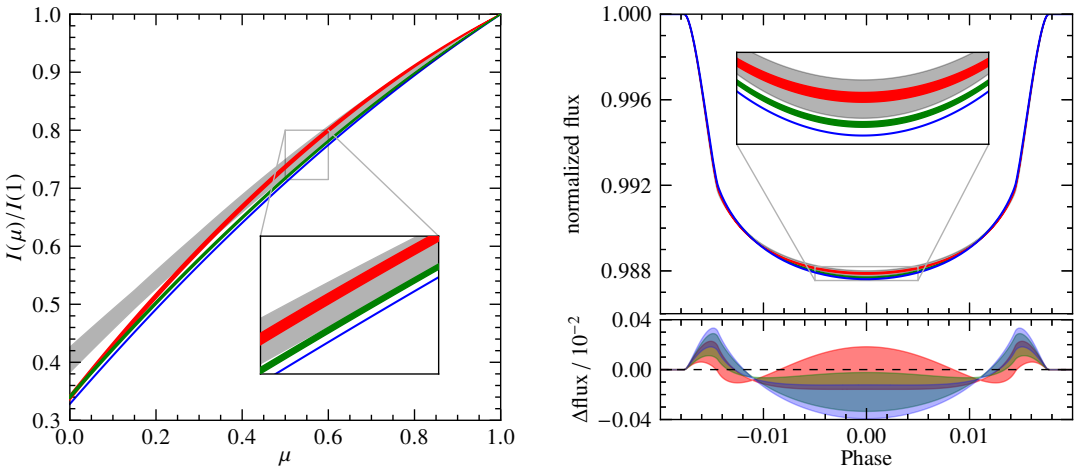

Figure 4.6: *Left*: Limb-intensity profiles of solar-like *Kepler* targets (*gray*) together with predicted profiles using ATLAS (*red*), PHOENIX 1D (*green*), and PHOENIX qs (*blue*) for the temperature interval of 5750 K to 5850 K. *Right*: Simulated transits using the shown limb intensities of the left panel and a planet-to-star radii ratio of $p = 0.1$. *Bottom panel*: Maximum and minimum transit residuals determined by subtracting model transit of my *Kepler* measurements from transits created using model predictions. Müller et al. (2013).

PHOENIX 1D, and PHOENIX qs. Clearly, all models predict too strong limb darkening, which is also visible at intermediate limb angles (zoom-in). However, the ATLAS predictions are found in between the measurements, whereas the PHOENIX predictions lie at the lower edge of the measured profiles or below, especially the quasi-spherical models. The fact of over predicted limb darkening will play a role in the analysis of the solar limb darkening in Chapter 5.

Transit light curves generated with the measured limb intensities of the five selected objects show slightly different shapes, as illustrated in the right panel of Fig. 4.6. For instance, the deepest transit is based on the limb intensity model which holds the strongest limb darkening: here the PHOENIX qs prediction. The residuals show the differences between transits generated using model predictions and those relying on my measurements. We can see that the PHOENIX qs prediction leads to the strongest residuals, with a peak amplitude of $4 \cdot 10^{-4}$, closely followed by PHOENIX 1D. The ATLAS models lead to residuals with nearly half of this value, and it seems to be the better choice for modeling transits. This result is in contrast to the χ^2 values found above, where I stated that the PHOENIX models are closer to my measurements. We have to keep in mind that the results are achieved for this specific and sharp temperature interval and might look different for other temperatures. Notably, the found residuals are in the order of 10^{-4}, which is detectable by *Kepler* (cf. σ_c in Table A.6). This is a self-consistent proof of my method, because if the simulated residuals would have been below *Kepler*'s detection limit, the transit fits should lead to the same results, e.g. indicated by larger errors, which is at least not the case for the objects chosen here. The influence of the chosen model prediction on the fitted transit parameters is discussed in Section 4.3.3.

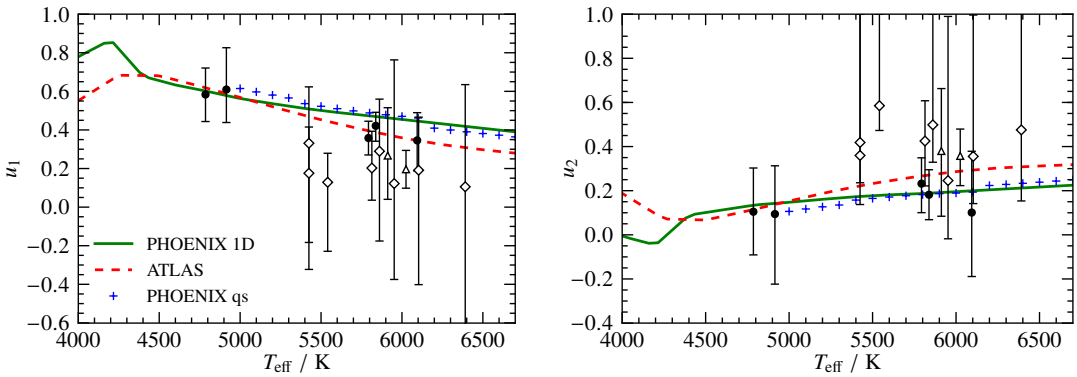

Figure 4.7: Quadratic LDCs determined by transit modeling of objects included in my high impact parameter sample (Müller et al., 2013, Table 2). *Dots*: Objects which have an impact parameter $b < 0.6$ according to my transit modeling. *Diamonds*: Results for objects with high impact parameters of $b > 0.8$. *Triangles*: Objects removed from Fig. 4.5 with $b > 0.7$.

4.3.1 Results for high impact parameters

During my studies of *Kepler* transit light curves it turned out that the results achieved from transiting systems which are highly inclined are special. TrES-2b, the object with the highest transit signal-to-noise ratio (δ/N, see Table A.6) in the whole *Kepler* sample, but with an impact parameter of $b = 0.85$, shows limb-darkening coefficients with remarkably large errors when compared to objects with lower signal-to-noise. To further investigate the effects on the measured limb-darkening coefficients, presumably caused by high impact parameters, I searched for objects in the *Kepler* planetary candidate list, which had to fulfill the criterion of an impact parameter larger than 0.8. This value was somewhat arbitrarily chosen, but was motivated by the value found for TrES-2b. I found 12 additional objects with significantly lower signal-to-noise ratios than given in my first sample. These objects constitute my *high-impact-parameter sample*, although I found that actually only seven objects have $b > 0.8$ according to my transit modeling, the remaining five have significantly smaller values (see Müller et al., 2013, Table 3). The determined limb-darkening coefficients for this sample are shown in Fig. 4.7, where I added TrES-2b and two more objects from my high-signal-to-noise sample with $b > 0.7$, as previously mentioned. At first glance nearly all objects with a low impact parameter ($b < 0.7$, dots) show good agreement with the model predictions, while the objects with a high impact parameter exhibit a systematic behavior: they show huge uncertainties and they lie below or above their predictions of u_1 and u_2, respectively. Howarth (2011) introduced the systematic behavior seen for the deviations using simulations (I will discuss this later on in Section 6.5). His predictions are nicely reproduced by my measurements and, therefore, his findings are verified empirically for the first time. However, he neglected an investigation of the errors, which I included in my studies.

I was able to measure the behavior of the standard errors of u_1 and u_2 as a function of the system impact parameter due to the variety of different b values given in my sample. I presented

the values for $2\sigma_{u_1} + 2\sigma_{u_2}$ in Fig. 9 of my paper. This plot illustrates that the errors are steeply increasing if $b > 0.8$. This result is very important, because it says that it becomes much more difficult or even impossible to measure the limb darkening in such systems. This can easily be explained by the planet's path over the stellar disk, which does not sample the full brightness distribution but only a part of it, and, therefore, this information is not fully included in the light curves. Beyond this empirical result, there exists an analytical solution for this error behavior, presented in Appendix B of my paper. Using Bayesian statistics, we need to know the posterior probability distribution (cf. Eq. 1.31) to obtain the uncertainties (or credibility intervals) of the coefficients. In the given case, the likelihood $\mathcal{L}$ is a function of χ^2 and we can write the posterior as

$$P(u_1,u_2|D) = \frac{P(u_1,u_2)\mathcal{L}(\chi^2)}{\iint P(u_1,u_2)\mathcal{L}(\chi^2)\,\mathrm{d}u_1\,\mathrm{d}u_2}\,. \tag{4.3}$$

We know that for an estimate of a 68 % confidence interval of two correlated parameters, the $\Delta\chi^2$ has to be set to 2.3 (e.g. Press et al., 2002). We can rewrite the posterior and get the expression

$$P(\Delta u_1,\Delta u_2|D) = \mathcal{L}_0 \cdot \mathrm{e}^{-1/2\left(\Delta\chi^2(\Delta u_1,\Delta u_2)\right)}\,, \tag{4.4}$$

with $\mathcal{L}_0$ being a normalization constant. For instance, we can derive the expectation value

$$E(\Delta u_i^2) = \mathcal{L}_0 \iint \Delta u_i \Delta u_i \cdot \mathrm{e}^{-1/2\left(\Delta\chi^2(\Delta u_1,\Delta u_2)\right)}\,\mathrm{d}(\Delta u_i)\,\mathrm{d}(\Delta u_i)\,. \tag{4.5}$$

It can be shown that the square root of the expectation value $E(\Delta u_i^2)$ corresponds to 1σ. The behavior of the credibility intervals can now be predicted for arbitrary impact parameters by evaluating the function $\Delta\chi^2$. The results are plotted in Figs. 11 and B.1 (left panel) in my paper. As shown by my measurements using *Kepler* objects with high orbital inclinations, this analytical solution reproduces the steep increase for impact parameters of 0.8 or larger as well as smallest errors for low impact parameters. Actually, the analytical solution illustrates that the uncertainties of u_1 and u_2 do not increase monotonically, but decrease slightly after a local maximum at $b \approx 0.5$. Furthermore, this prediction shows that u_1 is always slightly better constrained than u_2.

In conclusion, I can say that it is impossible to measure the individual limb-darkening coefficients u_1 and u_2 in systems with high impact parameters. However, it actually remains possible to measure the combination of the coefficients $u_\mathrm{C} = u_1 + u_2$. I plotted this sum for the objects discussed above ($b > 0.7$) in Fig. 4.8. We can see in this figure that the systematic behavior of the individual coefficients is gone and that the deviations from the model predictions are much smaller. In some cases the summed values even lie directly on the model predictions. In addition, the combination u_C shows much smaller uncertainties than the two coefficients alone. For instance, TrES-2b, the object with the deepest transit compared to the photometric noise (δ/N) in the *Kepler* sample with an impact parameter of $b = 0.85$, now shows the smallest error bars in Fig. 4.8. This object was also studied by Schröter et al. (2012),

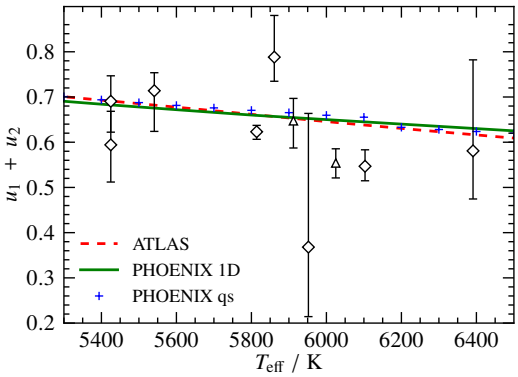

Figure 4.8: Sum of the linear and quadratic coefficients ($u_C = u_1 + u_2$) for objects with an impact parameter $b > 0.7$ in comparison to the summed model predictions (*labels*). See also Figs. 6 and 10 in my paper. Symbols are the same as in Fig. 4.7.

who pointed out that the quadratic limb-darkening law can be approximated by a constant function

$$\frac{I}{I(1)} = 1 - (u_1 + u_2)\,, \tag{4.6}$$

under the assumption that the planet only probes disk areas where $\mu \ll 1$. Thus, a transit fit would only be sensitive to the sum $u_1 + u_2$. However, the maximal μ-value achieved during the transit occultation (transit center) is 0.53 for TrES-2b. This value can be calculated using the equation

$$\mu_{\rm max} = \sqrt{1 - b^2} \tag{4.7}$$

(cf., Eq. 1.6), and this clearly does not comply with $\mu \ll 1$. Nonetheless, the idea of a constant intensity function expressed by the sum of the coefficients is not necessarily bad and I claim that the "median" limb angle sampled by the planet in such systems is even zero, which I will justify in the following. Obviously, sampled values of $\mu \approx 0$ would lead directly to Eq. 4.6 again.

In Fig. 4.9 I illustrate simulated transit light curves of the TrES-2 system, first, with an impact parameter of $b = 0$ (left panel) and, second, with its original impact parameter. The limb-darkening coefficients were set to the PHOENIX 1D prediction and additionally I show hypothetical transits for the same orbital parameters, but without limb darkening (uniform source). In the case of $b = 0$ we can see that a relatively short transit ingress phase is followed by a distinct mid-transit phase (t_2 to t_3, green area), in which the complete planet is in front of the stellar disk. In contrast, in transiting systems where the orbital geometry appears highly inclined, such as for TrES-2b, the ingress phase takes the major portion of the transit event (we remember Eq. 1.24 in this context). In the example shown here the ingress phase is even longer than the complete mid-transit phase. This is an important fact to substantiate the allegation that $\mu \approx 0$, since during the transit ingress or egress phase the outer most limb ($\mu = 0$ contributes to the light curve. After t_2 the contribution of non-zero μ-values ($0 < \mu \leq \mu_{\rm max}$) is only given in a relatively short time frame. Therefore, Eq. 4.6 is an appropriate approximation to describe the *sampled* limb darkening. This means that a transit fit mainly measures the intensity at the stellar limb, which is equivalent to a constant difference to the central brightness $I(1)$. It should be mentioned that due to the size of the planet Eq. 4.7 is only an approximation, and one could argue that the

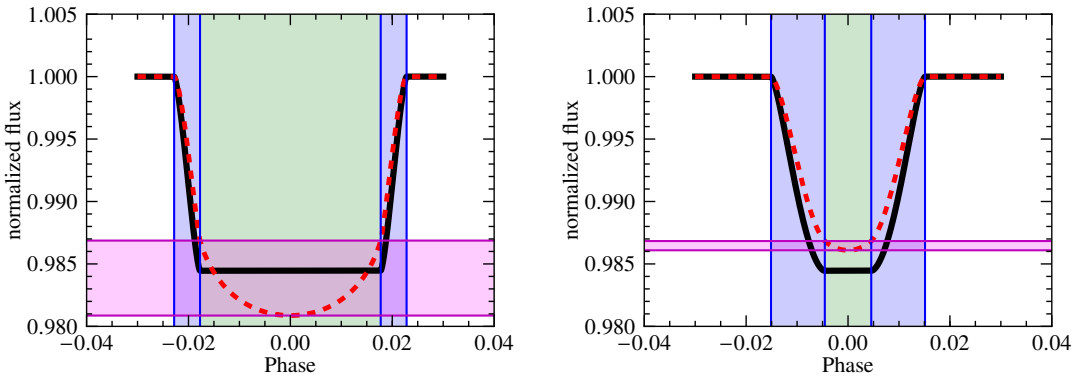

Figure 4.9: Simulated transit light curves using quadratic LD (*dashed*) and no LD (uniform source, *solid*). *Colored areas* indicating transit phases discussed in text. *Blue*: transit ingress and egress phases, *green*: whole planet is in front of the stellar disk, *magenta*: flux change during full-planet occultation. Transits generated using system parameters of TrES-2b, *left*: simulated impact parameter $b = 0$, *right*: original impact parameter $b = 0.85$.

planet even samples larger values than $\mu_{\max}$. This is actually true, but due to the non-linearity of μ the planetary disk covers a greater portion of $\mu < \mu_{\max}$ than $\mu > \mu_{\max}$ (see Fig. B.8).

Another clearly visible difference between these inclination scenarios is the change in transit depth during mid-transit phase. While the transit with an inclination of 90° shows a significantly different flux value between t_2 and transit center, the highly inclined version shows an almost constant flux. Again, this also supports the assumption that the planet samples a constant intensity difference to the central brightness as described by Eq. 4.6. In contrast, when assuming a uniform source, the transits show always the same depth independent of the impact parameter, as long as they are not grazing. Consequently, the difference between a highly inclined transit with limb darkening and a transit without limb darkening is only marginal, and they look very similar especially when some noise is given.

The phenomenon of smaller error margins visible for u_C as mentioned above can be explained using the simple error propagation. I know from my MCMC sampling that u_1 and u_2 are strongly anti-correlated which requires a slightly adapted error propagation for correlated variables, which can be expressed by

$$\sigma_{u_C}^2 = \sigma_{u_1}^2 + \sigma_{u_2}^2 + 2C_{u_1,u_2} \,. \tag{4.8}$$

The last term of this equation is the covariance ($C_{u_1,u_2} = \varrho_{u_1,u_2}\sigma_{u_1}\sigma_{u_2}$) with ϱ to be the correlation coefficient. This coefficient can directly be determined from the parameter traces sampled by the MCMC algorithm or analytically using Eq. B.20 of my paper. The analytical solution delivers the dependence of ϱ_{u_1,u_2} on the impact parameter, which is shown in Fig. B.1 (right panel) in my paper, and this confirms that the correlation between u_1 and u_2 is always negative. Therefore, Eq. 4.8 translates to

$$\sigma_{u_1}^2 + \sigma_{u_2}^2 - 2\sigma_{u_1}\sigma_{u_2} = (\sigma_{u_1} - \sigma_{u_2})^2 \,, \tag{4.9}$$

assuming for simplicity an impact parameter of $b = 1$. This means that the combination u_C is *always* better constrained than the individual coefficients, independent of the impact parameter. This is also visible in Figs. 11 and B.1 (middle panel) in Müller et al. (2013). Pál (2008) delivers a more detailed analysis of the correlations between the limb-darkening coefficients, e.g. for different planet-to-star radii ratios p.

4.3.2 Comparison of public transit parameters and my fits

As an additional byproduct, I compare the transit parameters published by the *Kepler* team to my results determined using the MCMC method. In Fig. 4.10 I show the planet-to-star radii ratios p, the orbital inclinations i, and the semimajor axis of the orbits a. It is clearly visible

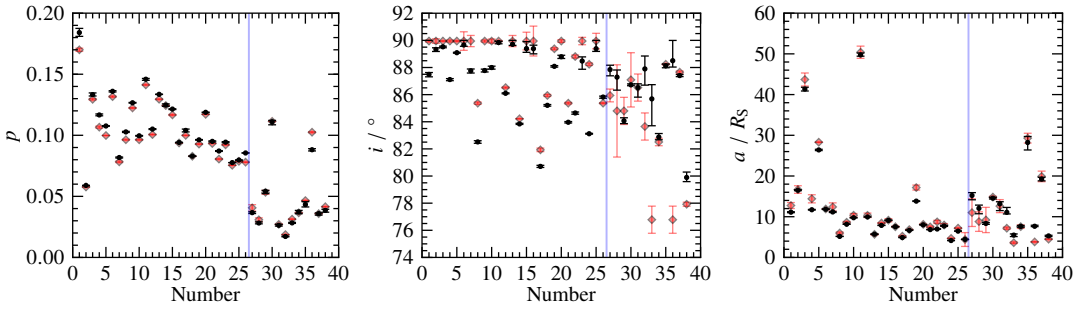

Figure 4.10: Comparison of measured transit parameters. *Dots*: Results of my MCMC sampling, *red diamonds*: public *Kepler* data (NASA, 2014). Error bars indicate the 1σ credibility intervals. Results *left* from the *blue vertical* line belong to my high signal-to-noise target sample, and on the *right* side of that line I present the results of my high impact parameter sample. Both samples sorted by $T_{\rm eff}$ (Müller et al., 2013, Table 3). See Fig. B.14 for residuals and a larger view.

that the MCMC results of most objects are not congruent with the parameters provided by the *Kepler* team. Due to the small uncertainties for most of these objects, I have to say that these deviations are significant. The main disparities are found in the orbital inclination and radii ratio, while the semimajor axis does not show pronounced differences for most objects. Looking at the radii ratios p, I assert that the *Kepler* team tends to measure slightly smaller values compared to mine. Out of 38 objects the radii ratios of 24 objects are on average 4 % smaller than those determined by my fitting approach, and only seven are identical in the range of their 1σ errors. The inclination angle shows a different behavior. Here 21 of my measurements lie clearly below the public *Kepler* values, and 11 are comparable. However, for 16 objects the *Kepler* team states the same inclination angle of 89.95°, which seems not likely to be fitted. For the values of the semimajor axis I found that 15 of the *Kepler* values are compatible with my results. 23 objects deviate significantly from each other, 17 are lying above mine , and 6 below. In the end, less than half of the objects here studied show almost the same parameters as published by the *Kepler* team. Especially the values of the inclination angle given by the *Kepler* team seem conspicuous to me. Therefore, I conclude that the transit parameters determined in my study are more reliable.

4.3.3 Evaluation of orbital parameters using their correlations

I showed in Table 4.2 that my measured quadratic limb-darkening coefficients show a deviation from theory, most significant for the quadratic coefficient u_2. Therefore, we now have an impression of how reliable these theoretical predictions are. The important question not answered yet is, which systematic influence would be introduced to the orbital parameters, if the limb darkening would be fixed to the predicted values in transit modeling. This can be answered by determining how the remaining parameters (p, i, a) deviate from my best-fit values, if the theoretical limb darkening would be chosen. This does not mean that I fix the limb-darkening coefficients and fit all transits again, this is actually not necessary. Fortunately, the parameter traces of the chosen MCMC approach hold all information I need to evaluate the mentioned parameters for all combinations of u_1 and u_2. This subsection is a supplement to Appendix B.5 of my paper (Müller et al., 2013), where I present a detailed theoretical background. I will now concentrate on the unpublished individual results, and present a procedure how the parameter evaluation can easily be implemented in a small algorithm.

My used MCMC sampler provides the parameter traces for every object in my sample, on whose basis the correlation coefficients between all parameters can be estimated. Together with the determined standard deviations we reach the covariance matrix $\boldsymbol{C}$ of the parameters. By definition, the inverse of the covariance matrix yields the Hessian matrix $\boldsymbol{H}$ written as

$$\boldsymbol{H} = \begin{pmatrix} \frac{\partial^2 f}{\partial p \partial p} & \frac{\partial^2 f}{\partial p \partial i} & \frac{\partial^2 f}{\partial p \partial a} & \frac{\partial^2 f}{\partial p \partial u_1} & \frac{\partial^2 f}{\partial p \partial u_2} \\ \frac{\partial^2 f}{\partial i \partial p} & \frac{\partial^2 f}{\partial i \partial i} & \frac{\partial^2 f}{\partial i \partial a} & \frac{\partial^2 f}{\partial i \partial u_1} & \frac{\partial^2 f}{\partial i \partial u_2} \\ \frac{\partial^2 f}{\partial a \partial p} & \frac{\partial^2 f}{\partial a \partial i} & \frac{\partial^2 f}{\partial a \partial a} & \frac{\partial^2 f}{\partial a \partial u_1} & \frac{\partial^2 f}{\partial a \partial u_2} \\ \frac{\partial^2 f}{\partial u_1 \partial p} & \frac{\partial^2 f}{\partial u_1 \partial i} & \frac{\partial^2 f}{\partial u_1 \partial a} & \frac{\partial^2 f}{\partial u_1 \partial u_1} & \frac{\partial^2 f}{\partial u_1 \partial u_2} \\ \frac{\partial^2 f}{\partial u_2 \partial p} & \frac{\partial^2 f}{\partial u_2 \partial i} & \frac{\partial^2 f}{\partial u_2 \partial a} & \frac{\partial^2 f}{\partial u_2 \partial u_1} & \frac{\partial^2 f}{\partial u_2 \partial u_2} \end{pmatrix} . \tag{4.10}$$

The determination of $\boldsymbol{H}$ is an important step, since it can be shown that the gradient of the posterior probability distribution, P, can be written as

$$\nabla \ln(P) = -\boldsymbol{H} \Delta \boldsymbol{x} , \qquad \text{with} \qquad \Delta \boldsymbol{x} = \Delta \boldsymbol{y} + \boldsymbol{\delta} . \tag{4.11}$$

$\Delta \boldsymbol{x}$ is a column vector, in which we can set one or more entries to fixed offsets δ_i, and adjust the remaining parameter offsets Δy_i so that the posterior P reaches again its maximum. In the case discussed here, I want to fix the offsets of the limb darkening coefficients. The parameter offsets Δy_i then represent the changes of the orbital parameters, expected if theoretical values for u_1 and u_2 are used in transit modeling. To achieve these parameter changes we first define the vector $\boldsymbol{\delta}$ containing the deviation from theory, found by my transit modeling (Table 4.2). This leads to the simple form

$$\boldsymbol{\delta} = (0,0,0,\Delta u_1, \Delta u_2)^{\mathrm{T}} . \tag{4.12}$$

This vector is then multiplied with the Hessian matrix, which results in a new vector $\boldsymbol{b} = \boldsymbol{H}\boldsymbol{\delta}$:

$$\boldsymbol{b} = \begin{pmatrix} \frac{\partial^2 f}{\partial p \partial u_1}\Delta u_1 + \frac{\partial^2 f}{\partial p \partial u_2}\Delta u_2 \\ \frac{\partial^2 f}{\partial i \partial u_1}\Delta u_1 + \frac{\partial^2 f}{\partial i \partial u_2}\Delta u_2 \\ \frac{\partial^2 f}{\partial a \partial u_1}\Delta u_1 + \frac{\partial^2 f}{\partial a \partial u_2}\Delta u_2 \\ \frac{\partial^2 f}{\partial u_1 \partial u_1}\Delta u_1 + \frac{\partial^2 f}{\partial u_1 \partial u_2}\Delta u_2 \\ \frac{\partial^2 f}{\partial u_2 \partial u_1}\Delta u_1 + \frac{\partial^2 f}{\partial u_2 \partial u_2}\Delta u_2 \end{pmatrix}. \tag{4.13}$$

We now remove the elements from $\boldsymbol{b}$ and $\boldsymbol{H}$ pertaining to the limb-darkening coefficients, which are the last two entries of $\boldsymbol{b}$ and the last two rows and columns of $\boldsymbol{H}$, and we obtain $\boldsymbol{b}'$ and $\boldsymbol{H}'$. The inverse of $\boldsymbol{H}'$ yields a new covariance matrix $\boldsymbol{C}'$ as if u_1 and u_2 where fixed to theoretical values during transit modeling. The vector of the absolute parameter changes $\Delta\boldsymbol{y}'$ is than calculated by multiplying the new covariance matrix with $\boldsymbol{\delta}'$,

$$\Delta\boldsymbol{y}' = \boldsymbol{H}'^{-1} \cdot (-\boldsymbol{b}'), \tag{4.14}$$

which "self-re-maximizes" the posterior.

I repeated this procedure for every object in my sample, which resulted in 38 parameter offsets for each orbital parameter (p, i, a). I normalized these offsets by the individual fit results of the parameters and show them in Fig. 4.11. We can see that the scatter of the points is

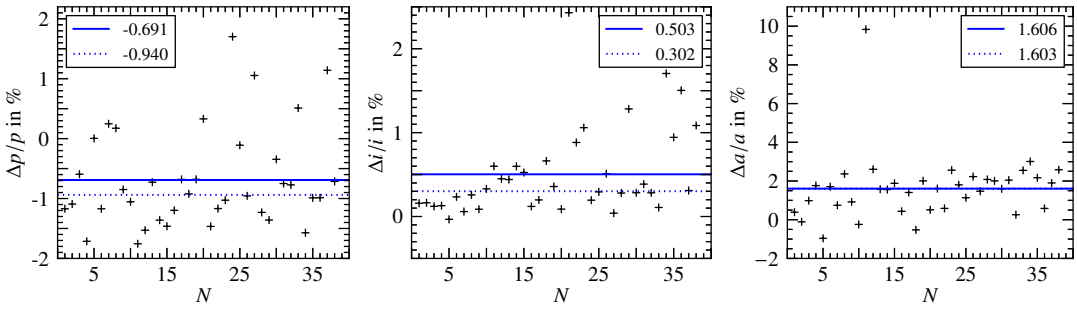

Figure 4.11: Individual relative parameter changes if LDCs are set as fixed parameters in transit modeling, after applying an constant offset to the theoretical LDCs. *Blue solid* line indicates the mean value of all points and the *dashed* line marks the median value. Points are sorted by effective temperature.

relatively large. For clarity I mark the mean and median values in the plots, which reveals that the semimajor axis reacts most sensitively to changes of the limb darkening. Depending on the chosen model prediction I get slightly different results for the mean parameter offsets, summarized in Table 4.3. The errors are on the oder of 1 %, which is not surprising when looking at the scatter visible in Fig. 4.11. Nonetheless, these values can serve as estimators for the systematic errors to be expected when theoretical limb-darkening coefficients are used. In any case, despite the large uncertainties we can see a trend of the parameters, e.g. that p tends to be smaller and this could be interpreted as smaller planet radii. This can probably be

Table 4.3: Relative parameter changes, if theoretical LDCs are used in transit modeling.

Model	$\Delta p/p$ in %	$\Delta i/i$ in %	$\Delta a/a$ in %
PHOENIX 1D [a)]	-0.7 ± 0.8	0.5 ± 0.5	1.6 ± 1.7
ATLAS [a)]	-0.5 ± 0.4	0.3 ± 0.2	0.9 ± 1.2
PHOENIX qs [b)]	-0.6 ± 0.7	0.4 ± 0.4	1.4 ± 1.5

Notes: Parameter changes are determined as described in text. Error estimates are determined as simple standard deviations from individual relative parameter changes of all 38 objects. [a)] Claret & Bloemen (2011), [b)] Claret et al. (2013).

explained by the fact that the limb darkening seems to be overestimated by theory, as already mentioned in the context of Fig. 4.6. Transits in front of stars with strong limb darkening are deeper than those with weak limb darkening. When comparing these results to the differences given in Table 4.2, it is conspicuous that the ATLAS predictions lead to smaller parameter offsets, although they show larger deviations from my measurements, at least when expressed in χ^2 values. This again demonstrates how complicated the search for an answer to the question "which model prediction is the most reliable" is.

We have to keep in mind that I used high quality space-based photometry to achieve these results. The discussion outlined here is therefore only of interest, if the data quality is comparable or even better, because in these cases the observer should fit the limb darkening during transit modeling. Especially in the case of ground-based observations the photometric quality is almost always at a level where the limb darkening should be fixed to the predicted values. The introduced systematic errors to the transit parameters would be small compared to errors caused by the normal noise of the data.

4.4 Time-correlated noise

At some point, most observers have to deal with the phenomenon of time-correlated noise, in fact in the case of time-series data, such as radial velocity measurements of the Rossiter-McLaughlin effect or – as in my case – observations of transit light curves. A simple example, where time-correlated noise can occur, is an increasing or decreasing airmass during observations. Thereby, the induced variation in signal strength then, consequently, causes a variation in the data-point errors. This example illustrates the time dependence of the errors, which also implies that the error σ_i depends on the error σ_{i-1} of the previous data point. This fact introduces long-range correlations in the time domain of the data set (see e.g., Beran et al., 2013).

There exist numerous sources of time-correlated noise, such as instrumental effects like aging, but also changing atmospheric conditions caused by clouds or dust particles, temperature and humidity drifts. The latter two are more important for spectroscopic observations than

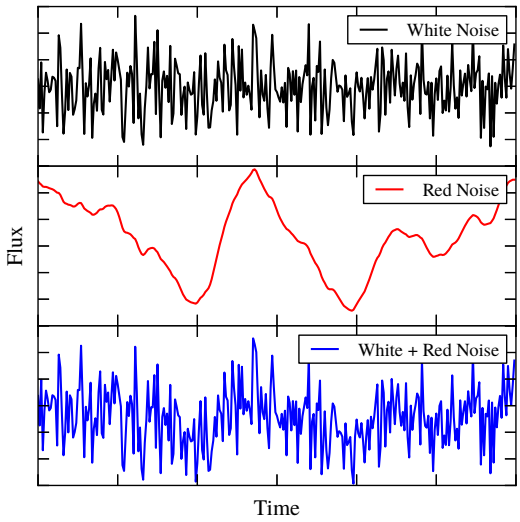

Figure 4.12: Simulated data with different kinds of noise. The *bottom panel* illustrates white noise data with a red noise contribution, such as a light curve of a slightly spotted star. In this case I added the red noise (*middle panel*) to Gaussian distributed data (*top panel*). See text for details. The axes are arbitrarily scaled. This figure is inspired by Pont et al. (2006, Fig. 2).

for photometric time series. Of course, stellar intrinsic variabilities like spots or oscillations engender time-correlated errors as well. If we think of normally distributed data the most probable error of individual data points can be derived from the Gaussian probability distribution. When this data set is modulated by an oscillation or influenced by other processes the individual data points can still be normal deviates (e.g., Deserno, 2002). However, if their variances are defined by Poisson statistic, then they are now time-dependent due to the oscillation. A histogram over the whole data set would not have a Gaussian shape anymore, which can be evidence of time-dependent noise in the data.

Normally distributed data has usually no correlation in time. A frequency analysis of such data would reveal that all frequencies have the same spectral power, or in other words: the power spectral density (PSD) is constant. Analogous to light, such a noise distribution is called "white noise". Noise which shows a time dependence has a PSD changing with frequency, such as "red noise" or "pink noise", which has a PSD of $1/f^2$ or $1/f$, respectively, where f denotes the frequency. In both cases, high frequencies (short periods) have less power than low frequencies (long periods).

There exist some numerical methods to generate pure red noise. For instance we can compute the running sum of Gaussian distributed random data. This is, obviously, the integral of the data. This integral introduces a factor of f^{-1} into the Fourier transform and therefore a factor of $1/f^2$ if the power is considered (see e.g., J. A. Barnes & Allan, 1966; Press, 1978). This new data set represents a random walk, also known as Brownian motion, which is the reason why red noise is also often called Brownian or Brown noise. However, in Fig. 4.12 (middle panel) I show simulated red noise data for which I used a different method. I sampled 300 normally distributed data points and calculated the Fourier transform of this data set. The resulting power spectrum was then multiplied by a filter function which has the form $1/f^2$, normalized by the lowest frequency. This new power spectrum is than transformed back to the time domain. Now, in Fig. 4.12 (middle panel) no high frequencies are visible anymore,

although they are still present. The amplitudes of these high frequencies are now strongly suppressed. The bottom panel of Fig. 4.12 shows the superposition of the top and middle panel. The result of this procedure is a data set with colored noise similar to a light curve of a spotted star often visible in high quality photometry.

The problem of time-correlated noise is well discussed in the literature and also in astronomical contexts (e.g., Press, 1978; Pont et al., 2006; Carter & Winn, 2009). However, in the following sections I go into some details of the analysis of colored noise in the case of transit light curves, especially if the data exhibits gaps and missing continuum parts between the planet eclipses.

4.4.1 Analyses of time-correlated noise in simulated data

There exist different methods to search for colorful noise in data sets; see e.g. Carter & Winn (2009) for a comparison of different methods. In this subsection I present correlated-noise analyses of simulated light curves using the so called "time-averaging" method, as outlined by Winn et al. (2007), which is based on the work of Pont et al. (2006). The basic idea of this method is to calculate the standard deviation of the residuals between observed and modeled data, denoted as σ_1, and also to calculate the standard deviations of these residuals after they were averaged over n points into M bins, denoted as σ_n. The forecasted behavior of the standard deviation of the binned residuals in the absence of colored noise should be $\sigma_n \approx \sigma_1/\sqrt{n}$, which is a good approximation in the case of a larger number of M (we will see what "a large number of M" means in this sense). If the data set exhibits colored noise, the determined standard deviations σ_n would be larger than the predicted ones by factors named β_n. These factors are of special interest, since they are suggested to increase the error estimates of the model parameters. In practice, the investigator determines the mean of a set of β_n, according to a range Δn, which is in the case of transit photometry 10 to 30 minutes, which corresponds to transit ingress and egress times (Winn et al., 2007; Carter & Winn, 2009). However, it should be noted that the predicted σ_n has a slightly different form than stated above. Winn et al. (2008, Eq. 2) presented the form

$$\sigma_n = \frac{\sigma_1}{\sqrt{n}} \left(\frac{M}{M-1} \right)^{1/2}, \tag{4.15}$$

the last factor arising probably from private communication between J. Winn and G. Kovacs without any further statements. Obviously, this equation is not defined when averaging over the whole data set; resulting M to be equal to one. The important question is, which values of M will appear in this analysis. Naturally, this depends on the important time scales in which we are interested. If we assume 30 minutes as relevant time scale and an arbitrary but not uncommon transit duration of the order of 2.5 hours (data cadence one minute), the lowest value of M necessary for the analysis would be set to five. Thus, the last factor of Eq. 4.15 would increase the predicted standard error by typically 12 % in the last bin step.

To get an impression of this specific red-noise analysis, I created some simple test cases using the `occultquad` code (Mandel & Agol, 2002) to generate a reasonable number of transit

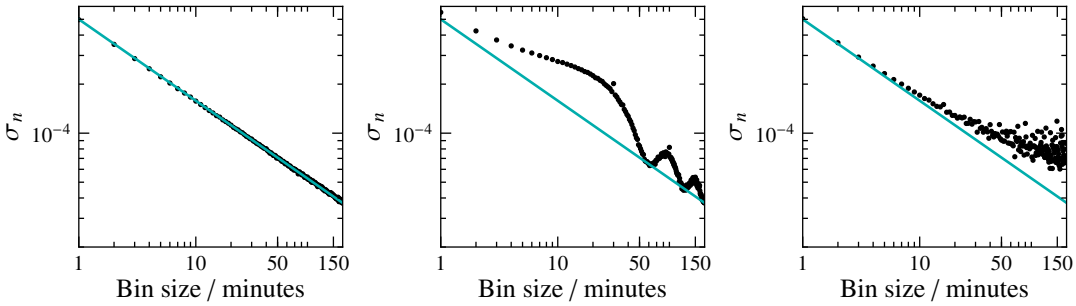

Figure 4.13: Correlated noise analysis of simulated data. Determined standard deviations of the residuals *(black dots)* plotted against bin size. White noise expectation is given as *cyan* colored line. *Left panel*: Result for a data set with pure white noise. *Middle panel*: Error behavior for a light curve with added sinusoidal oscillation. *Right panel*: White noise light curve with deleted continuum parts between transits.

light curves comparable to my chosen *Kepler* targets. In fact I generated a dataset with 80 transit events, with one minute cadence, and added some Gaussian distributed noise by using Eq. 1.29 with a standard deviation of $\sigma_1 = 0.0005$ (see Table A.4 for a detailed parameter list). The chosen value for σ_1 is also comparable to my chosen *Kepler* targets and leads to a *transit* signal-to-noise ratio (δ/N) of about 27. The resulting error behavior with increasing bin size is visualized in the following plots (Figs. 4.13 to 4.15).

The first simulated dataset is a whole light curve without any gaps, including continuum between all transits. The determined standard deviations σ_n follow the predicted error behavior quiet nicely (Fig. 4.13, left panel), as expected for pure white noise. This figure is similar to the one achieved by Kipping & Bakos (2011, Fig. 2) of *Kepler* photometry of TrES-2b using the same method as described above. I arbitrarily chose the upper value of the bin size (180 minutes), which is a small number for this simulated data set but made it feasible to use the same x-axis for all of my simulated light curves.

In my second simulation I added a sinusoidal oscillation to the data with a period of 60 minutes and an amplitude of $0.000\overline{3}$. This amplitude corresponds to a signal-to-noise (S/N) of only $0.\overline{6}$ and it is 45 times smaller than the transit depth, barely visible by eye in the light curve. Both values, period and amplitude, are arbitrarily chosen to fit my test and plot conditions best. Among the great variety of observable stellar oscillations and variabilities (see e.g., Aerts et al., 2010), these values are not uncommon and at least possible. The analysis of this light curve shows a significant deviation of the determined σ_n from the white noise prediction, depending on the bin size (Fig. 4.13, middle panel). The values of σ_n show an oscillating behavior with clearly visible local minima and maxima. The first local minimum is located at a bin size of 60 minutes, which is consistent with the chosen period of the added sinusoidal oscillation. This minimum is followed by minima at every harmonic of this period: 120 and 180 minutes (at the edge of this plot). The half of the period and those harmonics are visible as local maxima. The first two of them, located at bin sizes of 30 and 90 minutes, show singular points lying clearly above the course of the remaining standard deviations. At these bin sizes

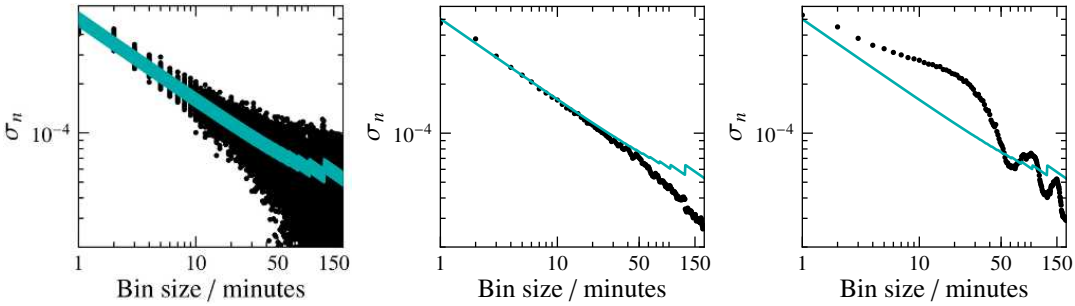

Figure 4.14: Correlated noise analysis of simulated data, continued. *Left panel*: individual results of 80 transits without continuum nor correlated noise. *Middle panel*: calculated mean values of the *left panel*. *Right panel*: distribution of σ_n for a light curve with added sinusoidal oscillation but removed continuum, using the same approach as used for the *middle panel*.

the scatter of the binned residuals increases significantly, since only halves of the introduced oscillation are combined into individual bins and, therefore, the involved data points are clearly lying above or below the mean of the data. Notably, the overall shape and the position of the local maxima and minima of this curve, do not depend on the phase of the oscillation, e.g. if a cosine is used to add oscillations to the data.

In comparison to real data, these previous examples are not very realistic, not least because of the idealized continuity of the light curves without any gaps. Real photometry results in most cases in non-evenly spaced data points, due to removed outliers or small differences in integration time or instrumental duty cycles, and also probably exhibits time-dependent noise. Obviously, the Earth's rotation makes a continuous observation of most positions of the sky impossible, at least in the optical wavelengths. Space based observations reduced these issues, but they were not able to eliminate them. In my case, where the main interest is focused on transit events, the investigated data normally consists only of the transit light curves, plus some short continuum parts for normalization issues. In ground based photometry this is automatically caused by the limited observation time. In space based observations the investigator often selects only transits from the light curve, neglecting most of the surrounding data. This can produce - depending on the orbital period - gaps of the order of days. Therefore, I deleted the continuum between the simulated transit events, leaving only one hour at every side of these transits. The analyzed behavior of the standard deviations σ_n, which constitutes my third test case, is shown in Fig. 4.13 (right panel). This result reveals, that almost all σ_n lie above the white noise prediction, with an increasing trend of the deviation towards larger bin sizes together with also increasing scatter. Thus, it seems to be likely to suppose that the data exhibits time-dependent noise, although this is not the case, since I generated the data only with white noise. This result can be explained by how the binning algorithm used for this analysis works. It averages all points in a time interval, which is moved in steps of the interval width through the whole data set. Thereby, the number of points n per bin M is not constant in time, since the bin size is almost never a multiple of the orbital period. Especially at the beginning and the end of the transit light curves the bins can consist of only a few data points,

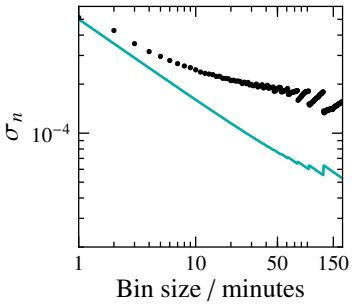

Figure 4.15: Correlated noise analysis of simulated data, continued. Resulting behavior of σ_n for light curve with added red-noise to every transit light curve individually. Continuum parts are deleted before analysis.

causing these bins to scatter in y-direction, increasing the determined standard deviations. This behavior is clearly a flaw of this method, and it has to be considered when analyzing data with significant gaps. Therefore, my idea was to carry out this time-averaging method for each transit light curve individually, forcing the algorithm to have the same number of points in every bin. For my simulated data set this approach yields 80 σ_n curves, plotted together in Fig. 4.14 (left panel). Depending on the also individually determined σ_1 values, the expectation of the standard deviations is now visible as a broad band. Due to a relatively strong scatter of every single σ_n curve, the error behavior also appears as spread over a wide y-range, especially for increasing bin sizes. My next step was to calculate the mean of these σ_n values for every single bin size. This leads to one σ_n curve with very low scatter, displayed in Fig. 4.14 (middle panel). The white noise expectation (Eq. 4.15) now shows a step-like structure together with an increasing trend, clearly visible for bin sizes larger than 50 minutes. The increase is caused by the last factor of Eq. 4.15, in this case $M = 2$. The steps are induced by the fact that the number of bins M does not evenly decrease with the bin size, since M is constant until the bin size reaches a value where not enough data points are left to fill the last bin exactly with n points.

Figure 4.14 (right panel) shows the resulting σ_n profile of the data set with the added sinusoidal oscillation, this time also with deleted continuum parts, using the aforementioned method. Clearly, this result comprises the same structure as given before in Fig. 4.13 (middle panel). I checked that both results are almost congruent, in error amplitude and period. Only the two prominent data points in Fig. 4.13 are not visible anymore, and the curve shows a slight scatter. We have to keep in mind that the orbital period (see Table A.4) is not a multiple of the added oscillation. As a consequence, the sinusoidal variations are phase shifted with respect to, say, the first transit point. This phase shift is of course different for every transit. So this plot can serve as a support of my introduced binning procedure.

In my last test case, I added some pure red noise to the simulated transit light curves, by calculating the cumulative sum of some Gaussian distributed random data with zero mean. These random data is generated for each transit event individually. The resulting values of the cumulative sum are arbitrarily multiplied by 0.05 before adding them to my data, just to keep the introduced variations as realistic as possible. The analyzed error behavior (Fig. 4.15) shows a clear difference to the prediction for all studied bin sizes. In addition the curve shows a clear sawtooth wave like shape, more pronounced at larger bin sizes. Thus, it is proven that this method is capable of detecting red-noise contributions.

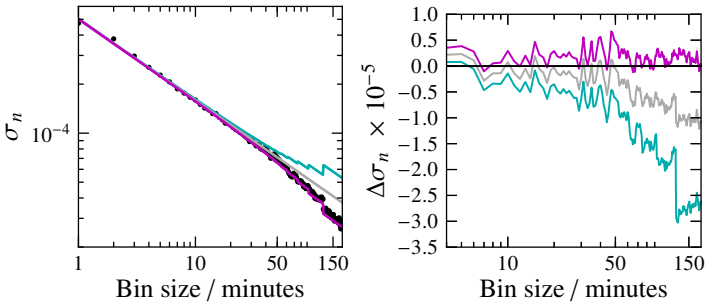

Figure 4.16: Comparison of different error expectations (*colored lines*) to determined white noise standard deviations (*dots*). *Right:* Residuals between dots and expectations. See text for color references.

Another important behavior of the determined standard deviations, is the fact that the values show a decreasing trend below the prediction with increasing bin size, as visible in Fig. 4.14 (middle panel). On closer inspection, the σ_n values begin to lie below the prediction at bin sizes around ten minutes. It is totally self-explanatory that it makes no sense to find the σ_n values below the white noise expectation. As I mentioned before, the ratio between σ_n and the expectation (β) is used to increase the parameter errors in the presence of time-correlated noise. However, the discussed phenomenon leads to a systematic underestimation of β and in some cases – depending on the time range we are interested in – to values of $\beta < 1$, which would be equivalent to decreasing the parameter errors. This described visible characteristic can also be found in the works of some other authors inspecting real data (e.g., Campo et al., 2011; Cubillos et al., 2013; von Essen et al., 2013), unfortunately they do not comment on this issue. Of course, this behavior is not visible in Fig. 4.13, where the whole continuum is included in the analysis, but this is only due to the still relatively large number of bins M for the chosen bin sizes n. It seems that theory systematically over-predicts the white noise error, especially when only a low number of bins is involved in the calculation of the standard deviation. If there is only one bin left, than it would not be possible to compute a standard deviation anymore. In this special case it would only be possible to compute the error of the mean, because the leftover bin *is* the mean of the whole residuals. In contrast, if there are two bins left, it is of course feasible to derive the standard deviation, but in principle we try now to determine the width of a Gaussian distribution out of only two points. It is then questionable how reliable this value is to represent the uncertainty of the individual bins.

There is a number of bins M for which it is not adequate anymore to calculate the standard deviation, if we try to determine the most probable error of one bin. However, in principle we are not interested in determining the real uncertainty of one bin. In fact, we are more interested in the amount of scatter of the binned residuals at a given bin size. The standard deviation serves in this sense as an estimator of the scatter, which has nothing to do with the real error of one bin. Therefore, the more important question is, how does the expectation of the determined standard deviations have to look like. In Fig. 4.16 I show again the results of the analysis of my white noise dataset together with two additional white noise expectations. To be consistent with my simulations discussed above, I show in cyan the error behavior as predicted by Eq. 4.15, while the gray and magenta lines represent

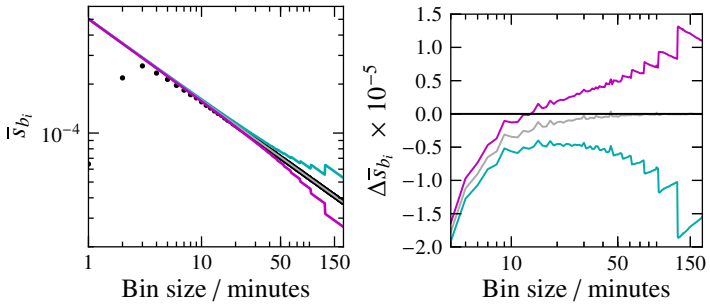

Figure 4.17: Comparison of different error expectations (*colored lines*) to the mean of the mean-errors $\overline{s}_{b_i}$ (*left*) and corresponding residuals (*right*). See text for more details.

$$\sigma_n = \frac{\sigma_1}{\sqrt{n}} \qquad \text{and} \qquad \sigma_n = \frac{\sigma_1}{\sqrt{n}} \left(\frac{M-1}{M} \right)^{1/2}, \tag{4.16}$$

respectively. Note that I invented the last factor of Eq. 4.16 by just inverting the fraction in the brackets of Eq. 4.15. Astonishingly, Fig. 4.16 bares that Eq. 4.16 is not such a bad guess, which gives a much better fit to the determined standard deviations. Actually the last factor is needed to achieve an unbiased estimator of the variance σ^2. However, as pointed out by Roesslein et al. (2007) it is an often neglected fact that this factor is *not* sufficient to correct the estimator of the standard deviation for bias. Due to the nonlinearity of the square root, the square root of the unbiased variance leads to a biased standard deviation! To achieve an unbiased estimator of σ one has to apply a correction factor mentioned by Kenney & Keeping (1951). In the specific case shown here this factor has the form

$$(b(M))^{-1} = \sqrt{\frac{M-1}{2}} \frac{\Gamma(\frac{M-1}{2})}{\Gamma(\frac{M}{2})}. \tag{4.17}$$

Nevertheless, this correction is in my case also not perfect for the prediction of the *binned* white noise error. It leads to slightly overestimated errors for a wide range of bin sizes. So I have to conclude that neither of the here mentioned white noise expectations are able to predict the behavior of the found standard deviations. Probably, the reason for this is that the measured standard deviations (dots in the figures) are not representing the real bin errors, but at least the prediction $\sigma_1/\sqrt{n}$ does. To prove this assertion my idea was to compute the real error of every single bin b_i, which is the error of a mean s_{b_i}, since every bin is a mean of n points. In the case where only one bin is left this would lead to one error value, but in all other cases this results in M mean errors. To get only one error per bin size I simply calculated the mean of all errors using

$$\overline{s}_{b_i} = \frac{1}{M} \sum_{i=1}^{M} \left[\frac{1}{n(n-1)} \sum_{j=1}^{n} (y_{j,i} - b_i)^2 \right]^{1/2}, \tag{4.18}$$

where $y_{j,i}$ stands for the j-th residual point in the i-th bin b. This equation should be a better representation of the probable error of one single bin when only a few bins are left, in contrast to the standard deviation. Figure 4.17 nicely illustrates the behavior of $\overline{s}_{b_i}$. These error values

follow directly the expectation $\sigma_1/\sqrt{n}$ for large bin sizes. Of course, Eq. 4.18 is a bad choice if a greater number of bins is left, which can be seen as a vast deviance from theory at bin sizes from 1 to ≈ 4 minutes. As we know, the standard deviation behaves contrarily. This brings me back to the point where I introduced the white noise expectation, which I quoted as a good approximation in the case of a large number of bins. Maybe $\overline{s}_{b_i}$ starts to follow the prediction $\sigma_1/\sqrt{n}$ where σ_n starts to deviate significantly from this prediction. This would be the point at which the white noise prediction is not appropriate enough for the σ_n values. To determine this point I show in Fig. 4.16 (right panel) the residuals between the expectations and the determined standard deviations. We clearly see that the σ_n values start to lie significantly below the prediction $\sigma_1/\sqrt{n}$ (gray) around bin sizes of 50 minutes, while the cyan prediction (Eq. 4.15) overestimates the standard error starting at bin sizes of 7 minutes. Therefore, the cyan line lies mainly below zero in this figure. In the right panel of Fig. 4.17 I present the residuals of the $\overline{s}_{b_i}$ values, which begin to lie close to the prediction $\sigma_1/\sqrt{n}$, also near to bin sizes of 50 minutes. From this point on $\overline{s}_{b_i}$ starts to represent the real bin error and σ_n stops to be an appropriate estimator for the bin error. The corresponding number of bins M of that point is given by the number of visible step like structures, start counting from the right with $M = 2$. According to my simulations this leads to $M > 7$ where $\sigma_1/\sqrt{n}$ is a good approximation to describe the behavior of the white noise error.

The presented problems and phenomena, like gaps in the data or, e.g., an overestimated noise expectation if Eq. 4.15 is considered, have to be accounted for in real data sets. Otherwise, the analysis would lead to an incorrect parameter error correction. In the next subsection, I will comment on the way in which I am dealing with these issues.

4.4.2 Correlated-noise analyses in *Kepler* light curves

As outlined in the previous subsection, a comprehensive analysis whether the observed data exhibits time-correlated noise is essential. Therefore, I made an analysis searching for time-dependent noise in the light curves of the 38 planetary candidates selected for my short cadence target sample. Kipping & Bakos (2011) carried out a comparable analysis of the *Kepler* photometry of TrES-2b (Q0 and Q1), including the unocculted continuum parts of this light curve. They conclude that there is no evidence for time-correlated noise in that data.

In contrast to the work of Kipping & Bakos (2011), I do not present the analysis of the continuum parts for which you need some kind of model describing the global variations, at least for every single *Kepler* quarter. I am only interested in the transit light curves of my selected objects, since only here I can find the sampled limb-darkening information. Consequently, my data sets have long gaps between the transit events and I have to account for them in the correlated noise analysis by investigating every single transit per object, as introduced in the previous subsection. The needed residuals are determined by subtracting the best-fit model from every transit light curve. The binning of the residuals is then repeatedly performed until the number of points per bin n reaches a value where only two bins are left per transit light curve.

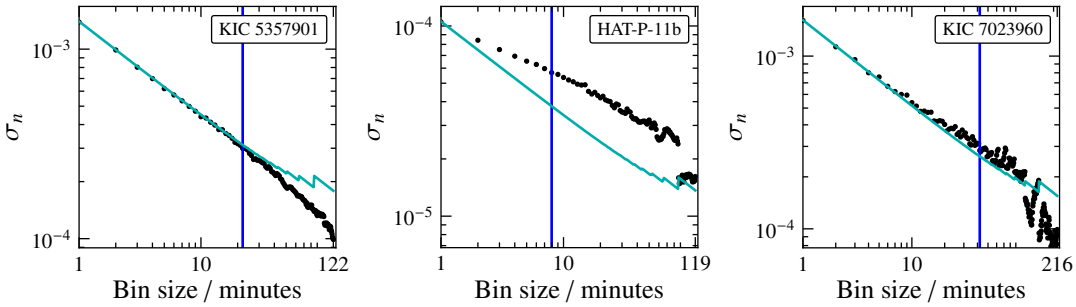

Figure 4.18: Some resulting σ_n curves of my colored noise analysis (*dots*). Transit ingress or egress durations are marked by *blue vertical* lines. *Cyan* lines indicate the white noise expectation (Eq. 4.15). The name of the specific *Kepler* target is given in the labels. The maximum bin size leading to $M = 2$ is additionally declared on the x-axis.

In Fig. 4.18, I present a few of the resulting σ_n curves, while all curves of the remaining objects can be found in the appendix (Figs. B.15 and B.16). The visible shapes shown here represent the variety of all remaining σ_n curves quite well. The scaling of the plot axes varies between the shown plots, especially the y-axis, caused by the different photometric noise of these objects. The x-axes are similar, thanks to the logarithmic scaling. In the end the axis-scaling is not so important, but more important is the shape of the σ_n curves and the relative deviation from the white noise prediction. Thus, a mutual comparison of these curves makes only sense if the shape is considered. In the left panel of Fig. 4.18 I show an example, where the analysis reveals that (almost) no correlated noise is present in the data. The σ_n values follow the prediction until they start to drop off somewhere near to transit ingress/egress duration. This result is similar to my white noise simulations shown in Fig. 4.14. In contrast, the middle panel is a good example where the data are affected by time-correlated noise. All points are clearly located above the predicted error behavior, except for the first one. This point is by definition equal to σ_1. And lastly, in the right panel I present a resulting curve, where the points lie only slightly over the prediction, and show a stronger scatter compared to the others. I have to mention, that significant scatter (especially at $M = 2$ or 3) is always visible in the σ_n curves of my objects, if only a low number of transits are considered for the analysis ($N_{\mathrm{transit}} \leq 10$). Thus, stronger scatter is not necessarily a sufficient criterion for the presence of time-correlated noise in my selected transit light curves.

Now, for the assessment of the amount of correlated noise in the data relevant for my transit studies, I have to determine the aforementioned correction factor β, and if time dependent noise is present, to increase the parameter errors by this factor. As outlined in the previous subsection, β is found as a mean of values β_n, which are in turn defined as ratios of the found σ_n to the white noise prediction. The mean is then determined over bin sizes, relevant for the analysis. Explicitly, I chose bin sizes between five minutes and the corresponding transit ingress duration. There are a few exceptions[4], where the transit ingress durations are exactly

[4] KIC 10318874, KIC 5084942, Kepler-68b, KIC 8456679

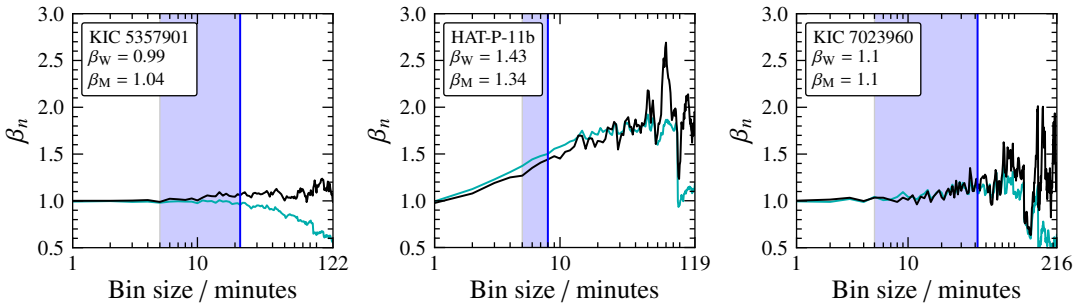

Figure 4.19: Determined β_n graphs for the objects given in Fig. 4.18. *Cyan lines*: ratios of measured σ_n to Eq. 4.15. *Black lines*: ratios of measured σ_n to determined σ_n of simulations. The *blue areas* marking the bin sizes used for determination of β_W (Winn) and β_M (Müller).

five minutes or even smaller. For these cases I included bin sizes starting at one minute in the calculation of β. I determined the transit ingress durations by using Eq. 1.28 and the corresponding best-fit parameters. The resulting β_n curves, which I present in Fig. 4.19 for the objects shown in Fig. 4.18, serve as a neat indicator whether the light curves are affected by time-dependent noise. Again all curves of the remaining objects are shown in the appendix in Fig. B.17. This time the scaling of the y-axis is the same in all plots, to ensure a better, direct comparison among all objects.

We learnt in the previous subsection that the presented theory tends to systematically overpredict the white noise error behavior. Consequently, the determined β_n values are underestimated. KIC 5357901 (Fig. 4.19 left panel) is a great example for this problem. The calculated β_n values (cyan line) tend to lie below one, leading to $\beta = 0.99$, which definitely makes no sense. This also clearly illustrates that it is not advisable to account larger bin sizes in the determination of β than the ingress duration, because this would lead to an even stronger underestimation of this factor (see, for interest, also first column of Fig. B.15). To deal with this issue, I have to find a better method to describe the white noise prediction. One possible solution, is to simply generate a simulated data set using my best-fit planetary parameters and than just perform the same correlated noise analysis as for the real data sets. It is important to use the time axis of the real data set and the same photometric noise. This method has the great advantage that also small gaps are considered in this new prediction, and that a $\beta < 1$ is not possible anymore. The β_n values are now easily determined by dividing the standard deviations of the binned residuals of the real data by the σ_n values of the simulated data, like

$$\beta_{M,n} = \frac{\sigma_n(\text{data})}{\sigma_n(\text{simul})}, \tag{4.19}$$

now given as black lines in Fig. 4.19. The needed correction factor β is determined like before. From this point on, I denote the correction factor as β_M if it is determined like introduced above, or β_W if it depends on Eq. 4.15.

As expected, the β_n values determined in this new way lead to a more realistic correction factor, and they now show no decreasing trend anymore (Fig. 4.19 left panel). Therefore, I

Table 4.4: Overview of the determined β-factors.

Identifier	β_W	β_M	Identifier	β_W	β_M	Identifier	β_W	β_M
Kepler-45b	1.04	1.05	TrES-2b	1.07	1.16	10318874	1.00	1.01
HAT-P-11b	1.43	1.34	12019440	1.01	1.05	5084942	1.00	1.03
11391018	1.08	1.17	Kepler-6b	1.05	1.09	12105051	1.04	1.09
5357901	0.99	1.04	Kepler-412b	1.03	1.09	*5771719*	1.73	1.75
8845026	1.36	1.42	Kepler-7b	1.07	1.13	Kepler-19b	1.09	1.14
BOKS-1b	1.15	1.24	9631995	1.09	1.13	Kepler-68b	1.07	1.08
6849046	1.00	1.06	Kepler-12b	1.05	1.10	8456679	1.01	1.01
Kepler-41b	1.03	1.10	Kepler-8b	1.04	1.09	8554498	1.08	1.20
9651668	1.19	1.25	Kepler-43b	1.09	1.15	*8684730*	1.70	1.90
8359498	1.05	1.09	10019708	1.05	1.11	3762468	1.18	1.19
7023960	1.10	1.10	HAT-P-7b	1.50	1.55	Kepler-25b	1.22	1.28
Kepler-15b	1.13	1.18	Kepler-5b	1.12	1.19	3861595	1.87	1.98
Kepler-17b	1.58	1.62	Kepler-13b	1.33	1.36			

Notes: Objects listed in *gray* color show $\beta_W \leq 1.25$. Objects with $\beta_W > 1.25$ and not discussed in my paper are set in *italic*. *Third column*: objects according to my high impact parameter sample ($b \geq 0.8$).

conclude that the creation of a simulated data set is the better choice for the determination of a white noise prediction. On average my β_M is 4 % larger than the widely used β_W (see Table 4.4). However, it is also possible that my found correction factor β_M is smaller than β_W, like it is the case for HAT-P-11b (middle panel). The analysis of the simulated data set produces σ_n values lying above the white noise prediction (Eq. 4.15). It seems that this time my method overpredicts the white noise error, but this is *not* the case. This can easily be explained by the fact that my simulation also accounts for gaps, since it uses the same time axis as the original data set. We have seen in Fig. 4.13, that significant gaps cause the measured standard deviations to lie conspicuously above the theoretical prediction, although the data are by creation normally distributed. In the special case of HAT-P-11b these small gaps are caused due to deleted outliers inside the transit light curves, leading to σ_n lying 7 % above the theoretical prediction.

The last object of this row (KIC 7023960, right panel) belongs to a group of objects, where the determined correction factors β_W and β_M do not differ significantly from each other. The found β factors reveal, that the correlated noise in the data is not as prominent as expected, if Fig. 4.18 right panel is compared to the left panel. Furthermore, this result also clearly displays, that the visible decreasing trend, if Eq. 4.15 is considered, is gone, although the measured σ_n of the real data exhibit relatively strong scatter.

With respect to Fig. 4.18, the results of my correlated noise analysis can by eye be divided into three groups: first, 17 objects showing no abnormal shapes and/or no significant deviation from the expectation; second, 11 data sets present prominent deviation from the white noise prediction; third, 10 remaining objects are only slightly deviant from the expectation. For a

further inspection and discussion only objects were considered, where $\beta_W \geq 1.25$, because lower values would have led to a barely visible increase in the error bars. In the end most of my selected targets (30) show a $\beta_W < 1.25$ while eight have significant colored noise contributions. Six of them are already discussed in my paper (Müller et al. (2013)). The remaining two, KIC 8684730 and KIC 5771719, belong to my target sample with large impact parameters ($b \geq 0.8$). Anyway, this class of objects show extraordinary large errors of all fit parameters, which is why a deeper look into both light curves is omitted.

A slight difference between the correction factors published in my paper and those given here, is explained by my improved bin-method of the residuals, unfortunately applied after publication. Nevertheless these differences are negligible and they do not influence my results.

Due to the less significant results and intrinsically larger error margins of the results obtained from my long cadence sample (Section 4.2), the analysis searching for time-correlated errors was not performed for these objects. The crude time resolution would only allow to obtain a few bin steps of the transit residuals, and for most objects even the ingress/egress durations are not resolved by the data sampling.

5 Limb Darkening of the Sun

The object which is predestinated to study the limb darkening, because it can easily be spatially resolved in observations and provides a very high signal-to-noise ratio, is our Sun. In principle, the limb-darkening effect can be seen by hobby or amateur astronomers, but the precise measurement is more difficult. Since the limb darkening of our Sun is well studied, a comparison between predictions and the solar limb darkening is self-evident. This could eventually give new insights about the credibility of the model atmospheres. On the other side, it also offers the great opportunity to check the validity of the different limb-darkening laws and their coefficients (e.g. determined by Claret & Bloemen (2011)).

In the following sections I will compare the measured solar limb darkening e.g. presented by Neckel & Labs (1994) to that obtained from a recent PHOENIX atmosphere (Table A.11). I will continue with the comparison of these measurements to the intensity distributions when using Claret & Bloemen (2011) limb-darkening coefficients. Differences will be quantified and I will come up with a special treatment of the intensity distribution of the actual PHOENIX model atmospheres.

5.1 Ground-based measurements compared to predicted LD

5.1.1 Adapting the results of Neckel & Labs

Between the years 1986 and 1990, Heinz Neckel and Dietrich Labs observed the solar limb darkening using the *McMath Solar Telescope* at *National Solar Observatory/Kitt Peak*. They gathered more than 5600 individual center-to-limb measurements of which every measurement in the years ’86 and ’87 has 30 different wavelengths in the range from 3033 Å to 10 990 Å. The whole observation campaign covers half a solar cycle (from minimum to maximum), and the authors state that there are no detectable variations which could influence the solar limb darkening. Small-scale variations like spots, faculae and also the granulation show an influence on the center-to-limb intensity distribution, but in the final *mean* these effects do not play any role.

The authors fitted the measured solar intensity distribution with a fifth order polynomial

$$P_5(\mu) = A_0 + A_1\mu + A_2\mu^2 + A_3\mu^3 + A_4\mu^4 + A_5\mu^5, \tag{5.1}$$

in the range between $\mu \simeq 0.1$ ($\approx 7''$ away from the limb) and $\mu = 1.0$. As a result they present six limb-darkening coefficients for each of the 30 wavelengths. I used Eq. 5.1 to present the

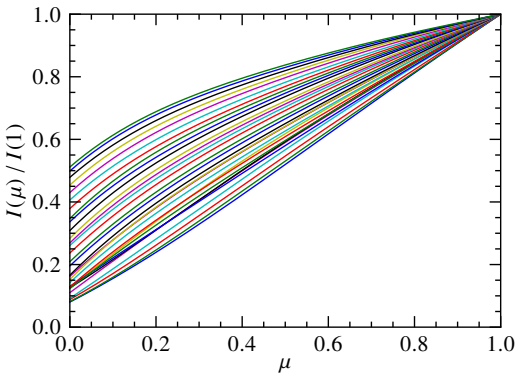

Figure 5.1: Normalized solar limb darkening for 30 wavelengths (3033 Å - 10 990 Å) using Eq. 5.1 with six LDCs provided by Neckel & Labs (1994) for each wavelength.

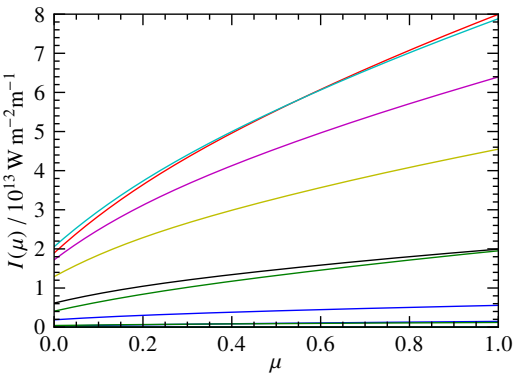

Figure 5.2: Absolute solar intensity as a function of μ using Eq. 5.2 for the same wavelength as in Fig. 5.1. Results are weighted with Johnson-V transmission coefficients.

different intensity profiles in Fig. 5.1. The color dependence of the solar LD is clearly visible, where longer wavelengths show a weaker LD (*top*) in contrast to shorter wavelengths which show a stronger LD (*bottom*). On the one hand, strictly speaking, all intensities at $\mu < 0.1$ are only extrapolated values, since these regions were not included in the fits. On the other hand, Neckel (2005) found that these values at the limb ($\mu = 0.0$) lead to absolute limb intensities, which can be translated into temperatures at the limb. These limb temperatures are found to be almost the same for each studied wavelength, as expected for a black body, and in good agreement with theory. This implies that the extrapolation of the intensities down to the stellar limb leads to correct values, which also have a physical sense.

Since the limb darkening is color dependent, the theoretical LDCs are determined for different passbands/astronomical filters (e.g. Johnson-Cousins UBVRI filters (Bessell, 1990) or instrumental response/transmission functions, like for the *Kepler* instrument (Van Cleve & Caldwell, 2009)). For a direct comparison of observed and predicted intensity distributions using theoretically determined LDCs and LD laws, I have to choose at least one of these passbands. The solar intensity distributions shown in Fig. 5.1 are individually normalized to the emitted flux at the solar disk center at the given wavelength. Therefore, these intensities have to be weighted, to achieve an intensity distribution as seen through, e.g., a Johnson-V filter. The unnormalized but weighted intensity at a wavelength λ_i can be written as

$$I(\mu, \lambda_i) = P_5(\mu)|_{\lambda_i} \cdot \pi B(\lambda_i, T) \cdot f_{\mathrm{Filter}}(\lambda_i)\,, \tag{5.2}$$

where B is Planck's law and f_{Filter} is the amount of transmitted light through the chosen filter at the given wavelength. For the Johnson-Cousins UBVRI filter functions I linearly interpolated between the transmission coefficients given in Bessell (1990). The resulting distributions of all wavelengths given by Neckel & Labs (1994) using this approach for a Johnson-V filter are

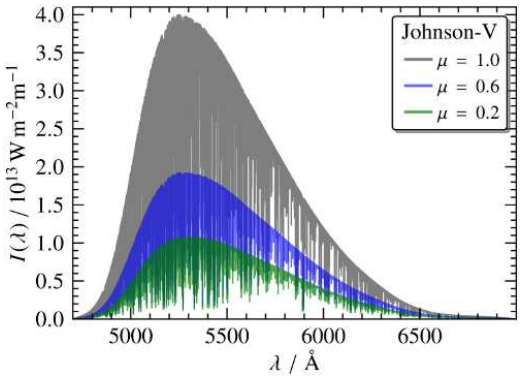

Figure 5.3: High resolution PHOENIX spectra for different limb angles (*lables*). Intensity is weighted by Johnson-V filter transmission curve.

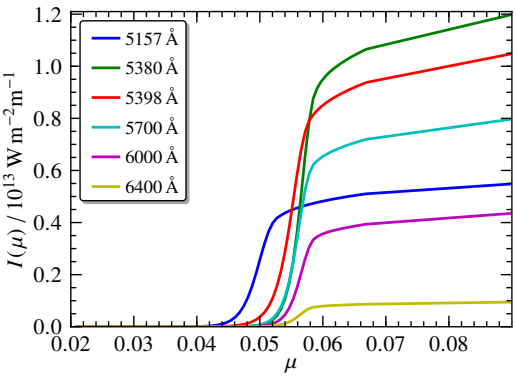

Figure 5.4: Limb intensities gathered from the mentioned PHOENIX spectrum. For comparison a few different wavelengths were chosen.

shown in Fig. 5.2. To get the normalized intensity profile I use the relation

$$\frac{I(\mu)}{I(1)} = \frac{\int I(\mu,\lambda)\,\mathrm{d}\lambda}{\int I(1,\lambda)\,\mathrm{d}\lambda} \approx \frac{\sum_i I(\mu,\lambda_i)}{\sum_i I(1,\lambda_i)}, \tag{5.3}$$

in which the integral is approximated by a sum of discrete wavelength intervals. The wavelengths chosen by Neckel & Labs (1994) cover the color dependence of the LD quite well, without any significant gaps or discontinuities (as we can see in Fig. 5.1). That implies that Eq. 5.3, which simply sums up all intensities and normalizes the result by its maximum, leads to a good description of the actual solar limb darkening as visible in Johnson-V filter band.

5.1.2 Comparison of Neckel, PHOENIX and Claret intensities

For the further investigations, I took a highly resolved model spectrum file which provides μ-dependent spectra, calculated using a spherical 3D PHOENIX-ACES model atmosphere (Table A.11 and Hauschildt & Baron (2010)). The parameters of this atmosphere are almost solar-like with an effective temperature of 5800 K, surface gravity of $\log(g) = 4.5$ and solar metallicity. In total there are 78 spectra included for different limb angles ranging from $\mu = 0.02$ to $\mu = 1$. To give a consistent comparison between the distribution calculated from Eq. 5.3 and these model intensities, I have to apply the same filter function f_{Filter} to all 78 spectra, like I did for the intensities provided by Neckel & Labs (1994). Three resulting spectra for different limb angles using a Johnson-V filter are shown in Fig. 5.3. The decreasing intensity at lower μ values is clearly visible. In this wavelength range (4700 Å - 7000 Å) PHOENIX provides more than 20 000 wavelength points with a resolution of 0.1 Å to 0.3 Å. Each wavelength point provides its own center-to-limb intensity profile. Figure 5.4 shows six different limb profiles near the limb at arbitrarily chosen wavelengths.

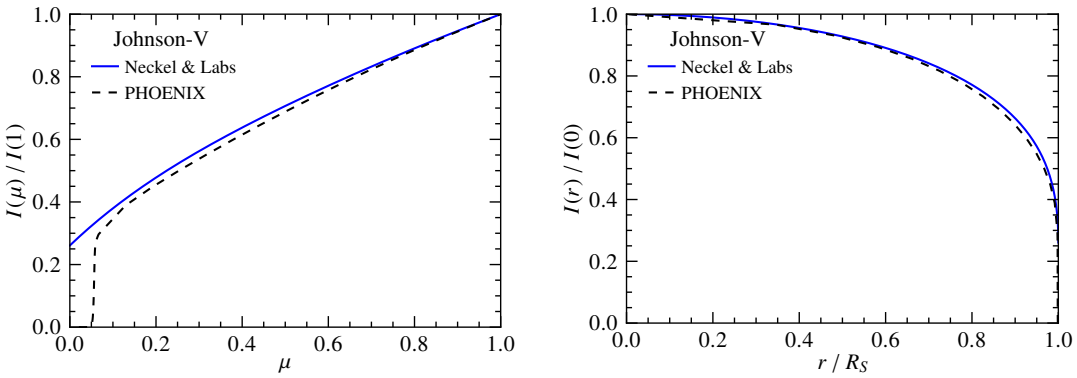

Figure 5.5: Comparison of the solar LD determined from Neckel & Labs (1994) (*solid*) and determined from a quasi-spherical PHOENIX atmosphere (*dashed*). Solar intensity distribution plotted against the limb angle μ (*left*), and plotted against the radial coordinate r (*right*).

In Fig. 5.5 I show the comparison between the LD calculated using Eq. 5.3 and the mentioned PHOENIX model atmosphere, both now weighted with a Johnson-V filter transmission curve. The eye-catching edge of the PHOENIX distribution near the limb, also clearly visible in Fig. 5.4, is a result of the spherical geometry of the model atmosphere. Plane-parallel model atmospheres do not show this significant drop off near the limb, and show – in contrast to the spherical models – a non-zero intensity at the limb. The steep decrease in intensity arises from the fact that spherical models predict much less material at the stellar limb (Orosz & Hauschildt, 2000), which leads to weaker extinction and scattering of light toward the observer, and to a weaker overall radiation at the limb. In principle this gap is negligible for a comparison between Neckel & Labs (1994) and PHOENIX, because the visible offset ($\Delta\mu \approx 0.055$) only corresponds to $\Delta r \approx 1.5 \cdot 10^{-3}\, R_S$. Expressed as an angular distance observed from Earth, this gap would span $1.4''$. The right panel of Fig. 5.5 illustrates how small this gap actually is when the solar intensity is plotted against the radial coordinate instead of using the limb angle. The more interesting part lies in the range of $\mu \approx 0.2 - 0.6$, which translates into almost 20 % of the solar radius, where the intensity seems to be underestimated by the model atmosphere. In this range the PHOENIX distribution shows on average 3.6 % less intensity than Neckel & Labs (1994). To quantify the total divergence, I need to determine the disk-integrated flux of both distributions. Needless to say that it is necessary to integrate the intensities in r-space

$$S_{\mathrm{disk}} = \int_0^{R_S} \int_0^{2\pi} I(r, \varphi) r \, \mathrm{d}\varphi \, \mathrm{d}r, \tag{5.4}$$

otherwise the resulting unit would be physically meaningless. The integration along φ can be executed directly and simplifies the equation to

$$S_{\mathrm{disk}} = 2\pi \int_0^{R_S} I(r) r \, \mathrm{d}r. \tag{5.5}$$

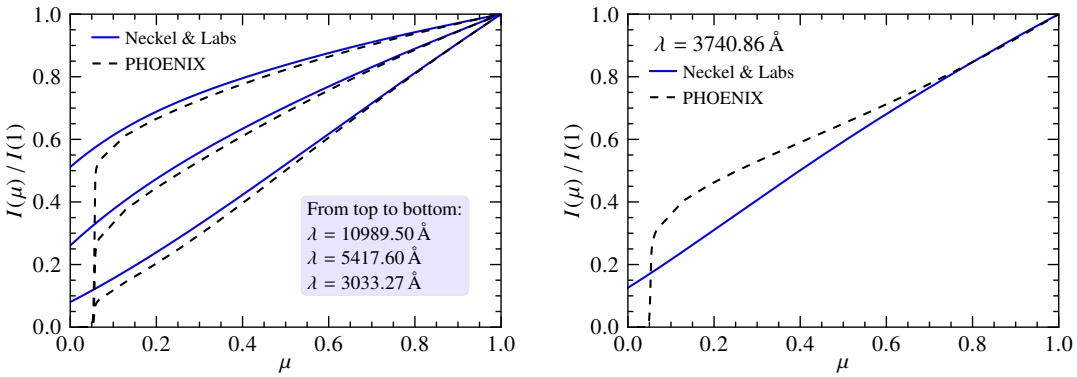

Figure 5.6: Comparison of limb intensity profiles at different wavelengths (*labels*). PHOENIX profiles are determined as a combination in wavelength intervals of ±0.15 Å around the given wavelengths. *Blue* curves are measurements of the Sun, plotted using Eq. 5.1 with LDCs taken from Neckel & Labs (1994).

This integration is performed numerically using the composite Simpson's rule (see, e.g., Mathews & Kurtis, 2004) and reveals that the distribution gathered from the PHOENIX atmosphere leads to 1.44 % less disk-integrated flux than virtually measured by Neckel & Labs (1994) in Johnson-V filter band.

The wavelength resolution of the PHOENIX spectra makes it possible to directly compare the limb darkening in each single wavelength measured in the observations, without applying any Planck- or filter functions like Eq. 5.2 does. This would exclude systematic effects possibly introduced by my approach. Due to the high wavelength resolution of the Neckel & Labs (1994) observations (< 0.1 Å) the given limb profiles calculated using Eq. 5.1 correspond to wavelength intervals with negligible size. Now it becomes necessary to transform the vacuum wavelengths given in the PHOENIX spectrum to those as measured in air, to get nearly the same spectral positions for comparison (for this transformation see Morton (2003) and references there). Of course, especially in the infrared regime the wavelength resolution of this PHOENIX spectrum is up to 0.3 Å, thus it is quite unlikely to find the same wavelength points as given by Neckel & Labs (1994) for the comparison. It is more likely, that each required wavelength is found between two PHOENIX wavelength points. For this reason I combine the PHOENIX limb intensities in wavelength intervals of ±0.15 Å for every wavelength given in Neckel & Labs (1994) before normalizing them. For almost all of the 30 wavelengths the limb intensities of the PHOENIX atmosphere lie below those that were directly measured on the Sun. Out of these, the differences amount to 0.29 - 2.28 % with a median value of 1.42 %, quite comparable with the value found in the Johnson-V filter band. I show three of them in Fig. 5.6 (*left*). All remaining profiles look very similar. This result emphasizes that PHOENIX really tends to underestimate the limb intensity of the Sun, as previously seen in the Johnson-V filter band and it is also assured that my approach introduces no significant systematic errors.

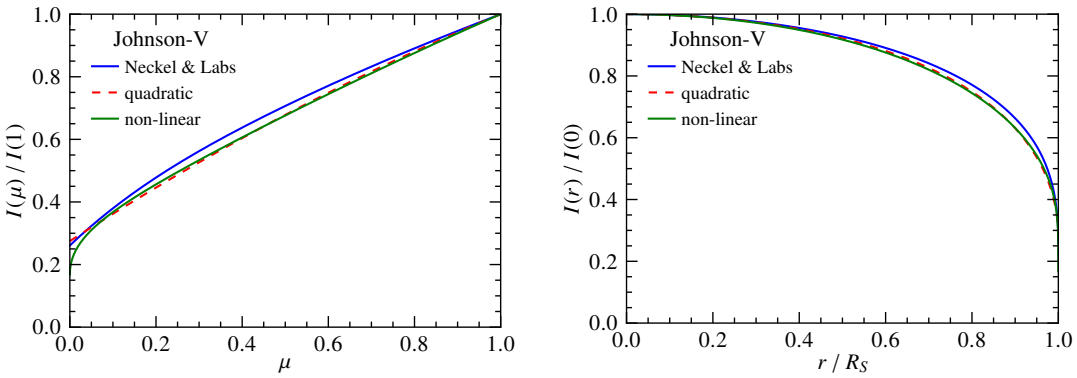

Figure 5.7: Comparison of the solar LD determined from Neckel & Labs (1994) (*blue solid*) and distributions generated using LDCs from Claret & Bloemen (2011) (*red* and *green*), both determined from plane-parallel PHOENIX atmospheres. Solar intensity distribution plotted against the limb angle μ (*left*) and plotted against the radial coordinate r (*right*).

At two wavelengths, namely 3740.86 Å and 4019.70 Å, the limb intensities of the PHOENIX atmosphere actually show higher values as those measured at the Sun. In the case of the limb profile at 4019.70 Å, the disk-integrated flux of the PHOENIX model is only 0.23 % *higher*, but at 3740.86 Å this value is larger than 4.5 %. The deviation from the measurement is clearly pronounced at this wavelength, as I show in the right panel of Fig. 5.6. In this case this wavelength point lies between two solar emission lines in the PHOENIX spectrum contributing significantly to the intensity at $\mu < 0.6$. Since the resolution of this model spectrum is not high enough, the requested wavelength point for comparison is not included and thus both adjacent points were taken for determining the limb profile causing both emission lines to contribute to it. In the second case the problem is very similar, but this time only one emission line is included in the creation of this limb profile. Additionally, two continuum points are included in my used interval of 0.3 Å, leading to a weaker deviation from the measurement. For a complete list of all deviations in disk-integrated flux at the used 30 wavelengths, given in percent, see Table A.7.

Figure 5.7 shows the comparison between solar LD and the intensity distribution calculated using quadratic and nonlinear LD laws together with LDCs taken from Claret & Bloemen (2011). The quadratic solution lies clearly below the measured solar distribution, even more distinctly than the previously shown PHOENIX distribution. Therefore, the quadratic LDCs from Claret & Bloemen (2011) lead to limb profiles which significantly underestimate the solar intensity distribution. The relative deviance in disk-integrated flux, again determined using Eq. 5.5 for both intensity profiles, amounts to 2.07 %. The intensity profile created using a nonlinear LD law actually lies slightly below the profile created with a quadratic law, as visible in the right panel of Fig. 5.7, which leads to an even stronger aberrance from the measurement (2.30 %). It is also worth mentioning that the quadratic LDCs taken from Claret et al. (2013), which are determined by fitting quasi-spherical PHOENIX atmospheres, also lead to intensity distributions showing a limb darkening which is too strong. In the presented

example of the Johnson-V filter band, these distributions show a slightly weaker deviation from the solar measurement. Expressed in disk integrated flux they predict about 1.7 % less than the measurements. For a complete list of differences in disk integrated flux in several filter bands, see Table A.8.

5.1.3 Rescaling of the μ-axis

Looking at the eye-catching gap of the limb intensities predicted by the PHOENIX atmosphere the question arises where the real limb of the stellar disk is located. Indeed, I showed that this gap is small compared to the whole stellar radius, but it should have an influence on transit start and end times if observed in front of such an atmosphere. To stay in my chosen example of the Johnson-V filter band, the found gap of $\Delta r \approx 1.5 \cdot 10^{-3}\ R_S$ corresponds to an 11 s shorter transit duration if a total duration of two hours and an impact parameter of zero is assumed. This difference in transit duration is clearly detectable with the accuracy of todays measurements and would have its major influence on the semimajor axis of the planetary system. Obviously, the solar and stellar radii depend on the wavelength range in which they are observed (see, e.g., Fig. 5.4). Due to the fact that the μ-dependent PHOENIX spectra are calculated for a wide wavelength range, we can actually inspect the variation in the *visual* stellar radius as a function of the wavelength.

To account for the smaller visual stellar radius in the determination of the limb darkening from a model atmosphere with spherical geometry, my idea was to rescale the μ-axis by setting $\mu = 0.0$ at the "real" stellar limb as seen by an observer using one specific photometric passband. In my definition this "real" limb is located at the minimum $\mu_{i,j}$ for which the intensity $I(\mu_{i,j}, \lambda_j)$ has a specific non-zero value. This minimum $\mu_{i,j}$ is found at a wavelength λ_j which is included in the chosen passband and then called $\mu_{\min}$. In practice I had to first normalize every single limb profile available in the specific wavelength range by its own disk center intensity. Then I listed all μ-values found at a normalized intensity value of 1/e for each wavelength λ_j. Out of these I determined the smallest μ-value which corresponds to the biggest visual stellar radius. Figure 5.8 illustrates this approach. I used the found μ-value to rescale the whole μ-axis according to

$$\mu_{\text{new}} = \frac{\mu - \mu_{\min}}{1 - \mu_{\min}}\,. \tag{5.6}$$

This leads to a slightly stretched PHOENIX intensity distribution with $(1 - \mu_{\min})^{-1} = 1.021$ as the stretching factor for the V-band. The result, again in Johnson-V filter band, is shown in Fig. 5.9. Now, the gap is significantly smaller as seen before in Fig. 5.5 and only amounts to $\Delta r \approx 3.1 \cdot 10^{-4}\ R_S$ ($\Delta\mu \approx 0.025$), which corresponds to 0.3″ as seen from Earth. The duration of a transit in front of this rescaled model distribution would last only 2 s shorter compared to the measured distribution, with the same conditions as assumed above. As a side effect, the stretching also reduces the gradient of the limb profile, which leads to a slightly weaker LD and therefore the PHOENIX limb profile is now in good agreement with the measurements of

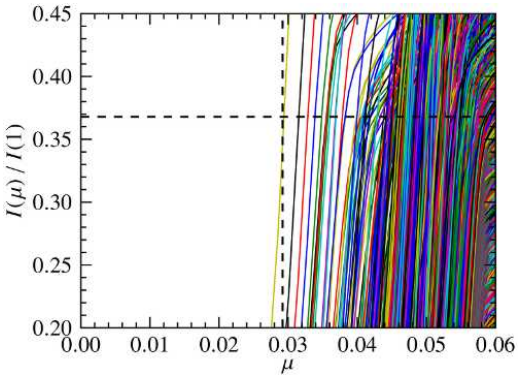

Figure 5.8: Illustration of the determination of $\mu_{\min}$. *Dashed* lines indicate the selection criterion for $\mu_{\min}$, found for a Johnson-V filter, at the intensity $I(\mu)/I(1) = 1/e$.

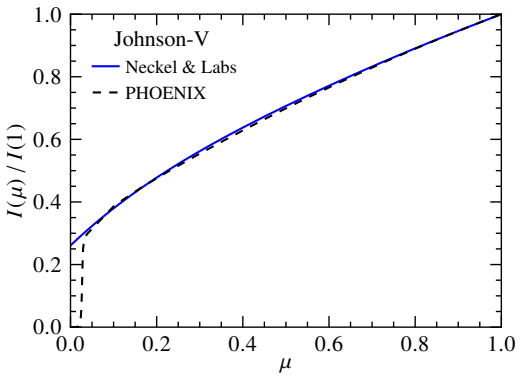

Figure 5.9: Comparison of the LD measured by Neckel & Labs (1994) and the rescaled PHOENIX model prediction using Eq. 5.6.

Neckel & Labs (1994) and the major intensity difference at intermediate limb angles seen in Fig. 5.5 is gone. In this way I reduced the difference in disk-integrated flux to 0.2 %, which is now smaller by a factor of seven. I can reproduce this result using Johnson-UBRI filter functions. In all of them the PHOENIX distribution lies below those computed from Neckel & Labs (1994) as it is the case in almost every single wavelength measured by the authors. A rescaling of the μ-axis of the PHOENIX predictions reduces this discrepancy in disk-integrated flux for all passbands except for the *Kepler* instrumental response function. In this case the unscaled PHOENIX distribution lies only marginally below the computed one (0.1 %), thus a rescaling even leads to a slightly overestimated disk-integrated flux (0.6 %). The reason for the small deviation without having rescaled the μ-axis is that the *Kepler* response function is really broad and includes wavelength regions strongly suppressed in the Johnson filters, which show weaker limb darkening like 6800 – 7400 Å. I will discuss the influence of the rescaling on the quadratic LDCs in the next subsection in more detail. The limb profiles determined for each of the mentioned passbands can be found in Fig. B.19. A detailed list of differences in disk-integrated flux is given in Table A.8.

I have to mention that the normalized intensity value of 1/e, at which I search for the biggest stellar radius, is in principle arbitrarily chosen. Although this value produces reasonable results, smaller or bigger values would also be possible. Furthermore, this value is not applicable to single wavelength points or narrow wavelength ranges, especially at shorter wavelengths (ultra violet or shorter). At these wavelengths the limb darkening is more pronounced and the normalized flux value of 1/e is reached far beyond this gap (see Fig. 5.6, left panel), leading to rather overestimated values of $\mu_{\min}$. In broader wavelength ranges like in my used passbands, this is no problem, because some wavelength points always show significantly weaker limb darkening (Fig. 5.6, right panel) where enough intensity is given at this gap to determine the "real" limb of the star using 1/e as an intensity threshold.

5.1.4 Determining quadratic LDCs from the limb profiles

We have seen in the previous subsections that the predicted limb darkening, as given by coefficients taken from Claret & Bloemen (2011) or Claret et al. (2013), underpredicts the intensity profile when compared to the measurements of Neckel & Labs (1994). Also the used PHOENIX atmosphere tends to predict a stronger limb darkening than expected from the measurements on the Sun. In other words, the predicted limb darkening in the studied cases is too strong to follow the solar intensity distribution.

I have shown that a rescaling of the μ-axis leads to a weaker limb darkening in all considered passbands. In general, this should manifest in lower values of the quadratic LDCs when determined from the model atmosphere, at least of u_1 (see Eq. 1.10). To get some specific values, I follow in principle the approach of Claret, performing a simple least squares fit to the model distributions. The remarkable intensity drop off near the limb of the spherical PHOENIX models now plays a crucial role and has certainly an influence on the fitted LDCs. The major question is how to account for this gap in the fit approach. As usual, there is more than one possible solution for this problem. Presumably, the simplest solution introduced by Claret & Hauschildt (2003), is the concept of "quasi"-spherical models. For the fit all points in the drop-off region are neglected, by defining a cut-off value $\mu \geq 0.1$ regardless of the used photometric passbands (Claret et al., 2012). This seems to me rather unphysical and I will now propose a different but also simple method, without neglecting the intensity points in the drop-off region.

First of all, I linearly interpolate between the intensity values of the model distribution. Since the PHOENIX model holds the major part of the μ-values in the drop-off region (58 out of 73), the linear interpolation provides an accurate description of this massively curved region. As the second and most important step I evaluate the model intensities at $\mu = \cos[\sin^{-1}(r)]$ (Eq. 1.6), with r being an evenly spaced array from 0 to 1. In this way I achieve a μ-axis, which is not evenly spaced, but rather holds an increasing density of points with increasing μ-values. In contrast, the limb region is now covered by much less points than before. A simple fit to this distribution is now weighted toward higher μ-values and the drop-off region at the limb has only a weak influence. This weighting at larger μ-values can be interpreted as sampling this distribution in r-space, like a transiting planet would do. I prefer this approach, because it is more closely related to the actual problem of measuring LDCs using transit modeling.

I performed the fit of the PHOENIX model distribution as introduced here and additionally using the conventional method with an evenly spaced μ-axis. I present the resulting quadratic LDCs in Table 5.1. In the case of the PHOENIX model, the two ways of fitting the distribution lead to different LDCs and to a marginally weaker limb darkening when an evenly spaced r-axis is used, although u_1 shows a slight increase. The curvature of a profile using these LDCs has decreased due to a lower value of u_2 compared to a fit using an evenly spaced μ-axis. These differences have only a weak influence on transit shapes, but for my further investigations I will only rely on the more elaborate way of fitting the intensity profiles using an evenly spaced r-axis transformed to μ, as introduced above.

Table 5.1: Comparison of quadratic LDCs in Johnson-V passband.

Model	u_1	u_2	u_{1w}	u_{2w}
Claret11	0.5624	0.1627		
Claret13 qs	0.5426	0.1825		
PHOENIX	0.5237	0.2012	0.5345	0.1791
PHOENIX μ_{rescaled}	0.5114	0.1820	0.5187	0.1678

Notes: Values in the first two columns are gathered from Claret & Bloemen (2011) (Claret11) and Claret et al. (2013) (Claret qs) quasi-spherical models or fitted to the used PHOENIX model distribution. In the latter case the last two columns hold fit values (u_{1w}, u_{2w}) using the described weighting of the μ-axis. See text for more details.

The rescaling of the μ-axis as outlined in Section 5.1.3 leads to a weaker limb darkening, finally confirmed by smaller LDCs. The rescaled PHOENIX distribution holds ca. 1 % more disk-integrated flux than the unscaled model. Certainly one could argue that my rescaling of the μ-axis is also not physically motivated, but precisely this rescaling leads to a good agreement with limb profiles determined using measurements of the Sun. A limb-darkening law, which is also capable of fitting the drop-off region like the exponential law (Claret & Hauschildt, 2003, Eq. 8) does not provide this advantage. Moreover, since this law is especially designed to keep the gap at the limb, transit modeling with this would lead to incorrect transit durations mostly correlated to the semimajor axis of the planet's orbit as already pointed out in the previous subsection.

The limb darkening of the Sun as seen in the *Kepler* passband is of special interest in my work. A comparison of my measured limb darkening using *Kepler* objects with intensity profiles or quadratic LDCs as determined from measurements of the Sun or from a model atmosphere would be reasonable. Therefore, I first have to determine the quadratic LDCs of a measured "mean" limb darkening of a sample of my target stars, with an effective temperature close to that of the Sun. For that purpose I chose a narrow temperature interval of 5750 K to 5850 K. In this temperature region I found 5 objects[1] in my high signal-to-noise target sample. The LDCs corresponding to the "mean" limb darkening are then found by simply calculating the mean of the corresponding LDCs. I verified that this leads to the same result as if I would first combine the individual limb profiles of these objects, and then fitting the quadratic limb-darkening law to this resulting distribution. The fitted mean LDCs for this tight solar-like temperature range are $\bar{u}_1 = 0.46 \pm 0.02$ and $\bar{u}_2 = 0.13 \pm 0.02$. In the same way I also fitted the limb profile deduced from the measurements of the Sun (Neckel & Labs, 1994). All resulting pairs of LDCs are summarized in Table 5.2. In principle, the limb darkening decreases in this table from left to right and also from top to bottom. In the *Kepler* passband this is not the case. Here, the quadratic fit to the calculated distribution based on Neckel & Labs' measurements holds surprisingly the strongest limb darkening. Additionally, it is also unusual that in this passband Claret11 shows the weakest limb darkening of all considered theoretical ones, closely followed

[1] KIC 7023960, Kepler-15b, Kepler-17b, KIC 12019440 and Kepler-6b

Table 5.2: Comparison of fitted quadratic LDCs in different filter bands.

Model	Johnson-V		*Kepler*		Johnson-R	
	u_1	u_2	u_1	u_2	u_1	u_2
Claret11	0.5624	0.1627	0.4729	0.1871	0.4439	0.2058
Claret13 qs	0.5426	0.1825	0.4883	0.1822	0.4526	0.1891
PHOENIX	0.5345	0.1791	0.4950	0.1723	0.4519	0.1743
PHOENIX μ_{rescaled}	0.5187	0.1678	0.4849	0.1642	0.4427	0.1658
Neckel & Labs	0.4778	0.2241	0.4709	0.2176	0.3975	0.2317
Mean LDCs $(\bar{u}_1, \bar{u}_2)$			0.46	0.13		

Notes: LDCs for Claret11 and Claret13 qs are taken from tables (see Table 5.1 for references). LDCs for the remaining models are determined in this work by fitting a quadratic LD law to the distributions, as described in text. The mean LDCs $(\bar{u}_1, \bar{u}_2)$ are calculated using measured LDCs from *Kepler* objects (Chapter 7). For a more complete listing for more photometric passbands, see Table A.9.

by the quadratic fit to the rescaled PHOENIX distribution, although it predicts the strongest limb darkening in all other passbands. The weakest limb darkening in the *Kepler* passband is given by my mean LDCs.

I will now only concentrate on the four sets of LDCs important for my work, namely Claret 11, PHOENIX μ_{rescaled}, Neckel & Labs and the mean LDCs. In Fig. 5.10 I visualize the limb profiles using these fitted coefficients and the resulting transit light curves using the `occultquad` routine (Mandel & Agol, 2002). The differences of these limb profiles are clearly visible. The quadratic description of the rescaled PHOENIX model and the Claret & Bloemen (2011) profile do not deviate much from each other in this photometric passband. Of course, these profiles lead to four different transit shapes, which is most prominent in the transit center. In the end we have to consider that these profiles only represent quadratic fits to the "real" intensity distributions. For a comparison of the underlying limb intensities, see Fig. B.19.

More important than the actual transit shapes is the influence of the quadratic LDCs determined here on the orbital and planetary parameters which I can calculate according to Section 4.3.3, if they are set as fixed parameters in transit modeling. Since this method is based on the covariance matrices of the five mentioned *Kepler* objects, the resulting changes in the parameters are related to these objects and amount to roughly -1 % of the measured radii ratio p. This result is consistent with the simulated transit profiles in Fig. 5.10, which shows that all LDCs used lead to deeper transits when compared to the one generated with the mean LDCs. This has to be compensated, e.g, by a decreasing p. The individual values depending on the used LDCs are given in Table 5.3. The parameter changes expected when $(\bar{u}_1, \bar{u}_2)$ are set as fixed coefficients should by constructionem be zero, which is the case. As also shown in Section 4.3.3 the 1σ errors in the fitted orbital parameters are often below 1 %, and in the special case of the objects chosen here, the standard error amounts to 0.3 %. This leads to the conclusion that the choice of the LDCs has a significant influence on the resulting orbital parameters and has to be considered as a systematic error in transit modeling. According to Table 5.3 my fit to the

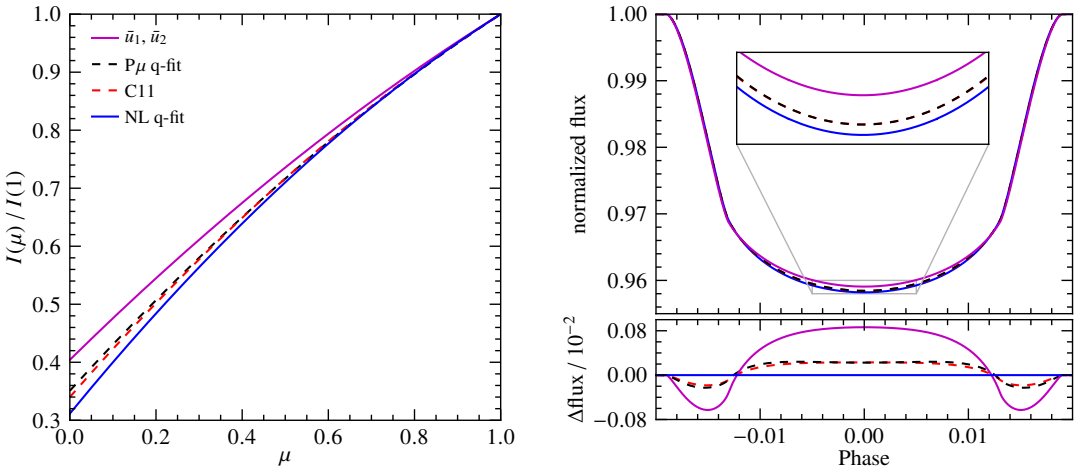

Figure 5.10: *Left*: four different limb profiles for a solar-like star observed in *Kepler* passband, produced by using the quadratic LD law. The sources of the LDCs are given as labels ($\bar{u}_1$, $\bar{u}_2$: mean LDCs of solar-like *Kepler* targets, Pμ q-fit: fit to the rescaled PHOENIX model, C11: LDCs from Claret & Bloemen (2011), NL q-fit: fit to the limb profile deduced from the measurements of Neckel & Labs (1994)). *Right*: simulated transit light curves using the aforementioned LDCs. *Bottom panel*: transit residuals in relation to NL q-fit.

rescaled PHOENIX limb profile provides LDCs leading to the smallest parameter changes if they are used in transit modeling.

We have to keep in mind that the only two cases in which the LDCs are determined by measurements are Neckel & Labs and my calculated mean LDCs. Therefore, it is even more remarkable that these results show the strongest mutual deviation when compared to the rest. This behavior in this photometric passband is in contradiction to the previous subsections where I found that the measurements of Neckel & Labs (1994) provide limb profiles, which always lie above those predicted by PHOENIX. Figure 5.10 clearly shows the opposite behavior. One possible explanation for this is that the prediction computed from the measurements by Neckel & Labs (1994) using Eq. 5.3 is not an adequate approximation in the broad *Kepler* passband. This assertion is supported by the fact that in the red wavelength regime (7000 Å to 9000 Å) only four out of thirty limb profiles are measured by the authors. Together with an increasing spacing between the chosen wavelengths points, I assume an inappropriate weighting of this wavelength range in my approach used to calculate filter-specific limb profiles from their measurements.

Table 5.3: Average relative parameter changes for solar-like *Kepler* objects.

Model	$\Delta a/a$ in %	$\Delta p/p$ in %	$\Delta i/i$ in %
Claret11	0.480	−0.784	0.599
Claret13 qs	0.616	−0.980	0.761
PHOENIX	0.624	−0.978	0.766
PHOENIX μ_{rescaled}	0.458	−0.721	0.563
Neckel & Labs	0.479	−1.134	0.774
Mean LDCs ($\bar{u}_1$, $\bar{u}_2$)	−0.001	0.002	−0.001

Notes: These mean parameter changes are re-maximizing the posterior of the selected five *Kepler* objects, if the fixed LDCs (Table 5.2) are used in transit modeling. See for more details Section 4.3.3.

5.2 Space-based measurements compared to predicted LD

In the previous section, I showed the comparison between high-quality ground based measurements of the solar limb darkening and model predictions. Since there exist also space-based observations of the Sun, e.g. carried out by the satellites SOHO[2], STEREO[3] and SDO[4], which have performed an almost continuous monitoring of the Sun in various spectral bands, it is appropriate to investigate these data concerning the solar limb darkening. Out of the mentioned spacecrafts, SDO is the newest, which is the reason why my following investigations are limited to this instrument.

5.2.1 Data acquisition and preparation

For my analysis I retrieved observations made by the *Solar Dynamics Observatory* (SDO) (Pesnell et al., 2012) found in the public data archive provided by the Joint Science Operations Center (JSOC)[5]. SDO carries different instruments like the Atmospheric Imaging Assembly (AIA). The AIA instrument (Lemen et al., 2012) produces full-disk images of the Sun in several passbands, most of them in the extreme ultraviolet, centered on iron lines. For the investigation of the disk intensity distribution comparable to the previous sections, I chose a passband located at a spectral position of the solar continuum (4500 Å). In total, I took 46 Fits-images spread over two days (19.07. and 23.07.2012). For the selection of these dates I ensured that no active regions were near the solar equator or the disk-center meridian.

The images have a resolution of 1024×1024 pixels and the Sun is always positioned in the center. To get the intensity distribution in one direction over the solar disk, we simply choose one central pixel row or column and get all pixel values as a function of the radial coordinate.

[2] http://sohowww.nascom.nasa.gov/
[3] http://stereo.gsfc.nasa.gov/
[4] http://sdo.gsfc.nasa.gov/
[5] http://jsoc2.stanford.edu/data/aia/

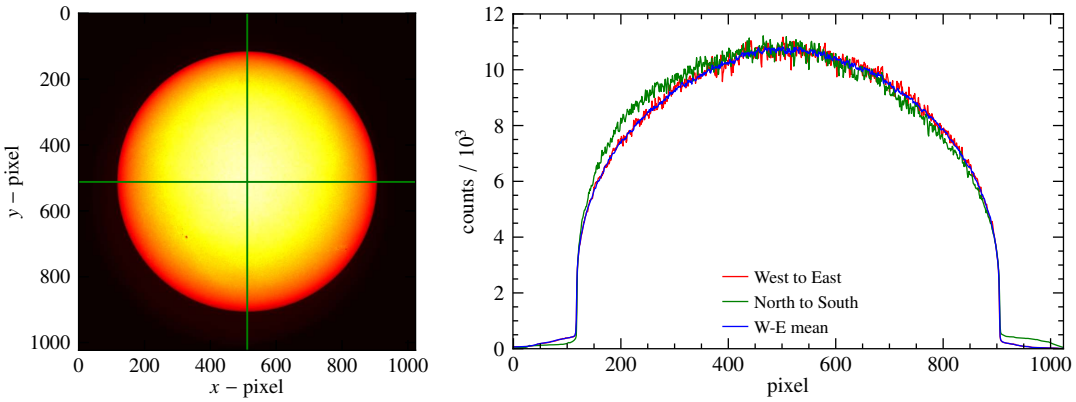

Figure 5.11: Solar limb darkening observed by SDO. *Left*: Image of the SDO AIA 4500 Å instrument (continuum, photosphere). Orientation: *top* north, *right* east. *Green* lines marking pixel rows used for the determination of the spatial brightness distribution. *Right*: Limb profiles resulting from the left image (*red*: horizontal pixel row, *green*: vertical pixel column, *blue*: mean of 21 horizontal columns).

I present the resulting limb profiles (in r-space) in Fig. 5.11 for two different directions. While on the left side of these profiles the north-to-south distribution lies considerably above the one achieved in the west-to-east direction, it lies below on the right side. This illustrates the asymmetric brightness distribution found in all images, more pronounced on the left side of this graph, visible as a clear gap between both profiles. The asymmetric brightness distribution is also visible in the left panel of Fig. 5.11. Most likely, this asymmetry is caused by instrumental or reduction effects. To reduce the scatter of the data, which is induced by solar granulation, I averaged over 21 horizontal rows around the central row. The resulting mean distribution is additionally plotted in Fig. 5.11. Beside a spatial average, I will in the following rely on a time average using the mentioned 46 individual observations.

Due to the mentioned asymmetry of the north-to-south profiles, I will take into account only the profiles which are acquired from horizontal pixel rows. Therefore, I averaged over five central rows in each of the 46 observations, to finally calculate the time average of these profiles. The reduction in scatter by using this approach can clearly be seen in Fig. 5.12. To check the symmetry, the profile of the eastern hemisphere is mirrored at disk center (pixel 513). Both profiles are almost congruent, except the regions at the edges of every image, where the west part shows more intensity, which is also visible in Fig. 5.11. Averaging these profiles does not introduce a systematic error like it would be the case for the north-to-south distribution.

To get the final limb profile we have to define a correct μ-axis, which is again – like discussed in the previous sections – a question of finding the real solar limb. This time I adopted the proposed method by Orosz & Hauschildt (2000), where the limb is found at the point where the slope of the intensity is the largest. In contrast to their Eq. 11, I determine the slope in $r-$space, because the measurements are obviously performed in this coordinate system. This

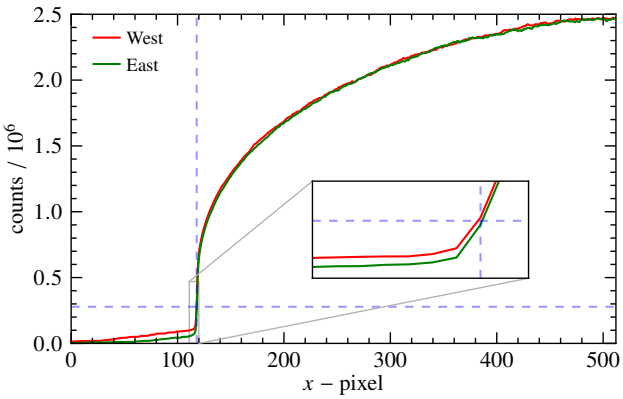

Figure 5.12: Solar disk intensity profiles of pixel rows of the western- and eastern hemisphere as measured by SDO's AIA4500 instrument. Profiles result from an average over 46 individual measurements. *Dashed lines* indicate the point with the largest slope.

leads to the expression,

$$\left.\frac{\mathrm{d}I}{\mathrm{d}r}\right|_i \approx \frac{I(i) - I(i-1)}{r(i) - r(i-1)}, \text{ with } i \in \mathbb{N}^*. \tag{5.7}$$

With the assumption $\Delta r = \text{const.}$, which is the case if the instrument introduces no aberration, the denominator is always constant and can in principle be neglected for the determination of the largest slope. I found pixel number 118 to be the point where to define the limb of the Sun ($\mu = 0$). The μ-axis is then defined by Eq. 1.6, where r is evenly spaced with $r = 0$ at pixel 512, and $r = 1$ at pixel 118.

5.2.2 Comparison to other LD descriptions

After the combination of disk-intensity measurements and the determination of the solar limb in the previous subsection, I am now able to compare the resulting limb darkening to some other limb-darkening laws, predictions, and measurements. For that purpose I chose the PHOENIX 3D model intensities using my "μ-rescaling" (Section 5.1.3) and the quadratic limb-darkening law together with coefficients taken from Claret & Bloemen (2011) in Strömgren-b filter. For the PHOENIX intensities I used a 10 Å wide rectangular filter function. Since the 4500 Å channel is centered on a continuum part of the solar spectrum, the resulting distribution should be also comparable to those measured by Neckel & Labs (1994) near this wavelength. Therefore, I opted for their coefficients corresponding to their measurement at 4451.25 Å and used Eq. 5.1 to create the corresponding limb profile. All resulting limb profiles are plotted together in Fig. 5.13.

The SDO profile lies significantly below all other intensity distributions and shows a positive curvature in the region where the divergence is strongest. Only in areas near the limb - at $\mu = 0.1$ - this profile almost agrees with the quadratic limb darkening and the one measured by Neckel & Labs. The difference to the limb darkening obtained from the PHOENIX model atmosphere, visible for almost the whole limb-angle range, is not related to the chosen rectangular filter function. I proved that it makes no difference to the PHOENIX profile, if a

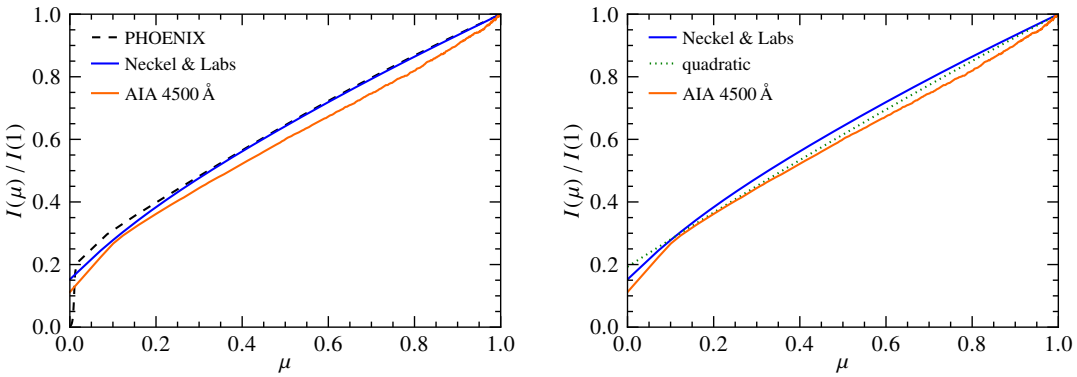

Figure 5.13: Comparison of measured solar limb darkening determined from Neckel & Labs (1994) (*blue*) and SDO (*orange*). The quadratic distribution is generated using LDCs from Claret & Bloemen (2011) in Strömgren-b filter (*green*), and rescaled PHOENIX intensities (*black*) are determined in a rectangular filter function.

Strömgren-b transmission curve is used, like for the quadratic limb-darkening law. To quantify the differences, I used again Eq. 5.5 to determine the disk-integrated fluxes of all profiles and additionally I determined quadratic LDCs by a least-squares fit (Table 5.4). The values

Table 5.4: Fitted quadratic LDCs and relative differences in disk-integrated flux.

Model	u_1	u_2	ΔS_{SDO} / %
Claret11	0.7321	0.0749	−2.67
Neckel & Labs	0.6497	0.1365	−4.72
PHOENIX μ_{rescaled}	0.6304	0.1564	−5.28
SDO AIA 4500 Å	0.9018	−0.1638	0.00

Notes: I define $\Delta S_{\mathrm{SDO}} = (S_{\mathrm{SDO}}/S_{\mathrm{model}}) - 1$. The disk-integrated fluxes of the given distributions are denoted as S_{model}. The LDCs are taken from Claret & Bloemen (2011) in the case of "Claret11" (Strömgren-b filter), and determined by a fit in all other cases. A negative sign in the flux differences indicates a percentage below the corresponding distribution.

of the relative flux differences confirm what we have seen in Fig. 5.13. The limb intensities determined using SDO observations underestimate the disk-integrated flux of the Sun in this specific spectral region by almost 5 %, when compared to the measurements of Neckel & Labs. The difference to the rescaled PHOENIX limb intensities is even larger. Therefore, it cannot be expected that the fitted limb-darkening coefficients agree. It is also remarkable that the SDO profile shows a positive curvature for a wide range of limb angles and the others do not. Thus, this profile is the only one showing a u_2 value which is clearly negative. I have to mention that these coefficients lead to a profile which is a good fit for values in the range $\mu = 0.2 - 1.0$, but of course a bad fit for the region close to the limb ($\mu = 0.0 - 0.2$). On the one hand, this is due to the fact that there are only nine data points in this region. So the fit is dominated by intensity values near disk center. On the other hand, a quadratic law with a negative u_2

has, according to Eq. 1.8, always a positive curvature and is not able to describe the predicted limb darkening given by the used models, since they all show a negative curvature. The best "agreement" between a model and the SDO limb darkening can be seen for the quadratic limb darkening using Claret coefficients for a Strömgren-b filter, but in the end I conclude that none of the used models are really compatible with the found SDO profile.

The discrepancy of the SDO limb profiles and the other descriptions can probably be explained by systematic errors, e.g. induced by the instrument, or the data reduction. There are two arguments supporting this assumption: First, the asymmetry found for the north-to-south profile is unlikely for the Sun; second, the pixel intensities at the edges of the images, clearly visible in Fig. 5.12 (pixel 0-118), are significantly different for each side, showing a step-like structure on closer inspection, and are constant in the time frame used. Without any further knowledge about the instrument and the reduction process these issues remain unresolved. Furthermore, if only the north hemisphere would be taken into account, the resulting limb profile would bear more intensity at intermediate limb angles, because in Fig. 5.11 the intensities lie clearly above the values from the west hemisphere. Due to the asymmetry a more detailed investigation is omitted. Although the obtained limb profile is not compatible with, e.g., the one measured by Neckel & Labs (1994), I showed that it is actually possible to get low noise and low scatter disk intensity values of the Sun using space-based observations.

6 A new Numerical Transit Algorithm

Modeling of extrasolar planet transit light curves can be done by an analytical approach, if the stellar disk is assumed as a uniform source without any limb darkening. The simple idea behind it, is to integrate the fraction of overlapping circles as a function of time. In the case of a limb-darkened source, the problem leads to elliptic integrals for which no analytical solution exists. Therefore, these integrals have to be approximated numerically, as it is the case in the routines of Mandel & Agol (2002) (see references in their routines). This semi-analytical solution is fast and accurate enough to use it in fitting and minimization approaches within this transit model.

With a permanently increasing accuracy of the photometry, it becomes possible to study system properties, such as the oblateness of planets or star spots, which were hidden in the noise before. Such circumstances make the required model approach more complicated and in the case of elliptical planets or stars even a transit in front of a non-limb-darkened source has no analytical solution anymore. Theses problems ask for numerical methods to compute and model transit light curves.

In the field of modeling extrasolar planet transit light curves there exist some works introducing numerical methods. For example Silva (2003) used an image of the Sun to simulate planetary transits in front of star spots. Tusnski & Valio (2011) have already simulated the effects of planetary rings and exomoons on transit light curves and Huber et al. (2010) presented planetary eclipse maps and the evolution of star spots by modeling space-based photometry. Nevertheless, there exists no work containing numerical analyses with different limb-darkening laws comparing them to conventional Mandel & Agol models, to the Sun, or to model atmospheres, especially for different impact parameters. Such an investigation based on an efficient fast Fourier transform (FFT) method has not been carried out yet.

I will first give an introduction of the theoretical and numerical methods used. Then I explain the process of creating the numerical counter parts of the star and the planet together with the transformation of the orbital parameters into this numerical algorithm. After that I will validate the precision of my algorithm by comparing the resulting light curves to those calculated using the `occultquad` routine (Mandel & Agol, 2002). Finally, to demonstrate the capabilities of my code, I select some observations of the Sun to generate transit light curves.

6.1 The numerical approach

The need for a numerical transit algorithm is mostly motivated by the idea to determine how a transit with "real" limb darkening is different from one generated with theoretical coefficients. The only question to be answered is, what actually is the real limb darkening. The great advantage of numerical methods is that this limb-darkening information can be drawn directly from a model atmosphere without the use of any coefficients or approximations formally known as limb-darkening "laws".

Limb intensities of model atmospheres have already been used directly in the synthesis of light curves of eclipsing binaries (see Orosz & Hauschildt, 2000). Nevertheless, the direct use of these limb intensities in the process of planetary transit light curve synthesis is new. Such a numerical algorithm should be efficient in the sense of short computation times. This is necessary if the algorithm should be used in a fitting approach where the model has to be evaluated many times during the minimization process. In the following subsections I will introduce a fast and accurate way to synthesize transit light curves numerically based on fast Fourier transforms.

6.1.1 Image convolutions and fast Fourier transforms

The convolution of two functions $f(x)$ and $g(x)$ can be interpreted as a weighting of all points in f with $g(x-\xi)$. As formally known, the convolution is defined as

$$(f * g)(x) = \int_{-\infty}^{+\infty} f(\xi) \cdot g(x-\xi)\,\mathrm{d}\xi = h(x) \tag{6.1}$$

(e.g., Butz, 2012). Because of the changing shift x in the argument of g, we say that the function g is slided over f. The convolution yields a new function $h(x)$ which describes the value of the integral evaluated at the point x. Therefore, we can also interpret the function $h(x)$ as the amount of x-dependent overlap of f and g.

As an often used example in the literature, we find the convolution of two identical square functions. The resulting function $h(x)$ is in this case a simple triangle function which describes the x-dependent fraction of the overlap between these functions as already mentioned above. To go one step further, I created two square signals with different lengths and unlike signs, according to

$$f(x) = \begin{cases} 1 & \text{if } 141 \le x \le 230, \\ 0 & \text{all other cases,} \end{cases} \quad \text{and} \quad g(x) = \begin{cases} -1 & \text{if } 1 \le x \le 45, \\ 0 & \text{all other cases.} \end{cases} \tag{6.2}$$

The square signal defined by function $f(x)$ is twice as long as the one defined by $g(x)$, namely 90 elements in contrast to 45 for $g(x)$. In the case of numerical simulations or measured data, such continuous functions are often not defined. They are replaced by sampled data sets

(vectors $\boldsymbol{f}$ and $\boldsymbol{g}$) with a finite number of elements M. Hence, the continuous convolution of Eq. 6.1 is now given by the summation of discrete products written as

$$(f * g)_x = \sum_{\xi=0}^{M-1} f_\xi \cdot g_{x-\xi} \,. \tag{6.3}$$

This discrete convolution of the square signals in $\boldsymbol{f}$ and $\boldsymbol{g}$ leads to a negative trapezoid with a depth of −45, which is the maximum amount of overlap area of both signals. The negative sign is induced by the negative data values in $\boldsymbol{g}$. This value can easily be verified by using Eq. 6.3, inserting some suitable values for x and ξ where neither $\boldsymbol{f}$ nor $\boldsymbol{g}$ are zero. For example, this is fulfilled for $x = 141 + 45$ and $141 \leq \xi \leq 185$ (cf. Eq. 6.2), and the discrete convolution yields

$$(f * g)_{186} = \sum_{\xi=141}^{185} f_\xi \cdot g_{186-\xi} = 45\,[1 \cdot (-1)] \,. \tag{6.4}$$

In my example this value has no unit and would depend on the number of data points sampled in the square signals. To get a more descriptive value of the depth we can apply a reasonable normalization. Thus, I chose the area of the square signal sampled in $\boldsymbol{f}$ (with $\Delta x = 1\,\mathrm{px}$) which then translates Eq. 6.3 into

$$h_x = \frac{1}{z} \sum_{\xi=0}^{M-1} f_\xi \cdot g_{x-\xi} \,, \quad \text{with} \quad z = \sum_{x=0}^{M-1} f_x \,, \tag{6.5}$$

and gives −0.5 as the result of the convolution for $x = 186$ like chosen above. The convolution of my assumed data sets now leads to a negative trapezoid whose depth is normalized, and its absolute value can be interpreted as the maximum fraction of signal $\boldsymbol{f}$ covered by signal $\boldsymbol{g}$. I created this example, because a negative trapezoid is rather similar to a transit light curve. Sure, the occulted stellar flux cannot lead to negative values in the light curve, but this should not be a problem. I can find a different normalization which fits this physical boundary condition. For my goal of synthesizing planetary transits, I claim the resulting data set to be one where no occultation is taking place and the depth should be related to the total amount of light blocked. This is achieved by adding 1 to Eq. 6.5 and we obtain

$$h_x = 1 + \frac{1}{z} \sum_{\xi=0}^{M-1} f_\xi \cdot g_{x-\xi} \,. \tag{6.6}$$

In Fig. 6.1 I illustrate both test samples used and the normalized result. The square signals can now be interpreted as slices of the occulted star and the eclipsing planet. The widths of these slices can be attributed to one of the spacial dimensions of the objects. If these slices are the disk-center slices, then the widths are equal to the diameters. In my example the height of the source signal $\boldsymbol{f}$ is one at every point on the hypothetical disk slice, which translates into a uniform source without limb darkening. The summation over all f_x is in any case the “slice-integrated” flux, which is partially blocked by the shutter signal. As illustrated in

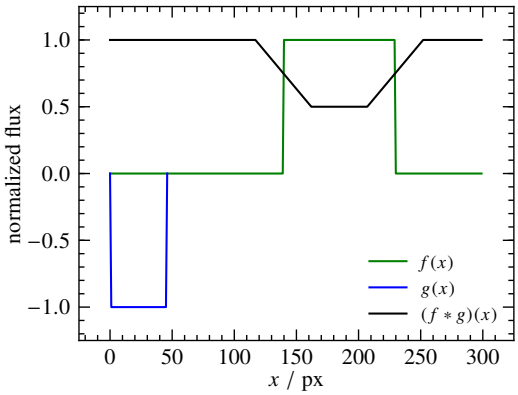

Figure 6.1: Example of the convolution of two square signals. The graphs can be interpreted as follows: the *green* curve represents the "source signal", the *blue* one is the "shutter" and the *black* one is the normalized result of the convolution following Eq. 6.6.

Fig. 6.1, the result of the convolution using Eq. 6.6 is a trapezoid with a depth of exactly 50 %. Under the given conditions, this is the anticipated result, since a hypothetical planet which has half the area of the star should also block half of the integrated flux in "transit center".

Although the presented example is simple, there are only a few steps missing to convert the trapezoid into a real transit light curve. One of them is the introduction of a limb-darkened source. The limb-darkening information can here easily be applied to the source signal $\boldsymbol{f}$ which can be done by *any* analytical function or data set. Another problem is the lack of geometric information of the bodies like their sizes and shapes because up to now my example has obviously only one spatial dimension. The expansion of the example into two dimensions requires the discrete convolution to be defined in two dimensions. As given in the literature (e.g., Kim & Casper, 2013) the expansion is performed by introducing an additional index. The two-dimensional discrete convolution is then written as

$$(S * P)_{x,y} = \sum_{\phi=0}^{N-1} \sum_{\xi=0}^{M-1} S_{\xi,\phi} \cdot P_{x-\xi,y-\phi} \,, \tag{6.7}$$

where the vectors $\boldsymbol{f}$ and $\boldsymbol{g}$ are now given as images (matrices), where in my case $\boldsymbol{S}$ maps the surface brightness distribution of the eclipsed star (Fig. 6.2) and $\boldsymbol{P}$ represents the planetary disk. As in the one-dimensional case, we can now imagine that one image is shifted pixel by pixel over the other. The result of this convolution is then also an image. However, for the application of creating planetary transits, we expect only a one-dimensional result namely, a light curve. Because we have the additional information that the planet passes along a well-defined path in front of the stellar disk, defined by the system impact parameter, it should be possible to simplify this equation. In fact it would make sense to limit one sum in Eq. 6.7 to the rows (or columns) which are occulted during transit, and additionally fix y to the central row of the planet's path. To end up with a normalized transit light curve, I apply a similar normalization than given in Eq. 6.6

$$t_x = 1 + \frac{1}{z} \sum_{\phi=A}^{B} \sum_{\xi=0}^{M-1} S_{\xi,\phi} \cdot P_{x-\xi,y-\phi} \,, \quad \text{with} \quad z = \sum_{x=0}^{N-1} \sum_{y=0}^{M-1} S_{x,y} \,. \tag{6.8}$$

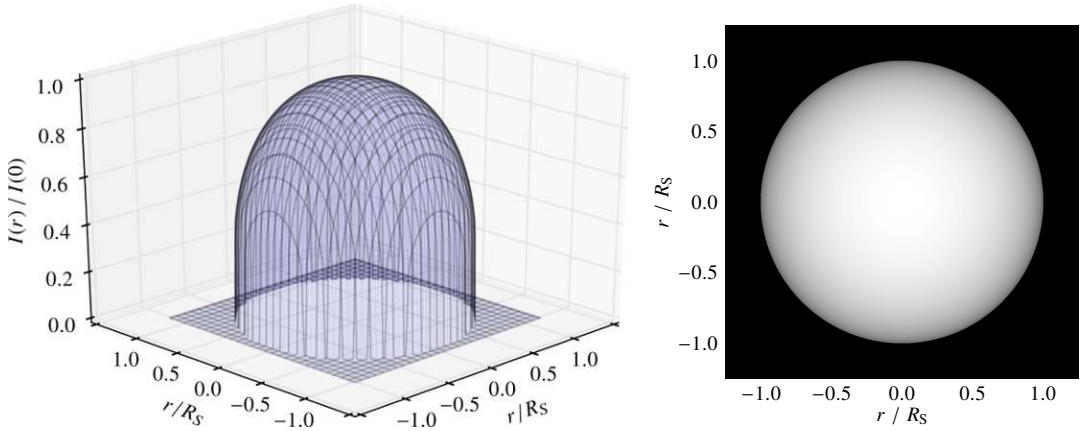

Figure 6.2: Illustration of the 2D matrix $\boldsymbol{S}$, showing a simulation of a limb-darkened star. For the limb darkening I used Eq. 5.1 ($P_5(\mu)$), together with coefficients determined for the Johnson-V filter band (Table A.10). *Left*: 3D projection of the disk intensity distribution. One row (or column) is similar to $f(x)$ in Fig. 6.1, but now with limb darkening. *Right*: image of the generated star.

A and B depend on the choice of y and the diameter of the planet, and z is proportional to the disk-integrated flux. Now the result would be only one-dimensional and contains a transit light curve in front of a limb-darkened source. Nevertheless, each row or column in the image resulting from Eq. 6.7 actually represents an individual transit light curve, namely for all possible impact parameters! Only the proper normalization is missing. In addition to all possible impact parameters, it delivers also all possible directions over the stellar disk, such as from north to south or east to west (see Fig. 6.3). This is pretty neat in the case of non-rotational symmetric stellar disk intensities or arbitrary spot distributions, but it is more efficient to limit the computation to one impact parameter as in Eq. 6.8.

So far I showed that it is possible to generate numerical transit light curves via a convolution, but until now I did not comment on the accuracy. However, it is obvious that the accuracy of this method is related to the precision of the input images and therefore depending on their resolutions. To get "enough" precision it is reasonable to aim at several 10^6 or 10^7 pixels; I will discuss the accuracy's dependence on the resolution later on in Section 6.2. The straight forward summations of the pixel-by-pixel products in Eq. 6.8 become now computationally intensive. A further increased resolution would lead to even longer computation times and this asks for an improvement of this method. As proven in several books about functional analysis (e.g., Butz, 2012), the convolution can be reduced to the calculations of simple products by transforming both functions or data sets into the Fourier-space. The relation

$$t_x = (f * g)_x \leftrightarrow \mathcal{H}_j = \mathcal{F}_j \cdot \mathcal{G}_j \,, \tag{6.9}$$

is called *convolution theorem*, where $\mathcal{F}$ and $\mathcal{G}$ are the Fourier transforms of $\boldsymbol{f}$ and $\boldsymbol{g}$. For sampled data the one-dimensional discrete Fourier transform (DFT) and its inverse (iDFT) are

given by

$$\mathcal{F}_j = \frac{1}{N}\sum_{x=0}^{N-1} f_x \, \mathrm{e}^{-2\pi \mathrm{i} x j/N} \;\leftrightarrow\; f_x = \sum_{j=0}^{N-1} \mathcal{F}_j \, \mathrm{e}^{2\pi \mathrm{i} x j/N}. \tag{6.10}$$

The two-dimensional expansion is again achieved by adding a set of indices for the additional direction, which introduces an extra summation to be performed and is written as

$$\mathcal{F}_{u,v} = \frac{1}{MN}\sum_{x=0}^{M-1}\sum_{y=0}^{N-1} S_{x,y} \, \mathrm{e}^{-2\pi \mathrm{i}\left(\frac{ux}{M}+\frac{vy}{N}\right)} \;\leftrightarrow\; S_{x,y} = \sum_{u=0}^{M-1}\sum_{v=0}^{N-1} \mathcal{F}_{u,v} \, \mathrm{e}^{2\pi \mathrm{i}\left(\frac{ux}{M}+\frac{vy}{N}\right)}. \tag{6.11}$$

In comparison to Eq. 6.7 it seems that the Fourier transform is not a great step towards an improvement in the performance of the convolution, because we have now to calculate $3N^4$ sums and products instead of only N^4 (for $M = N$). This includes the DFT of $\boldsymbol{S}$ and $\boldsymbol{P}$, and the inverse transformation of $\mathcal{H}_{u,v}$ back to the spatial domain. To bring the Fourier transform in a form which is computationally efficient, it is now time to introduce the concept of the *fast Fourier transform* (FFT). There exist some different implementations of it, but the most commonly used is based on the work made by Cooley & Tukey (1965). The main idea is to apply a signal decomposition, which splits the data into two halves, namely into data belonging to the even and odd indices, respectively. This is repeated as often as the data set can be divided by two. Obviously, this signal decomposition requires the number of sampled data points to be $N = 2^\gamma$, with $\gamma = \log_2 N$ to be an integer, which is the number of steps needed for the decomposition. For each step of the decomposition there are $N/2$ so called butterfly computations with two summations each. The total number of computations relevant for the computation time is proportional to $N \log_2 N$. Because the further details of this algorithm are rather complex by itself and not important for my work, I would like to refer to, e.g., Brigham (1974) and Smith (1997) who describe the used FFT algorithm in great detail. However, I showed that the computation time of the FFT is proportional to $N \log_2 N$, or in my two-dimensional case proportional to $N^2 \log_2 N^2$. For the example of the image convolution shown in Fig. 6.3 the overall computation time is approximately proportional to $3(N^2 \log_2 N^2)$, neglecting the calculation of the products $\mathcal{F}_{u,v} \cdot \mathcal{G}_{u,v}$. In contrast to Eq. 6.7 with N^4 additions, the FFT convolution requires a factor of about 17 000 less computations, if N is set to 1000. This makes the FFT a highly efficient tool to calculate the convolution of large data sets or images.

I introduced above that the convolution of two images, namely of a star and a planet, can produce transit light curves. The possibilities of such a numerical transit algorithm are diverse and now only a question of the underlying images, and not of equations anymore. For the shapes of some transiting objects, such as asteroids or comets, no analytical descriptions are available. Therefore, numerical algorithms are predestinated to handle arbitrary shapes of the occulting objects. By utilizing the fast Fourier transform, this convolution becomes a highly efficient way of synthesizing such transit light curves. In the next subsection I will comment on the implementation in detail, e.g., how the conversion of the common transit parameters is performed as well as about some further optimizations.

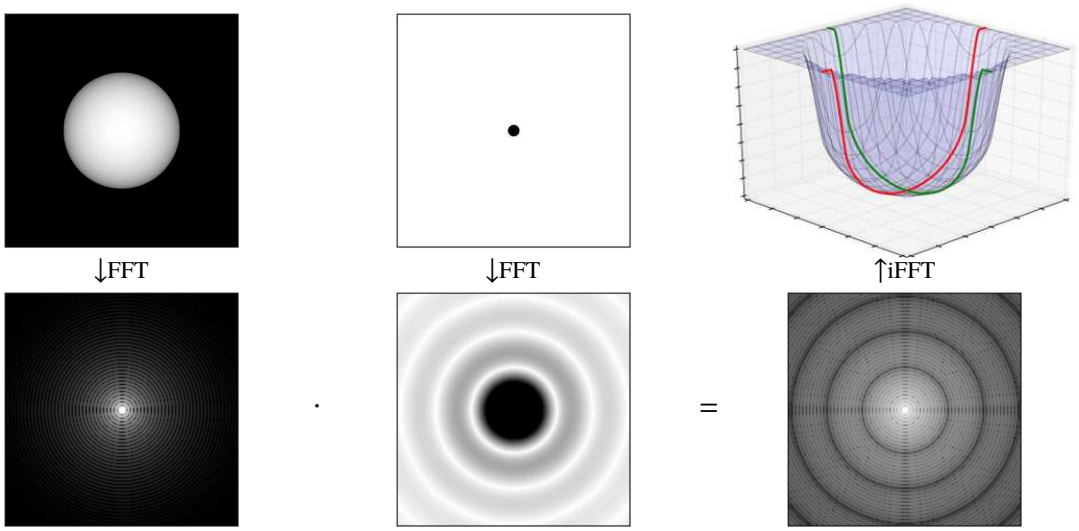

Figure 6.3: Illustration of creating numerical transits by image convolution. *Top panels*: Input images of the star and the planet (*left* and *middle* panel), and the resulting transit image shown in 3D projection (*right*). Every line in the right image represents a transit light curve for different directions over the star and different impact parameters. *Bottom panels*: Corresponding amplitudes ($\sqrt{a^2 + \mathrm{i}b^2}$) in the frequency domain after performing a fast Fourier transform of the top panels. The spectra are centered and in logarithmic scale.

6.1.2 Creating stars, planets, and numerical transits

In the previous subsection I introduced the principles of a technique to numerically generate transit light curves. I showed that a convolution of a star and planet image delivers an image which holds transit light curves for all possible inclinations and directions over the stellar disk (Fig. 6.3, upper right panel). The whole process can be divided into a few steps: creating star and planet images, defining a stellar stripe as transit path for a given impact parameter, convolution, normalizing, and creation of a proper time axis. I will now walk through these steps to describe some important details of my algorithm.

The most fundamental part of the algorithm is to provide input images, which are representing the stellar intensity distribution and the planet as an occulting mask. In principle we can do this in two different ways, namely creating these images on our own or preparing real observations for input. For the second option only the image of the eclipsing object has to be prepared in the way that the background intensity should be zero and the object "intensity" itself has to be -1 according to Section 6.1.1 (other values may also be possible[1], e.g., for eclipsing binaries or brown dwarfs, but not discussed here). The creation of the input images depends on the chosen resolution of the star, which I denote as D_S. This value gives the diameter of the star in pixels and also defines the resolution of the planetary array, which is calculated from the radii

[1] Negative values indicate opaque objects, zero totally transparent, and positive values simulate emission.

ratio p according to

$$D_\mathrm{P} = D_\mathrm{S} \cdot p \iff p = \frac{D_\mathrm{P}}{D_\mathrm{S}} = \frac{R_\mathrm{P}}{R_\mathrm{S}} \,. \tag{6.12}$$

This relation implies that the value of D_S should not be set too small, otherwise this would lead to a crude sampling of the planetary disk and in the end to an inaccurate light curve. After this simple definition of the image sizes, both objects are now generated in a similar way, just by using a simple equation for defining a circle

$$r = \sqrt{x^2 + y^2} \,. \tag{6.13}$$

Thereby x and y are pixel coordinates with the point of origin set to the image centers. For the planetary disk this means that all pixels in the range smaller or equal to $\sqrt{x^2 + y^2} = D_\mathrm{P}/2$ are set to -1 and all other to zero. For the stellar image this is the same process, but in addition we want to add some limb darkening. For instance, this can be done by any arbitrary limb-darkening law. Together with Eq. 6.13 we can write

$$\frac{I(\mu)}{I(1)} = 1 - u_1(1 - \sqrt{1 - r^2}) - u_2(1 - \sqrt{1 - r^2})^2. \tag{6.14}$$

As introduced in Chapter 5, it is now by far more interesting to directly use the limb intensities obtained from a model atmosphere, instead of using an arbitrary function whose coefficients are somehow determined by a fit to the "same" model intensities. As in the Chapter mentioned, I linearly interpolate between the model limb intensities to account for the significantly higher disk resolution of my stellar image. By directly using model limb intensities we have the opportunity to evaluate transit light curves in any wavelength range, together with arbitrary filters or instrumental response functions. Even transits in individual lines are now possible.

In contrast to the previous subsection, the input images are now created with different sizes (D_S and D_P). This means that both objects fit directly into these images without any spacing border. For the process of the FFT convolution this has the consequence that the resulting transit light curves are sampled without transit start and end times. To understand this behavior we can imagine that the whole planet is placed on and at the edge of the stellar image and then slided over the disk to end up at the opposite edge. Hence, for some central impact parameters the convolution always starts with the planet in front of the star, which leads to already occulted parts of the stellar disk. Consequently, I need to add an additional border to one of the images with at least the width of the planet's diameter, to cover t_1 and t_4 in the creation of the transits. The amount of pixels D_f to add on every side can be obtained from

$$D_f = f D_\mathrm{P} \qquad \text{with} \qquad f \geq 1 \,. \tag{6.15}$$

So at least the first and the last data point after convolution are now continuum points, independent of the given impact parameter.

Although the convolution of these images leads to an image which provides transits for all possible inclinations, I want to limit the convolution to only one impact parameter. This

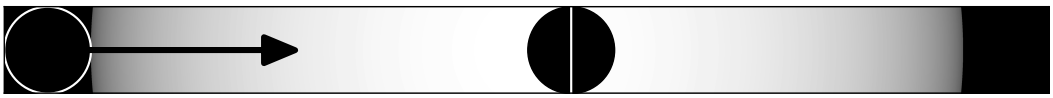

Figure 6.4: Image of the stellar stripe used for the FFT convolution. The planet "start" position is indicated by a *white* circle. The planetary disk is then virtually shifted in the direction of the arrow over the disk. The *white* vertical line indicates the pixel position where the convolution is stopped.

reduces the computation time and allows increasing the resolution of the input images due to lower memory consumption. The definition of the stellar stripe in front of which the planetary disk passes depends on the planet's size (in pixel) and of course the system impact parameter b. This value can easily be translated into the needed pixel coordinates, since we know that the path over the stellar disk center (at $D_S/2$) is given for $b = 0$, and for the case where the planet center touches the stellar limb during transit center (at D_S) if $b = 1$ is given. The pixel positions (start counting at zero) of (b_m) and the upper and lower boundaries are then defined as

$$b_m = \frac{D_S}{2} + \frac{bD_S}{2} - 1, \qquad b_1 = b_m - \frac{D_P}{2}, \qquad b_2 = b_1 + D_P. \tag{6.16}$$

This defines the stellar stripe $S_{x,[b_1,b_2]}$, which I show in Fig. 6.4. At this point all important input parameters are implemented in the algorithm. The limb darkening is included in the stellar image, the radii ratio p is given by the size ratio of the images, the inclination i and the semimajor axis a are included in the impact parameter b. Hence, we can start synthesizing transit light curves by image convolution.

For the convolution of this stripe with the planet I used the routine `fftconvolve` from the publically available SciPy package (Jones et al., 2001). This algorithm does exactly what I showed in Fig. 6.3; it computes an FFT of both images, multiplies them, and performs an inverse FFT. Additionally, this routine can handle input images which do not have the same size by adding as many zeros as needed to the smaller image and then cutting some parts off in the convolved result. The normalization of the output is performed as shown in Eq. 6.8, by summing up all pixel values of the whole stellar image, which is the disk-integrated flux in arbitrary units, dividing the output by this value and adding one. The number of transit data points resulting from this convolution depends only on the sizes of the input images and can be estimated by

$$N_{TP} = (D_S + 2D_f - D_P) + 1 \approx D_S\,. \tag{6.17}$$

For small values of D_P, the number is roughly the same as the number of pixels of the stellar diameter D_S. Normally this should be of the order of several thousand points. Compared to observational data, this is an enormous amount of data points. Although, we probably would need only a few hundred for modeling an observed transit, we have to keep in mind that the accuracy of the simulation strongly depends on the image resolutions.

The computation time of the convolution and the accuracy of the result depend on the number of elements in the input images. Due to the symmetry it is possible to nearly halve the computation time by cutting off almost half of the stellar stripe defined above (vertical line

in Fig. 6.4). This would result in a half transit light curve and the second half is created by a flipped copy of the first half. This is of course only possible in simple cases, e.g., for spotless stellar disks, where the expected transit event is symmetric around the transit center. To estimate the numerical performance of this optimized convolution, which means transit data points per second, I generated numerical transits for different input image resolutions and measured the computation time of the convolution. In Fig. 6.5 I plotted the computation time against the number of data points in one transit, by using Eq. 6.17. As mentioned before, the

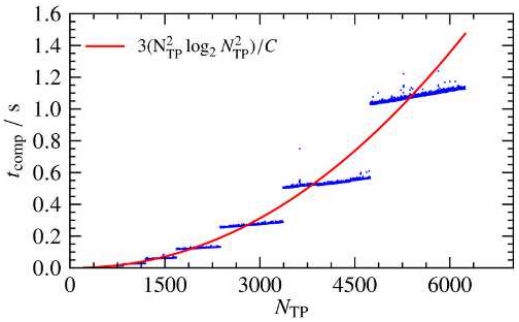

Figure 6.5: Numerical performance of my code. Computation time needed for the convolution of the arrays, plotted against the resulting amount of transit data points. The red curve is the approximation of the computation time with $C = 2 \cdot 10^9$ as system specific constant of proportionality. The plot is valid for an Intel® Pentium Core™2 Duo CPU with 3 GHz.

computation time of the FFT convolution is proportional to $3(N^2 \log_2 N^2)$. The used algorithm always fulfills the requirement that the number of data points has to be 2^γ needed for the FFT, by adding zeros to both input images. What we see in Fig. 6.5 is compatible with this assertion. At every point where the number of elements of the input arrays are rounded to the next higher value of γ, the computation time makes a clear jump. Although, these values are relatively high for modeling a single transit light curve, this method of generating synthetic transit light curves has a great advantage: the process of the FFT convolution can be parallelized. This means that the convolution of every single pixel row of the input images can be performed on a single CPU. This is maybe not practical, especially if $D_P \approx 400$. However, if needed, we can go one step further and compute the convolution on graphics cards. These are optimized for image processing and nowadays there are thousands of processing units on one single graphics card. As shown by Podlozhnyuk (2007) the image convolution has already been performed with NVidia CUDA, but without using the FFT.

The last important item missing is the definition of a time axis for the resulting transit light curve. Until now, every transit data point represents one step of shifting the planetary disk over the stellar image. This leads to data points which are sampled with the same mutual spacing. Just adding an equidistant time axis would be inappropriate because due to the curved orbit the sky-projected velocity of the planet is not constant in front of the stellar disk. Therefore, the new time axis has to be computed by using

$$t_i = \cos^{-1}\left[\frac{1}{\sin(i)}\sqrt{1-\frac{z_i^2}{a^2}}\right]\omega^{-1} \qquad \text{with} \qquad z_i = x_i^2 + b^2, \tag{6.18}$$

which is in principle the inversion of the sky-projected distance between the object centers $z(t_i)$ (Eq. 1.26), since we here know the distance $z(t_i)$ and want to know the corresponding

time. Although this equation accounts for a curved transit path over the stellar disk, the image convolution has an obvious disadvantage: the transit paths are straight lines for all inclinations. According to Eq. 1.26, tilted orbital planes lead to planetary traces which are seen in projection as parts of ellipses, so they are slightly curved. The convolution cannot account for this behavior. However, this is actually a negligible issue and we will see in the next subsection that the resolution of the input images are significantly more important for the accuracy of the synthesized transit light curves. Especially for large semimajor axes the approximation of a straight transit path is excellent. In this sense large semimajor axes mean all values larger than 4 R_S. See for interest Fig. B.13 where I compare hypothetical transit paths for different semimajor axes.

6.2 Comparison to a semi-analytical model

The most important question to be answered beside the computational speed of my algorithm is the accuracy when compared to transits generated using a semi-analytical approach. Obviously, like the computation speed the accuracy is expected to be a function of the resolution of my input arrays. The more precise the stellar and planetary images, the higher is the accuracy of the resulting transit light curves. To quantify this precision, I compare my numerical transits to those generated with the widely used `occultquad` routine (Mandel & Agol, 2002), which I also used for my analyses of *Kepler* objects. I synthesized a numerical transit light curve with the transit parameters of KIC 5084942 and quadratic limb-darkening, and I used the same parameters for the creation of the semi-analytical transit model. Then I determined the residuals between the two models and determined the maximum of the absolute values. To get the evolution of the accuracy as a function of the image resolution I repeated this procedure again with increasing D_S like before in Section 6.1.2 and visualize the result in Fig. 6.6. As

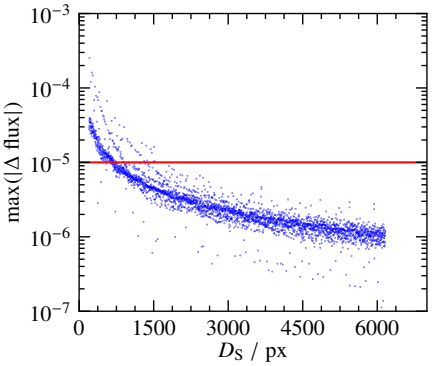

Figure 6.6: Precision of my numerical transit algorithm. Maximum deviation from a semi-analytical transit model plotted against the resolution of the stellar input array (diameter of the stellar disk in pixels, D_S). Y-axis is in logarithmic scale. *Red* horizontal line indicates the order of *Kepler*'s cumulative detection limit (Section 3.3). Shown are 3000 points.

expected, we can see that the maximum deviation from the semi-analytical model decreases as the resolution of the stellar input array is increased, which is equivalent to an increasing accuracy of my algorithm. This plot is promising in the sense that it shows that the accuracy achieved is comparable to the photometric precision of the *Kepler* photometer. Especially those values found at resolutions larger than $D_S \approx 3000$ indicate residuals which should not

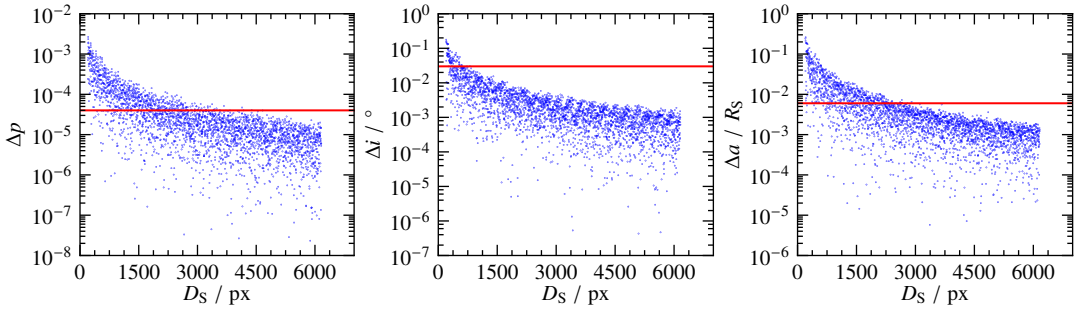

Figure 6.7: Individual parameter accuracy of my numerical code. Differences between the fitted and the initial parameters plotted against increasing image resolution. From left to right: Radii ratio p, inclination angle i, and semimajor axis a. Y-axis is in logarithmic scale. *Red* horizontal lines indicate the smallest individual parameter errors of my *Kepler* target sample: $\sigma_{\mathrm{min},p} = 4 \cdot 10^{-5}$, $\sigma_{\mathrm{min},i} = 0.03°$, $\sigma_{\mathrm{min},a} = 6 \cdot 10^{-3}\ R_S$ (Müller et al., 2013, Table 3).

be resolved by *Kepler* because they are in the order of $5 \cdot 10^{-6}$ and thus they should be hidden in the noise. In contrast, resolutions around $D_S \approx 1000$ would give rise to residuals at the $1\,\sigma$ level of *Kepler*'s accuracy.

The maximum of the absolute values of the difference between the Mandel & Agol model and the numerical transit is not necessarily the best value to describe the accuracy of my numerical transit. It can only serve as an estimator for the expected residuals and whether they would be detectable with a specific photometric instrument, e.g., *Kepler*. The influence on transit parameters resulting by a fit, when using my numerical code, is much more interesting. To study this, I created numerical transits (of course without noise) and then fitted these transit light curves with the `occultquad` code. The differences between the fitted parameters and the initial values of my numerical transit model show the total systematic error which is caused by the numerical accuracy of my code. In the present case I set the two limb-darkening coefficients as fixed and let the planet-to-star radii ratio p, the inclination angle i, and the semimajor axis a as free parameters in the fitting approach. The fitting code used is based on the downhill simplex algorithm. To check the convergence characteristics of this fit algorithm in this particular situation and to test whether it is able to find the input values, I first created a test case in which I fitted a transit created with `occultquad`. It turned out that the fitted parameters are the same as the input values and hence I continue using this fit algorithm. In particular, I generated roughly 3000 individual numerical transit light curves with increasing input array resolution, but this time each of these transits were fitted. The resulting differences between the input parameters and the fit results (Fig. 6.7) can be interpreted as a more precise measure of the accuracy of my code. If these differences are smaller than the smallest error found for these parameters in my *Kepler* sample, then I reached a resolution of the input arrays where my numerical code produces synthetic light curves which are accurate enough to model *Kepler* data. In Fig. 6.7 we can see that the differences between the fit values and the input parameters are clearly decreasing with increasing image resolution and at some point indeed starting to be smaller than the parameter errors. We also see a scatter in these differences, like

in Fig. 6.6, which is caused by rounding errors and the finite quantization of these parameters. Remember that, e.g., the impact parameter is quantized, due to the finite amount of pixels defining the radius of the stellar disk ($D_S/2$). Although we can see that the differences are already rather small for resolutions between 1000 to 3000 pixels, such as for Δp in the order of 10^{-6} to 10^{-8}, we have to consider the upper most boundaries of these point clouds as the achieved accuracy. If we look at Fig. 6.7 we can see that the inclination angle i is well enough determined by a resolution of $D_S \approx 1000\,\mathrm{px}$. This is a small value compared to the other parameters. Looking at the planet-to-star radii ratio, which shows the smallest absolute errors of these parameters, an image resolution around 5000 pixels would be enough to generate transit light curves to which a fit shows smaller deviations from the input parameters than the smallest errors of my *Kepler* target sample.

The analyses shown above proved that my numerical transit algorithm is accurate and comparable to semi-analytical models. It is worth to mention that the chosen *Kepler* object (KIC 5084942), whose parameters were used here for the simulations, has one of the smallest planet-to-star radii ratios in my sample. That my numerical code is even able to accurately synthesize transit light curves of such small planets is in the end the most credible indicator of its numerical precision. Furthermore, in contrast to a semi-analytical approach my numerical algorithm has some advantages which I present in the following.

6.3 Oblateness and planets with rings

Most transiting exoplanets known today orbit close to their host stars (probably biased by the detection method). Hence, it can be assumed that their spin rotation is slowed down due to tidal forces or even tidally locked to their host stars. Nevertheless, there is an increasing number of detected Jupiter-like planets which are further away from their host stars, undergoing significantly less tidal interaction. These planets could rotate fast enough to show oblateness because their equatorial diameter is increased by centrifugal forces. We know from our own solar system that, for instance, Jupiter is an oblate spheroid due to its fast rotation which lasts only about 10 hours. This results into an equatorial diameter which is almost 7 % larger than the polar diameter. In contrast to our solar system planets the spin rotation of exoplanets is so far mostly unknown, since it is hard to measure, but as reported by Snellen et al. (2014) there exists at least one measurement of the rotation rate of a fast rotating exoplanet, β Pictoris b. It shows a rotation period of only eight hours, which is faster than Jupiter's, and, therefore, this planet should exhibit a significant amount of oblateness. During a transit event such planets do not act as a simple circular shutter anymore, but rather as an ellipse.

The effects of oblateness on planetary transit light curves have been discussed by J. W. Barnes & Fortney (2003). I have shown that my numerical approach has a high precision when compared to the `occultquad` routine, therefore, I will use the planetary oblateness to demonstrate some capabilities of my code and try to reproduce some of their results. The capability to simulate

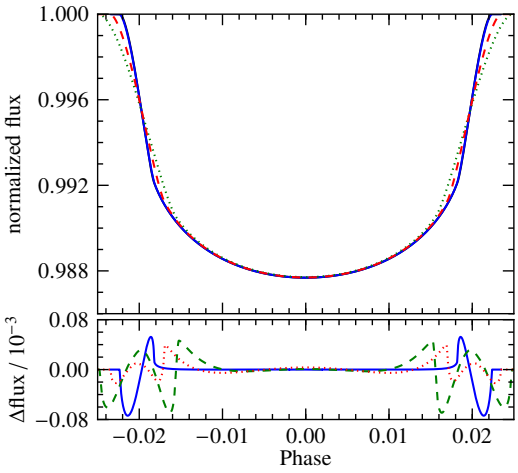

Figure 6.8: Comparison of transit light curves of a Jupiter-like planet with different amount of oblateness. *Top*: Numerically simulated transits. *Bottom*: Residuals (simulation minus best fit). Simulated Jupiter-like oblateness given in *blue* ($b_{\mathrm{ell}}/a_{\mathrm{ell}} = 0.935$), two extreme examples $b_{\mathrm{ell}}/a_{\mathrm{ell}} = 0.4$ (*red*) and $b_{\mathrm{ell}}/a_{\mathrm{ell}} = 0.2$ (*green*). $P_{\mathrm{orb}} = 2.47\,\mathrm{d}$, $u_1 = 0.5187$, $u_2 = 0.1678$.

oblate planets is simply implemented in my numerical algorithm by introducing an ellipse equation of the form

$$r^2 = \frac{x^2}{a_{\mathrm{ell}}^2} + \frac{y^2}{b_{\mathrm{ell}}^2}, \tag{6.19}$$

to create an elliptical planet. The semimajor and semiminor axis of the planet shape are denoted as a_{ell} and b_{ell}, respectively. To achieve a Jupiter-like oblateness, I set the ratio $b_{\mathrm{ell}}/a_{\mathrm{ell}}$ to 0.935 and used a stellar resolution of 25 Mpx ($D_{\mathrm{S}} = 5000\,\mathrm{px}$) together with limb-darkening coefficients from Table 5.2 (PHOENIX μ-rescaled, Johnson-V). For simplicity I chose an impact parameter of zero. The differences between a transit with and without Jupiter-like oblateness are hard to detect and only visible in the residuals of Fig. 6.8. These are determined by subtracting a best-fit transit light curve of this simulated data set. As pointed out by J. W. Barnes & Fortney (2003) this is the only way to determine appropriate residuals. Using a model of a circular planet which has the same orbital parameters and also blocks the same amount of light (same disk area as the planet with oblateness) is questionable, because the investigator has no prior information on the system and normally has to leave all parameters free in the fitting process. In this way the simulation yields residual signatures which would probably be found in real data sets. I fitted p, i, and a, while I set the limb darkening as fixed parameters under the assumption that it is known from model atmospheres. We can see that the major effect occurs during transit ingress and egress, mainly caused by the slightly increased transit duration. This signature is the same for transit start and end, because I neglected a tilt of the planet's rotation axis in relation to the orbital plane, otherwise this would not be the case. To visualize changes in the transit shape I generated two additional transit events with rather extreme values of $b_{\mathrm{ell}}/a_{\mathrm{ell}}$ (see caption of Fig. 6.8), with the constraint to cover the same amount of stellar surface area. This leads to almost the same transit depth and also to nearly the same residuals. According to my simulation one would need a photometric precision of about $4 \cdot 10^{-5}$ to detect these signatures (2σ level). This is in agreement with the findings of J. W. Barnes & Fortney (2003) and, furthermore, could be detected in *Kepler* data (see Section 3.3).

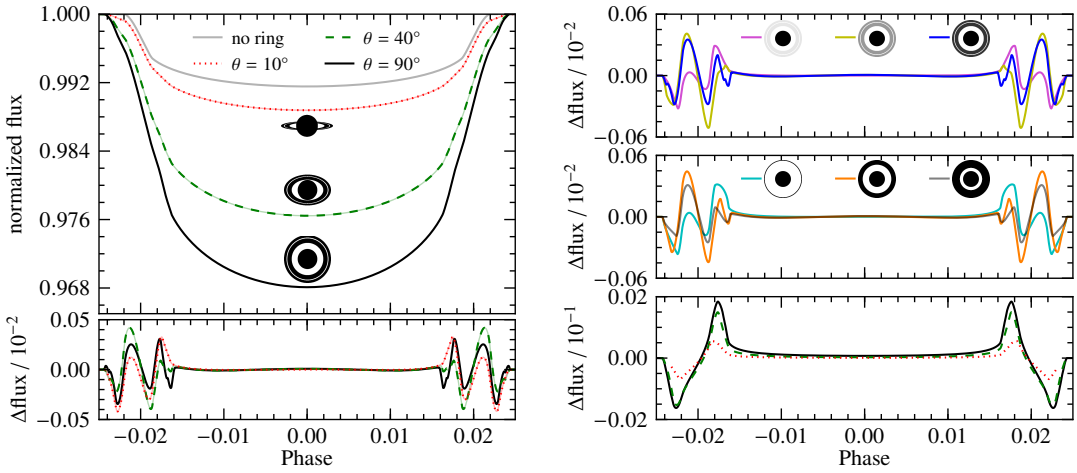

Figure 6.9: Transits and residuals for different ring properties. *Left*: Simulations for different ring tilts (*labels*). *Right*, *top*: Residuals for different optical thicknesses $\tau = 0.105$ (magenta), $\tau = 0.511$ (yellow), and $\tau = 1.609$ (blue). *Middle*: Results after varying the radius of the inner ring edge $R_{\rm in} = 2.3\,R_{\rm P}$ (cyan), $R_{\rm in} = 1.8\,R_{\rm P}$ (orange), and $R_{\rm in} = 1.4\,R_{\rm P}$ (gray) ($R_{\rm out} = 2.39\,R_{\rm P}$). *Bottom*: Residuals achieved using a hypothetical planet with identical orbital parameters but larger radius to occult same amount of disk area of the host star (no fit).

The second promising test case is the simulation of transits where the planet has rings, like Saturn. Like planets with oblateness, planets with rings are more likely to be found far away from their host stars since tidal interactions would hamper the formation of rings. We know from our solar system that all gas-giant planets have more or less pronounced ring systems from which we might infer that exoplanets could have rings as well. The detection of rings around exoplanets would give insights to planetary formation and about the life times of their rings. However, up to know there is no discovery reported.

Although there already exists some work inspecting simulated ring-induced transit signatures and estimations of the detection limits (J. W. Barnes & Fortney, 2004; Ohta et al., 2009), I will again present some similar results using my numerical approach. As input parameters I used a Saturn-like planet and varied the viewing angle of the ring plane θ between 90° (face on) and 10° (nearly edge on). In contrast to the mentioned publications, I will simulate Saturn's rings including the Cassini Division. For the ring dimensions I used the values given by IAU & USGS (2014). For simplicity I set the optical thickness of the A and B ring to infinity and of the Cassini Division to zero. In principle my code would be able to set arbitrary opacities for different parts of the rings, but it is not implemented yet, hence, the A and B ring have the same. We will see later on that for the detection of ring signatures it is actually more important in which photometric passband the transit will be observed. For my simulations I used the same conditions as before in the case of oblateness. The resulting transits (Fig. 6.9) remarkably differ in transit depth, depending on the ring's orientation. Due to the smaller projected occulting area in the tilted case, the transit depth decreases with θ, down to an amount only induced by the planet size. Consequently, the biggest effect on a transit light

curve is introduced by a face-on ring system. This means that planetary rings erroneously lead to an abnormal planet size, because they are normally not included in transit modeling and signatures are hidden in the noise. However, the face-on ring system does not introduce the strongest residuals. In my test case a tilt angle of $\theta = 40°$ leads to slightly stronger signatures in the residuals and, therefore, it is easier to be detected than a face-on ring (see Fig. 6.9, left). This is surprising but consistent with the findings of J. W. Barnes & Fortney (2004) and caused by the subtracted best fit planet model, where no ring is included. It becomes coherent when looking again at the light curves in Fig. 6.9, where we can clearly see that a face-on ring induces only very slight distortions to the transit flanks. The planet-ring system is circular and therefore symmetric in this case. If we look at the slightly tilted case ($\theta = 10°$) the occulting shape is not rotational symmetric with respect to the line of sight. This leads under this planetary conditions to marginally deeper dips in the residuals than in the face-on case. Obviously, in this geometry some parts of the rings do not contribute to the light curve because they are hidden behind or lying in front of the planetary disk. For values of θ where this is given, it is not to be expected that the signature in the residuals becomes largest. For Saturn this condition is indeed fulfilled, if θ is about 40°. I tested several other ring radii and different combinations of R_{in} and R_{out} which lead to different values of θ at which the residuals are maximized. In some cases the best detectability was even achieved when parts of the ring were hidden (e.g., $R_{\mathrm{in}} = 2.3\,R_{\mathrm{P}}$, $R_{\mathrm{out}} = 1.3\,R_{\mathrm{P}}$, $\theta \approx 10°$), which shows that the problem is more complicated and needs a deeper investigation.

We know from observations that the solar system planetary rings show various optical thicknesses. To go one step further than the mentioned publications I will compare the residuals when using different opacities of the rings leaving the geometry face on. I chose arbitrary transmissivities of 90 %, 60 %, and 20 % and show the residuals in Fig. 6.9 (right, top panel). The most transparent test case shows obviously the weakest influence on the transit light curve and has therefore the lowest detectability compared to the others. The peak value in the residuals is found at $3.2 \cdot 10^{-4}$. In contrast, the ring with the highest optical thickness produces only somewhat larger residuals ($3.5 \cdot 10^{-4}$), which is unexpected. One would rather expect that the detectability increases continuously with optical thickness, but at least for my ring properties this is not the case. I found the largest residuals for a transmissivity of about 60 %, which translates into $5.1 \cdot 10^{-4}$.

As the planetary rings in the solar system, rings around exoplanets could have various spatial dimensions, which set constraints on the detection limits. In the middle panel of Fig. 6.9 I show the residuals of my third test case, where I simulated planetary rings with different radii of the inner ring edge R_{in}. I set the outer ring edge R_{out} to $2.39\,R_{\mathrm{P}}$, which causes a decrease in ring width when R_{in} is increased. The ring with a moderate width causes the strongest residuals ($4.4 \cdot 10^{-4}$), while the broadest and the thinnest rings show weaker signals ($\approx 3.4 \cdot 10^{-4}$). These results indicate that a pronounced inner gap and also a ring with a significant width have a positive impact on the detectability.

The residuals determined without subtracting a best fit model, but a simulated transit using a ring-less planet with the same orbital conditions, increased in size to cover the same amount

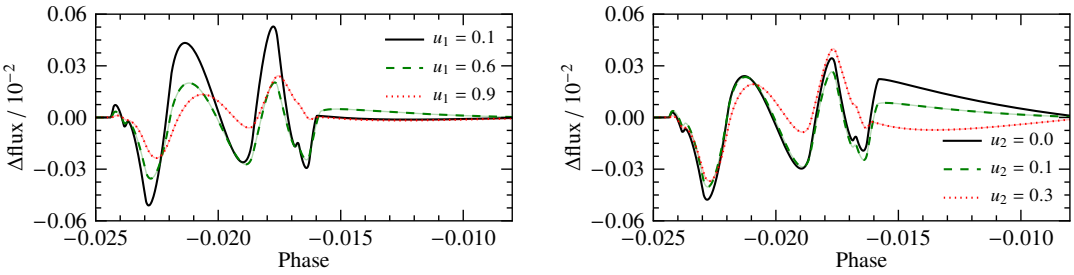

Figure 6.10: Transit residuals for limb darkening of different intensities. *Left*: Residuals when u_1 is varied and u_2 fixed to 0.1. *Right*: Residuals when u_2 is varied and u_1 fixed to 0.5. For all simulations the ring tilt was set to face on ($\theta = 90°$). Small dip near phase −0.024 and the small bump in the third dip are caused by the Cassini Division.

of surface area, are shown in Fig. 6.9 (bottom panel). These signatures are only caused by the rings and the later transit ingress and the earlier egress. Compared to the others shown above, they show an amplitude which is up to a factor of 3 larger and largest for the face on geometry and smallest for the slightly tilted case. Nevertheless, as already pointed out one would never see these residuals, because one would perform a ring-less fit without any a priori information about the system, which would lead to the previously shown weaker residuals. In the end, to give a 2σ detection of the ring-induced signatures of a Saturn-like planet, I determine a photometric precision of $2 \cdot 10^{-4}$ or better, which is similar to that found by, e.g, Ohta et al. (2009). Actually, *Kepler* delivered photometry with a comparable precision (Section 3.3), which offers the opportunity to detect rings around exoplanets. To detect the Cassini Division we would need a photometric accuracy of about 10^{-5}, which is four times smaller than the signatures caused by, e.g., Jupiter's oblateness and, therefore, beyond *Kepler*'s range. These results lead to the conclusion that it could be possible that some exoplanets which are believed to be highly inflated may actually have unresolved rings.

More important for my work than the influence of the ring size or orientation on the residuals is to study the influence of limb darkening on the detectability of planetary rings. Therefore, I created a number of numerical transits of a Saturn-like planet (ring face-on) and varied the limb-darkening coefficients of the host star. I started with varying u_1 and set u_2 to 0.1 and continued with varying u_2 and set u_1 to 0.5. All transit light curves were again fitted (limb darkening was fixed and set to the given values). I present the transit residuals in Fig. 6.10 together with the used coefficients. Due to the symmetry in my simulations I only show the residuals of the transit ingress. The second half of the transits show identical signatures. If we look at the left panel of Fig. 6.10 we can see that different values of u_1 lead to clearly different residuals. The major effect reveals a change in the amplitude, namely an increasing value of u_1 causes smaller residuals and, therefore, a decreased detectability. In the case of $u_1 = 0.6$ the peak value of the residuals reaches only 33 % of that reached when the linear coefficient is set to 0.1. In the right panel of Fig. 6.10 this effect is less pronounced but also present. The signature generated with $u_2 = 0.1$ has a peak value which is 15 % smaller than $u_2 = 0.0$ and only 1 % larger than the one with $u_2 = 0.3$. In principle we can interpret increasing values

of the coefficients as a stronger limb darkening. u_1 has a greater effect on the strength, while u_2 mainly defines the curvature (Eqs. 1.8 and 1.10), and this explains the weaker differences of the residuals seen in the right panel. Eventually, we learn from these results that a weaker limb darkening has a positive influence on the detectability of rings. This is caused by the higher contrast at the limb (no light/light) when the planet starts to occult the star. In the more limb-darkened case the transition between minimum and maximum occulted intensities lasts longer and causes the ring information to be smeared out in time. We can see that even the third dip in these residuals almost vanishes when the limb darkening increases and the peak positions are shifted to higher phase values. Therefore, the choice of the photometric passband plays a role which means that transit observations in the infrared would be the best opportunity to detect rings around exoplanets, because we know that in these wavelength regimes the stellar limb darkening is significantly weaker (see, e.g., Knutson et al., 2007). However, a high signal-to-noise ratio remains the most important premise to detect planetary rings.

My simulations demonstrate only some aspects of the effects on transit light curves introduced by planetary rings, to show the remarkable capabilities of my numerical code. For a deeper look into this topic I recommend the publications mentioned above. For example, they also include tilt angle dependent ring opacities, which I neglected in my simulations, because I used only a face-on ring when the opacity was changed or an infinite optical depth if θ or the limb-darkening coefficients were changed. Furthermore, J. W. Barnes & Fortney (2004) included diffraction depending on the particle's size, which is not possible with my code. Nevertheless, I showed that my code is able to simulate structures like the Cassini Division and that they are very difficult to detect and require a remarkable photometric precision not achieved today.

6.4 Numerical transits and the Sun

The outstanding advantage of my numerical approach is not only that any arbitrary shape of the occulting body can be simulated but also various properties of the occulted object can be assumed. Among others these could be the intensity distributions obtained from model atmospheres in any filter band, spot/surface maps, or specific shapes, e.g., oblateness on fast rotating stars. Beside simulations, my method is also capable of using real observations of the Sun. In the following I will present some numerically generated transit light curves using such observations and investigate differences, e.g., when compared to a model atmosphere.

6.4.1 Comparing PHOENIX and Neckel intensities

In Chapter 5 I showed different limb-darkening models compared to the limb intensities found for the Sun (Neckel & Labs, 1994). I fitted these intensities using a quadratic limb-darkening law, to create simulated transits with the resulting coefficients for comparison. Now I go one step further and create transit light curves which do not have to rely on any limb-darkening

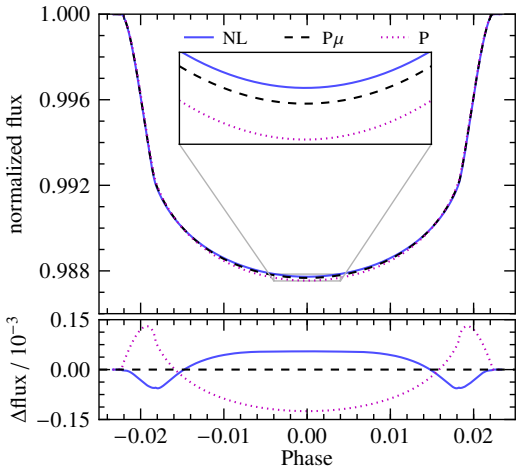

Figure 6.11: Numerical transit light curves using different solar-like limb-darkening models (*labels*), all in Johnson-V filter. P indicates LD information from the mentioned PHOENIX model atmosphere, Pμ the corresponding rescaled distribution, and NL Neckel & Labs (1994) intensities. *Bottom* panel shows the residuals.

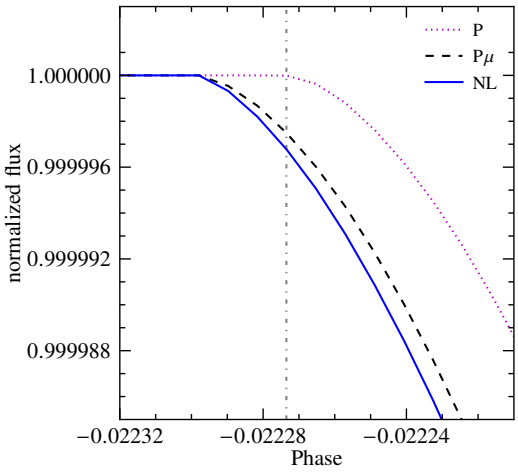

Figure 6.12: Zoom-in to the transit ingress phase of some numerical transits using different limb-darkening descriptions (*labels*: PHOENIX, PHOENIX μ_{rescaled}, Neckel & Labs (1994)) in Johnson-V passband. *Vertical* line marks the late transit start (t_1) in the case of the 3D PHOENIX atmosphere (see Section 5.1.3).

law. Instead I use the disk intensity distribution taken directly from a model atmosphere. No systematic error related to an inaccurate fit or model function is present anymore in this approach. Furthermore, the often discussed question whether the fit should be flux conserving or not becomes obsolete.

For my show cases and for the comparison to transits using measured limb darkening of the Sun, I chose a Jupiter-sized planet and generated transit light curves in the Johnson-V filter. I used the intensity distribution of a 3D PHOENIX atmosphere, as introduced in Chapter 5, and created the stellar disk with 5000 pixels in diameter. For simplicity I set the impact parameter to zero, letting the planet pass directly in front of the stellar equator. In Fig. 6.11 I show the resulting transit light curves when using slightly different limb-darkening descriptions of the Sun. In detail these are the mentioned PHOENIX atmosphere, the distribution after rescaling the μ-axis (Section 5.1.3), and the disk intensity distribution created by using a fifth-order polynomial (Eq. 5.1) based on the measurements of Neckel & Labs (1994). For the latter one the coefficients are taken from Table A.10. On the one hand, this plot allows me to investigate the effects of my rescaling of the μ-axis on transit shapes, or in other words, which systematics are introduced by the unscaled PHOENIX model. On the other hand, I can compare the resulting transits directly to a transit based on real measurements of the Sun. This is more relevant for planetary transit observers than only looking at the differences between the underlying limb intensities. Here I prefer to inspect the residuals determined in relation to the transit using the rescaled PHOENIX distribution. This means that I subtracted this transit from the others. We can clearly see in these residuals that the transits are not

congruent. This is of course not surprising because also the limb intensities are not congruent. The differences are visible during the transit ingress and egress phase but more expanded in time when the complete planet is in front of the the star, heading toward the disk center. The strongest deviation is given in the case of the unscaled PHOENIX distribution with a peak value of $1.3 \cdot 10^{-4}$. In contrast, the deviation to the transit generated with the Neckel & Labs distribution is only half as large ($0.5 \cdot 10^{-4}$). This leads to the conclusion that the PHOENIX distribution which is rescaled with my described method is the better choice when deriving limb-darkening predictions. The easiest way to compare these transits is to look at their transit center depths (visible in the inset of Fig. 6.11). In the here chosen photometric passband the unscaled PHOENIX distribution yields the deepest transit, while the Neckel & Labs distribution shows the most shallow transit. This order is the same in all tested photometric systems except for *Kepler*'s response function. If we think of the results of Section 5.1.2 and those summarized in Table A.8, then this order is self-evident. I found that the limb profiles produced by PHOENIX lead to less disk-integrated flux than those measured by Neckel & Labs in almost all of their studied wavelength intervals (Table A.7). In the rescaled case this effect is still there but significantly weaker. Stellar disks synthesized using this stronger limb darkening predicted by PHOENIX are slightly darker in total (except for the disk center: here the normalized intensity is by definition always one) and, therefore, the planet seems to be larger by causing a deeper transit.

Although we talk about small effects the photometric precision of *Kepler* actually allows us to detect residuals of the presented magnitude. For instance, to hide the resulting signatures caused by the unscaled PHOENIX distribution in the noise, the photometric precision has to be worse than $\approx 2.6 \cdot 10^{-4}$. The amplitude of the residuals mentioned above would then be only half the size of the noise. For the residuals measured to the transit model generated with a Neckel & Labs distribution I determine a limit of $\approx 10^{-4}$ for the photometric precision. If light curves with a higher signal-to-noise are given, then we have to ask which limb-intensity prediction is the more accurate one. For lower accuracies this is irrelevant since the measurement of the Sun and the rescaled PHOENIX prediction cannot be distinguished. The differences between transits, using them as limb-darkening information, would be hidden in the noise and, therefore, these models would be virtually the same. In fact, both limits mentioned above are detectable by *Kepler*, but not in today's ground-based photometry. Therefore, a fit of the limb darkening is not only possible but *necessary* for many objects in the *Kepler* data, simply because we do not know which theoretical limb-darkening prediction is correct. The question whether we should use a "more accurate" limb-darkening law than the quadratic law in the transit modeling, such as the nonlinear law, is not relevant. The difference between a transit using the quadratic law and one using the nonlinear law is in the order of 10^{-6} which is not detectable by *Kepler*.

Beside the effects introduced by the stronger limb darkening of the PHOENIX predictions, I also reported the effect induced by the pronounced gap of the spherical symmetric models at the outermost limb in Section 5.1.3. I found that the duration of a planetary occultation will be shorter by about ten seconds, depending on the orbit's inclination and semimajor axis. In Fig. 6.12 I show a zoom-in to the transit ingress phase of the numerical transits discussed

above. This plot nicely visualizes the later ingress caused by the PHOENIX model prediction (P) compared to the ingress of a transit using the measurements of the Sun (NL). For the orbital parameters used here the transit duration using the PHOENIX model is two times 5.2 seconds shorter. This is 1.1 ‰ of the transit duration. Some of my selected *Kepler* objects show a transit duration with an uncertainty of less than 10 seconds (e.g., HAT-P-7b) or a relative error of only 0.4 ‰. As visible, the rescaled PHOENIX model (Pμ) is much more accurate and has almost the same transit start time like the one based on NL. Hence, the PHOENIX model introduces a systematic error when set as limb-darkening information, which has a measurable effect on the transit duration and, therefore, on all remaining orbital parameters. This has the consequence that all limb-darkening "laws", which try to fit the steep drop-off region at the limb of the spherical model intensities (e.g., Claret & Hauschildt (2003, Eq. 8)), introduce this systematic error as well. My recommended rescaling of PHOENIX's limb intensities does not lead to such a systematic influence or only to a negligible amount not resolved with *Kepler*'s photometry.

In the end I conclude from the shown comparison that the rescaled PHOENIX limb profile holds the more elaborate disk intensity distribution than the unscaled one. The differences between transits, which rely on Neckel & Labs measurements and the rescaled PHOENIX intensities, reach their maximum during transit ingress or egress and transit center, and remain undetected for a Jupiter-sized planet if the signal-to-noise is less than ≈10 000. For the unscaled distribution this limit is reached earlier ($S/N \approx 3800$). Furthermore, my numerical approach made it feasible to visualize the effect of the pronounced gap at the limb of the spherically symmetric PHOENIX models on transit light curves, which in fact has a measurable influence on transit durations. For this reason I do not recommend to use the "pure" intensity distribution or limb-darkening laws intended to fit this gap in transit modeling.

6.4.2 Synthetic transits using space-based observations

Modern monitoring of the Sun is often carried out by satellites, which are able to produce high quality images of different parts of the solar atmosphere. These images are convenient to use them for simulated planet eclipses and they can directly be used as input for my numerical transit algorithm. The only requirement which has to be fulfilled is that the images must show the whole Sun.

To create a numerical transit light curve using space-based observations I chose data collected by SDO, like before in Chapter 5. I start with a FITS file from the AIA 4500 Å instrument, whose wavelength corresponds to a continuum part of the solar spectrum (photosphere). In contrast to the previous sections the resolution is now fixed to that given by the observation. With the solar limb found at pixel 118 (Section 5.2.1) and the image resolution of 1024×1024 pixels, this leads to a solar disk diameter of 788 pixels. As a consequence, the number of out-of transit points is now a function of the planet-to-star radii ratio p ($N = 2(118 - 788p)$). If the planetary radius is chosen too large ($p > 118/788$), it would be impossible to generate a complete transit light curve without adding some extra black pixels to the edges of the AIA

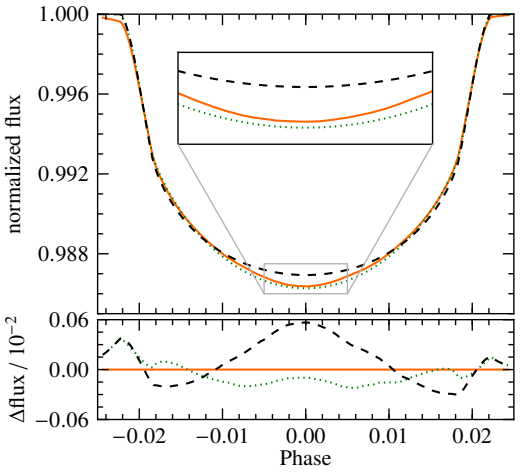

Figure 6.13: Numerical transit light curves using a SDO/AIA 4500 Å FITS-image (*orange*, 19.07.2012) and the μ-rescaled PHOENIX atmosphere (*dashed*). Also given: a semi-analytical transit (`occultquad`) with a quadratic LD law ($u_1 \approx 0.90$, $u_2 \approx -0.16$, Table 5.4, *dotted*). *Bottom panel*: residuals in relation to the SDO transit.

image. In my case this should not be a problem, because for my synthetic transits I will use $p = 0.1$ to simulate a Jupiter-like planet.

In Fig. 6.13 I present the resulting numerical transit light curve together with some other synthetic transits. I used the same parameters as in the previous subsection and an observation with no active regions near or in areas occulted by the planet. The resulting transit shape looks quite normal, but flux values before transit ingress and after egress are not one. This is caused by the unphysical pixel values in the dark image areas around the Sun, seen in Figs. 5.11 and 5.12. These parts of the light curve are not important and can be neglected in a comparison to other transit models. Hence, we can limit our attention to phase values between ±0.022, where this transit, compared to the one generated using the PHOENIX atmosphere in a narrow spectral region (4500 Å ± 5 Å), deviates most in the transit center. This is clearly visible in the residuals, which shows that there is also a slight mismatch of the overall transit shapes. However, this is not surprising, because we saw in Section 5.2 that both limb darkenings significantly deviate from each other. I stated that instrumental effects or residuals of the reduction process are the most probable reasons for the incorrect disk intensity distribution. For further comparison of the SDO transit I additionally used the `occultquad` routine to create a transit with the limb-darkening coefficients fitted in Section 5.2.2. Actually, the SDO transit is described quite well by this transit and the residuals are much smaller compared to the PHOENIX model. Yet, this model also gives no perfect match to the numerical transit of the SDO observation, which can probably be explained by the fact that the quadratic fit to the limb intensities in Section 5.2.2 is influenced by instrumental peculiarities.

Much more interesting than planet eclipses of totally quiet regions are transits in front of, e.g., spots or faculae. For that purpose I chose SDO observations taken on the 26th of September 2011, where some active regions north of the solar equator were seen as a spot group in the 4500 Å image. I changed the orbital inclination to $i = 89°$ to fully cover the spots by the hypothetical planet, which corresponds to an impact parameter of $b = 0.14$. I show the resulting numerical transit light curve together with its transit path in front of the solar disk in

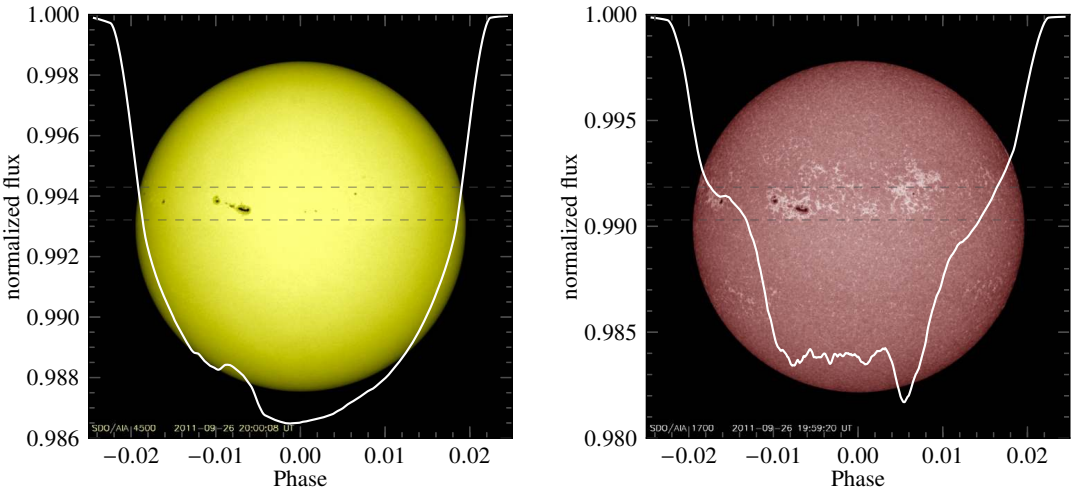

Figure 6.14: Numerical transit light curves in front of solar active regions (*white*). *Dashed* lines marking the transit path ($i = 89°$). The background images are taken from the SDO image archive[2]. *Left*: Narrow-band image in 4500 Å (photosphere), *right* 1700 Å (temperature minimum, photosphere). Wavelength information taken from Lemen et al. (2012).

Fig. 6.14. As expected, the transit signature shows a nice bump at the phase position where the planet passes in front of the spot group. Such signatures have already been observed and modeled on active planet hosts, such as HD 189733 (Pont et al., 2007) and CoRoT-2 (Wolter et al., 2009). Therefore, my numerical transit method gives an opportunity to test spot-modeling algorithms, e.g., if the resulting parameters like spot size, shapes, and orientation are reasonable. Furthermore, my algorithm is capable to simulate real spot evolution scanned by the transiting planet, just by using more than only one SDO observation as input, which are separated by multiples of the orbital period.

The great advantage of the simulations using SDO observations is that I am able to synthesize the same transit in different wavelengths, which would in real observations only be possible by performing multi-color photometry or spectro-photometry. Hence, I simply chose SDO observations made with the AIA instrument at 1700 Å. I show the resulting numerical transit light curve in Fig. 6.14 (right). This transit shows an uncommon shape and has a depth of $\delta \approx 1.8\,\%$ which is clearly deeper compared to the one generated using the 4500 Å observations ($\delta \approx 1.4\,\%$). The shape and depth can be explained by faculae visible as bright areas in the image. They cover a larger fraction of the solar disk than the spots. This is the reason why the bump, when the spots are being passed by the planet, is not visible anymore. Instead of creating bumps, the faculae are producing dips when being occulted by the planet, which is nicely demonstrated by the deepest point in that light curve.

To demonstrate an even more extreme case, I took an SDO observation made at the same date, which was acquired at 94 Å corresponding to soft X-ray emission of the solar corona. To

[2] http://sdo.gsfc.nasa.gov/assets/img/browse/

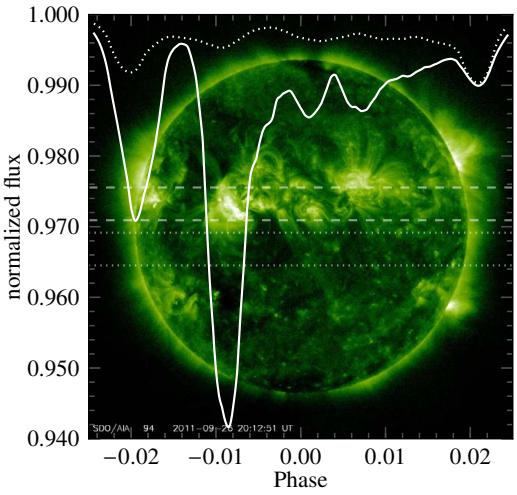

Figure 6.15: Numerical transit light curves in soft X-rays (SDO/AIA 94 Å), $E_{\text{Photon}} = 132\,\text{eV}$. *Solid* line is the resulting transit light curve in front of the active regions ($i = 89°$), transit path horizontal lines (*dashed*). *Dotted* lines show the transit light curve and corresponding transit path ($i = 91°$) in front of nearly inactive regions.

simulate transit light curves in X-rays might sound a little bit far-fetched, but actually there already exist real transit observations in X-rays of HD 189733b as reported by Poppenhaeger et al. (2013). My numerical light curve presented in Fig. 6.15 shows no similarity to a common transit light curve anymore and by high chance it would not be identified as such an event. The unusual shape is a result of the irregular spatial brightness distribution of the corona and, in contrast to observations in the optical wavelength regime, it is reasonable to observe a longer transit duration caused by the extended corona. This easily explains why we do not see any out-of transit data points in the figure. This can simply be changed by adding black areas around the Sun, but my intention was to leave the FITS-files unchanged. The deepest point of this light curve shows a transit depth of almost 6 %, which is produced by occultation of the most prominent light source in this images, which corresponds to the spot group visible in the optical. It is important to mention that one also sees considerably bright active regions in this X-ray image, which do not have prominent optical counter parts (cf. Fig. 6.14, left). Therefore, a quiet optical transit light curve is no proper indicator for the absence of bright coronal regions visible in X-rays.

At coronal wavelengths one expects to see limb brightening in the transit light curve as reported by Poppenhaeger et al. (2013). Actually, in the presented example this is not the case, since the variations due to the active coronal regions dominate the brightness distribution. To simulate a transit which shows clear limb brightening, I changed the orbital inclination of my model to achieve a transit path over a less active region. In fact, I used the same impact parameter as before, but this time the transit path lies south of the solar equator. This numerical transit light curve clearly has a shallower profile and the parts before and after transit center are more symmetric (Fig. 6.15, dotted line). We are now also able to see some kind of limb brightening, visible as almost equally deep dips at transit ingress and egress, and an increased flux level between them. Additionally, the transit shows some variations, which are induced by coronal holes and brighter areas from the active regions projected into this transit path. See also Llama & Shkolnik (2015) who created similar results in parallel to my thesis.

The image of the Sun presented in Fig. 6.15 nicely illustrates the brightness distribution in soft X-rays and shows us that the intensity is of course not evenly distributed over the solar disk. When the Sun is in an active phase a transiting planet would produce a light curve, which is most likely distorted by bright active regions. This is supported by the spatial extent of the active regions, because they are larger in X-rays than in optical wavelengths. Therefore, it is unlikely to observe a typical limb brightened transit, this is only possible if the Sun is in an inactive phase. Furthermore, we know that the Sun is not a very active star, especially when compared to, e.g., CoRoT-2 or HD 189733, where the spot coverage is significantly larger than on the Sun. From these insights I assume that it is even more unlikely to observe the typical limb brightened transit shape and the real transit depth on these active stars. For some more numerical transit light curves in different AIA narrow-band images see Fig. B.20.

6.5 The effect of highly inclined orbits

I. D. Howarth already discussed the influence of large system impact parameters on fitted limb-darkening coefficients in transit modeling (Howarth, 2011, Fig. 4). He generated transit light curves using the four parameter nonlinear limb-darkening law and fitted them using a transit model with the quadratic limb-darkening representation. He found that the coefficients determined in this way indeed depend on the impact parameter.

I already confirmed his findings with empirical studies of *Kepler* objects in Müller et al. (2013) and Section 4.3.1, but I now want to go one step further. The question I want to answer is whether I can extend his results using a more precise description of the limb intensities in contrast to a least squares fit to model intensities using some arbitrary "law". For this purpose my numerical transit model is predestinated to generate a transit light curve with making use of limb intensities obtained directly from a spherically-symmetric 3D-PHOENIX atmosphere. In detail, I followed his approach by creating transit light curves with different system impact parameters varied between 0 and 0.9. The planet-to-star radii ratio and the semimajor axis was arbitrarily set to and 7.9 R_S, respectively. The resolution was set to 2500 rows, which yielded roughly 2900 transit data points. To achieve comparable results, I used the same solar like model atmosphere as in the previous chapter and applied my rescaling of the μ-axis (Section 5.1.3). As a photometric filter function, I chose the Johnson-V transmission curve. These light curves were then fitted with the mentioned `occultquad` routine using a downhill-simplex algorithm. For a reliable error estimate all fit values were used as initial values for a MCMC sampling. The resulting quadratic LDCs are shown in Fig. 6.16. The determined pair of coefficients for $b = 0$ is only consistent with the quadratic coefficient u_2 (1D-PHOENIX). For u_1 the result lies more or less directly between both model predictions. However, one should mention that these values are totally consistent with my obtained fit results of this limb profile in Table 5.2. With increasing impact parameter the resulting coefficients show an increasing deviation from these values. Also clearly visible is the increase in the 1σ uncertainties. This behavior is already discussed in my paper (Müller et al., 2013) and also seen in the studies of Howarth (2011), but he did not carry out an investigation of the statistical

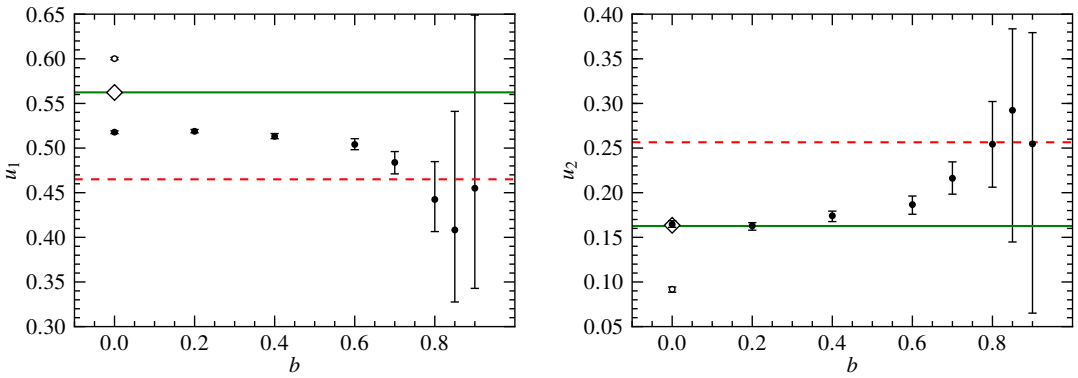

Figure 6.16: Fitted quadratic LDCs (*dots*) of simulated numerical transit light curves with increasing system impact parameters. The numerical transits use a 3D PHOENIX atmosphere as LD information. *Colored lines* indicate predicted LDCs for the Sun taken from Claret & Bloemen (2011) (*green/solid*: PHOENIX, *red/dashed*: ATLAS). *Diamonds*: verification of my numerical transit and fit method, see text. *Empty circles*: fitted LDCs of a simulated transit produced semi-analytically with nonlinear limb-darkening information.

errors. Due to the huge uncertainties the decrease in deviation from the initial values implied at $b = 0.9$ is insignificant, but also slightly visible in the work of Howarth.

Finally, I am able to reproduce his findings using a numerical transit algorithm together with limb intensities directly obtained from a model atmosphere. This is in contrast to the use of an arbitrary limb-darkening law which has no physical foundation. However, Howarth made a more complete analysis using more photometric systems and also including the linear limb-darkening law.

To test the validity of my approach, I created a numerical transit using the quadratic limb-darkening law together with coefficients predicted for the Sun (green lines in Fig. 6.16). I fitted this transit using a semi-analytical transit model again with quadratic limb-darkening law. The resulting coefficients reproduce the values used for the numerical light curve (diamond symbols in Fig. 6.16). This proves that the analytical limb darkening is implemented correctly in the algorithm and that the fit method is able to determine the correct limb darkening. However, as visible in Fig. 6.16 the fitted quadratic coefficients do not agree with the predicted coefficients anymore when the transit light curves are generated using a PHOENIX atmosphere or if they are generated semi-analytically using a four parametric nonlinear limb-darkening law (dots and circles).

7 Scientific Publications

7.1 The corona and companion of CoRoT-2a. Insights from X-rays and optical spectroscopy

S. Schröter, S. Czesla, U. Wolter, H. M. Müller, K. F. Huber, and J. H. M. M. Schmitt
Astronomy & Astrophysics, Volume 532, id.A3, 12 pp. (Aug. 2011)

The CoRoT-2 system, consisting of a very active G-dwarf orbited by a hot Jupiter and a gravitationally bound companion, most likely an inactive K-dwarf, is one of the most interesting planet hosting systems to date. The optical light curve of CoRoT-2A shows periodic variations caused by a significantly spotted surface. CoRoT-2b, the transiting hot Jupiter, makes it feasible to study its host star's surface, e.g. using planetary eclipse mapping (e.g., Huber et al., 2010).

The characterization of the whole system and especially of the host star CoRoT-2A is indispensable to understand the development and phenomena in this system. In the work of Schröter et al. (2011), in which I participated, we determined e.g. the effective temperature and surface gravity of CoRoT-2A using high resolution optical spectroscopy. The optical spectra were obtained by Klaus F. Huber using the UVES spectrograph at the Very Large Telescope. The whole data reduction of the spectra was carried out by Sebastian Schröter, who afterwards begun with individual line analyses to determine $T_{\rm eff}$ and $\log g$. At this point we started the cooperation. To provide a more comprehensive study of the fundamental stellar parameters, we used the software tool *Spectroscopy Made Easy* (Valenti & Piskunov, 1996). My expertise on this tool, acquired during a visit to Professor N. Piskunov in Uppsala, Sweden, was essential for the whole spectral analysis (see also Chapter 2 of this thesis). Therefore, the published values for $T_{\rm eff}$, $\log g$, ξ, and the individual element abundances were obtained in close cooperation of S. Schröter and me. However, this work is not included in my thesis, because I am not the main author and the major contribution to the publication is clearly provided by S. Schröter.

7.2 A consistent analysis of three years of ground- and space-based photometry of TrES-2

S. Schröter, J. H. M. M. Schmitt, and H. M. Müller
Astronomy & Astrophysics, Volume 539, id.A97, 10 pp. (Mar. 2012)

The transiting exoplanet TrES-2b is one of the best studied objects. Not only because it is included in the *Kepler* field, but also because of the high number of ground-based observations. Due to the high impact parameter of the orbiting planet the system is of special interest. Deduced transit parameters should be sensitive to orbital changes, e.g. caused by undetected additional planets around TrES-2A. I tried to obtain multi-band photometry with the BUSCA instrument at the 2.2 m telescope at Calar Alto myself in 2010. The observations were proposed by Dimitris Mislis, who previously observed TrES-2 with the Oskar-Lühning-Teleskop of Hamburg observatory and also with BUSCA (Mislis et al., 2010). However, the data I acquired is not usable due to bad weather conditions during both granted observation nights.

The work by Schröter et al. (2012) aims to rule out previously proposed inclination changes of TrES-2b's orbital plane (Mislis et al., 2010). Therefore, Sebastian Schröter combined ground- and space-based observations and modeled all available transits individually. His approach is in contrast to my work, since I model all available transits in parallel. However, he also used an MCMC sampling as I do, to account for strong correlations and to get reliable error estimates. As an improvement he proposed to use the *Adaptive Metropolis* algorithm (Haario et al., 2001) (see also Section 1.3.1 of this thesis). To ensure that this modified Metropolis algorithm yields the same results as the normal Metropolis-Hastings algorithm, I simulated transit light curves and used both sampling approaches. The results were compared to each other and it turned out that they are consistent. I also repeated this procedure with the *Kepler* data of TrES-2, with the same result. The major contribution to Schröter et al. (2012) was delivered by S. Schröter and, therefore, this work is also not included in this thesis.

7.3 High-precision stellar limb-darkening measurements

H. M. Müller, K. F. Huber, S. Czesla, U. Wolter, and J. H. M. M. Schmitt
Astronomy & Astrophysics, Volume 560, id.A112, 20 pp. (Dec. 2013)

The following work (Müller et al., 2013) is the result of an in-depth transit analysis of the best available light curves of transiting exoplanets provided by the *Kepler* mission. As already outlined in Chapter 4, the study comprises seven *Kepler* quarters, namely quarters zero to six. Most notably, the data is recorded with high time resolution (short-cadence mode), with a bin time of about one minute. This work concentrates on transit modeling to determine the stellar limb darkening as well as the orbital parameters. The resulting limb-darkening coefficients are compared to widely used predictions and significant deviations are discussed. Furthermore,

the work provides simulations and an analytical approach to the correlation and error behavior of the measured limb-darkening coefficients as a function of the system impact parameter.

As main author I delivered the major contribution to this work. That includes amongst others the target selection, the data handling, and the analysis. For that, I programmed a Python class that has the ability to read in all available light curves of any *Kepler* object and that normalizes and fits all observed transits. The coauthors helped me to interpret the results and provided contributions to the theoretical approach and the simulations to be found in the appendix.

A&A 560, A112 (2013)
DOI: 10.1051/0004-6361/201322079

Astronomy & Astrophysics

High-precision stellar limb-darkening measurements

A transit study of 38 *Kepler* planetary candidates⋆

H. M. Müller, K. F. Huber, S. Czesla, U. Wolter, and J. H. M. M. Schmitt

Hamburger Sternwarte, Universität Hamburg, Gojenbergsweg 112, 21029 Hamburg, Germany
e-mail: hmueller@hs.uni-hamburg.de

Received 13 June 2013 / Accepted 25 September 2013

ABSTRACT

Context. Planetary transit light curves are influenced by a variety of fundamental parameters, such as the orbital geometry and the surface brightness distribution of the host star. Stellar limb darkening (LD) is therefore among the key parameters of transit modeling. In many applications, LD is presumed to be known and modeled based on synthetic stellar atmospheres.
Aims. We measure LD in a sample of 38 *Kepler* planetary candidate host stars covering effective temperatures between 3000 K and 8900 K with a range of surface gravities from 3.8 to 4.7. In our study we compare our measurements to widely used theoretically predicted quadratic limb-darkening coefficients (LDCs) to check their validity.
Methods. We carried out a consistent analysis of a unique stellar sample provided by the *Kepler* satellite. We performed a Markov chain Monte Carlo (MCMC) modeling of low-noise, short-cadence *Kepler* transit light curves, which yields reliable error estimates for the LD measurements in spite of the highly correlated parameters encountered in transit modeling.
Results. Our study demonstrates that it is impossible to measure accurate LDCs by transit modeling in systems with high impact parameters ($b \gtrsim 0.8$). For the majority of the remaining sample objects, our measurements agree with the theoretical predictions, considering measurement errors and mutual discrepancies between the theoretical predictions. Nonetheless, theory systematically overpredicts our measurements of the quadratic LDC u_2 by about 0.07. Systematic errors of this order for LDCs would lead to an uncertainty on the order of 1% for the derived planetary parameters.
Conclusions. We find that it is adequate to set the commonly used theoretical LDCs as fixed parameters in transit modeling. Furthermore, it is even indispensable to use theoretical LDCs in the case of transiting systems with a high impact parameter, since the host star's LD cannot be determined from their transit light curves.

Key words. stars: atmospheres – planetary systems – methods: data analysis – techniques: photometric

1. Introduction

Since the early studies of eclipsing binary light curves the center-to-limb intensity distribution of stellar disks has played an important role in photometric analyses (e.g., Russell & Shapley 1912). For optical wavelengths this distribution shows a darkening toward the stellar limb, which is easily seen on the Sun. This so-called limb darkening (LD) depends on the surface temperature of the underlying stars and is difficult to measure when the stellar disk remains unresolved. In the early stages of LD studies, this intensity trend was theoretically described by a linear formula provided by Schwarzschild (1906). This linear description has been used to model a verity of observed data, such as eclipsing binary light curves, and it is still in use in analyses of the Rossiter-McLaughlin effect (Ohta et al. 2005) or in Doppler imaging (e.g., Nesvacil et al. 2012). More complicated descriptions of LD have been proposed (e.g., Kopal 1950) and adopted by several other authors. Although these models are commonly referred to as limb-darkening "laws", they are only approximations of the real stellar LD.

When modeling LD in, say, transit light curves, the LD laws are parameterized by some sets of coefficients. These are either left as free fit parameters during data analysis or determined beforehand by model atmospheres and kept fixed in the actual light curve modeling. The determination of LD coefficients (LDCs) for a variety of different laws using model atmospheres has been carried out by many authors (e.g., Wade & Rucinski 1985; van Hamme 1993; Sing 2010; Howarth 2011a; Claret & Bloemen 2011). Whether these theoretical LDCs are used and fixed or freely fitted in light curve models can have significant effects on the results. Although it clearly is preferable to fix parameters in a fit that can be determined in some other way, it is not clear how reliable these theoretical LDCs are. After all, they only represent approximations to model atmospheres. Direct measurements of LD can only be carried out for a few exceptional stars with a spatially resolved surface, such as Betelgeuse (Haubois et al. 2009) using interferometric observations or, most notably, our Sun (Neckel & Labs 1994).

The importance of a correct description of LD was recognized once researchers began to study light curves of transiting extrasolar planets (Charbonneau et al. 2000). Transit light curves are an important tool for studying the physical parameters of exoplanets, such as their radii and densities. Stellar LD is often considered as nuisance parameter in transit modeling, which is strongly correlated to the other model parameters (Carter et al. 2008). Thus, prior knowledge of the LDCs would significantly reduce the uncertainty in the physical parameters of the planets. However, transit light curve analysts have to choose from a variety of LD laws and select appropriate theoretical LDCs. These choices are often quite arbitrary, and incorrect coefficients

⋆ Table 3 and appendices are available in electronic form at http://www.aanda.org

A&A 560, A112 (2013)

can introduce large errors in the derived model parameters; this is one of the reasons why many researchers tend to leave their LDCs as free fit parameters.

There is an ongoing debate whether theoretical LDCs and LD laws are accurate enough to describe the real stellar brightness distribution. Today, high-precision transit light curves of planets and eclipsing binaries render it feasible to study stellar LD for a substantial number of stars with high accuracy. Some studies measure LD using eclipsing binary stars (e.g., Heyrovský 2007; Claret 2008) and found disagreements between empirical and predicted LDCs using the linear limb-darkening law. Knutson et al. (2007) note in their study of HD 209458b that even the four parametric nonlinear LD law leads to clear residuals when they use the predicted LDCs. Southworth (2008) used up to five different LD laws in planetary transit models and stated that "the solutions of all but the highest-quality transit light curves are *not* adversely affected by the choice of LD law". Southworth also tested the effects of setting LDCs to predicted values for some objects and found that the resulting planetary parameters show no significant differences from leaving the LDCs free; however, he also found the same disagreements for HD 209458A as Knutson et al. (2007). Other authors found further disagreements between theoretical and measured LDCs, as e.g. Kipping & Bakos (2011a) for Kepler-5b, also included in our analysis, and Sing (2010) for seven CoRoT targets. On the one hand these studies seem to suggest that it is necessary to fit the LDCs when modeling light curves, as already claimed by other authors (e.g., Southworth 2008; Csizmadia et al. 2013); on the other hand, there are also objects which show good agreement with the theoretical LDCs (Bordé et al. 2010) and one always has to keep in mind that the determined LDCs usually have rather large errors.

There are 3D hydrodynamic atmospheric models that predict a slightly weaker limb darkening than 1D models, potentially indicating a systematic deficiency of the 1D approach. As demonstrated by Asplund et al. (2009), these 3D models successfully reproduce the solar LD (see also, Trampedach et al. 2013). The deviation between the solar 1D and 3D models compared by Asplund et al. (2009) amounts to roughly 10% in terms of flux at intermediate limb angles in the visible, which corresponds to a 10% deviation in the LDCs. Hayek et al. (2012), who apply similar 3D models to exoplanet host stars, ascribe the weaker limb darkening to a shallower temperature gradient in the photosphere. However, this behavior has not been reproduced in the 3D solar models computed by Hauschildt & Baron (2010), who combine the radiative transfer of the PHOENIX code with a snapshot of a hydrodynamic model of the photosphere (Caffau et al. 2007; Wedemeyer et al. 2004).

In the end, the core question is still not conclusively answered: Are the theoretical LDCs compatible with empirical ones? The aim of this work is to take another step toward a consistent answer to this question. Although today it is hardly possible to directly observe LD for many stars, some dozen light curves of the *Kepler* space telescope show sufficient precision to indirectly analyze stellar LD with high accuracy. Furthermore, using only one instrument with one spectral response function allows us to consistently analyze the stellar LD with a wide diversity of parameters.

In this paper we present measurements of the quadratic limb-darkening coefficients using high-quality space-based transit light curves of 38 *Kepler* planetary candidate host stars divided into 26 target stars with highest signal-to-noise ratios (SNRs) and 12 objects with large system impact parameters. We concentrate on how well our determined LDCs agree with the theoretically predicted coefficients from commonly used model atmospheres for main sequence stars (PHOENIX and ATLAS). In Sect. 2 we explain our selection criteria of *Kepler* objects, our data preparation, and our transit normalization. Section 3 provides information on the used routines, on the modeling approach, and the error analysis. Section 4 is dedicated to objects showing time correlated noise or other anomalies presumably caused by instrumental effects, while in Sect. 5 we present our results and compare them to predictions. In Sect. 6 we summarize our results and provide conclusions concerning the treatment of limb darkening in transit modeling.

2. Data priming and selection of suitable objects

2.1. Target selection

For our analysis we retrieved the *Kepler* data of quarters Q0 to Q6 from the NASA Mikulski Archive for Space Telescopes (MAST[1]). *Kepler* produces photometric light curves in two different sampling modes: long cadence (LC) and short cadence (SC) with sampling rates of about half an hour and one minute, respectively. The data consist of different data releases from release 4 to 7, depending on the quarter and the sampling mode. The raw data have been processed using *Kepler*'s photometric analysis (PA) pipeline, which includes barycentric time correction, detection of cosmic ray events, and background removal. This leads to the raw aperture photometry (SAP) flux. We used the corrected aperture photometry (PDCSAP) flux for our investigations, which is the result of *Kepler*'s pre-search data conditioning (PDC) pipeline applied to the raw flux. In addition to the PA, the PDC corrects for systematic errors, such as jumps and exponential decays caused by the instrument, and removes excess flux within the target apertures which could be induced by background or foreground stars in crowded fields or by physically bound companions. Such a third light contribution can affect planet parameters in transit modeling, e.g. mentioned for CoRoT-2b (Alonso et al. 2008) or TrES-2b (Daemgen et al. 2009). Further information on the reduction process is presented in the data release notes provided by the *Kepler* Data Analysis Working Group[2].

As of February 2013, the *Kepler* space mission has discovered 2321 planetary candidates, 322 of them are observed in SC mode. The false positive rate among the planetary candidates, although still under debate (see Fressin et al. 2013, and references there), appears to be low, of the order of 10%. Due to the longer integration time of LC data, the resulting transit light curves contain less spatial information on the host star than those observed in SC mode. For this reason we restrict our investigation to the planetary candidates recorded in SC mode because we need the highest temporal resolution available to spatially resolve LD on the stellar disk. For all selected light curves we removed invalid data points and all points marked by the SAP_QUALITY flag, and we used *Kepler*'s TIME axis in BJD (adding the BJDREFI value contained in the FITS-header).

2.1.1. High signal-to-noise target sample

For an appropriate analysis of limb darkening we require transit light curves with extremely high SNRs, many data points during the occultations, and short orbital periods to gather as many transits as possible. These are idealized requirements and light

[1] http://archive.stsci.edu/kepler/
[2] http://archive.stsci.edu/kepler/release_notes

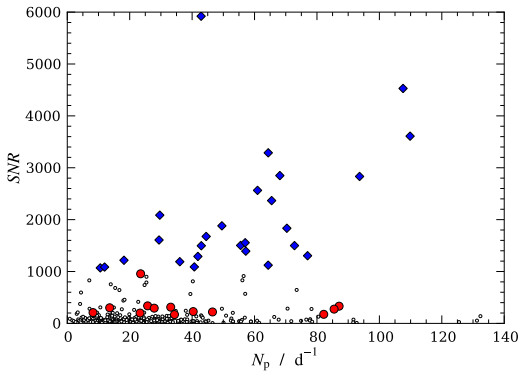

Fig. 1. *Kepler* signal-to-noise ratios (SNR) of short cadence planetary candidates as of 2012/02/27, versus number of transit data points per day (N_p). Large markers indicate our target selection. *Diamonds*: high signal-to-noise sample ($SNR \geq 1000$), *big circles*: sample with high impact parameters $b \geq 0.8$ ($SNR \geq 150$).

curves combining them are rare in real data sets. We made use of the public released Kepler planetary candidates list[3] (KPCL) to select light curves which fulfill these conditions best. This list provides each light curve's SNR (see Borucki et al. 2011, Table 2 and Chap. 4) and important system parameters, such as orbital period and transit duration, for all planetary candidates. To illustrate our selection procedure we show in Fig. 1 the *SNR* value plotted against the number of transit data points per day of each object $N_p = (t_{dur}/t_{cad})P_{orb}^{-1}$, where t_{dur} denotes the transit duration and t_{cad} represents *Kepler*'s cadence of data acquisition (≈60 s). Most objects are found at *SNR* values ≲200 and with less than 50 transit data points per day. To obtain the most reliable results, we only select the 26 objects with a *SNR* larger than 1000 which constitute our high signal-to-noise sample. These objects are listed in Table 1.

2.1.2. Targets with a high impact parameter

Measurements of LDCs strongly depend on the spatial information contained in the transit light curve. In the case of highly inclined transiting systems, synonymous with a large impact parameter, the planet crosses only a limited part of the stellar surface at the limb and the transit does not contain information on the brightness distribution at the disk center. The impact parameter $b = (a/R_S)\cos i$ characterizes the path of the transit across the stellar disk. It depends on the semimajor axis a, normalized by the stellar radius R_S, and the inclination angle i. An impact parameter of $b = 0$ corresponds to an inclination angle of 90°, i.e., a transit passing across the center of the disk, for $b = 1$, the center of the planet touches the stellar limb at transit center.

Howarth (2011b) simulated the effect of an increasing impact parameter on measured LDCs. He showed for different passbands that the measured LDCs show a systematic deviation from the model prediction. This means that a large impact parameter must be accounted for when fitting transit light curves and interpreting the results; most likely the LDCs of such systems will show much larger uncertainties even for very high SNR because the brightness distribution from the center to the limb is not covered by the data.

Following the work of Howarth (2011b) and studies made by our group for TrES-2 (Schröter et al. 2012), we also investigate systems with high impact parameters. Since TrES-2 is the only system in our high signal-to-noise sample with an impact parameter larger than 0.8, we decreased our SNR threshold from 1000 to 150 and selected all objects with an impact parameter $b \geq 0.8$ from the KPCL. This leads to 13 additional systems. One object of this sample turned out to be a highly active binary system and was rejected from the list, leaving the high impact parameter sample with 12 members listed in Table 2.

[3] http://archive.stsci.edu/kepler/planet_candidates.html

Table 1. Our high signal-to-noise target sample ordered by increasing T_{eff}.

Kepler ID	δ/N	T_{eff}/K	log g	Name	$N_{transit}$
5794240	11.5	3948	4.72	Kepler-45b	23
10748390	45.6	4766	4.59	HAT-P-11b	18
11391018	15.1	4787	4.58		7
5357901	10.7	5087	4.59		68
8845026	15.6	5490	4.49		1
9595827	11.3	5504	4.54	BOKS-1b	22
6849046	8.9	5541	4.32		63
9410930	8.9	5585	4.49	Kepler-41b	141
9651668	15.7	5722	4.55		86
8359498	12.2	5731	4.45		97
7023960	15.6	5768	4.50		6
11359879	13.6	5786	4.42	Kepler-15b	70
10619192	17.3	5787	4.45	Kepler-17b	154
11446443	60.6	5814	4.38	TrES-2b	167
12019440	8.8	5826	4.49		74
10874614	17.2	5826	4.42	Kepler-6b	133
7877496	9.4	5912	4.44		153
5780885	15.7	5934	4.04	Kepler-7b	70
9631995	13.6	5972	4.41		47
11804465	22.0	6011	4.23	Kepler-12b	82
6922244	9.9	6025	4.11	Kepler-8b	120
9818381	9.3	6082	4.37	Kepler-43b	114
10019708	6.9	6214	4.41		75
10666592	40.4	6264	3.79	HAT-P-7b	206
8191672	10.7	6297	3.99	Kepler-5b	121
9941662	41.7	8848	3.94	Kepler-13b	92

Notes. T_{eff} and log(g) are taken from the *Kepler* planetary candidates list. δ/N is our mean SNR for the transit signal calculated in Sect. 2.3 and $N_{transit}$ gives the number of transits used for our modeling.

2.2. Light curve normalization

The *Kepler* data show irregular variability caused by instrumental effects and residuals of the reduction process including variations between different *Kepler* quarters. Furthermore, some objects show intrinsic variability, e.g. caused by starspots. Hence every transit light curve requires an individual normalization which we perform by fitting a second order polynomial to the surrounding out-of transit measurements. A simple linear fit is insufficient to properly remove stellar or instrumental variations while higher orders turned out to result in instable fits. We chose a duration of $\Delta t_{conti} = 4.5$ h for the off-transit parts which leads to ≈540 data points used for the normalization of each transit. Equation (2) yields the lower and upper boundary times of the normalization interval calculated relative to the nth transit center $t_{c,n}$. We used the time of the first recorded transit center t_0

Table 2. High-impact-parameter sample (see Sect. 2.1.2).

Kepler ID	δ/N	$T_{\rm eff}$/K	log g	Name	$N_{\rm transit}$
10318874	2.5	4786	4.49		131
5084942	1.4	4915	4.55		114
12105051	2.7	5425	4.50		135
5771719	10.5	5425	4.21		12
2571238	2.2	5541	4.53	Kepler-19b	37
11295426	2.6	5793	4.28	Kepler-68b	39
8456679	2.0	5838	4.42		165
8554498	3.4	5861	4.19		91
8684730	4.3	5952	4.19		2
3762468	3.6	6094	4.41		9
4349452	6.0	6103	4.07	Kepler-25b	17
3861595	4.2	6391	3.81		29

Notes. $N_{\rm transit}$ denotes the total number of transits used for our modeling.

(BJD-2 454 900) and the orbital period $P_{\rm orb}$ given in the planetary candidates list to determine the transit center times $t_{{\rm c},n}$:

$$t_{{\rm c},n} = t_0 + 54\,900 + nP_{\rm orb} \quad (1)$$

$$t_{{\rm conti},\pm} = t_{{\rm c},n} \pm \left(\frac{t_{\rm dur}}{2} + t_{\rm tol} + \Delta t_{\rm conti}\right). \quad (2)$$

To account for inaccurate transit durations and orbital periods possibly contained in the planetary candidates list, we adopted a tolerance $t_{\rm tol}$ of 0.5 h, which results in a buffer of about 30 data points before the start of the transit $t_1 = t_{{\rm c},n} - t_{\rm dur}/2$ and after its end $t_4 = t_{{\rm c},n} + t_{\rm dur}/2$, respectively. Both off-transit parts around a transit had to contain at least four data points each, otherwise the transit was discarded. The total number $N_{\rm total}$ of accepted transit light curves is listed in Table B.1.

Even after removing the data points flagged by the pipeline, a few outlying data points remain that cannot be attributed to noise and should not be taken into account for the normalization process. To identify such outliers we determined the median absolute deviation (MAD) within the selected continuum parts and set $0.6745^{-1}MAD$ as 1σ error (Hampel 1974), which is a robust estimator of the standard deviation of normally distributed data in the presence of outliers; all data points 3σ away from the median of the continuum flux were filtered out.

All transit light curves were normalized by dividing them by a second order polynomial according to

$$\mathcal{F}_{\rm norm}(t) = \frac{\mathcal{F}(t)}{at^2 + bt + c}. \quad (3)$$

The coefficients a, b, and c were determined using a downhill simplex algorithm on the intervals $[t_{{\rm conti},-}, t_1 - t_{\rm tol}]$ and $[t_4 + t_{\rm tol}, t_{{\rm conti},+}]$ minimizing χ^2.

2.3. Assessment of transit data quality

In this section, we revisit the light curve normalization and analyze white and red noise in our transit light curves.

2.3.1. Refining the normalization

To search for poorly normalized transit light curves, we developed a filter algorithm which applies three linear fits to the normalized continuum. The first fit includes the whole 9 h of continuum selected for the normalization. The absolute value of the resulting gradient had to be lower than 1.5×10^{-7} d^{-1}. Transits with higher values were discarded. For the remaining transits the left and right continuum parts were fitted separately. We set a gradient threshold of 1.5×10^{-3} d^{-1} which must not be exceeded by the fits. The threshold values were determined by eye after the inspection of normalized transit light curves; transits showing higher values displayed significant inconsistencies in their normalization.

In addition to this automatic method, it was necessary to discard transits manually, such as in the case where the transits are well normalized but distorted by starspots (HAT-P-11b) or where individual transit light curves show a much larger dispersion of data points than the majority of the other transits. The transit light curves rejected by these two methods are listed in Table B.1. The remaining number of transits used in our analysis is given by $N_{\rm transit}$ in Tables 1 and 2.

2.3.2. Outlier removal and signal to noise

Outlier removal inside transit light curves is difficult if the real transit depth and shape are unknown. To remove prominent outliers, we used a sliding median filter of window size 10 min and rejected all points more than 4σ away.

The transit quality was measured by calculating the mean SNR per transit (δ/N) for each object in our sample. We determine the difference between the continuum level (=1) and the median flux value at transit center $\mathcal{F}_{\rm min}$ determined in a 10 minutes interval around the transit center; this difference was defined to be our transit depth δ and the signal of the planet. We prefer this definition of the transit depth because it does not depend on the transit model. One could also use the radius ratio p resulting from a model fit as an estimator for the transit depth; however, this fit parameter would be correlated to other parameters, especially the LDCs. The noise value was calculated using $0.6745^{-1}MAD$ in the corresponding continuum levels. The resulting mean signal-to-noise values are listed in Tables 1 and 2. We emphasize that these δ/N values are not to be confused with the *SNR* which is used to estimate the photometric quality of a data set (see Fig. 1). The δ/N estimates how much stronger the transit signal is than the photometric noise; for all objects in our samples δ/N is much smaller than the *SNR* values given in the KPCL.

2.3.3. Correlated noise analysis

Parameter estimates based on transit light curve modeling can be severely impeded by red (i.e., correlated) noise, whose sources are manifold including unaccounted for stellar variability and instrumental effects. However, the latter are likely small on transit timescales in the *Kepler* data. Kipping & Bakos (2011b) thoroughly study red noise in the *Kepler* light-curve of TrES-2 and find "no strong evidence for correlated noise".

To check whether our transit light curves are affected by red noise, we follow the approach of Pont et al. (2006), which is based on a comparison of unbinned and binned residuals (see Carter & Winn 2009, Eq. (36)). In this approach red noise, if present, is accounted for in a conventional white-noise analysis by multiplying the measurement errors with a correction factor β.

Our analysis shows that the assumption of uncorrelated noise is justified in 32 of our 38 sample stars. In the remaining six objects we find red noise and correct the error estimates. They are discussed in Sect. 4.

3. Determination of transit parameters

3.1. Analytic transit model

When fitting transit data one has to determine at least five parameters: the center time of the first observed transit t_0, the orbital period $P_{\rm orb}$, the ratio of the stellar and planetary radii p, the inclination angle i, and the semimajor axis $a/R_{\rm S}$. Fitting the stellar limb darkening requires additional fit parameters depending on the adopted limb-darkening law. Here, we choose the quadratic limb-darkening law

$$\frac{I(\mu)}{I(1)} = 1 - u_1(1-\mu) - u_2(1-\mu)^2, \tag{4}$$

introducing two additional parameters u_1 and u_2. The variable μ is defined as $\cos\theta$ where θ is the angle between the line of sight and the inward surface normal pointing to the occulted surface area. Hence, $I(1)$ is the intensity at the disk center where $\theta = 0°$. To model each transit light curve with the given parameters, we used the FORTRAN routine `occultquad`[4] developed and provided by Mandel & Agol (2002), which generates a semi-analytical transit model. We assumed circular orbits ($e = 0$) for all objects in our selection.

3.2. Transit timing and parameter determination

A precise knowledge of the orbital period $P_{\rm orb}$ and time of the transit center t_0 is essential in the fitting process. Clearly, inaccurate values of $P_{\rm orb}$ and t_0 make a correct determination of the remaining transit parameters impossible. Hence, it is essential to determine $P_{\rm orb}$ and t_0 as accurately as possible.

As a first step we used the transit model introduced in Sect. 3.1 to fit these two parameters for each object using a downhill simplex algorithm, keeping all other parameters fixed to the values given in KPCL. The initial values for $P_{\rm orb}$ and t_0 were also taken from that list. The results of this fitting method were used as initial values for an MCMC sampling algorithm (Sect. 3.3).

After determining $P_{\rm orb}$ and t_0, we fitted the remaining parameters: the ratio of the star-planet radii p, the inclination angle i, the semi major axis a, and the quadratic LDCs u_1 and u_2. Again we started with a downhill simplex algorithm with initial parameter values taken from KPCL on the MAST website; afterward, we used these fit results as initial values for our MCMC sampling described in the following. We neither bin nor phase-fold the transit light curves during the fitting process.

3.3. MCMC modeling

We used a Markov chain Monte Carlo (MCMC) approach to sample from the posterior distribution of the parameters using 10^6 iterations of the sampler and discarding a burn-in of 40 000 iterations. The mean values of the parameter traces were then interpreted as the most probable parameters. We used the 68.3% highest probability density intervals (HPD) as our error estimate. For those parameters which require error propagation, such as the impact parameter b, we applied the corresponding equation to the MCMC parameter traces; then the HPD of the parameter can be determined from that new distribution.

The computation time for our 10^6 iterations per object was up to 15 h, depending mainly on the amount of transit light curves. All MCMC calculations make extensive use of routines of `PyAstronomy`[5], a collection of Python routines providing an interface to fitting and sampling algorithms of the PyMC (Patil et al. 2010) and SciPy (Jones et al. 2001) packages.

[4] `http://www.astro.washington.edu/users/agol`

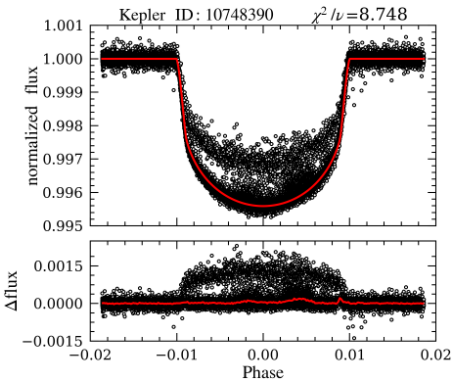

Fig. 2. Normalized and phase-folded transit light curve of HAT-P-11b. The manually deleted transit light curves are included, clearly visible above our best-fit model shown in red. This model only uses 18 out of 95 transits (see Table B.1).

4. Objects requiring special consideration

Some objects in our sample require special treatment, due to instrumental or other peculiarities such as red noise. Their analysis is detailed below.

4.1. HAT-P-11 (KIC 10748390)

HAT-P-11b (KIC 10748390), first reported on by Bakos et al. (2010), shows some transit light curves which cannot be properly normalized using Eq. (3). This is due to the fact that the continuum flux seems to be biased by an additive offset, which differs between the affected transits. The additive term influences the relative transit depth, in particular, higher absolute flux levels lead to a lower value of $1 - \mathcal{F}_{\rm min}$.

The affected transits can be identified in Fig. 2 by a systematic deviation from the transit mean greatly exceeding the statistical noise. Additionally, HAT-P-11A shows starspots transited by the planet resulting in bumps distorting at least some transit profiles (Sanchis-Ojeda & Winn 2011).

In our analysis, we removed all transits that show detectable starspot crossings or cannot be normalized appropriately due to the offset problem (see Table B.1). Nonetheless, we find a red-noise contribution in the residuals of the remaining transit light curves, leading to a correction factor of $\beta \approx 1.49$ (see Sect. 2.3). We ascribe the red noise in this case to unresolved starspot signatures.

4.2. KIC 8845026

The light curve of KIC 8845026 is modulated with a peak-to-peak amplitude of ≈0.2% and a period of roughly 4 days, likely due to rotational modulation. Due to the long orbital period of ≈66.5 d, our data contains only five transits. The transit duration

[5] `http://www.hs.uni-hamburg.de/DE/Ins/Per/Czesla/PyA/PyA/index.html`

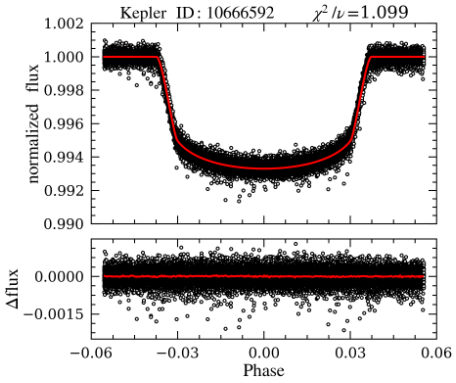

Fig. 3. Normalized and phase-folded transit light curve of HAT-P-7b. Ten manually deleted transit light curves are included.

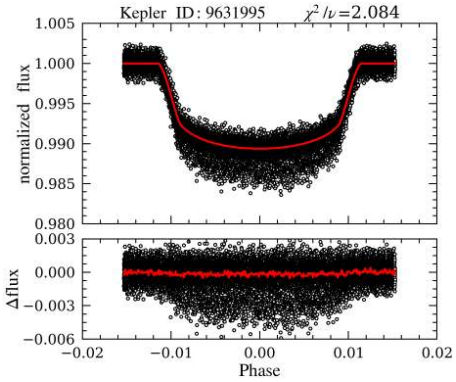

Fig. 4. Normalized and phase-folded transit light curve of KIC 9631995. Eight manually deleted transit light curves are included in this figure.

amounts to nearly 20 h, which is comparable to the observed variability timescales and affects the transit profile. Thus, we find that different transits cannot be consistently normalized and show different depths after normalization. We decided to limit our analysis to the transit light curve showing the lowest red-noise contribution ($\beta = 1.36$).

4.3. HAT-P-7b and KIC 9631995

Figures 3 and 4 show the normalized and phase-folded transit light curves of KIC 10666592 (HAT-P-7b, Pál et al. 2008) and KIC 9631995. Our filter algorithm introduced in Sect. 2.3 found all transits to be well normalized for both objects. Also our outlier removal showed no inconsistencies for the transits of these data sets. However, some transit light curves had to be removed manually because they show outliers significantly below the average light curve and a stronger dispersion probably caused by instrumental effects or the data reduction. While KIC 9631995 shows white noise in the remaining transit light curves, we find red noise in HAT-P-7b and corrected for it by using $\beta = 1.60$.

4.4. Kepler-17b and KIC 3861595

Kepler-17b (KIC 10619192) shows red noise in the residuals of our transit modeling (see Fig. B.2, last row). Its light curve has previously been discussed by Désert et al. (2011), who report rotational variability with a peak-to-peak amplitude on the order of 3% and prominent starspot crossing events. Therefore, the correlated noise is likely attributable to starspots. Our analysis yields a correction factor of $\beta \approx 1.65$.

The situation is similar for KIC 3861595, a member of our high impact parameter sample, in the light curve of which we also detect red noise, leading to $\beta \approx 1.94$. Its light curve shows potential rotational modulation with a peak-to-peak amplitude of about half a percent. Consequently, the red noise may be introduced by starspot crossings for this object.

4.5. Kepler-13

Kepler-13 (KIC 9941662) transits the hottest star of our sample. Its light curve has been studied by Barnes et al. (2011), who report on an asymmetry in the model residuals which they attribute to gravitational darkening. The same asymmetry is seen in our analysis, resulting in a red noise detection ($\beta \approx 1.40$). Furthermore, the *Kepler* aperture contains a second star contributing about 45% of the observed flux (Szabó et al. 2011), which we take into account in our modeling. We argue that the asymmetry introduced by gravitational darkening is on the order of 10^{-4} and does not severely affect our analysis. Furthermore, we verified that the limb-darkening coefficients do only slightly depend on the third light contribution (in the order of $\approx \pm 0.01$), which is relatively well known. Therefore, we retain Kepler-13 in our sample.

5. Results and discussion

In Table 3 we show the results of our transit modeling, which we use in the following analysis. We compare these results to the quadratic LDCs predicted by Claret & Bloemen (2011) for *Kepler*'s spectral response function. Table 3 shows all seven determined transit parameters for all objects in our sample. In Sect. 5.2 we provide a detailed discussion on the fitted LDCs of our high signal-to-noise sample.

5.1. Theoretical LDCs

The key aim of our study is the comparison of our LD measurements with model LDCs determined from stellar atmosphere models. To this end we use the LDCs of Claret & Bloemen (2011). They are given in tables[6] on which we linearly interpolate. The coefficients are determined from 1D-plane-parallel PHOENIX and ATLAS model atmospheres using two different methods (Claret 2000, Chap. 2.2): a flux-conserving fit method and a simple least squares fit to the theoretical stellar intensity distribution. These two fit methods lead to slightly different values of u_1 and u_2.

In Figs. 5 and 7 we show theoretical LDCs as a function of effective temperature derived from stellar atmosphere models with surface gravity $\log(g) = 4.5$, metallicity [M/H] = 0.0, and micro-turbulent velocity $\xi = 2.0\,\mathrm{km\,s^{-1}}$, in comparison to our measured LDCs. LDCs assigned as dotted lines come from the flux conserving fit method.

[6] http://vizier.u-strasbg.fr/viz-bin/VizieR?-source=J/A%2BA/529/A75

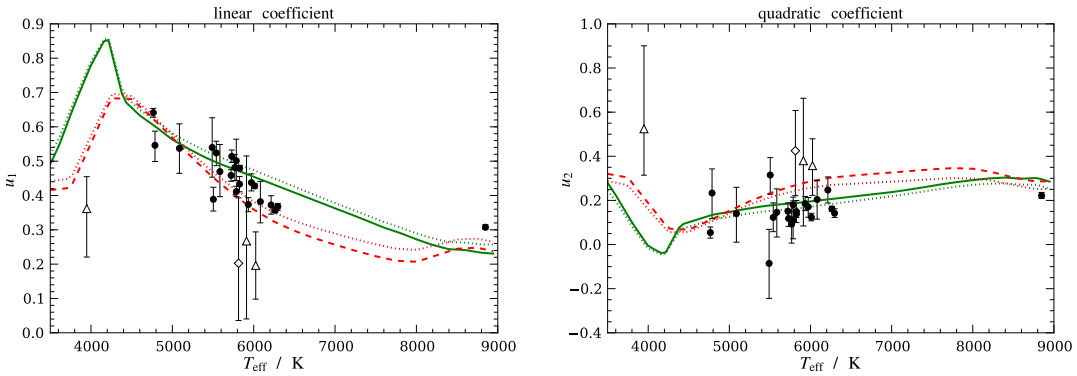

Fig. 5. Quadratic LDCs determined by MCMC for our high signal-to-noise target sample (see Table 1). For comparison, the graphs show model predictions based on PHOENIX (solid) and ATLAS (dashed) atmospheric models, taken from Claret & Bloemen (2011). The dotted lines show Claret and Bloemen's LDCs determined for the same atmospheres by different methods (see Sect. 5.1). The diamond symbol indicates TrES-2, which has the highest impact parameter of this sample ($b = 0.845$). Triangles mark conspicuous objects, discussed in Sect. 5.3.

Apparently the LDCs do not only depend on the effective temperature but also on the other stellar parameters. The parameters used to derive the theoretical LDCs presented in Figs. 5 and 7 may not be appropriate for all stars in our sample. To estimate the influence of surface gravity and metallicity on the LDCs, we investigated different parameter sets and present the results in Figs. A.1 and A.2. We conclude that changes in metallicity or surface gravity in the ranges reasonable for our sample, have only a small effect on the predicted quadratic LDCs for stars in the temperature range of 4600 to 7800 K. Objects colder than $T_{\rm eff} \lesssim 4600$ K show a stronger dependence on these parameters. This is important for the analysis of the coldest object in our selection. The theoretical LDCs determined from PHOENIX model atmospheres for each object, adopting the surface gravities from the KPCL, are listed in Table 3.

5.2. High signal-to-noise sample

Looking at the left panel of Fig. 5, we identify four objects that lie significantly below the theoretical predictions and have large error bars. Three are marked with triangles, TrES-2 is specifically marked with a diamond symbol. They have effective temperatures of 3948 K, 5814 K (TrES-2), 5912 K, and 6025 K, listed in Table 1. The right panel of Fig. 5 shows the measured values of u_2. Again the same four objects lie among those with the largest errors, we discuss them in detail in Sect. 5.3.

Out of 26 objects 21 show a good agreement, within their errors, with at least one of the model predictions of u_1. In contrast, the theoretical values of u_2 tend to be systematically too high in the temperature range between 5300 to 6500 K. Subtracting an offset of ≈0.05 leads to a significantly better agreement between the measurements and the predictions of u_2. Most of the fitted LDCs are consistent with those determined from one of the two model atmospheres, whereas the PHOENIX predictions seem to be the better choice for u_2 in the regime of $T_{\rm eff} > 4600$ K.

Most objects of our sample have effective temperatures between 5000 K and 6400 K, which corresponds to F-, G-, and K-stars. Only a few exceptions, such as the ones at ≈4000 K and ≈8900 K, are lying outside of this conglomerate. Thus, our analysis of LDCs will be most reliable in the regime of solar-like stars, where we have a significant number of objects; the two exceptions can serve as indicators for the reliability of theoretical LDCs in more extreme regimes.

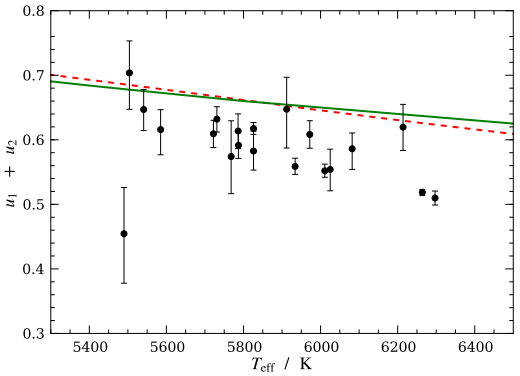

Fig. 6. Sum of the linear and quadratic limb-darkening coefficients for objects with an impact parameter $b < 0.8$ of our high signal-to-noise sample in comparison to the summed model predictions (solid: PHOENIX, dashed: ATLAS).

For a better illustration of the agreement between measured and theoretical LDCs, we present the sum of the quadratic LDCs $u_1 + u_2$ in Fig. 6 in the temperature range of 5300 K to 6500 K in which most objects of our sample are located. In this case the theoretical predictions from PHOENIX and ATLAS models are virtually identical. If the observed u_1 and u_2 are independently consistent with the models, their sum has to agree with the theory as well. However, out of 20 objects only four lie on the model predictions within their errors while 16 objects show significantly lower values. The median value of the residuals is $\Delta_{u_1+u_2} = -0.07 \pm 0.01$. As already seen for the values of u_2, there appears to be an offset between measurements and predictions, which is, at least in the case of PHOENIX models, largely caused by a systematic shift of the u_2 values. This indicates that the coefficient of the quadratic term in the LD law is slightly overestimated by theory, as already suggested by the right panel of Fig. 5.

A&A 560, A112 (2013)

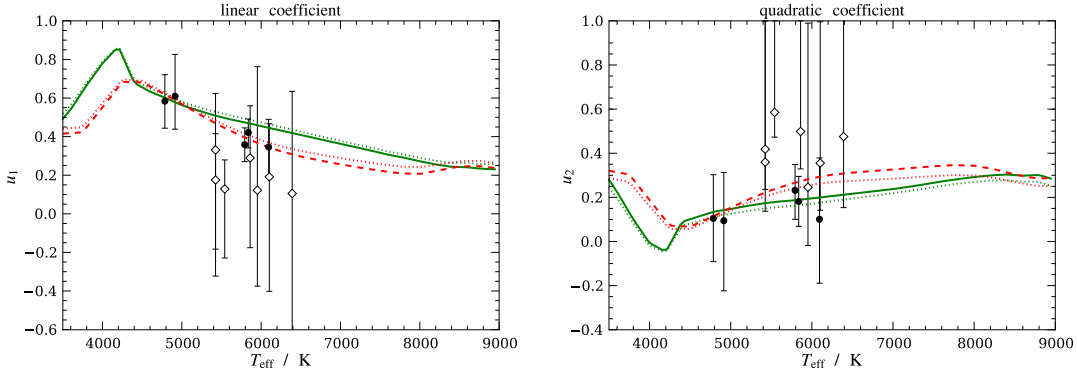

Fig. 7. Same as Fig. 5 for objects with impact parameters larger than 0.8 as given in the *Kepler* planetary candidates list (i.e. our high-impact-parameter sample, see Table 2). According to *our* transit modeling only objects marked with *diamonds truly* have $b \geq 0.8$ while we found $b < 0.8$ for the objects indicated by *dots*.

5.3. Outlier objects

Figure 5 contains several points with relatively large errors. In this section we discuss the four objects with the highest uncertainties in both LDCs u_1 and u_2, which are also the objects with the largest deviation from the predictions. In the left panel of Fig. 5, these objects lie clearly below the LDC predictions and are marked with triangles and a diamond symbol. Below, we discuss them in order of increasing effective temperature.

According to the KPCL, the first "outlier", KIC 5794240, has an effective temperature of 3948 K and a surface gravity of $\log(g) = 4.72$. Most objects in the KPCL have $T_{\rm eff}$ credible to within ±200 K and $\log(g)$ with errors of about ±0.4 (Brown et al. 2011). As already stated in Sect. 5.1, the theoretical predictions in Fig. 5 are based on atmosphere models with $\log(g) = 4.5$. Although this is consistent with the estimated error of the measured $\log(g)$, the influence of $\log(g)$ on the LDCs becomes important for $T_{\rm eff} \lesssim 4600$ K (see Fig. A.1), which is the case for KIC 5794240. In this temperature range an increase in $\log(g)$ leads to significantly lower values of u_1. An agreement with the measurement is reached for a $\log(g)$ of about 5.0 using ATLAS model atmospheres. Surface gravities of 5.0 or higher are not uncommon for M5-dwarfs (see PASTEL catalog, Soubiran et al. 2010) and are fully consistent with the above error estimate.

The metallicity $Z = [{\rm M/H}]$ also has a significant influence on u_1 and u_2 in this temperature region (see Fig. A.2). Potentially, the Z value of KIC 5794240 (=0.2) is poorly determined since most metallicities of the KPCL are highly uncertain (Brown et al. 2011). A lower metallicity of, e.g., $[{\rm M/H}] = -0.3$, leads to theoretical LDCs consistent with the observation. In the light of our analysis, a subsolar metallicity of KIC 5794240 seems to be more reasonable than its super-solar metallicity stated in the Kepler Input Catalog (Brown et al. 2011).

Finally, the light curve of KIC 5794240 indicates substantial stellar activity. The visible photometric variations suggest rotational modulation due to starspots. It is reasonable to expect that some of the spots are occulted by the planet when crossing the disk, leading to deformations of the transit profile (see, e.g., Huber et al. 2010). The detailed investigation of how starspots influence the determination of LDCs is beyond the scope of this work, however, the strong temperature dependence of LD suggests a non-negligible effect for substantially spotted stars. Thus, the inconsistency with the model and the large uncertainties of the measured LDCs of KIC 5794240 could also reflect the effects of stellar activity on its light curve.

The diamond symbol in Fig. 5 marks the second "outlier", TrES-2, an intensively studied exoplanetary system. It has the highest SNR of all planet host stars in the *Kepler* sample. Nonetheless, the uncertainties of the LDCs are large ($\sigma \approx \pm 0.2$) compared to other objects with lower SNRs, and the determined LDCs are inconsistent with the model predictions. However, TrES-2 has a rather large impact parameter of $b = 0.85$ and, therefore a nearly grazing transit, which is the reason for the big uncertainties of the measured LDCs and the large deviation from theory. We investigate this behavior in Sect. 5.4 in detail.

The last two objects of our outlier sample, KIC 7877496 and KIC 6922244 (Kepler-8b), show the same behavior as TrES-2. The number of available and fitted transit light curves for both objects are comparable to TrES-2. These systems also have high impact parameters of $b \approx 0.8$ (see Table 3) which causes the strong deviation from the theoretical LDCs of these objects and big uncertainties.

5.4. Objects with high impact parameters

As discussed in the previous section, TrES-2, Kepler-8, and KIC 7877496 show a common behavior due to their large impact parameters: they exhibit large uncertainties in their fitted LDCs and lie below the theoretical models for u_1 and above for u_2. A similar behavior has already been found by Howarth (2011b) who simulated the influence of a high impact parameter on the determination of quadratic LDCs.

To further investigate this behavior, we analyze a sample of twelve objects with impact parameters larger than 0.8 as given in the KPCL (see also Sect. 2.1.2 and Table 2). Our measured quadratic LDCs are presented in Fig. 7 and compared to the same theoretical values as in Fig. 5.

According to our transit modeling, 5 of the 12 objects actually have $b < 0.8$ (see Table 3). For those systems, the impact parameters of the KPCL appear to be incorrect. These objects, marked as dots in the figure, agree well with the model predictions. The others have impact parameters of $b > 0.8$ (diamond symbols) and significantly deviate from theory in the same manner as those discussed in Sect. 5.3. Again we can see that u_1 is

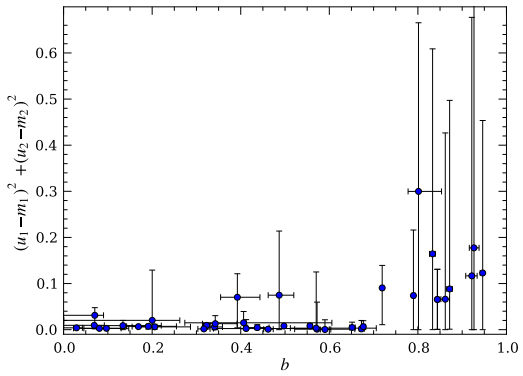

Fig. 8. Summed quadratic deviation of measured LD coefficients from those calculated from PHOENIX models versus impact parameter.

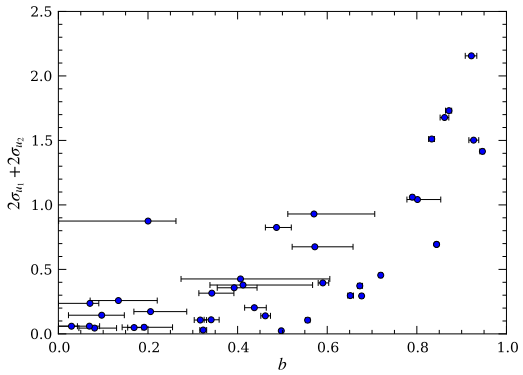

Fig. 9. Summed width of the 68.3% HPD intervals for u_1 and u_2 versus the impact parameter b as determined by MCMC. See text for details.

systematically underestimated while the values of u_2 lie above the prediction.

Figure 8 illustrates the increase in the deviation between measurements and theory with increasing impact parameter. It shows the sum of the squared differences between the measured LDCs and the PHOENIX model predictions denoted by m_1 and m_2 as a function of b for all objects of our study. The differences between measurements and theory are small for impact parameters up to about 0.8. However, for objects with impact parameters $b \gtrsim 0.8$ the deviations from the model predictions as well as the measurement errors increase significantly. Hence, for impact parameters exceeding about 0.8 a reliable determination of LDCs from a transit light curve fit becomes intricate.

A similar behavior as found in Fig. 8 can also be seen if only the measurement errors are considered – independently of the atmospheric model predictions (m_1 and m_2). This is shown in Fig. 9, where we plot the summed widths of the 68.3% credibility intervals for u_1 and u_2, against our measured system impact parameters. For b around 0.8 and larger, a considerable increase in the resulting uncertainties is detectable. It seems that there is some transition at $b \approx 0.8$ where the determination of LDCs becomes much more difficult. We discuss this behavior in more detail in Sect. 5.6.

Setting the LDCs as free fit parameters influences the determination of the remaining transit parameters due to strong correlations. This applies especially to the case of large b, as a consequence it is highly inadvisable to fit the LDCs in systems with high impact parameters.

5.5. Deviations between measured and predicted LDCs and their influence on transit modeling

Figure 5 illustrates the key result of our study, namely the relation between the measured and predicted limb-darkening coefficients. Considering the difference between the PHOENIX and ATLAS model predictions as the systematic uncertainty of the theoretical LDCs, we find that our values derived for the linear coefficient u_1 are fully consistent with the models within these uncertainties. Thus, the predictions of u_1 span an allowed band of coefficients confirmed by our measurements. On the other hand, both ATLAS and PHOENIX tend to overestimate the quadratic LDC u_2 when compared to our measurements.

The typical deviation between our measurements and the model predictions amounts to about 0.05 both in u_1 and u_2. We estimated the influence of such deviations in the LDCs on the planetary parameters derived by transit modeling: as outlined in Sect. B.5, we derive a Gaussian approximation for the posterior probability distribution, modify the limb-darkening coefficients based on the alleged deviations,

Assuming that the discrepancy in $\Delta_{u_1+u_2}$ (cf., Sect. 5.2) is exclusively caused by a deviation in u_2, we use this approach to derive average relative changes of $\Delta a/a = 1.3\%$, $\Delta i/i = 0.4\%$, and $\Delta p/p = -0.6\%$. Comparing our LD measurements to the PHOENIX predictions, we find average offsets of $\Delta u_1 = -0.05 \pm 0.01$ and $\Delta u_2 = -0.03 \pm 0.01$. These translate into relative parameter changes of $\Delta a/a = 1.6\%$, $\Delta i/i = 0.5\%$ and $\Delta p/p = -0.7\%$. Hence, the deviations in the LDC found in our study result in moderate errors on the order of one percent in relative accuracy with the semimajor axis responding most sensitively to changes in the LDCs.

5.6. Correlation between the quadratic LDCs and their systematic uncertainties

In the previous sections, we have demonstrated that the quadratic LDCs u_1 and u_2 can be determined with small measurement errors and that the result is in reasonable agreement with theory for *small* and *moderate* impact parameters. Our MCMC analysis shows that both LDCs are strongly correlated. If we take a look at the combination $u_C = u_1 + u_2$, we see that this parameter has a substantially lower error than the two coefficients alone. It seems to be an inherent property of the quadratic LD model that the combination u_C is always much better constrained than the individual LDCs.

This is even the case for systems with $b \gtrsim 0.8$. Here, u_1 and u_2 show large errors and deviations from theory, but their sum u_C shows significantly smaller errors and is still consistent with the model predictions. The sum of u_1 and u_2 is presented in Fig. 10 along with the theoretical LDCs; the deviations from the theory are significantly smaller than in Fig. 7 for the individual coefficients.

As already pointed out by Schröter et al. (2012, Eq. (1)), the quadratic LD law can be approximated by a constant function

$$\frac{I}{I(1)} = 1 - (u_1 + u_2) \tag{5}$$

A&A 560, A112 (2013)

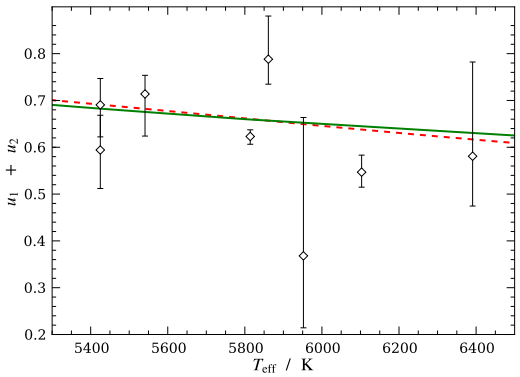

Fig. 10. Sum of the linear and quadratic coefficients $u_C = u_1 + u_2$ for objects with an impact parameter $b > 0.8$ in comparison to the summed model predictions (*solid*: PHOENIX, *dashed*: ATLAS).

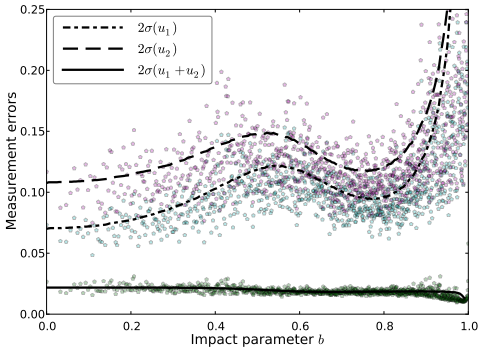

Fig. 11. Simulated measurement errors (*dots*) for the individual LDCs u_1 (*cyan*), u_2 (*purple*) and for the sum $u_1 + u_2$ (*green*) as determined by transit modeling. For the simulation we used fixed parameters only the impact parameter was varied between 0 and 1. The overplotted *lines* show our analytical solutions (see Appendix B for details).

under the assumption $\mu \ll 1$, i.e. systems with very high impact parameters[7]. Physically, this means that one only measures the brightness at the stellar limb, which does not show a functional relation to μ anymore but is only a constant difference to the central brightness $I(1)$. In such systems a transit fit would only be sensitive to the sum of the LDCs.

Although this certainly is part of the explanation, our analysis shows that the situation is more complex. We present an analytical approximation for the errors of the LDCs in Appendix B. We find that u_C is *always* better constrained than the individual coefficients *independent* of the impact parameter, which is a general characteristic of the quadratic LD law; this result is visualized in Fig. 11. Only for high values of b we find that the individual LDCs are *virtually* unconstrained by transit modeling.

The analytical solution given in Appendix B allows investigating the errors and the correlation of u_1 and u_2. We compare our results to simulations using a transit model with fixed planetary parameters; only the impact parameter is varied between 0 and 1. Our results are presented in Figs. 11 and B.1. The behavior of the simulations is reproduced by theory: the measurement errors of u_1 and u_2 are smallest for low impact parameters and dramatically increase for $b \gtrsim 0.8$. This resembles our observations. Interestingly, the error does not increase monotonically, but decreases slightly after a local maximum at about $b \approx 0.5$ before it rises steeply again. This means that LDCs are slightly better constrained for values of ≈0.8 than for values of ≈0.5.

Our simulations and our analytical treatment show the same behavior of the correlation of u_1 and u_2 as a function of the impact parameter. Both coefficients are highly anti-correlated even for small impact parameters. Their correlation coefficient decreases to -1 for $b \approx 1$, where their individual errors increase rapidly. This is the explanation for the behavior visible in Fig. 7, where u_1 and u_2 values for high impact parameters have not only much larger errors but also lie systematically below the prediction for u_1 and above it for u_2. Their strong anti-correlation is well visible in this regime and a shift of u_1 in one direction is compensated by a shift of u_2 to the other direction.

[7] For e.g. $b = 0.85$, the maximum value of μ transited by the planet is $\mu_{\rm max} \approx 0.5$. Clearly, this does not comply with $\mu \ll 1$.

6. Summary and conclusions

The measurement of stellar limb darkening (LD) is notoriously difficult, because almost no stellar disk can be spatially resolved. A new and promising opportunity to measure stellar LD is the use of high-precision transit light curves. Here, the planet serves as a scanner of the stellar brightness distribution during its disk passage.

From the list of *Kepler* planetary candidates, we construct two samples: (1) a high signal-to-noise sample with 26 objects and (2) a sample comprising 12 high impact-parameter systems ($b \geq 0.8$). However, according to our transit modeling, only seven of the alleged 12 planetary systems in our high impact-parameter sample truly deserve this designation. The majority of our sample objects are late F-, G-, and early K-type main-sequence stars spanning an effect temperature range from 4600 K to 6400 K.

We measure the quadratic LDCs u_1 and u_2 using a Bayesian MCMC approach and compare them to theoretical predictions based on PHOENIX and ATLAS stellar atmosphere models. Our results show that reliable limb-darkening coefficients (LDCs) can be determined using the most accurate transit observations of the *Kepler* space telescope.

The differences between the PHOENIX and ATLAS model predictions are as large as 0.1 in both LDCs in the effective-temperature regime under consideration. For the linear coefficient, u_1, our measurements are mainly distributed between the PHOENIX and ATLAS model predictions. Interpreting the deviation between the models as systematic uncertainty, we argue that our u_1 measurements agree with the theoretical predictions. In fact, they are equally consistent with either.

For the quadratic coefficient, u_2, our measurements do show a systematic offset: most of our measurements lie below the predictions of both atmospheric models. However, on average, u_2 deviated by -0.1 from the ATLAS and by -0.03 from the PHOENIX models. This yields $\chi^2_{\rm PHOENIX} = \chi^2_{\rm ATLAS}/4$ making the PHOENIX models a better fit.

Nonetheless, our measurements show a slightly weaker limb darkening than either model. Interestingly, the 3D-hydrodynamic atmospheric models presented by Asplund et al. (2009) predict a LD weaker by an amount comparable to our findings (see also Hayek et al. 2012; Trampedach et al. 2013).

However, this prediction is not universally shared among hydrodynamic 3D models (Hauschildt & Baron 2010).

An important factor for the measurement of LDCs is the impact parameter of a system. All our measurements for objects with high impact parameters show deviations from the theoretical LDCs. This has already been suggested by simulations (Howarth 2011b). According to our Figs. 8 and 9, we find that impact parameters in the range of $b \gtrsim 0.8$ are critical in the sense that for those the uncertainties in u_1 and u_2 increase drastically. Only their sum $u_1 + u_2$ can still be reliably determined. This behavior can be reproduced in our analytical approximation of the transit modeling with quadratic LDCs.

We note that the surface gravity $\log(g)$ and metallicity Z significantly influence the theoretical LDCs only for effective temperatures below 4500 K and in a narrow region above 7500 K. For stars outside these temperature ranges, i.e., all but two of our sample stars, the theoretical LDCs can be used without introducing a severe error resulting from inaccurately known $\log(g)$ and Z values.

Although we do find a deviation between theory and measurements, we estimate that the error propagated into the remaining fit parameters by fixing the LDCs to theoretical values amounts to roughly one percent for the semimajor axis, inclination, and planetary radius determined by light curve modeling and thus should be negligible for many applications.

Therefore, we conclude that the quadratic LDCs can be fixed to theoretical values (e.g., tabulated by Claret & Bloemen 2011) in the process of transit analysis. For high impact parameter systems ($b \gtrsim 0.8$) or observations with significantly lower *SNR* than the *Kepler* data, we even recommend to fix the LDCs to model predictions, since the LDCs remain badly constrained by transit modeling in both cases.

Acknowledgements. This paper includes data collected by the *Kepler* mission. Funding for the *Kepler* mission is provided by the NASA Science Mission directorate. The *Kepler* observations were obtained from the NASA Mikulski Archive for Space Telescopes (MAST). H.M.M. is supported in the framework of the DFG-funded Research Training Group *Extrasolar Planets and their Host Stars* (DFG 1351/2).

References

Alonso, R., Auvergne, M., Baglin, A., et al. 2008, A&A, 482, L21
Asplund, M., Grevesse, N., Sauval, A. J., & Scott, P. 2009, ARA&A, 47, 481
Bakos, G. Á., Torres, G., Pál, A., et al. 2010, ApJ, 710, 1724
Barnes, J. W., Linscott, E., & Shporer, A. 2011, ApJS, 197, 10
Batalha, N. M., Rowe, J. F., Bryson, S. T., et al. 2013, ApJS, 204, 24
Bordé, P., Bouchy, F., Deleuil, M., et al. 2010, A&A, 520, A66
Borucki, W. J., Koch, D. G., Basri, G., et al. 2011, ApJ, 736, 19
Brown, T. M., Latham, D. W., Everett, M. E., & Esquerdo, G. A. 2011, AJ, 142, 112
Buchhave, L. A., Latham, D. W., Johansen, A., et al. 2012, Nature, 486, 375
Caffau, E., Steffen, M., Sbordone, L., Ludwig, H.-G., & Bonifacio, P. 2007, A&A, 473, L9
Carter, J. A., & Winn, J. N. 2009, ApJ, 704, 51
Carter, J. A., Yee, J. C., Eastman, J., Gaudi, B. S., & Winn, J. N. 2008, ApJ, 689, 499
Casagrande, L., Schönrich, R., Asplund, M., et al. 2011, A&A, 530, A138
Charbonneau, D., Brown, T. M., Latham, D. W., & Mayor, M. 2000, ApJ, 529, L45
Claret, A. 2000, A&A, 363, 1081
Claret, A. 2008, A&A, 482, 259
Claret, A., & Bloemen, S. 2011, A&A, 529, A75
Csizmadia, S., Pasternacki, T., Dreyer, C., et al. 2013, A&A, 549, A9
Daemgen, S., Hormuth, F., Brandner, W., et al. 2009, A&A, 498, 567
D'Agostini, G. 2003, Rep. Prog. Phys., 66, 1383
Demarque, P., Woo, J.-H., Kim, Y.-C., & Yi, S. K. 2004, ApJS, 155, 667
Désert, J.-M., Charbonneau, D., Demory, B.-O., et al. 2011, ApJS, 197, 14
Fressin, F., Torres, G., Charbonneau, D., et al. 2013, ApJ, 766, 81
Hampel, F. R. 1974, J. Am. Stat. Assoc., 69, 383
Haubois, X., Perrin, G., Lacour, S., et al. 2009, A&A, 508, 923
Hauschildt, P. H., & Baron, E. 2010, A&A, 509, A36
Hayek, W., Sing, D., Pont, F., & Asplund, M. 2012, A&A, 539, A102
Heyrovský, D. 2007, ApJ, 656, 483
Howarth, I. D. 2011a, MNRAS, 413, 1515
Howarth, I. D. 2011b, MNRAS, 418, 1165
Huber, K. F., Czesla, S., Wolter, U., & Schmitt, J. H. M. M. 2010, A&A, 514, A39
Jones, E., Oliphant, T., Peterson, P., et al. 2001, SciPy: Open source scientific tools for Python, http://www.scipy.org
Kipping, D., & Bakos, G. 2011a, ApJ, 730, 50
Kipping, D., & Bakos, G. 2011b, ApJ, 733, 36
Knutson, H. A., Charbonneau, D., Noyes, R. W., Brown, T. M., & Gilliland, R. L. 2007, ApJ, 655, 564
Kopal, Z. 1950, Harvard College Observatory Circular, 454, 1
Mandel, K., & Agol, E. 2002, ApJ, 580, L171
Neckel, H., & Labs, D. 1994, Sol. Phys., 153, 91
Nesvacil, N., Lüftinger, T., Shulyak, D., et al. 2012, A&A, 537, A151
Ohta, Y., Taruya, A., & Suto, Y. 2005, ApJ, 622, 1118
Pál, A. 2008, MNRAS, 390, 281
Pál, A., Bakos, G. Á., Torres, G., et al. 2008, ApJ, 680, 1450
Patil, A., Huard, D., & Fonnesbeck, C. J. 2010, J. Stat. Software, 35, 1
Pont, F., Zucker, S., & Queloz, D. 2006, MNRAS, 373, 231
Press, W. H., Teukolsky, S. A., Vetterling, W. T., & Flannery, B. P. 2002, Numerical recipes in C++: the art of scientific computing (Cambridge University Press)
Russell, I. H. N., & Shapley, H. 1912, ApJ, 36, 239
Sanchis-Ojeda, R., & Winn, J. N. 2011, ApJ, 743, 61
Schröter, S., Schmitt, J. H. M. M., & Müller, H. M. 2012, A&A, 539, A97
Schwarzschild, K. 1906, Nachrichten von der Gesellschaft der Wissenschaften zu Göttingen, Mathematisch-Physikalische Klasse, 41
Sing, D. K. 2010, A&A, 510, A21
Soubiran, C., Le Campion, J.-F., Cayrel de Strobel, G., & Caillo, A. 2010, A&A, 515, A111
Southworth, J. 2008, MNRAS, 386, 1644
Szabó, G. M., Szabó, R., Benkő, J. M., et al. 2011, ApJ, 736, L4
Trampedach, R., Asplund, M., Collet, R., Nordlund, Å., & Stein, R. F. 2013, ApJ, 769, 18
Valenti, J. A., & Piskunov, N. 1996, A&AS, 118, 595
van Hamme, W. 1993, AJ, 106, 2096
Wade, R. A., & Rucinski, S. M. 1985, A&AS, 60, 471
Wedemeyer, S., Freytag, B., Steffen, M., Ludwig, H.-G., & Holweger, H. 2004, A&A, 414, 1121

Pages 12 to 20 are available in the electronic edition of the journal at http://www.aanda.org

Table 3. Transit modeling results.

Kepler ID	χ^2/ν	t_0/BJD-2400000	$P_{\rm orb}$/d	p	$i/^\circ$	$a/R_{\rm S}$	b	u_1	u_2	m_1	m_2
5794240	1.01	$55374.562419^{+0.000093}_{-0.000091}$	$2.455233922^{+0.000004964}_{-0.000004646}$	$0.18409^{+0.00343}_{-0.00309}$	$87.49^{+0.14}_{-0.18}$	$11.113^{+0.115}_{-0.119}$	$0.487^{+0.033}_{-0.025}$	$0.362^{+0.093}_{-0.141}$	$0.525^{+0.376}_{-0.210}$	0.459	0.269
10748390	1.58	$54957.812605^{+0.000022}_{-0.000020}$	$4.887801513^{+0.000000332}_{-0.000000392}$	$0.05891^{+0.00021}_{-0.00025}$	$89.34^{+0.17}_{-0.23}$	$16.510^{+0.182}_{-0.172}$	$0.191^{+0.063}_{-0.049}$	$0.641^{+0.012}_{-0.013}$	$0.054^{+0.025}_{-0.025}$	0.604	0.130
11391018	1.11	$55193.613335^{+0.000265}_{-0.000267}$	$30.360537304^{+0.000047543}_{-0.000048105}$	$0.13326^{+0.00142}_{-0.00108}$	$89.53^{+0.05}_{-0.07}$	$41.356^{+0.443}_{-0.478}$	$0.342^{+0.049}_{-0.029}$	$0.546^{+0.041}_{-0.047}$	$0.233^{+0.109}_{-0.116}$	0.600	0.133
5357901	0.99	$55186.735148^{+0.000061}_{-0.000060}$	$3.797016682^{+0.000001398}_{-0.000001544}$	$0.11665^{+0.00081}_{-0.00068}$	$87.11^{+0.07}_{-0.08}$	$11.712^{+0.080}_{-0.084}$	$0.590^{+0.013}_{-0.010}$	$0.537^{+0.071}_{-0.073}$	$0.140^{+0.119}_{-0.129}$	0.551	0.152
8845026	0.91	$55192.874587^{+0.000551}_{-0.000546}$	$66.468599870^{+0.000196987}_{-0.000209565}$	$0.10902^{+0.00091}_{-0.00084}$	$89.16^{+0.10}_{-0.12}$	$26.672^{+0.463}_{-0.496}$	$0.392^{+0.051}_{-0.038}$	$0.540^{+0.086}_{-0.087}$	$-0.085^{+0.154}_{-0.159}$	0.502	0.177
9595827	1.24	$55372.542724^{+0.000100}_{-0.000109}$	$3.905079476^{+0.000007906}_{-0.000008610}$	$0.13602^{+0.00050}_{-0.00055}$	$89.66^{+0.34}_{-0.09}$	$11.834^{+0.069}_{-0.042}$	$0.070^{+0.020}_{-0.070}$	$0.389^{+0.035}_{-0.034}$	$0.315^{+0.079}_{-0.087}$	0.500	0.178
6849046	1.01	$55186.054615^{+0.000078}_{-0.000071}$	$4.225382002^{+0.000001974}_{-0.000001896}$	$0.08179^{+0.00040}_{-0.00040}$	$87.76^{+0.13}_{-0.16}$	$11.172^{+0.121}_{-0.133}$	$0.437^{+0.027}_{-0.022}$	$0.524^{+0.034}_{-0.037}$	$0.123^{+0.066}_{-0.065}$	0.496	0.184
9410930	1.02	$55187.280522^{+0.000055}_{-0.000057}$	$1.855557735^{+0.000000625}_{-0.000000631}$	$0.10275^{+0.00046}_{-0.00045}$	$82.51^{+0.09}_{-0.10}$	$5.163^{+0.024}_{-0.024}$	$0.673^{+0.006}_{-0.005}$	$0.470^{+0.079}_{-0.073}$	$0.146^{+0.106}_{-0.112}$	0.492	0.181
9651668	1.05	$55186.469037^{+0.000036}_{-0.000036}$	$2.684326788^{+0.000000753}_{-0.000000661}$	$0.12662^{+0.00029}_{-0.00028}$	$87.78^{+0.10}_{-0.11}$	$8.163^{+0.030}_{-0.034}$	$0.317^{+0.014}_{-0.014}$	$0.459^{+0.017}_{-0.017}$	$0.151^{+0.038}_{-0.035}$	0.479	0.186
8359498	1.04	$55095.865683^{+0.000042}_{-0.000047}$	$3.578781383^{+0.000000768}_{-0.000000776}$	$0.09958^{+0.00026}_{-0.00026}$	$88.00^{+0.10}_{-0.12}$	$9.749^{+0.054}_{-0.055}$	$0.341^{+0.018}_{-0.016}$	$0.514^{+0.019}_{-0.018}$	$0.118^{+0.037}_{-0.036}$	0.479	0.186
7023960	1.01	$55200.706412^{+0.000307}_{-0.000290}$	$30.882587765^{+0.000063027}_{-0.000059394}$	$0.14590^{+0.00065}_{-0.00088}$	$89.85^{+0.08}_{-0.10}$	$49.734^{+0.481}_{-0.303}$	$0.134^{+0.087}_{-0.063}$	$0.481^{+0.038}_{-0.038}$	$0.093^{+0.095}_{-0.086}$	0.476	0.186
11359879	1.12	$55097.841168^{+0.000062}_{-0.000058}$	$4.942780930^{+0.000001376}_{-0.000001359}$	$0.10508^{+0.00036}_{-0.00036}$	$86.10^{+0.03}_{-0.04}$	$9.946^{+0.037}_{-0.035}$	$0.677^{+0.004}_{-0.004}$	$0.501^{+0.063}_{-0.058}$	$0.112^{+0.086}_{-0.086}$	0.474	0.189
10619192	1.47	$55185.678033^{+0.000023}_{-0.000022}$	$1.485710910^{+0.000000209}_{-0.000000206}$	$0.13354^{+0.00017}_{-0.00019}$	$89.71^{+0.29}_{-0.13}$	$5.707^{+0.010}_{-0.008}$	$0.029^{+0.013}_{-0.048}$	$0.412^{+0.015}_{-0.015}$	$0.180^{+0.035}_{-0.032}$	0.474	0.188
11446443	1.00	$54955.762536^{+0.000007}_{-0.000007}$	$2.470613289^{+0.000000054}_{-0.000000062}$	$0.12468^{+0.00103}_{-0.00097}$	$83.84^{+0.04}_{-0.04}$	$7.873^{+0.045}_{-0.037}$	$0.845^{+0.001}_{-0.002}$	$0.203^{+0.190}_{-0.167}$	$0.425^{+0.183}_{-0.203}$	0.472	0.190
12019440	1.02	$55187.210074^{+0.000074}_{-0.000081}$	$3.243258657^{+0.000001713}_{-0.000001505}$	$0.12146^{+0.00025}_{-0.00039}$	$89.39^{+0.51}_{-0.27}$	$9.099^{+0.060}_{-0.024}$	$0.097^{+0.050}_{-0.074}$	$0.433^{+0.022}_{-0.022}$	$0.150^{+0.050}_{-0.050}$	0.471	0.188
10874614	1.06	$55003.006282^{+0.000030}_{-0.000028}$	$3.234699401^{+0.000000325}_{-0.000000370}$	$0.09412^{+0.00008}_{-0.00013}$	$89.39^{+0.26}_{-0.38}$	$7.551^{+0.029}_{-0.011}$	$0.081^{+0.049}_{-0.035}$	$0.480^{+0.007}_{-0.007}$	$0.138^{+0.015}_{-0.016}$	0.471	0.190
7877496	1.06	$55186.290523^{+0.000052}_{-0.000049}$	$1.720860242^{+0.000000625}_{-0.000000474}$	$0.10399^{+0.00109}_{-0.00122}$	$80.71^{+0.08}_{-0.08}$	$4.893^{+0.027}_{-0.028}$	$0.790^{+0.003}_{-0.003}$	$0.267^{+0.248}_{-0.227}$	$0.380^{+0.283}_{-0.296}$	0.464	0.192
5780885	1.06	$55094.298833^{+0.000059}_{-0.000053}$	$4.885488569^{+0.000001392}_{-0.000001118}$	$0.08291^{+0.00012}_{-0.00012}$	$85.21^{+0.06}_{-0.06}$	$6.662^{+0.022}_{-0.022}$	$0.556^{+0.005}_{-0.005}$	$0.374^{+0.020}_{-0.021}$	$0.185^{+0.033}_{-0.031}$	0.462	0.202
9631995	1.04	$55010.249540^{+0.000090}_{-0.000089}$	$7.891441215^{+0.000002425}_{-0.000002448}$	$0.09625^{+0.00025}_{-0.00022}$	$88.09^{+0.05}_{-0.06}$	$13.826^{+0.073}_{-0.076}$	$0.462^{+0.011}_{-0.010}$	$0.438^{+0.026}_{-0.024}$	$0.171^{+0.042}_{-0.047}$	0.459	0.195
11804465	1.08	$55004.008327^{+0.000034}_{-0.000030}$	$4.437964146^{+0.000000522}_{-0.000000513}$	$0.11879^{+0.00013}_{-0.00013}$	$88.79^{+0.11}_{-0.13}$	$8.018^{+0.019}_{-0.020}$	$0.169^{+0.018}_{-0.014}$	$0.428^{+0.007}_{-0.008}$	$0.124^{+0.018}_{-0.017}$	0.456	0.200
6922244	1.04	$55003.433596^{+0.000061}_{-0.000067}$	$3.522499050^{+0.000000824}_{-0.000000831}$	$0.09502^{+0.00041}_{-0.00043}$	$83.96^{+0.05}_{-0.05}$	$6.841^{+0.025}_{-0.026}$	$0.719^{+0.004}_{-0.004}$	$0.196^{+0.098}_{-0.098}$	$0.358^{+0.122}_{-0.135}$	0.455	0.203
9818381	1.06	$55095.452081^{+0.000055}_{-0.000063}$	$3.024092350^{+0.000000890}_{-0.000000823}$	$0.08711^{+0.00032}_{-0.00031}$	$84.65^{+0.07}_{-0.09}$	$6.983^{+0.036}_{-0.041}$	$0.651^{+0.007}_{-0.006}$	$0.382^{+0.059}_{-0.062}$	$0.204^{+0.085}_{-0.089}$	0.450	0.199
10019708	1.01	$55186.214857^{+0.000095}_{-0.000095}$	$3.268694474^{+0.000001964}_{-0.000002029}$	$0.09436^{+0.00043}_{-0.00043}$	$88.48^{+0.31}_{-0.61}$	$7.735^{+0.088}_{-0.095}$	$0.206^{+0.081}_{-0.037}$	$0.372^{+0.027}_{-0.027}$	$0.247^{+0.059}_{-0.059}$	0.437	0.204
10666592	1.22	$54954.357843^{+0.000011}_{-0.000010}$	$2.204734886^{+0.000000069}_{-0.000000087}$	$0.07764^{+0.00004}_{-0.00004}$	$83.12^{+0.04}_{-0.05}$	$4.152^{+0.006}_{-0.006}$	$0.497^{+0.003}_{-0.003}$	$0.357^{+0.007}_{-0.007}$	$0.162^{+0.011}_{-0.012}$	0.438	0.199
8191672	1.04	$55005.579469^{+0.000076}_{-0.000074}$	$3.548462518^{+0.000001041}_{-0.000000982}$	$0.07972^{+0.00006}_{-0.00009}$	$89.39^{+0.61}_{-0.20}$	$6.459^{+0.023}_{-0.008}$	$0.069^{+0.023}_{-0.069}$	$0.368^{+0.009}_{-0.011}$	$0.142^{+0.020}_{-0.019}$	0.433	0.214
9941662	1.15	$55002.945748^{+0.000010}_{-0.000011}$	$1.763586522^{+0.000000194}_{-0.000000160}$	$0.08553^{+0.00007}_{-0.00007}$	$85.82^{+0.10}_{-0.12}$	$4.434^{+0.011}_{-0.010}$	$0.323^{+0.008}_{-0.007}$	$0.308^{+0.007}_{-0.007}$	$0.222^{+0.014}_{-0.013}$	0.238	0.289
10318874	1.04	$55093.402844^{+0.000111}_{-0.000102}$	$2.508055888^{+0.000001193}_{-0.000001244}$	$0.03666^{+0.00070}_{-0.00070}$	$87.84^{+0.32}_{-0.46}$	$15.217^{+0.699}_{-1.056}$	$0.572^{+0.085}_{-0.051}$	$0.584^{+0.137}_{-0.140}$	$0.105^{+0.198}_{-0.196}$	0.600	0.133
5084942	1.04	$55093.535792^{+0.000230}_{-0.000244}$	$3.105510489^{+0.000003711}_{-0.000003464}$	$0.02819^{+0.00088}_{-0.00068}$	$87.29^{+0.53}_{-0.96}$	$12.064^{+0.787}_{-1.335}$	$0.570^{+0.136}_{-0.058}$	$0.609^{+0.217}_{-0.171}$	$0.094^{+0.219}_{-0.318}$	0.578	0.142
12105051	1.03	$55093.891709^{+0.000131}_{-0.000122}$	$2.624236881^{+0.000001595}_{-0.000001574}$	$0.05406^{+0.00088}_{-0.00178}$	$84.07^{+0.22}_{-0.21}$	$8.342^{+0.209}_{-0.213}$	$0.862^{+0.010}_{-0.010}$	$0.331^{+0.292}_{-0.514}$	$0.360^{+0.640}_{-0.222}$	0.509	0.174
5771719	1.20	$55193.071064^{+0.000231}_{-0.000236}$	$12.265052908^{+0.000017074}_{-0.000015924}$	$0.11110^{+0.00109}_{-0.00251}$	$86.72^{+0.07}_{-0.06}$	$14.556^{+0.185}_{-0.204}$	$0.833^{+0.006}_{-0.007}$	$0.176^{+0.239}_{-0.498}$	$0.418^{+0.581}_{-0.183}$	0.506	0.184
2571238	1.02	$55099.012623^{+0.000457}_{-0.000455}$	$9.286892387^{+0.000018938}_{-0.000019084}$	$0.02632^{+0.00073}_{-0.00066}$	$86.51^{+0.28}_{-0.70}$	$13.174^{+0.503}_{-1.671}$	$0.801^{+0.052}_{-0.024}$	$0.129^{+0.150}_{-0.358}$	$0.585^{+0.415}_{-0.112}$	0.496	0.179
11295426	1.09	$55066.244228^{+0.000359}_{-0.000353}$	$5.398749891^{+0.000006948}_{-0.000006425}$	$0.01720^{+0.00015}_{-0.00036}$	$87.90^{+0.95}_{-1.20}$	$11.078^{+1.200}_{-0.398}$	$0.406^{+0.199}_{-0.133}$	$0.358^{+0.087}_{-0.088}$	$0.232^{+0.117}_{-0.131}$	0.473	0.192
8456679	1.03	$55094.724206^{+0.000218}_{-0.000213}$	$1.735135943^{+0.000001524}_{-0.000001596}$	$0.02828^{+0.00040}_{-0.00041}$	$85.69^{+1.05}_{-1.98}$	$5.480^{+0.293}_{-0.355}$	$0.412^{+0.155}_{-0.074}$	$0.421^{+0.070}_{-0.080}$	$0.182^{+0.113}_{-0.113}$	0.470	0.190
8554498	1.01	$55004.215819^{+0.000183}_{-0.000179}$	$4.780330575^{+0.000003353}_{-0.000003228}$	$0.03720^{+0.00130}_{-0.00142}$	$82.87^{+0.26}_{-0.20}$	$7.627^{+0.227}_{-0.193}$	$0.946^{+0.004}_{-0.006}$	$0.290^{+0.270}_{-0.465}$	$0.498^{+0.502}_{-0.169}$	0.468	0.196
8684730	0.80	$55378.830016^{+0.001000}_{-0.001044}$	$46.149188888^{+0.001483927}_{-0.001465711}$	$0.04331^{+0.00238}_{-0.00198}$	$88.13^{+0.13}_{-0.15}$	$28.224^{+1.481}_{-1.829}$	$0.922^{+0.012}_{-0.014}$	$0.122^{+0.641}_{-0.497}$	$0.246^{+0.744}_{-0.264}$	0.461	0.199
3762468	1.02	$55186.994938^{+0.000830}_{-0.000793}$	$3.003842949^{+0.000023116}_{-0.000020842}$	$0.08817^{+0.00085}_{-0.00099}$	$88.50^{+1.49}_{-0.47}$	$7.656^{+0.248}_{-0.087}$	$0.200^{+0.062}_{-0.200}$	$0.346^{+0.144}_{-0.158}$	$0.101^{+0.278}_{-0.290}$	0.448	0.199
4349452	0.90	$55036.968723^{+0.000285}_{-0.000253}$	$12.720361269^{+0.000011436}_{-0.000010691}$	$0.03589^{+0.00056}_{-0.00125}$	$87.40^{+0.08}_{-0.08}$	$19.250^{+0.437}_{-0.441}$	$0.872^{+0.006}_{-0.008}$	$0.191^{+0.275}_{-0.593}$	$0.356^{+0.641}_{-0.214}$	0.449	0.207
3861595	1.06	$55005.923285^{+0.000214}_{-0.000197}$	$3.849387685^{+0.000006109}_{-0.000006487}$	$0.03850^{+0.00178}_{-0.00285}$	$79.89^{+0.77}_{-0.59}$	$5.281^{+0.315}_{-0.271}$	$0.927^{+0.011}_{-0.011}$	$0.105^{+0.530}_{-1.027}$	$0.475^{+1.018}_{-0.322}$	0.428	0.204

Notes. Errors are 68.3% HPD intervals except for *Kepler* IDs set in italic. These are enlarged due to red noise contribution. m_1 and m_2 are predicted LDCs from Claret tables for the specific $T_{\rm eff}$ and $\log(g)$ (Tables 1 and 2). Below the horizontal line we present the fit results of our high impact parameter sample.

Appendix A: Influence of stellar parameters on the theoretical LDCs

Stellar limb darkening depends on fundamental stellar parameters as, e.g., the effective temperature $T_{\rm eff}$ and the surface gravity $\log(g)$. For a plausible comparison between theoretically determined and measured LDCs it is necessary to know the correct stellar parameters for each studied object. While the *Kepler* Input Catalog (KIC, Brown et al. 2011) already provides $T_{\rm eff}$, $\log(g)$, and metallicities Z determined using ground-based photometric observations, the *Kepler* planetary candidates list (KPCL) offers values determined using other methods, e.g., spectroscopic follow up observations. The fundamental parameters of the *Kepler* stars are determined by four different methods as described by Batalha et al. (2013). The method actually applied to the object at hand is indicated by the $f_{T_{\rm eff}}$-flag given in the KPCL. They can be divided into two groups: The first group (0, 1) uses photometric data and, e.g., matches the KIC parameters to Yonsei-Yale stellar evolution models (Demarque et al. 2004). The second group (2, 3) uses spectroscopic follow-up observations determining the parameters using *spectroscopy made easy* SME ($f_{T_{\rm eff}} = 3$, Valenti & Piskunov 1996) or the *stellar parameter classification* tool SPC ($f_{T_{\rm eff}} = 2$, Buchhave et al. 2012), see KOI-list[8] for further details. Naturally, the stellar parameters derived by spectroscopic methods are more reliable. None of our target stars has an $f_{T_{\rm eff}}$-flag equal to 0, 14 have $f_{T_{\rm eff}} = 1$, and the majority has $f_{T_{\rm eff}}$ of equal to 2 or 3 (see Table A.1). In the case of photometrically determined parameters ($f_{T_{\rm eff}} = 1$) one has to keep in mind that the stellar parameters, especially the metallicities, have the highest uncertainties. In this case, the typical errors of $T_{\rm eff}$ and $\log(g)$ are about ±200 K and 0.4, whereas Z is basically undetermined (Brown et al. 2011). The uncertainties decrease, especially for $\log(g)$ and Z, for parameters derived by spectroscopic methods.

The influence of $\log(g)$, Z, and the micro-turbulent velocity ξ on the LDCs varies with effective temperature. This has already been theoretically studied, e.g. by Claret (2000) for a four parameter nonlinear LD law. We discuss the influence for the parameter range relevant for our analysis by using Claret & Bloemen (2011) LDCs (for ATLAS models). Since the quadratic coefficient u_2 shows virtually the same behavior as u_1, we concentrate on u_1. In Fig. A.1 we show the effect of $\log(g)$ on u_1 by calculating the difference between u_1 determined with $\log(g) = 4.5$ and values of u_1 for a slightly higher (4.8) and lower (4.3) surface gravity. For effective temperatures in the range from ≈4500 K to ≈7500 K, which covers the majority of stars in our sample, there is no significant influence of the surface gravity. However, especially for cooler stars ($T_{\rm eff} \lesssim 4500$ K) the LD becomes sensitive to $\log(g)$.

Figure A.2 shows the result of a similar analysis, this time varying the stellar metallicity Z. Again the effect on the LDC is strongest for stars cooler than ≲4500 K, but there are already significant deviations in the range between 4500 K to ≈6500 K. A change in metallicity of ±0.5 in this temperature range results in a maximum Δu_1 of ±0.05.

The micro-turbulent velocity has only a rather weak influence on the LDCs. The difference Δu_1 calculated between u_1 determined for $\xi = 0.1\,{\rm km\,s^{-1}}$ and $\xi = 8.0\,{\rm km\,s^{-1}}$ never exceeds ±0.015 and, thus, is negligible.

We conclude that metallicities and surface gravities do not have a crucial effect on predicted LDCs for stars in the

[8] http://archive.stsci.edu/kepler/koi/help/columns.html

Table A.1. $f_{T_{\rm eff}}$-flags of our selection sorted by $T_{\rm eff}$, as given in the KPCL.

Kepler ID	$f_{T_{\rm eff}}$	*Kepler* ID	$f_{T_{\rm eff}}$	*Kepler* ID	$f_{T_{\rm eff}}$
5794240	1	11446443	2	10318874	3
10748390	2	12019440	1	5084942	2
11391018	1	10874614	3	5771719	1
5357901	1	7877496	1	12105051	2
8845026	1	5780885	3	2571238	3
9595827	1	9631995	3	11295426	3
6849046	2	11804465	3	8456679	2
9410930	1	6922244	3	8554498	3
9651668	1	9818381	2	8684730	2
8359498	2	10019708	1	3762468	1
7023960	1	10666592	2	4349452	3
11359879	2	8191672	3	3861595	2
10619192	2	9941662	1		

Notes. See text for details. Third column: objects according to our selection made in Sect. 2.1.2.

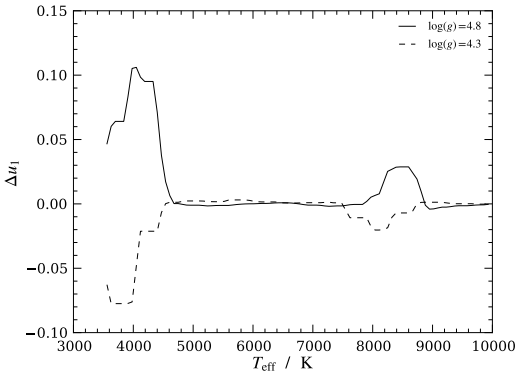

Fig. A.1. Influence of $\log(g)$ on the LDC u_1. Shown is the difference between u_1 determined with $\log(g) = 4.5$ and values of u_1 using a higher (4.8) and lower (4.3) surface gravity, over a wide temperature range (ATLAS models).

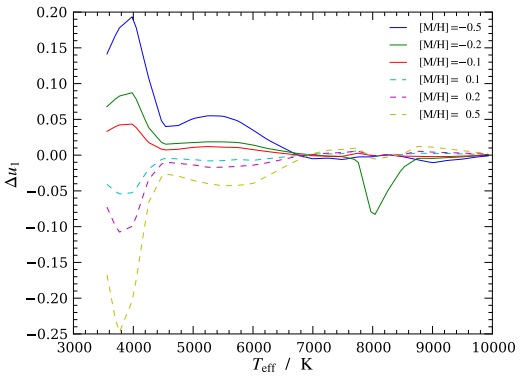

Fig. A.2. Influence of the stellar metallicity on u_1. Differences between u_1 determined with [M/H] = 0.0 and values of u_1 using different metallicities are plotted against $T_{\rm eff}$ (ATLAS models).

A&A 560, A112 (2013)

temperature range of 4500 to 7500 K. We note that for most objects in the solar neighborhood the absolute value of Z is lower than 0.5 (Casagrande et al. 2011) and it is appropriate to assume that our ignorance of the metallicity of the *Kepler* planetary candidates does not introduce a significant bias for the determination of theoretical LDCs. The most important parameter is the effective temperature which is often quite reliably determined even when using only color indices.

Appendix B: Analytical approach to the limb-darkening fits

In the following we provide an analytical approach to the problem of fitting limb-darkening coefficients. Our treatment aims at a fundamental understanding of the accuracy and correlation of limb-darkening coefficients determined from transit fits.

To simulate the measurement errors, we carried out a Monte-Carlo simulation. In particular, we constructed transit light curves for a hypothetical planet with a period of $P_{\rm orb} = 2.47$ d, a semimajor axis of $a = 8.4$ stellar radii, and a small planet-to-star radii ratio of $p = 10^{-3}$. The small planet size is important for our comparison of these simulations to our analytical results which are only valid for small p ($\ll$1). We set the values of the quadratic limb darkening to $u_1 = 0.5$ and $u_2 = 0.2$. Using these parameters, we created simulated light curves with a δ/N of 60 (as defined in Sect. 2.3) and 85 equidistantly distributed photometric points during the transit. Although we kept the temporal cadence constant, we allowed the time axis to shift with respect to the transit center in consecutive runs to avoid systematics arising from an unrealistically symmetric simulation. We then proceeded to sample from the posterior probability distribution using an MCMC algorithm and the transit models provided by Mandel & Agol (2002) with the LDCs as only free parameters. The resulting Markov-chains allow credibility intervals for the LDCs and the correlation coefficient ϱ to be derived. Each point in Figs. 11 and B.1 represents an individual simulation.

B.1. Modeling the transit profile

In our approach, we consider the following simplified transit light curve model

$$y(t_i) = 1 - \frac{\left[1 - u_1\,(1-\mu(t_i)) - u_2\,(1-\mu(t_i))^2\right]\,p^2}{1 - \frac{u_1}{3} - \frac{u_2}{6}}, \tag{B.1}$$

where t_i is the ith time of measurement, $\mu = \cos(\theta)$ where θ is the angle between the line of sight and the inward surface normal of the position on the stellar surface occulted by the planet, p is the ratio of the planetary and stellar radii, and u_1 and u_2 are the linear and quadratic limb-darkening coefficients. The model described by Eq. (B.1) considers the amount of light blocked due to the size of the planet but it neglects all other geometrical effects caused by the extent of the planet. In particular the planet passes only *one* $\mu-$value per time step, which is fully consistent with our chosen small planet approximation ($p \ll 1$). The numerator accounts for the light blocked by the planetary disk, while the denominator ensures a renormalization of the entire brightness.

Given a circular planetary orbit with a period $P_{\rm orb}$, inclination i, and a semimajor axis a, in units of stellar radii, $\mu(t_i)$ is given by

$$\begin{aligned}\mu(t_i) &= \sqrt{1 - a^2\left[\cos^2(i)\cos^2(\omega t_i) + \sin^2(\omega t_i)\right]} \\ &= \sqrt{1 - z(t_i)^2},\end{aligned} \tag{B.2}$$

where $z(t_i)$ denotes the sky-projected distance between the centers of the planet and the star. For a large semimajor axis we can approximate $\mu(t_i)$ by

$$\mu(t_i) = \sqrt{1 - v^2 t_i^2 - b^2}, \tag{B.3}$$

where $v = 2\pi a P_{\rm orb}^{-1}$ is the orbital velocity and $b = a\cos(i)$ is the impact parameter, both in units of stellar radii.

B.2. Expansion of χ^2

Given a number of measurements, m_i, with measurement errors σ, the χ^2-statistics is defined as

$$\chi^2 = \frac{\sum_i (y(t_i) - m_i)^2}{\sigma^2}. \tag{B.4}$$

This expression can be expanded to second order with respect to the limb-darkening coefficients u_1 and u_2:

$$\begin{aligned}\chi^2 \;\approx\; & \chi^2(\tilde{u}_1, \tilde{u}_2) + \sum_j \left(u_j - \tilde{u}_j\right)\frac{\partial}{\partial u_j}\chi^2 \\ & + \frac{1}{2}\left(\sum_j \left(u_j - \tilde{u}_j\right)\frac{\partial}{\partial u_j}\sum_l \left(u_l - \tilde{u}_l\right)\frac{\partial}{\partial u_l}\chi^2\right).\end{aligned} \tag{B.5}$$

Expanding around the χ^2-minimum, $\chi^2(\tilde{u}_1, \tilde{u}_2)$, encountered for some combination of limb-darkening coefficients $\tilde{u}_1$ and $\tilde{u}_2$, the χ^2-increase, $\Delta\chi^2$, caused by a deviation from the best-fit parameters reads

$$\begin{aligned}\Delta\chi^2 \;\approx\; & \frac{1}{2}\left(\Delta u_1^2\frac{\partial^2\chi^2}{\partial u_1^2} + \Delta u_2^2\frac{\partial^2\chi^2}{\partial u_2^2} + 2\Delta u_1\Delta u_2\frac{\partial^2\chi^2}{\partial u_1\partial u_2}\right) \\ =\; & \frac{1}{2}\left(\Delta u_1^2 A_1 + \Delta u_2^2 A_2 + 2\Delta u_1\Delta u_2 A_{12}\right),\end{aligned} \tag{B.6}$$

where the various A coefficients are abbreviations for the second derivatives of χ^2 and with $\Delta u_1 = u_1 - \tilde{u}_1$ and $\Delta u_2 = u_2 - \tilde{u}_2$.

Equation (B.6) describes an ellipse with semimajor axis, $a_{\rm ell}$, semiminor axis, $b_{\rm ell}$, and rotation angle α, which may alternatively be written as

$$\begin{aligned}1 \;=\; & \left(\frac{\cos^2\alpha}{a_{\rm ell}^2} + \frac{\sin^2\alpha}{b_{\rm ell}^2}\right)x^2 + \left(\frac{\sin^2\alpha}{a_{\rm ell}^2} + \frac{\cos^2\alpha}{b_{\rm ell}^2}\right)y^2 + \\ & 2\cos\alpha\sin\alpha\left(\frac{1}{a_{\rm ell}^2} - \frac{1}{b_{\rm ell}^2}\right)xy,\end{aligned} \tag{B.7}$$

when we rotate the Cartesian coordinate system clockwise to achieve a counterclockwise rotation of the ellipse. Comparing Eqs. (B.6) and (B.7), we determine

$$\begin{aligned}\tan 2\alpha &= \frac{2A_{12}}{A_1 - A_2} \\ a_{\rm ell}^2 &= \frac{4\Delta\chi^2}{(A_1 + A_2) + B} \\ b_{\rm ell}^2 &= \frac{4\Delta\chi^2}{(A_1 + A_2) - B},\end{aligned} \tag{B.8}$$

where B serves as an abbreviation for $\sqrt{(A_1 + A_2)^2 + 4A_{12}^2}$. To obtain the 68% confidence interval for two parameters of interest, $\Delta\chi^2$ needs to be set to 2.3 or to 6.18 for 95% confidence interval, respectively (Press et al. 2002).

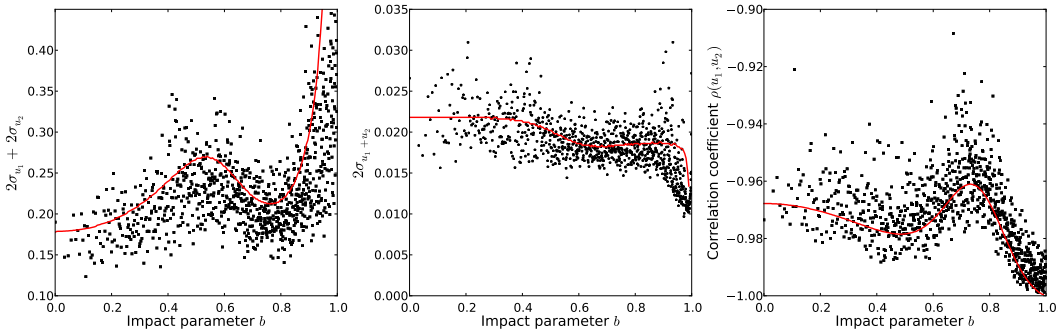

Fig. B.1. Comparison of simulations (*dots*) and our analytical solutions (*lines*). *Left and center*: dependency of the measurement errors on the system impact parameter b. *Right*: correlation coefficients of the LDCs with increasing b. See Sect. B.4 for details.

B.3. The derivatives of χ^2

The second derivative of χ^2 with respect to the limb-darkening coefficients can be written as

$$\frac{\partial^2\chi^2}{\partial u_j \partial u_l} = \frac{2}{\sigma^2}\sum_i \left(\frac{\partial y(t_i)}{\partial u_j}\frac{\partial y(t_i)}{\partial u_l} + (y(t_i) - m_i)\frac{\partial^2 y(t_i)}{\partial u_j \partial u_l}\right). \tag{B.9}$$

The expressions for the partial derivatives read

$$\frac{\partial y}{\partial u_1} = 6\,\frac{p^2\left(4 + u_2 - 6\mu - 3\,u_2\,\mu + 2\,u_2\,\mu^2\right)}{(-6 + 2\,u_1 + u_2)^2}$$

$$\frac{\partial y}{\partial u_2} = \frac{-6\,p^2\left(1 - 3\mu + 2\mu^2\right)u_1 - 6\,p^2\left(-5 + 12\mu - 6\mu^2\right)}{(-6 + 2\,u_1 + u_2)^2}$$

$$\frac{\partial^2 y}{\partial u_1 \partial u_1} = -24\,\frac{p^2\left(4 + u_2 - 6\mu - 3\,u_2\,\mu + 2\,u_2\,\mu^2\right)}{(-6 + 2\,u_1 + u_2)^3}$$

$$\frac{\partial^2 y}{\partial u_2 \partial u_2} = 12\,\frac{p^2\left(-5 + u_1 + 12\mu - 3\,u_1\,\mu - 6\mu^2 + 2\,\mu^2 u_1\right)}{(-6 + 2\,u_1 + u_2)^3}$$

$$\frac{\partial^2 y}{\partial u_1 \partial u_2} = -6\,p^2\left(\frac{(14 - 2\,u_1 + u_2 - 30\,\mu + 6\,u_1\,\mu)}{(-6 + 2\,u_1 + u_2)^3}\right.$$

$$\left. + \frac{-3\,u_2\,\mu + 12\,\mu^2 - 4\,\mu^2 u_1 + 2\,u_2\,\mu^2}{(-6 + 2\,u_1 + u_2)^3}\right). \tag{B.10}$$

These derivatives can be evaluated for any combination of limb-darkening coefficients. The orbit configuration and times of measurement are contained in μ according to Eq. (B.3).

Especially the last term in Eq. (B.9) is a nuisance, because it depends on the actual data set through m_i. As we, however, expand around the χ^2-minimum, the expectation value of this term equals zero, because $(y(t_i) - m_i)\,\sigma^{-1}$ follows a standard normal distribution. The expectation value of the absolute value, $|\sum_i (y(t_i) - m_i)\,\sigma^{-1}|$, is $\sqrt{2\pi^{-1}}\,\sqrt{N}$, where N is the number of data points. We use this expression to check the influence of this term on our calculations.

B.4. Credibility intervals

To obtain credibility intervals, we need the posterior probability distribution, i.e., the distribution of the parameters given the data, $P(u_1, u_2|D)$. Likelihood, $\mathcal{L}$, and χ^2 are related according to

$$\mathcal{L}(\chi^2) \sim \mathrm{e}^{-\frac{1}{2}\chi^2}. \tag{B.11}$$

Applying Bayes' theorem, we obtain the posterior probability distribution

$$P(u_1, u_2|D) = \frac{p(u_1, u_2)\mathcal{L}(\chi^2)}{\int\limits_{u_1,u_2} p(u_1, u_2)\mathcal{L}(\chi^2)\,\mathrm{d}u_1\,\mathrm{d}u_2} \tag{B.12}$$

$$= \frac{\mathcal{L}(\chi^2)}{\int\limits_{u_1,u_2} \mathcal{L}(\chi^2)\,\mathrm{d}u_1\,\mathrm{d}u_2}, \tag{B.13}$$

where $p(u_1, u_2)$ represents the prior probability distribution, and the second equality holds for uniformly distributed priors. Using the expansion of χ^2, the likelihood can be recast as

$$\mathcal{L}(\Delta u_1, \Delta u_2) = \mathrm{e}^{-\frac{1}{2}\left(\Delta\chi^2(\Delta u_1, \Delta u_2) + \chi^2(\tilde{u}_1, \tilde{u}_2)\right)} \tag{B.14}$$

where $\chi^2(\tilde{u}_1, \tilde{u}_2)$ represents the χ^2-minimum, and the expression for $\Delta\chi^2$ has already been derived in Eq. (B.6). Hence, the posterior probability distribution becomes

$$P(\Delta u_1, \Delta u_2|D) = \mathcal{L}_0\,\mathrm{e}^{-\frac{1}{2}\left(\Delta\chi^2(\Delta u_1, \Delta u_2)\right)}. \tag{B.15}$$

Here, $\mathcal{L}_0$ is a constant that normalizes the posterior. It is found by integration of Eq. (B.15) over Δu_1 and Δu_2 from $-\infty$ to $+\infty$, which yields $\mathcal{L}_0^{-1} = 4\pi(A_1 A_2 - A_{12}^2)^{-1/2}$. We note that the limits of integration are actually unphysical, because u_1 and u_2 are confined to within an interval reaching from 0 to 1. Additionally, $u_1 + u_2$ must not exceed 1, which would produce negative brightness on the stellar limb. Nonetheless, we argue that the approximation is appropriate as long as the $\Delta\chi^2$ ellipse is sufficiently confined.

Parameter correlation is an important aspect in model fitting and error analysis. The correlation coefficient for u_1 and u_2 is given by

$$\varrho(u_1, u_2) = \frac{E(\Delta u_1 \Delta u_2)}{\sqrt{E(\Delta u_1^2)E(\Delta u_2^2)}}, \tag{B.16}$$

A&A 560, A112 (2013)

where E denotes the expectation value. The numerator is given by

$$E(\Delta u_1 \Delta u_2) = \mathcal{L}_0 \iint \Delta u_1 \Delta u_2 \times e^{-\frac{1}{4}(\Delta u_1^2 A_1 + \Delta u_2^2 A_2 + 2\Delta u_1 \Delta u_2 \Delta u_1 A_{12})} \, d(\Delta u_1)\, d(\Delta u_2)$$
$$= \mathcal{L}_0 \int \frac{-2A_{12}\sqrt{\pi}}{A_1^{3/2}} \Delta u_2^2 e^{-\frac{\Delta u_2^2 (A_1 A_2 - A_{12}^2)}{4A_1}} \, d(\Delta u_2)$$
$$= -\frac{2A_{12}}{A_1 A_2 - A_{12}^2}. \quad \text{(B.17)}$$

Similarly, we derive

$$E(\Delta u_1^2) = \frac{2A_2}{A_1 A_2 - A_{12}^2} \quad \text{(B.18)}$$

$$E(\Delta u_2^2) = \frac{2A_1}{A_1 A_2 - A_{12}^2}. \quad \text{(B.19)}$$

Based on Eqs. (B.18), (B.19), and (B.17), we obtain the correlation coefficient

$$\varrho(u_1, u_2) = -\frac{A_{12}}{\sqrt{A_1 A_2}}. \quad \text{(B.20)}$$

We note that the correlation between u_1 and u_2 is always negative just by our analytical approach and reaches maximum for $b = 1$. The anti-correlated behavior in our simulations is well reproduced by this analytical solution as can be seen in Fig. B.1.

The posterior integral over Δu_1 or Δu_2, e.g.,

$$p(\Delta u_1) = \mathcal{L}_0 \int e^{-\frac{1}{4}(\Delta u_1^2 A_1 + \Delta u_2^2 A_2 + 2\Delta u_1 \Delta u_2 \Delta u_1 A_{12})} \, d(\Delta u_2)$$
$$= \mathcal{L}_0 \frac{2\sqrt{\pi}}{\sqrt{A_2}} e^{-\frac{\Delta u_1^2 (A_1 A_2 - A_{12}^2)}{4A_2}} \quad \text{(B.21)}$$

yields the marginal probability distributions of the parameters. Equation (B.21) shows that the marginal distributions are Gaussian. Therefore, the width, w, of the 68% credibility interval is given by $w_{i,68\%} = 2\sqrt{E(\Delta u_i^2)}$; the 95% credibility interval's width is $w_{i,95\%} = 2w_{i,68\%}$. Finally, we derive the width of the credibility interval for $\Delta u_1 + \Delta u_2$. In particular, we calculate the variance of $\Delta u_1 + \Delta u_2$

$$E\left((\Delta u_1 + \Delta u_2)^2\right) = 2\frac{A_1 + A_2 - 2A_{12}}{A_1 A_2 - A_{12}^2}. \quad \text{(B.22)}$$

The same result is obtained when applying error propagation considering the correlation of Δu_1 and Δu_2. The resulting error then depends on the correlation coefficient found in Eq. (B.20), which is always negative and close to -1. This leads to the conclusion that the sum of the anti-correlated parameters $u_1 + u_2$ is always better constrained than the individual parameters (Fig. 11). For an increasing impact parameter b also the absolute value of the anti-correlation increases toward its maximum of 1, which leads to decreasing errors of $u_1 + u_2$.

Our result is visualized in Fig. B.1, which shows the development of the measurement errors (left and middle panel) and the correlation (right panel) for different impact parameters b. The points are MCMC results coming from the simulations described in the beginning of this section. The lines show our theoretical predictions using the same planetary parameters and LDCs.

For a more detailed analysis of the correlations of LDCs and other light curve parameters see Pál (2008). Although his model is more complex, his results are consistent with our analysis.

B.5. Parameter evaluation using correlations

Based on the parameter traces obtained during the MCMC sampling, the covariance matrix, $\mathbf{C}$, can be estimated, whose elements are the expectation values

$$C_{i,j} = E\left[(x_i - E(x_i))(x_j - E(x_j))\right], \quad \text{(B.23)}$$

given the parameters x_i and x_j. Using the covariance, we locally approximate the posterior probability distribution, P, by a multivariate Gaussian (cf., D'Agostini 2003),

$$P \sim \exp\left(-\frac{1}{2}\left((\boldsymbol{x} - E(\boldsymbol{x}))^{\mathrm{T}} \mathbf{H} (\boldsymbol{x} - E(\boldsymbol{x}))\right)\right) \quad \text{(B.24)}$$

and, therefore,

$$\ln(P) = c - \frac{1}{2}\left(\Delta\boldsymbol{x}^{\mathrm{T}} \mathbf{H} \Delta\boldsymbol{x}\right) = c - \frac{1}{2}\sum_i \sum_j \Delta x_i \Delta x_j H_{i,j}, \quad \text{(B.25)}$$

where $\boldsymbol{x}$ is the column vector summarizing the parameter values, $\Delta\boldsymbol{x}$ is defined as $\boldsymbol{x} - E(\boldsymbol{x})$, $\mathbf{H}$ denotes the Hessian matrix, and c is a normalization constant. The Hessian matrix is the inverse of the covariance matrix, $\mathbf{H} = \mathbf{C}^{-1}$; both matrices are symmetric so that $H_{i,j} = H_{j,i}$.

The derivative with respect to the variable Δx_k reads

$$\frac{\partial \ln(P)}{\partial \Delta x_k} = -\frac{1}{2}\left(2\sum_i H_{i,k} \Delta x_i\right), \quad \text{(B.26)}$$

and, therefore, the gradient can be written as

$$\nabla \ln(P) = -\mathbf{H}\Delta\boldsymbol{x}. \quad \text{(B.27)}$$

We, now, fix one or more of the offsets, Δx_m, to a fixed value, δ_m, and adjust the remaining parameters so that the posterior, P, is again maximized. To that end, we split $\Delta\boldsymbol{x}$ into two components, $\Delta\boldsymbol{y}$ and $\boldsymbol{\delta}$, so that $\Delta\boldsymbol{x} = \Delta\boldsymbol{y} + \boldsymbol{\delta}$. Further, we demand that $\boldsymbol{\delta}$ be a fixed vector of offsets and $\Delta\boldsymbol{y}$ contains zero entries for any nonzero element in $\boldsymbol{\delta}$ (or offsets fixed to zero). In this case, the term $\Delta\boldsymbol{x}^{\mathrm{T}}\mathbf{H}\Delta\boldsymbol{x}$ from Eq. (B.25) can be rewritten as

$$\Delta\boldsymbol{x}^{\mathrm{T}}\mathbf{H}\Delta\boldsymbol{x} = \Delta\boldsymbol{y}^{\mathrm{T}}\mathbf{H}\Delta\boldsymbol{y} + 2\boldsymbol{y}^{\mathrm{T}}\mathbf{H}\boldsymbol{\delta} + \boldsymbol{\delta}^{\mathrm{T}}\mathbf{H}\boldsymbol{\delta}. \quad \text{(B.28)}$$

Defining $\boldsymbol{b} = \mathbf{H}\boldsymbol{\delta}$, we can write

$$\Delta\boldsymbol{x}^{\mathrm{T}}\mathbf{H}\Delta\boldsymbol{x} = \sum_i \sum_j \Delta y_i \Delta y_j H_{i,j} + 2\sum_i \Delta y_i b_i + \boldsymbol{\delta}^{\mathrm{T}}\mathbf{H}\boldsymbol{\delta}. \quad \text{(B.29)}$$

By definition, those Δy_i for which δ_i is nonzero, i.e., the fixed parameters, vanish. Therefore, the indices i and j in Eq. (B.29) only need to cover the range with nonzero Δy_m. Using $\Delta\boldsymbol{y'}$, indicating the vector $\Delta\boldsymbol{y}$ with the zero elements removed, $\boldsymbol{b'}$ with the same convention, and $\mathbf{H'}$ with the associated columns and rows removed, we write

$$\Delta\boldsymbol{x}^{\mathrm{T}}\mathbf{H}\Delta\boldsymbol{x} = \Delta\boldsymbol{y'}^{\mathrm{T}}\mathbf{H'}\Delta\boldsymbol{y'} + 2\boldsymbol{y'}^{\mathrm{T}}\boldsymbol{b'} + \boldsymbol{\delta}^{\mathrm{T}}\mathbf{H}\boldsymbol{\delta}. \quad \text{(B.30)}$$

The gradient of the posterior with respect to the variables Δy_i becomes

$$\nabla \ln(P(\Delta\boldsymbol{y})) = \mathbf{H'}\Delta\boldsymbol{y'} + \boldsymbol{b'}. \quad \text{(B.31)}$$

Table B.1. Table of deleted transits.

Kepler ID	N_{total}	Deleted automatically	Deleted manually	N_{transit}
5794240	36	1, 7, 12, 15, 16, 18, 21, 24, 28, 31, 32, 33, 34		23
10748390	95	53, 82, 94	1, 3, 5, 7, 8, 10, 11, 12, 14, 15, 16, 17, 19, 20, 21, 22, 23 24, 25, 26, 27, 28, 29, 30, 31, 32, 33, 34, 35, 36, 37, 39 40, 42, 44, 45, 47, 48, 50, 51, 52, 54, 55, 56, 57, 58, 60 61, 62, 63, 64, 66, 67, 68, 69, 70, 71, 72, 74, 75, 76, 77 78, 79, 80, 83, 84, 85, 87, 89, 91, 92, 93, 95	18
11391018	7			7
5357901	70	49, 61		68
8845026	5	1	2, 3, 5	1
9595827	22			22
6849046	63			63
9410930	142	26		141
9651668	101	48, 49, 69, 73, 79, 80, 92, 93, 95, 98, 100, 101	96, 97, 99	86
8359498	98	85		97
7023960	8	1, 8		6
11359879	71	29		70
10619192	178	20, 33, 60, 61, 65, 70, 79, 81, 82, 83, 84, 86 87, 88, 89, 90, 94, 95, 123, 125, 133, 158	80, 91	154
11446443	169	19, 26		167
12019440	82	3, 46, 48, 49, 51, 54, 80, 82		74
10874614	136	16, 70, 76		133
7877496	154	33		153
5780885	70			70
9631995	55		11, 12, 13, 14, 15, 16, 17, 18	47
11804465	82			82
6922244	126	1, 5, 6, 8, 9, 65		120
9818381	116	4, 12		114
10019708	83	14, 17, 23, 63, 69, 71, 75, 81		75
10666592	216		1, 2, 72, 73, 74, 75, 76, 77, 78, 79	206
8191672	122	6	119	120
9941662	96		7, 47, 73, 77	92
10318874	141	40, 44, 45, 46, 50, 56, 57, 60, 68, 70		131
5084942	114			114
12105051	135			135
5771719	13	3		12
2571238	37			37
11295426	39			39
8456679	198	2, 6, 7, 8, 9, 10, 11, 14, 15, 16, 17, 19, 20, 21, 24, 29, 30	1, 3, 4, 5, 12, 13, 18, 22, 23, 25, 26, 27, 28, 31, 32, 33	165
8554498	91			91
8684730	2			2
3762468	59	1, 3, 4, 5, 6, 8, 9, 10, 11, 12, 13, 14, 15, 16, 17 19, 20, 21, 22, 23, 24, 25, 26, 29, 30, 31, 32, 33 34, 35, 36, 37, 38, 39, 40, 42, 43, 45, 46, 48, 49 50, 52, 53, 54, 55, 56, 57, 58, 59		9
4349452	17			17
3861595	29			29

Notes. N_{total} gives the total number of detected transit light curves in quarter 0 to 6, while N_{transit} denotes the number of transits after discarding bad ones as described in Sect. 2.3. The number sets indicate the specific transit number of deleted transits start counting from 1.

The maximum of the posterior is, thus, found by solving the equation

$$\nabla \ln(P(\Delta \boldsymbol{y})) = 0 \;\rightarrow\; \Delta \boldsymbol{y}' = -\mathbf{H}'^{-1} \boldsymbol{b}'. \tag{B.32}$$

Evaluating this expression, we determine how a systematic shift in one or more variables given by $\boldsymbol{\delta}$ affects the remaining parameters, Δy_i.

If there are only two variables, of which we fix the first one to δ_1, we find the following expression for the change in the second, required to maximize the posterior given this constraint:

$$H_{2,2}\Delta y_2 + \delta_1 H_{2,1} = 0 \rightarrow \Delta y_2 = -\delta_1 \frac{H_{2,1}}{H_{2,2}}; \tag{B.33}$$

note that we have not used primed quantities here. If the variables are entirely uncorrelated ($H_{2,1} = 0$), a change in the first cannot be compensated by a change in the second. In case of correlations, the remaining values need to be adapted.

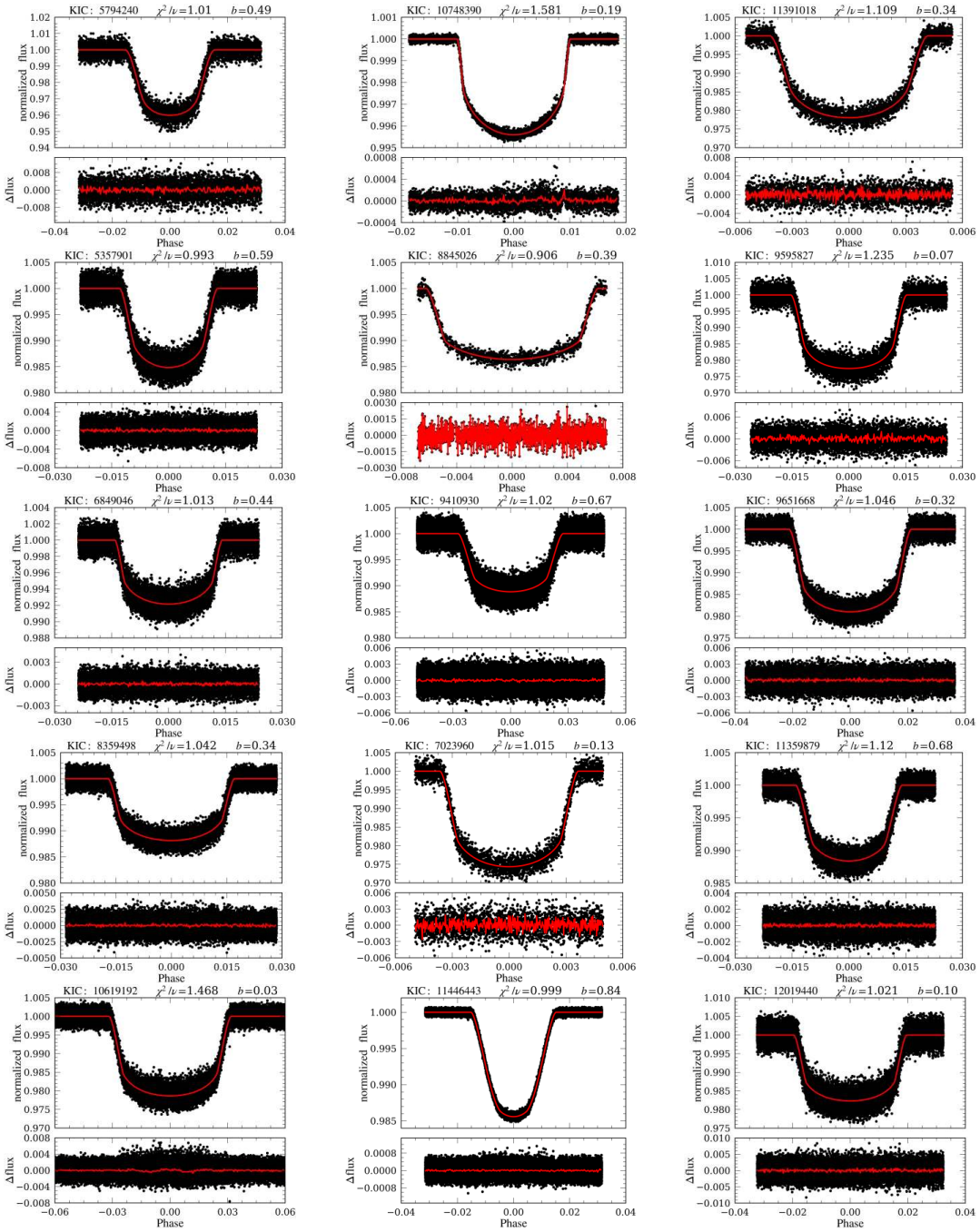

Fig. B.2. *Top panels*: normalized, phase folded transit light curves and best-fit models for the high signal-to-noise sample (Table 1). *Bottom panels*: residuals for individual data points and overplotted rebinned residuals (*red*) with one minute bin time. Objects ordered by increasing $T_{\rm eff}$ from the upper left to the lower right corner.

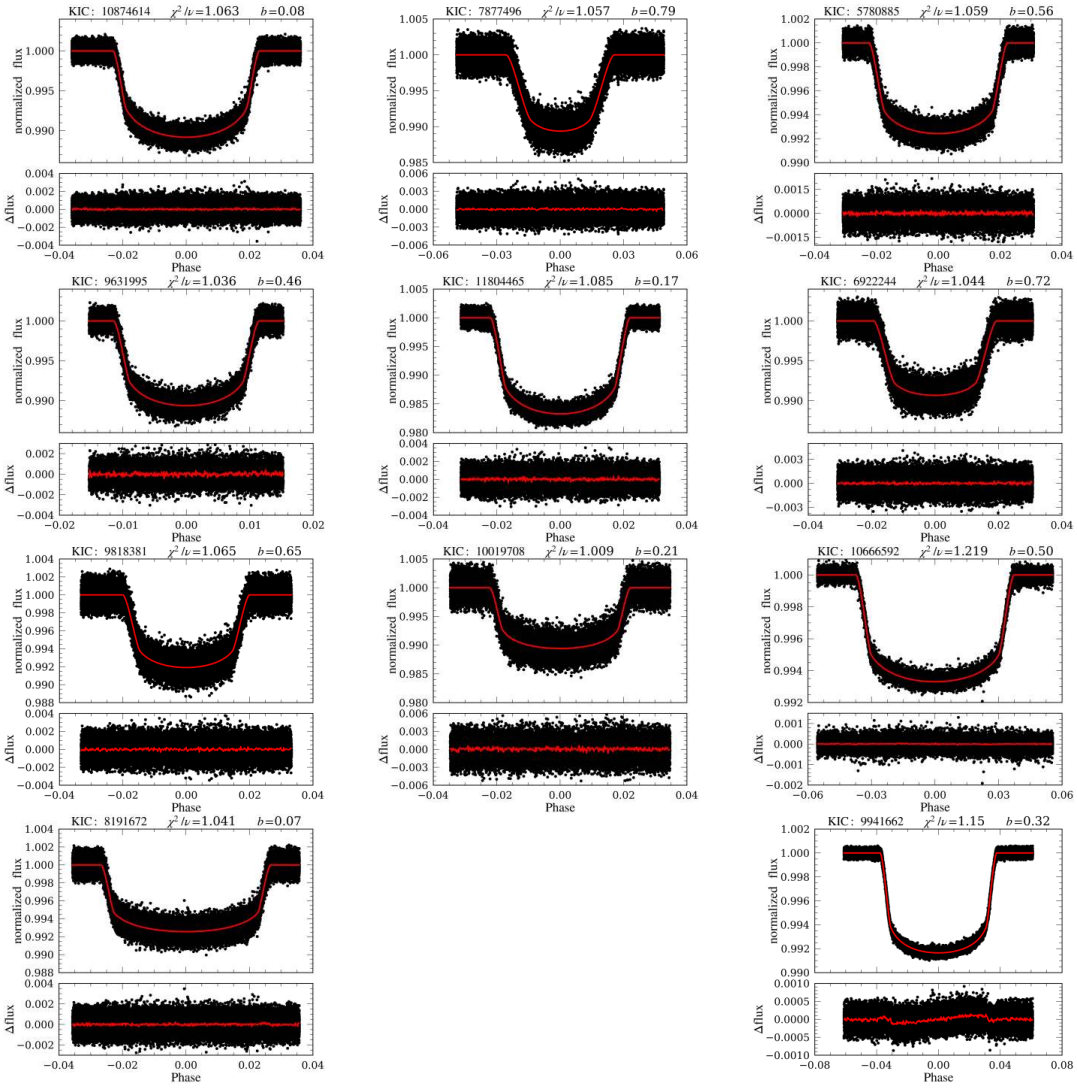

Fig. B.2. continued.

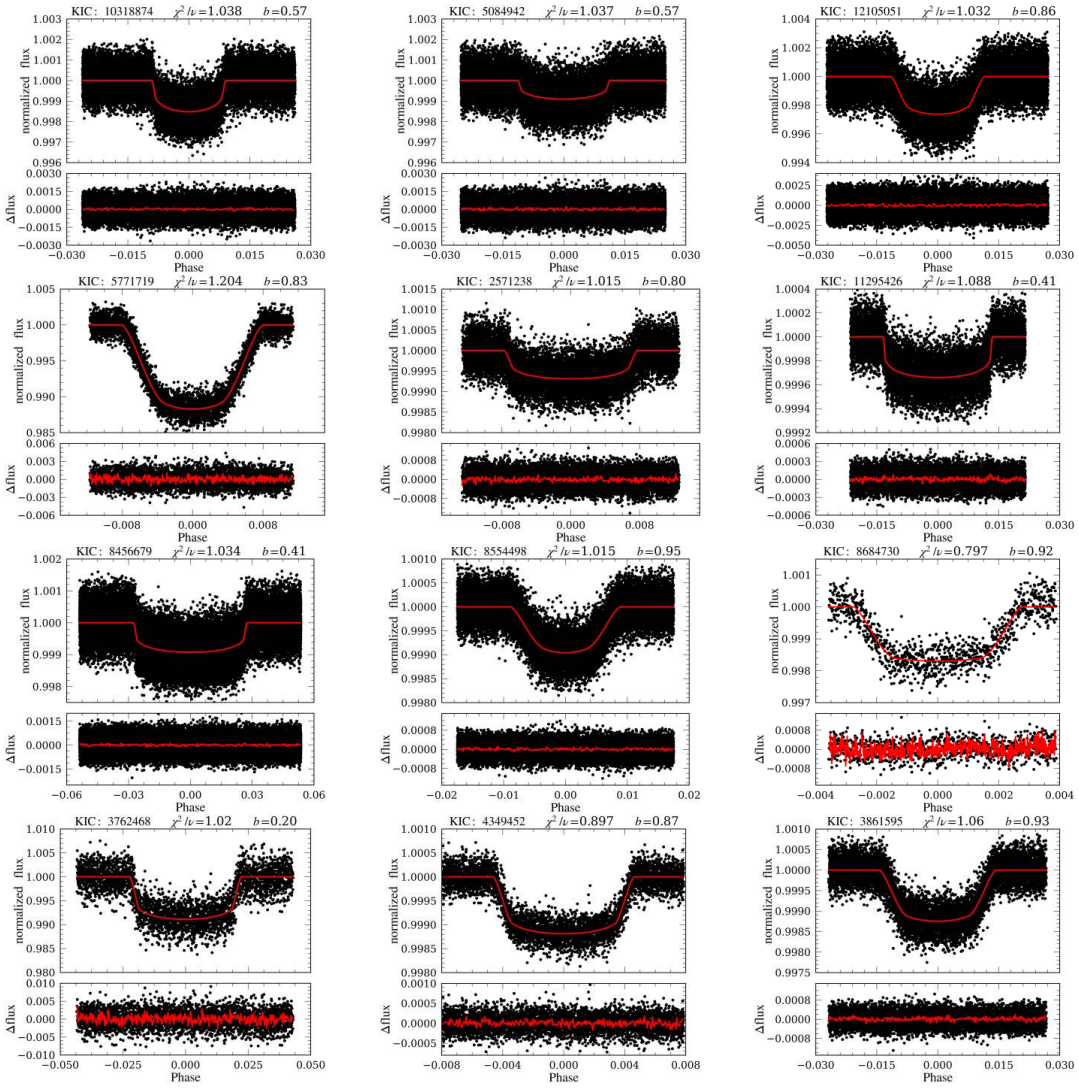

Fig. B.3. *Top panels*: normalized, phase folded transit light curves and best-fit models for the object sample with high impact parameters (Table 2). *Bottom panels*: residuals for individual data points and overplotted rebinned residuals (*red*) with one minute bin time. Objects ordered by $T_{\rm eff}$ from the upper left to the lower right corner.

8 Summary and Outlook

In my PhD thesis simulations and measurements of the limb darkening of planet hosting stars were presented. For the precise measurements the tool of planetary transit modeling was utilized. Spectral observations and analyses were carried out to determine fundamental stellar parameters, which are important for the prediction of limb darkening. As a feasibility study spectro-photometric observations of an active host star were presented. Limb intensities of a recent model atmosphere were compared to measurements obtained from the Sun. To account for found differences a rescaling of the model intensities was proposed. Finally, a numerical transit algorithm was developed to be independent of limb-darkening approximations and to be able to use model intensities directly. Furthermore, the code is capable of using any kind of input images, e.g., space-based observations of the Sun or a planet with rings. In the following I will summarize the major results of my thesis and I will give an outlook on some possible future work.

8.1 Summary and conclusions

To summarize the results of my PhD thesis I will treat the chapters individually, with a short outline followed by the important results highlighted by blue vertical lines. From the introduction (Chapter 1) only results from Section 1.3.2 and Section 1.3.3 will be presented, while Chapter 3 (The *Kepler* Space Mission) is totally omitted.

Modeling of planetary transits

For transit modeling the data quality is of special interest. This includes the amount of noise in the data, but also the achieved time resolution. To give an estimate about the credibility of the resulting fit parameters in the presence of different noise levels or long integration times I presented corresponding simulations. First, I generated transit light curves for three different planet radii (1 R_{Earth}, 1.02 R_{Jup}, 1.32 R_{Jup}) and added Gaussian distributed noise to achieve transit signal-to-noise ratios (δ/N) in the range from 5 to 150 for all three planet sizes. These transits were fitted individually.

> I showed in Fig. 1.14 that in the lack of photometric precision it is impossible to determine the quadratic LDCs. One needs at least a δ/N of about 60 to get credible results. For lower values (e.g., in most ground-based photometry) one has to fix the LDCs to values given

> by predictions because a fit of the LDCs together with the remaining transit parameters would not provide correct values. Due to strong correlations also the remaining transit parameters would be incorrect. The limiting δ/N is independent of the planet size and, therefore, this measure is more descriptive than the simple photometric signal-to-noise (see Fig. B.3).

To estimate the influence of the time resolution on the parameters achieved by transit modeling I again performed simulations. This time I generated a light curve, which holds 25 transits. The data was rebinned to simulate different integration times in the range from one to 30 minutes. The resulting transits were then fitted like before.

> The resulting model parameters were presented as a function of the bin time in Fig. 1.16. The parameters show a clear trend for increasing bin time. For transit durations of three hours or shorter I recommend to only use photometry with integration times of at most two minutes. In the case of longer integration times the fitted parameters substantially deviate from the correct values. As recommended by Kipping (2010), I also evaluated the model at a smaller bin size (one minute), then rebinned to 30 minutes and fitted again. This method leads to the correct fit parameters. However, the uncertainties in the parameters are larger compared to fit results of data with short integration times.

Due to the number of the available limb-darkening laws a question often arising is which of these laws should be used in transit modeling. I used the linear, the quadratic, and the nonlinear limb-darkening law and created transit light curves for different planet-to-star radii ratios. I determined the residuals between transits of the same planet-to-star radii ratio but with different limb darkening descriptions. The residuals are now only induced by the different limb-darkening laws. The maximum of these residuals was used as an estimator for the required δ/N at which these residuals are significant.

> Figure 1.17 reveals that the residuals between the linear and the quadratic law become significant from a transit signal-to-noise (δ/N) of about 40, depending on the planet-to-star radii ratio. If $R_S = 1\,R_{Sun}$ is assumed, then for a planet size of $1\,R_{Jup}$ the δ/N should not exceed ≈ 85. For δ/N values larger than this, the quadratic law should be used. Looking at the residuals between the quadratic and the nonlinear law, I found that the differences become significant beyond a δ/N of about 85 (≈ 200 for $1\,R_{Jup}$). Thus, the quadratic law is sufficient until a δ/N of 200 is achieved for a Jupiter-like planet. However, even for $\delta/N = 400$ the resulting parameters do not differ much from the expected parameters ($\Delta p = +0.3\,‰$, $\Delta i = +0.1\,‰$, $\Delta a = +0.6\,‰$). Therefore, laws with higher orders than the quadratic law are not necessary given today's photometry. Additionally, this analysis shows that transits of small planets are more affected by an incorrect limb-darkening description than those of larger planets.

Spectral observations and analyses

Transiting planets offer the opportunity to study stellar surface brightness distributions. Beside limb darkening that also includes spots and faculae. To measure the temperature of these features one needs at least transit observations in different color bands. For that purpose I carried out spectro-photometric observations of the active planet host star CoRoT-2A.

> The obtained transit light curves were not usable for the intended purpose due to several issues. The instrumentation used did not provide a sufficient time resolution caused by long integration times, long lasting CCD read-outs, and performed "dithering". The target and reference star had to be placed at the edges of the small field-of-view, leading to a time- and color-dependent flux loss of the target star at the percent level. Unfortunately, there were no observations made before the transit events, which hampers a credible normalization and detrending of the light curves.

For predictions of the limb darkening one needs to know some fundamental parameters of the stars, such as the effective temperature or the surface gravity. These parameters can, e.g., be determined from spectral observations. I used the spectroscopic analysis tool Spectroscopy Made Easy (SME, Valenti & Piskunov, 1996) to analyze VLT/UVES high-resolution spectra of two planet host stars (ε Eridani and CoRoT-2A).

> The resulting values of $T_{\rm eff}$, $\log g$, $v \sin i$, and ξ were presented. In the case of $T_{\rm eff}$ and $\log g$ two different approaches were used. First, these parameters were determined together with the other parameters in a global fit, second, they were treated individually fitting the H_α and Na D lines. In both cases the results are quite similar and they are consistent. All determined values were compared to those in the literature and found to be in good agreement. In the case of CoRoT-2A the results were published in Schröter et al. (2011).

Limb darkening of *Kepler* objects

During my work I studied the transits of a set of 46 *Kepler* planetary candidate host stars. These were selected according to their *SNR* value (Section 4.1) and constitute a sample of the highest-quality transiting planets in the *Kepler* field. Due to the planet acting as a probe that scans the stellar brightness distribution during its transit, I was able to measure the limb darkening. I modeled more than 3000 individual transit light curves by using a Markov-Chain Monte-Carlo approach to determine the most probable transit parameters for each object in my sample. The measured coefficients of the linear and the quadratic limb-darkening law were presented and compared to predictions. The selected target stars span a wide range of effective temperatures from 4000 K to almost 9000 K and all of them are main sequence stars. However, the majority of my sample has spectral types of late F, G, and early K. The results using *Kepler* data with high temporal resolution have been published in A&A (Müller et al., 2013), while results obtained with long cadence (LC) data are exclusively available in Section 4.2.

LC data with high signal-to-noise is suitable to measure the linear limb darkening coefficient. Most of these objects show small uncertainties in the determined LDCs. The majority of the measured LDCs lies clearly below the predictions, which can be interpreted as a significant overestimation of linear limb darkening by theory (Fig. 4.2). The deviation amounts to −0.1 in the case of predictions determined by a least squares fit or in the best case −0.03 when the flux conserving fit method (Claret, 2000) was used. Thus, the LDCs predicted by the flux conserving method turned out to be more reliable for the linear limb darkening. In contrast, the fit results of the quadratic LDCs using LC data mostly show large uncertainties caused by the insufficient time resolution (Fig. 4.3). Therefore, I presented the analysis of the quadratic limb darkening using short cadence (SC) *Kepler* data. Differences between the measured LDCs and the PHOENIX or ATLAS predictions were translated into systematic transit parameter errors, which occur if theoretical LDCs are fixed in transit modeling. The induced error by using fixed quadratic LDCs is in the order of 1 % for the planet-to-star radii ratio p and the inclination i, and slightly larger for the semimajor axis a (Table 4.3). In the case of ground-based photometry, where the δ/N is almost always at a low level, I conclude that the quadratic LDCs should be fixed using predictions. The systematic error in the transit parameters is small compared to the uncertainties caused by the poor data quality. For transiting planets with large impact parameters (definitely for $b > 0.8$, but setting in already at $b > 0.7$) the deduced LDCs deviate systematically from theory. This was previously recognized by Howarth (2011) and now empirically reproduced by my work. Furthermore, the uncertainties in the quadratic LDCs in such systems are considerably large and I presented an analytical approach to describe these behaviors. Consequently, for transiting planets with an impact parameter of $b > 0.7$ the LDCs should be fixed in transit modeling. Overall, a slightly weaker limb darkening than predicted was measured together with a systematically weaker curvature expressed with small values of the quadratic limb-darkening coefficient u_2.

The analysis of time-correlated noise is a crucial step in studies of time-series data. In the presence of such noise the standard approach is to increase the resulting parameter errors by a certain factor β (Carter & Winn, 2009). This factor is determined as the ratio of measured standard deviation, σ_n, and the white noise prediction. The measured standard deviation is determined after the data set has been time-averaged over intervals relevant for the analysis (Winn et al., 2007). I simulated transit light curves and presented a time-correlated noise analysis based on this time-averaging method.

The used approach is capable of detecting oscillations hidden in the noise. Although the simulated oscillation was phase shifted in each transit, this method shows characteristic signatures, which – if seen in real data – could easily be attributed to oscillations. I showed that gaps in the light curve, e.g., missing continuum parts, lead to σ_n values significantly deviating from the white noise prediction. Therefore, the red noise analysis has to be carried out for each transit individually and is then averaged to one result.

However, according to my simulations the widely used white noise prediction (Eq. 4.15) seems to be incorrect. This equation overestimates σ_n for a low number of remaining bins M (Fig. 4.14). The resulting values of β are thus systematically underestimated. I presented a more reasonable approach, which is to simulate the time-series data by using the best fit model and adding Gaussian noise with the standard deviation of the real data. The simulation must have the same time-axis including all gaps or missing data points. Then the time-correlated noise analysis is performed for this simulation. Since the simulation holds only white noise one can use the resulting σ_n as a reliable white noise prediction for the analysis of the real data. By using this method one achieves $\approx 4\,\%$ larger β values, which I consider more reliable. Furthermore, I empirically found a better equation (Eq. 4.16) for the white noise prediction. I pointed out that the standard deviation only represents the probable error of one bin, if a large number of bins is left with a lower boundary of 7 to 8 bins. For less bins the mean of the errors of the means (Eq. 4.18), approaches $\sigma_1/\sqrt{N}$, hence, this value turned out to be a better estimator of the bin error.

Limb Darkening of the Sun

A well suited object to compare measurements of the limb darkening to predictions is the Sun. Its limb darkening has already been measured by several authors with high accuracy. For comparison I used the work of Neckel & Labs (1994), which provides measurements ranging from the UV to the near infrared and a most recent PHOENIX model atmosphere (Table A.11). The results were presented in several Johnson filters as well as for some specific wavelengths (Figs. 5.5 and 5.6). Systematic deviations were quantified and translated into transit parameter changes occurring if model predictions are used in transit modeling. Finally, space-based observations of the Sun were used to determine the solar limb darkening again.

I found that there are significant differences between models and measurements at small and intermediate limb angles. The model intensity distributions lie systematically below the measurements. This means that the emitted stellar flux is underestimated by theory or, in other words, the limb darkening is overestimated. In the Johnson-V filter band this amounts to 1.44 %. Nevertheless, the overall shapes of the PHOENIX model limb profiles are quite comparable to those measured by Neckel & Labs (1994) in almost all individual wavelengths and all photometric passbands. Only the steep intensity drop-off close to the limb is not shared by the measurements. Although the authors measured only intensities for $\mu > 0.1$, they argue that their extrapolated values down to $\mu = 0$ are reasonable, since they have a physical meaning (Neckel, 2005). From the point of view of transit modeling non-zero intensities at the limb are essential, because the transit starts when light is blocked and if the line-of-sight is perpendicular to the surface normal (cf., Eq. 1.5). I found that this predicted drop-off leads to an 11 s shorter transit duration because the stellar disk appears $1.5 \cdot 10^{-3}\,R_S$ smaller for a typical total duration of two

hours. To account for these effects I presented a rescaling of the μ-axis for the model atmospheres. That led to an improvement in the intensity profiles with smaller deviations from measurements in terms of disk-integrated fluxes. For instance, in the Johnson-V filter this deviation was now reduced to 0.2 %. The determination of LDCs from this model distribution was then also investigated. Due to a higher amount of intensity points close to the limb the LDC fits are mostly influenced by that region. Therefore, I recommend to revise the original μ-axis, where it is defined as $\sqrt{1-r^2}$ with r to be an equi-distant grid of radial coordinates. A fit to this distribution combined with the rescaling led to distributions more compatible with the measurements. The outermost stellar limb in the models ($r = 1$) could be determined as proposed by Orosz & Hauschildt (2000, Eq. 11) as the point of the highest slope in r-space. When this intensity distribution is transformed into the μ-space, I suppose that even the steep drop off is only weakly pronounced or even not visible anymore. Although I had to rescale the intensity distribution of the PHOENIX atmosphere, I think that the agreement of measurements and model is a clear indicator for the excellent quality of the PHOENIX model atmospheres.

Numerical Transits

In transit modeling one important step is the choice of the limb-darkening law and, in the case of poor photometric precision, the LDCs which belong to it. However, the limb-darkening laws are only approximations to the real intensity distributions. There exist different fitting approaches, e.g., least squares and flux conserving (Claret, 2000) and I showed that the fitted LDCs depend on the underlying μ-axis. It would be more reasonable to use the model intensities directly in transit modeling. This problem asks for numerical methods, which offer the opportunity to compare the resulting transits to conventional transit models and to transits using measurements of the solar disk intensity distribution. For these purposes I presented an efficient numerical transit algorithm, which is capable of using the limb intensities directly from a PHOENIX atmosphere as well as any other limb-darkening description.

My algorithm is based on fast Fourier transforms, providing an accuracy of $5 \cdot 10^{-6}$ or better when compared to a conventional transit model (Fig. 6.6). The accuracy depends on the selected resolution, which is only limited by computational power. The algorithm produces several thousand transit data points within a fraction of a second (Fig. 6.5). Compared to a numerical transit algorithm where the planet is moved step by step across the stellar disk, my method is about 80 times faster and additionally leading to an amazingly high time resolution. Fits of transit light curves, which were generated with my code using the quadratic limb-darkening law, led to the input values of the coefficients. This serves as a cross-check that the transit fitting approach using the `occultquad` routine does not introduce some systematics and, hence, it is justified using it for limb-darkening studies. My algorithm is capable to generate transits based on arbitrary shapes of the planet and the star. I presented the cases of planetary oblateness and planets with rings.

Transit simulations of planets with rings have already been carried out by several authors, however, my focus was set on the detectability of ring induced signatures given different limb darkening (Fig. 6.10). It turned out that weaker limb darkening leads to a better detectability. Furthermore, I presented the signatures of Saturn's Cassini Division for the first time and estimated the required photometric accuracy to about $5 \cdot 10^{-6}$. Beyond having introduced the first transit light curves directly using limb intensities from a model atmosphere, I presented transits based on images made by the solar space observatory SDO. These comprise transits in optical and in shorter wavelengths like soft X-rays (Fig. 6.15). I selected transit paths over quiet and active solar regions, which revealed that bright active regions heavily distort the classical transit shape. Finally, I was able to reproduce the simulated behavior of the fitted quadratic LDCs with increasing impact parameter as presented by Howarth (2011). However, without relying on a nonlinear limb-darkening law, but rather using the model intensities from a PHOENIX atmosphere directly.

8.2 Looking ahead

During the work on this PhD thesis I had some further ideas on how to extend my work. These were left unfinished but could possibly be completed in future work. In this section I am going to summarize these ideas.

Further limb-darkening measurements

In the presented work precise measurements of the stellar limb darkening were carried out by utilizing space-based observations. The given accuracy of the quadratic LDCs is at least for some objects higher than differences between theoretical predictions originating from different model atmospheres. Future missions like ESA's PLAnetary Transits and Oscillations (PLATO)[1], NASA's Transiting Exoplanet Survey Satellite (TESS)[2], and NASA's James Webb Space Telescope (JWST)[3] will offer an even higher photometric precision than *Kepler*. These data sets could then be used to study the limb darkening in even more detail. Due to the probably higher amount of stars with high S/N available, the achieved limb darkening could then be used to investigate the natural diversity of the stellar limb darkening with the same or similar characteristics ($T_{\rm eff}$, $\log g$, and so on). According to my studies such diversity is already indicated by the scatter in the most precise measurements in my sample in the vicinity of 5800 K (Fig. 5 of Müller et al. (2013)). Furthermore, these upcoming precise measurements possibly require the use of more complicated limb-darkening laws ($\delta/N > 400$), especially in the case of small Earth-sized transiting planets (cf., Fig. 1.17).

[1] http://sci.esa.int/plato/
[2] http://tess.gsfc.nasa.gov/
[3] http://www.jwst.nasa.gov/

Transit observations in the infrared – where almost no limb darkening is present – would offer the opportunity to pin down the remaining orbital parameters with high precision. These observations already exist, e.g., using the SOFIA[4] instrument or the Spitzer[5] space telescope. Follow up observations of the same objects, e.g., using PLATO could then be used to determine only the limb darkening, keeping the other parameters fixed or at least free given precise prior distributions for the MCMC sampling.

Transit modeling

For my limb-darkening studies I used the tool of planetary transit modeling. Even though, the models offer a high accuracy, they are not able to generate transits without an analytical limb darkening descriptions. For further transit simulations, with planets, moons, asteroids and in principle bodies with any kind of shape, my numerical code should be parallelized. My code is also capable of simulating gray planetary atmospheres or semi-opaque planetary rings. The usage of the code in the process of transit fitting could also be the next step. Transits for all possible impact parameters could be generated at once and only the planet properties have to be varied. For this purpose an implementation on modern graphics cards would be reasonable.

As an interesting aspect, I found simulated transits in different photometric pass bands to show two points where the light curves intersect (Fig. 1.12). Furthermore, these points show a similar normalized flux value as it would be given during a transit in front of a hypothetically non-limb-darkened star. This leads to the conclusion that these points are only weakly dependent on or even independent of the limb darkening. For a theoretical confirmation I use a simplified transit model for a point-like planet and a stellar disk with quadratic limb darkening (Müller et al., 2013, Eq. B.1), which is written as

$$y = 1 - p^2 \frac{1 - u_1(1-\mu) - u_2(1-\mu)^2}{1 - \frac{u_1}{3} - \frac{u_2}{6}} \,. \tag{8.1}$$

By setting the quadratic coefficient, u_2, to zero I obtain a transit model which is valid for the linear limb-darkening law. This model should now be independent of u_1 for one specific limb angle μ. To determine that point I consider the partial derivative

$$\frac{\partial y}{\partial u_1} = p^2 \frac{\frac{2}{3} - \mu}{\left(1 - \frac{u_1}{3}\right)^2} \stackrel{!}{=} 0 \,. \tag{8.2}$$

This derivative is zero when $\mu = 2/3$, which means the flux level at this position is indeed independent of the linear limb darkening coefficient. For more complex limb-darkening functions such a point is not guaranteed. However, I verified that the intersection of the transits appears still in the vicinity of $\mu = 2/3$ for the quadratic and nonlinear limb-darkening laws.

[4] http://www.nasa.gov/mission_pages/SOFIA/index.html
[5] www.spitzer.caltech.edu/

Although this intersection is not totally congruent, further studies of this behavior could be promising. If it would be true that there exist such points without any or weak limb-darkening contribution in real transits, one would be able to determine the planet-to-star radii ratio directly from two individual points in the light curve. This would reduce the number of fit parameters by one. For an empirical confirmation one would need multi-band photometry of transits, e.g., provided by CoRoT. The effect that limb intensities from atmospheres with different T_{eff} intersect is already known (Neilson & Lester, 2012, Fig. 1) and the presented phenomenon could have the same or a similar origin.

At any rate, the limb darkening is a very important parameter for current and future studies, not only of planetary transit light curves, but also for future spectroscopic observations. Especially in the emergent field of planetary atmosphere studies, a precise knowledge of the limb darkening will be indispensable.

Appendices

A Tables

Table A.1: Center coordinates of the chosen details from *Kepler* full frame images shown in Fig. 3.4.

CCD Channel	α	δ
15	$18^h\,43^m\,11^s$	$+47°17'47''$
41	$19^h\,28^m\,58^s$	$+44°08'44''$
43	$19^h\,16^m\,08^s$	$+44°41'17''$
56	$19^h\,21^m\,42^s$	$+51°41'31''$

Notes: Equinox 2000. Used file `kplr2012179140901_ffi-cal.fits` downloaded at MAST. A map of the CCD channels is given in Fig. B.9.

Table A.2: Start-/end dates of all *Kepler* quarters.

Quarter	Start	End	Duration in Days
0	May 2nd, 2009	May 11th, 2009	9.7
1	May 13th, 2009	Jun. 15th, 2009	33.5
2	Jun. 20th, 2009	Sep. 16th, 2009	88.7
3	Sep. 18th, 2009	Dec. 17th, 2009	89.3
4 [a)]	Dec. 19th, 2009	Mar. 19th, 2010	89.8
5	Mar. 20th, 2010	Jun. 23th, 2010	94.7
6	Jun. 24th, 2010	Sep. 22th, 2010	89.8
7	Sep. 23th, 2010	Dec. 22th, 2010	89.4
8	Jan. 6th, 2011	Mar. 14th, 2011	66.7
9	Mar. 21th, 2011	Jun. 26th, 2011	97.4
10	Jun. 27th, 2011	Sep. 28th, 2011	93.4
11	Sep. 29th, 2011	Jan. 4th, 2012	97.1
12	Jan. 5th, 2012	Mar. 28th, 2012	82.6
13	Mar. 29th, 2012	Jun. 27th, 2012	90.3
14	Jun. 28th, 2012	Oct. 3th, 2012	97.2
15	Oct. 5th, 2012	Jan. 11th, 2013	97.6
16	Jan. 12th, 2013	Apr. 8th, 2013	85.8
17	Apr. 9th, 2013	May 11th, 2013	31.8

Notes: Information drawn from FITS-headers. [a)] For broken CCD channels only 20 days available.

Table A.3: Values for the determination of the spectral resolution.

λ/Å	$\lambda/\Delta\lambda$	λ/Å	$\lambda/\Delta\lambda$
6928.73	56259	6934.81	64580
6918.12	55120	6935.67	66184
7179.30	52656	6909.82	67301
7050.85	52623	6913.59	69306
7282.28	59586	6929.12	61791

Notes: This table lists the wavelengths for the chosen telluric lines and the corresponding spectral resolution. The $\Delta\lambda$ is determined by a fit to the given lines using a Voigt profile ($\Delta\lambda \approx$ FWHM = $2\sqrt{2\ln 2}\,\sigma$). The values in the left two columns belong to the spectrum of ε Eridani and the right columns belong to the spectrum of CoRoT-2A.

Table A.4: Transit parameters for simulated colored-noise analysis.

Parameter	Value
R_P/R_S	0.10508
i/ °	90.0
a/R_S	9.9461
u_1	0.5013
u_2	0.1122
P_{orb}/ d	4.94278
t_{dur}/ h	4.2
$t_{ingress}$/ m	24.1
σ_1	0.0005

Notes: This table lists the chosen system parameters to generate a simulated dataset used for the time-correlated noise analysis (Section 4.4.1). The duration of the whole transit (t_{dur}) and of the ingress ($t_{ingress}$) are deduced values. Limb darkening coefficients are arbitrarily chosen from a 5800 K star measured in my *Kepler* sample (Kepler-15b).

Table A.5: Transit modeling results based on long cadence data.

Kepler ID	χ^2/ν	p	$i/^\circ$	a/R_S	b	u_1	u_2	m_1	m_2
5794240	1.29	$0.19116^{+0.00781}_{-0.00417}$	$86.57^{+0.80}_{-0.55}$	$10.352^{+0.568}_{-0.340}$	$0.619^{+0.084}_{-0.110}$	$0.231^{+0.438}_{-0.285}$	$0.270^{+0.730}_{-0.242}$	0.459	0.269
3749365	1.36	$0.16417^{+0.00951}_{-0.00495}$	$88.04^{+0.92}_{-1.38}$	$8.965^{+0.365}_{-0.361}$	$0.306^{+0.204}_{-0.127}$	$0.714^{+0.145}_{-0.173}$	$0.001^{+0.303}_{-0.711}$	0.630	0.114
5358624	1.38	$0.14352^{+0.00204}_{-0.00165}$	$87.92^{+0.28}_{-0.41}$	$11.049^{+0.207}_{-0.261}$	$0.401^{+0.072}_{-0.042}$	$0.691^{+0.071}_{-0.098}$	$-0.254^{+0.187}_{-0.170}$	0.578	0.141
5357901	1.43	$0.11655^{+0.00530}_{-0.00239}$	$87.03^{+0.27}_{-0.55}$	$11.560^{+0.299}_{-0.530}$	$0.599^{+0.083}_{-0.035}$	$0.597^{+0.181}_{-0.268}$	$0.126^{+0.338}_{-0.595}$	0.551	0.152
9115800	1.34	$0.12912^{+0.00210}_{-0.00299}$	$86.39^{+0.15}_{-0.18}$	$11.823^{+0.249}_{-0.261}$	$0.744^{+0.023}_{-0.015}$	$0.306^{+0.373}_{-0.517}$	$0.148^{+0.840}_{-0.323}$	0.538	0.161
11414511	1.41	$0.12557^{+0.00294}_{-0.00208}$	$87.00^{+0.38}_{-0.88}$	$8.688^{+0.217}_{-0.429}$	$0.455^{+0.108}_{-0.044}$	$0.587^{+0.110}_{-0.159}$	$-0.103^{+0.293}_{-0.270}$	0.508	0.176
8544996	1.75	$0.12772^{+0.00263}_{-0.00219}$	$88.03^{+0.39}_{-0.94}$	$10.216^{+0.305}_{-0.440}$	$0.352^{+0.148}_{-0.056}$	$0.620^{+0.064}_{-0.117}$	$-0.167^{+0.232}_{-0.182}$	0.503	0.177
9595827	1.56	$0.14143^{+0.00221}_{-0.00175}$	$87.89^{+0.27}_{-0.48}$	$11.034^{+0.215}_{-0.292}$	$0.407^{+0.078}_{-0.045}$	$0.531^{+0.063}_{-0.097}$	$-0.028^{+0.195}_{-0.185}$	0.500	0.178
6849046	1.07	$0.08433^{+0.00115}_{-0.00116}$	$86.87^{+0.31}_{-0.41}$	$10.415^{+0.300}_{-0.397}$	$0.570^{+0.054}_{-0.035}$	$0.726^{+0.113}_{-0.124}$	$-0.292^{+0.179}_{-0.180}$	0.496	0.184
9410930	1.34	$0.10390^{+0.00170}_{-0.00085}$	$82.12^{+0.26}_{-0.36}$	$5.048^{+0.067}_{-0.088}$	$0.692^{+0.020}_{-0.013}$	$0.767^{+0.232}_{-0.062}$	$-0.201^{+0.098}_{-0.322}$	0.492	0.181
3935914	1.19	$0.12397^{+0.00353}_{-0.00257}$	$82.76^{+0.57}_{-0.95}$	$5.318^{+0.153}_{-0.241}$	$0.670^{+0.061}_{-0.028}$	$0.294^{+0.192}_{-0.350}$	$0.418^{+0.582}_{-0.180}$	0.483	0.184
9166862	1.34	$0.12078^{+0.00101}_{-0.00199}$	$88.75^{+1.25}_{-0.41}$	$10.008^{+0.354}_{-0.107}$	$0.218^{+0.069}_{-0.218}$	$0.430^{+0.045}_{-0.072}$	$0.165^{+0.180}_{-0.139}$	0.481	0.185
9651668	1.30	$0.12390^{+0.00051}_{-0.00100}$	$89.01^{+0.99}_{-0.31}$	$8.427^{+0.127}_{-0.044}$	$0.146^{+0.045}_{-0.146}$	$0.445^{+0.023}_{-0.023}$	$0.236^{+0.073}_{-0.072}$	0.479	0.186
8359498	1.26	$0.09870^{+0.00155}_{-0.00252}$	$88.01^{+0.74}_{-1.17}$	$9.608^{+0.590}_{-0.254}$	$0.333^{+0.184}_{-0.094}$	$0.447^{+0.036}_{-0.053}$	$0.291^{+0.157}_{-0.123}$	0.479	0.186
7849854	1.21	$0.11309^{+0.00638}_{-0.00742}$	$86.53^{+1.14}_{-2.19}$	$7.294^{+0.426}_{-0.568}$	$0.441^{+0.228}_{-0.107}$	$0.534^{+0.112}_{-0.181}$	$0.409^{+0.591}_{-0.161}$	0.479	0.186
11359879	1.24	$0.10280^{+0.00186}_{-0.00149}$	$86.32^{+0.17}_{-0.28}$	$10.140^{+0.163}_{-0.239}$	$0.651^{+0.036}_{-0.019}$	$0.389^{+0.131}_{-0.188}$	$0.320^{+0.282}_{-0.284}$	0.474	0.189
11446443	1.13	$0.12462^{+0.00085}_{-0.00216}$	$83.93^{+0.09}_{-0.10}$	$7.918^{+0.065}_{-0.090}$	$0.837^{+0.006}_{-0.006}$	$0.200^{+0.190}_{-0.390}$	$0.520^{+0.480}_{-0.143}$	0.472	0.190
12019440	1.30	$0.12373^{+0.00186}_{-0.00201}$	$87.83^{+0.55}_{-1.06}$	$8.689^{+0.280}_{-0.329}$	$0.329^{+0.145}_{-0.068}$	$0.543^{+0.060}_{-0.098}$	$-0.087^{+0.208}_{-0.154}$	0.471	0.188
7877496	1.15	$0.10393^{+0.00192}_{-0.00261}$	$80.95^{+0.26}_{-0.40}$	$4.962^{+0.084}_{-0.097}$	$0.780^{+0.018}_{-0.011}$	$0.404^{+0.289}_{-0.479}$	$0.263^{+0.736}_{-0.278}$	0.464	0.192
5780885	1.35	$0.08335^{+0.00039}_{-0.00036}$	$85.03^{+0.18}_{-0.21}$	$6.604^{+0.065}_{-0.084}$	$0.572^{+0.018}_{-0.014}$	$0.460^{+0.040}_{-0.048}$	$0.049^{+0.073}_{-0.069}$	0.462	0.202
9631995	1.43	$0.09605^{+0.00123}_{-0.00102}$	$88.11^{+0.22}_{-0.35}$	$13.862^{+0.329}_{-0.436}$	$0.456^{+0.070}_{-0.040}$	$0.485^{+0.039}_{-0.067}$	$0.115^{+0.136}_{-0.097}$	0.459	0.195
11804465	1.38	$0.11910^{+0.00047}_{-0.00049}$	$88.69^{+0.31}_{-0.55}$	$7.995^{+0.075}_{-0.078}$	$0.182^{+0.074}_{-0.042}$	$0.425^{+0.012}_{-0.017}$	$0.115^{+0.045}_{-0.036}$	0.456	0.200
9818381	1.15	$0.08513^{+0.00198}_{-0.00210}$	$85.45^{+0.72}_{-0.98}$	$7.390^{+0.350}_{-0.453}$	$0.587^{+0.091}_{-0.060}$	$0.318^{+0.130}_{-0.208}$	$0.338^{+0.375}_{-0.256}$	0.450	0.199
10019708	1.27	$0.09922^{+0.00147}_{-0.00130}$	$85.73^{+0.46}_{-0.84}$	$6.967^{+0.202}_{-0.298}$	$0.519^{+0.078}_{-0.038}$	$0.597^{+0.094}_{-0.157}$	$-0.245^{+0.215}_{-0.199}$	0.437	0.204
9941662	1.31	$0.06088^{+0.00010}_{-0.00008}$	$86.61^{+0.31}_{-0.38}$	$4.510^{+0.032}_{-0.029}$	$0.267^{+0.028}_{-0.022}$	$0.371^{+0.007}_{-0.007}$	$0.129^{+0.015}_{-0.015}$	0.238	0.289

Table A.6: Photometric quality of my *Kepler* short cadence sample.

Kepler ID	S/N	σ	δ/N	$(S/N)_c$	σ_c
5794240	288	$3.47 \cdot 10^{-3}$	11.5	1382	$7.24 \cdot 10^{-4}$
10748390	10325	$9.69 \cdot 10^{-5}$	45.6	43804	$2.28 \cdot 10^{-5}$
11391018	685	$1.46 \cdot 10^{-3}$	15.1	1812	$5.52 \cdot 10^{-4}$
5357901	714	$1.40 \cdot 10^{-3}$	10.7	5885	$1.70 \cdot 10^{-4}$
8845026	1188	$8.42 \cdot 10^{-4}$	15.6	1188	$8.42 \cdot 10^{-4}$
9595827	500	$2.00 \cdot 10^{-3}$	11.3	2345	$4.27 \cdot 10^{-4}$
6849046	1130	$8.85 \cdot 10^{-4}$	8.9	8972	$1.11 \cdot 10^{-4}$
9410930	795	$1.26 \cdot 10^{-3}$	8.9	9437	$1.06 \cdot 10^{-4}$
9651668	828	$1.21 \cdot 10^{-3}$	15.7	7674	$1.30 \cdot 10^{-4}$
8359498	1031	$9.70 \cdot 10^{-4}$	12.2	10157	$9.85 \cdot 10^{-5}$
7023960	609	$1.64 \cdot 10^{-3}$	15.6	1491	$6.71 \cdot 10^{-4}$
11359879	1172	$8.53 \cdot 10^{-4}$	13.6	9806	$1.02 \cdot 10^{-4}$
10619192	816	$1.23 \cdot 10^{-3}$	17.3	10123	$9.88 \cdot 10^{-5}$
11446443	4236	$2.36 \cdot 10^{-4}$	60.6	54735	$1.83 \cdot 10^{-5}$
12019440	500	$2.00 \cdot 10^{-3}$	8.8	4298	$2.33 \cdot 10^{-4}$
10874614	1592	$6.28 \cdot 10^{-4}$	17.2	18365	$5.45 \cdot 10^{-5}$
7877496	884	$1.13 \cdot 10^{-3}$	9.4	10932	$9.15 \cdot 10^{-5}$
5780885	2066	$4.84 \cdot 10^{-4}$	15.7	17287	$5.78 \cdot 10^{-5}$
9631995	1281	$7.81 \cdot 10^{-4}$	13.6	8782	$1.14 \cdot 10^{-4}$
11804465	1310	$7.63 \cdot 10^{-4}$	22.0	11860	$8.43 \cdot 10^{-5}$
6922244	1061	$9.42 \cdot 10^{-4}$	9.9	11623	$8.60 \cdot 10^{-5}$
9818381	1151	$8.69 \cdot 10^{-4}$	9.3	12286	$8.14 \cdot 10^{-5}$
10019708	658	$1.52 \cdot 10^{-3}$	6.9	5657	$1.77 \cdot 10^{-4}$
10666592	6033	$1.66 \cdot 10^{-4}$	40.4	86587	$1.15 \cdot 10^{-5}$
8191672	1435	$6.97 \cdot 10^{-4}$	10.7	15786	$6.33 \cdot 10^{-5}$
9941662	9088	$1.10 \cdot 10^{-4}$	41.7	87171	$1.15 \cdot 10^{-5}$
10318874	1658	$6.03 \cdot 10^{-4}$	2.5	18974	$5.27 \cdot 10^{-5}$
5084942	1547	$6.47 \cdot 10^{-4}$	1.4	16514	$6.06 \cdot 10^{-5}$
12105051	1019	$9.82 \cdot 10^{-4}$	2.7	11834	$8.45 \cdot 10^{-5}$
5771719	902	$1.11 \cdot 10^{-3}$	10.5	3125	$3.20 \cdot 10^{-4}$
2571238	2990	$3.34 \cdot 10^{-4}$	2.2	18185	$5.50 \cdot 10^{-5}$
11295426	7735	$1.29 \cdot 10^{-4}$	2.6	48305	$2.07 \cdot 10^{-5}$
8456679	2151	$4.65 \cdot 10^{-4}$	2.0	27628	$3.62 \cdot 10^{-5}$
8554498	3570	$2.80 \cdot 10^{-4}$	3.4	34051	$2.94 \cdot 10^{-5}$
8684730	2590	$3.86 \cdot 10^{-4}$	4.3	3663	$2.73 \cdot 10^{-4}$
3762468	409	$2.44 \cdot 10^{-3}$	3.6	1227	$8.15 \cdot 10^{-4}$
4349452	5050	$1.98 \cdot 10^{-4}$	6.0	20824	$4.80 \cdot 10^{-5}$
3861595	3443	$2.90 \cdot 10^{-4}$	4.2	18544	$5.39 \cdot 10^{-5}$

Notes: Objects sorted by $T_{\rm eff}$ (see, Müller et al., 2013, Tab. 3). Column notation from left to right: KIC identifier, photometric signal-to-noise, continuum noise, transit-depth-to-noise, cumulative signal-to-noise (Eq. 3.1), and the corresponding cumulative photometric precision.

Table A.7: Relative differences in disk-integrated flux between PHOENIX and the Sun.

λ/Å	$(S_P/S_N - 1)$ / %	λ/Å	$(S_P/S_N - 1)$ / %	λ/Å	$(S_P/S_N - 1)$ / %
3033.27	−1.64	4279.30	−0.29	6109.75	−1.49
3108.43	−1.87	4438.85	−0.87	6409.70	−1.39
3204.68	−1.49	4451.25	−1.05	6694.00	−1.42
3298.97	−2.28	4573.45	−1.16	7008.75	−1.48
3499.47	−0.47	4774.27	−1.25	7487.10	−1.46
3658.75	−1.99	4929.05	−1.28	8117.60	−1.35
3740.86	4.56	5199.30	−2.21	8696.00	−1.52
3909.15	−1.69	5417.60	−1.41	9488.50	−1.55
4019.70	0.23	5599.50	−1.43	10 466.00	−1.12
4163.19	−0.84	5798.80	−1.48	10 989.50	−1.25

Notes: Wavelength points for comparison are taken from Neckel & Labs (1994). The disk-integrated fluxes (S_P: PHOENIX, S_N: Sun) are determined by numerical integration (see Chapter 5 for details). A negative sign indicates percentage that PHOENIX lies below the disk-integrated flux of the Sun. Wavelengths are measured in air.

Table A.8: Disk-integrated flux aberrancies from the Sun in different filter bands.

Filter	ΔS_P / %	$\Delta S_{P\mu}$ / %	ΔS_{Cq} / %	$\Delta S_{Cq'}$ / %	ΔS_{Cn} / %	$\Delta S_{Cn'}$ / %
Johnson-U	−3.32	−2.34	3.95	−1.79	3.55	−1.70
Johnson-B	−1.10	−0.28	−1.48	−0.76	−1.59	−0.69
Johnson-V	−1.44	−0.20	−2.07	−1.66	−2.30	−1.69
Johnson-R	−1.14	−0.50	−1.21	−1.22	−1.51	−1.32
Johnson-I	−1.41	−0.86	−1.19	−1.47	−1.53	−1.60
Kepler	−0.12	0.56	0.71	0.17	0.41	0.09

Notes: I define $\Delta S_x = (S_x/S_N) - 1$. The disk-integrated fluxes are denoted as S_P: PHOENIX, $S_{P\mu}$: PHOENIX μ-rescaled, S_{Cq}: quadratic and S_{Cn}: nonlinear LD (LDCs taken from Claret & Bloemen (2011)), and $S_{Cq'}$ and $S_{Cn'}$ are also quadratic and nonlinear LD (LDCs taken from Claret et al. (2013)). S_N is the disk-integrated flux of the Sun in the given filter band; see Chapter 5 for more details. For the corresponding limb-intensity profiles of the first three columns see Fig. B.19.

Table A.9: Comparison of fitted quadratic LDCs in various filter bands.

Model	Johnson-U		Johnson-B		Johnson-V	
	u_1	u_2	u_1	u_2	u_1	u_2
Claret11	0.7137	0.0387	0.7471	0.0565	0.5624	0.1627
Claret13 qs	0.8897	−0.0629	0.6975	0.1231	0.5426	0.1825
PHOENIX	0.8768	0.0249	0.6944	0.1416	0.5345	0.1791
PHOENIX μ_{rescaled}	0.8581	0.0249	0.6798	0.1357	0.5187	0.1678
Neckel & Labs	0.7517	0.1348	0.6568	0.1651	0.4778	0.2241
Model	Johnson-R		Johnson-I		*Kepler*	
Claret11	0.4439	0.2058	0.3335	0.2325	0.4729	0.1871
Claret13 qs	0.4526	0.1891	0.3596	0.1945	0.4883	0.1822
PHOENIX	0.4519	0.1743	0.3694	0.1572	0.4950	0.1723
PHOENIX μ_{rescaled}	0.4427	0.1658	0.3621	0.1490	0.4849	0.1642
Neckel & Labs	0.3975	0.2317	0.3023	0.2257	0.4709	0.2176
Mean LDCs ($\bar{u}_1$, $\bar{u}_2$)					0.4613	0.1344

Notes: LDCs for Claret11 and Claret13 qs are taken from tables (see Table 5.1 for references). LDCs for the remaining models are determined by fitting a quadratic LD law to the distributions using a different fitting method as used by Claret (see Section 5.1.4 for details).

Table A.10: Limb-darkening coefficients for $P_5(\mu)$ (Eq. 5.1).

Filter	A_0	A_1	A_2	A_3	A_4	A_5
Johnson-U	0.118 12	0.952 06	0.170 42	−0.565 99	0.469 12	−0.143 72
Johnson-B	0.154 43	1.241 38	−1.005 33	1.242 42	−0.898 57	0.265 68
Johnson-V	0.260 90	1.317 16	−1.458 88	1.705 47	−1.137 19	0.312 54
Johnson-R	0.328 69	1.332 83	−1.808 13	2.335 69	−1.680 11	0.491 03
Johnson-I	0.426 74	1.242 72	−1.829 60	2.326 06	−1.624 76	0.458 83
Kepler	0.273 02	1.316 29	−1.548 03	1.910 80	−1.330 85	0.378 77

Notes: These LDCs are determined by a least-squares fit to limb profiles deduced from Neckel & Labs (1994) in several filter bands. The worst residuum is of the order of 10^{-15}.

Table A.11: Excerpt of the PHOENIX logfile.

```
install_hand: deactivated for CTC machines
*****************************************************************************************************************************************
*                                  ******  *     * ******* ******* *     *   ***   *     *                                              *
*                                  *     * *     * *     * *       **    *    *     *   *                                               *
*                                  *     * *     * *     * *       * *   *    *      * *                                                *
*                                  ******  ******* *     * *****   *  *  *    *       *                                                 *
*                                  *       *     * *     * *       *   * *    *      * *                                                *
*                                  *       *     * *     * *       *    **    *     *   *                                               *
*                                  *       *     * ******* ******* *     *   ***   *     *                                              *
*                                                                                                                                       *
*                                                  #####  ######                                                                        *
*                                                 #     # #     #                                                                       *
*                                                       # #     #                                                                       *
*                                                  #####  #     #                                                                       *
*                                                       # #     #                                                                       *
*                                                 #     # #     #                                                                       *
*                                                  #####  ######                                                                        *
*                                  ==================================================                                                   *
*                                                    Version: 16.03.01A                                                                 *
*                                                      27/May/2011                                                                      *
*                                          written by Peter H. Hauschildt,                                                              *
*                                     Edward Baron, Travis Barman, and Andreas Schweitzer                                               *
*                                              general model atmosphere version                                                         *
*                                  ==================================================                                                   *
*****************************************************************************************************************************************

This run was started at 20120323:165214.175
stellar model with GAIA v2.2 setup, old solar
the most important code/model parameters are:
-----------------------------------------------
no. of depth points: layer=  64              max. no. of angles per halfsphere (DOME): muemax= 4

using new partition function method  asymptotic hydrogenic parts (LTE) enabled

H- opacity setup used: 0
(0: John (1988) data, uses implicit Saha factor)
(1: direct data, uses H- pressure for b-f)

molecular line blanketing is considered    albedo for single scattering:  0.0000D+00   line/continuum threshold ratio:  1.0000D-04

phoenix: list of molecular lines used: [...] total number of sources: 128

H2O line lists are used : Barber + Tennyson (BT2)

This information is for the outer radius:
new giant mode in effect
model:   teff :     5800. k
         radius:  7.77E+10 cm
         log(g):       4.50 [cm/s**2]
         mass loss:  0.0000D+00 msun/yr
         outer pressure: 1.000E-04 dyn/cm**2

phoenix: setting dotrns = .false.!
         small output: level=0
output of angular radiation field selected
angles: mu
unit for output:  7
layer that will be printed: 1
no output of zeta factors


CPU timing information:
structure integration:            151.0 atomic line selection:              7.5 molecular line selection:          99.2
fuzz line selection:                 .0 Cassandra line selection:            .0 cont + molecular opacity:         60.9
LTE line opacity:                  30.4  (atomic Voigt lines)             20.4  (atomic Gauss lines)             6.1
 (molecular Voigt lines)            1.4  (molecular Gauss lines)            1.9  (fuzz lines)                     .0
NLTE  opacity:                       .2 radiative rates:                     .1 radiative transfer:             302.0
rad acc. & opac. avg.:               3.9 RT MPI communication:               .1 total time for spectrum:        419.4
MPI collwl communication:            .1 solve NLTE stat eqs:                 .0 temperature correction:           .1
evolution code:                      .0
```

Notes: This PHOENIX logfile output was generated during the computation of high-resolution spectra for different limb angles μ. Molecular lines are included. Most of this logfile is omitted.

B Figures

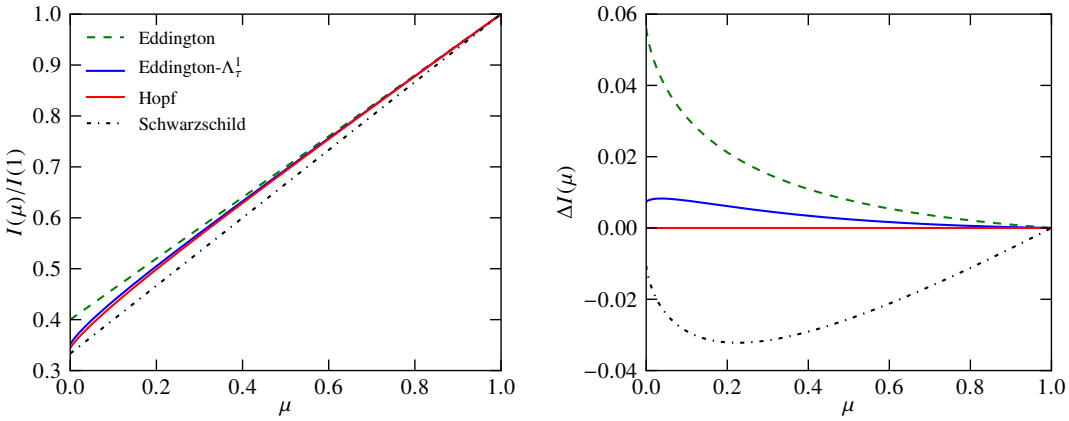

Figure B.1: Theoretical limb-darkening profiles for planar gray atmospheres (*left*). Details of the different predictions (*labels*) are discussed in Section 1.1.2. *Right*: Residuals of the profiles, determined by subtracting the limb darkening predicted by Hopf. Non-linear predictions are shown in solid lines.

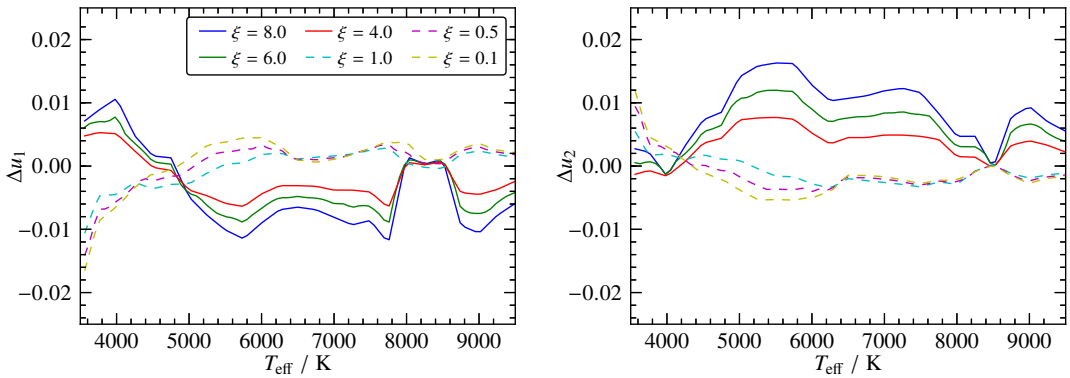

Figure B.2: Influence of the micro turbulent velocity ξ on the quadratic LDCs u_1 (*left*) and u_2 (*right*). Shown are the differences between theoretical LDCs determined with $\xi = 2.0\,\mathrm{km\ s^{-1}}$ and LDCs using different velocities (*labels*). (ATLAS models). See Section 1.1.3 for details.

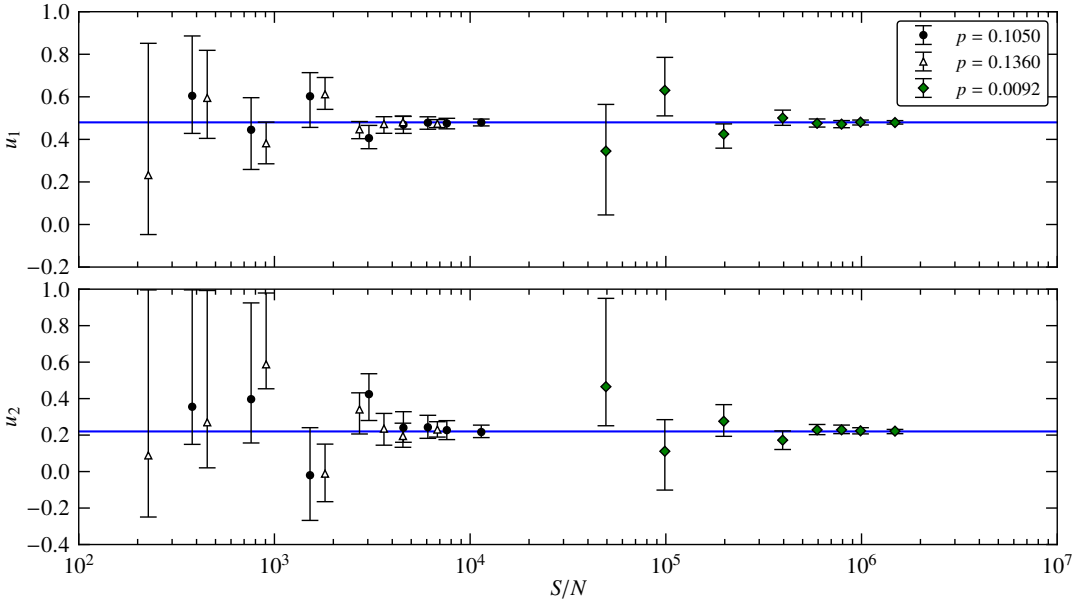

Figure B.3: Fitted quadratic LDCs of simulated transits with different S/N values. *Blue lines* indicate the values used for synthesizing the transits ($u_1 = 0.48$, $u_2 = 0.22$). The remaining orbital parameters where chosen as $p = 0.105$, $i = 88°$, $a = 11.2\,R_S$, which lead to a transit duration of about 3 hours. The error bars correspond to 68 % confidence intervals. For the simulation I used three different planet sizes (*labels*), which all have the same transit signal-to-noise ratios ($\delta/N = 5$, 10, 20, 40, 60, 80, 100, 150).

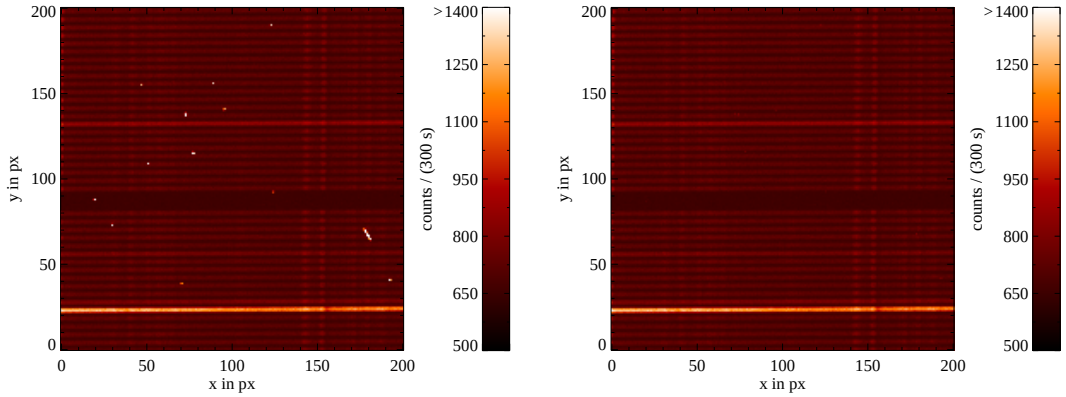

Figure B.4: Zoom-in to PPak CCD raw images. On the *left* I present the image before, and on the *right* after my applied cosmic removal. Cosmics are visible as white dots.

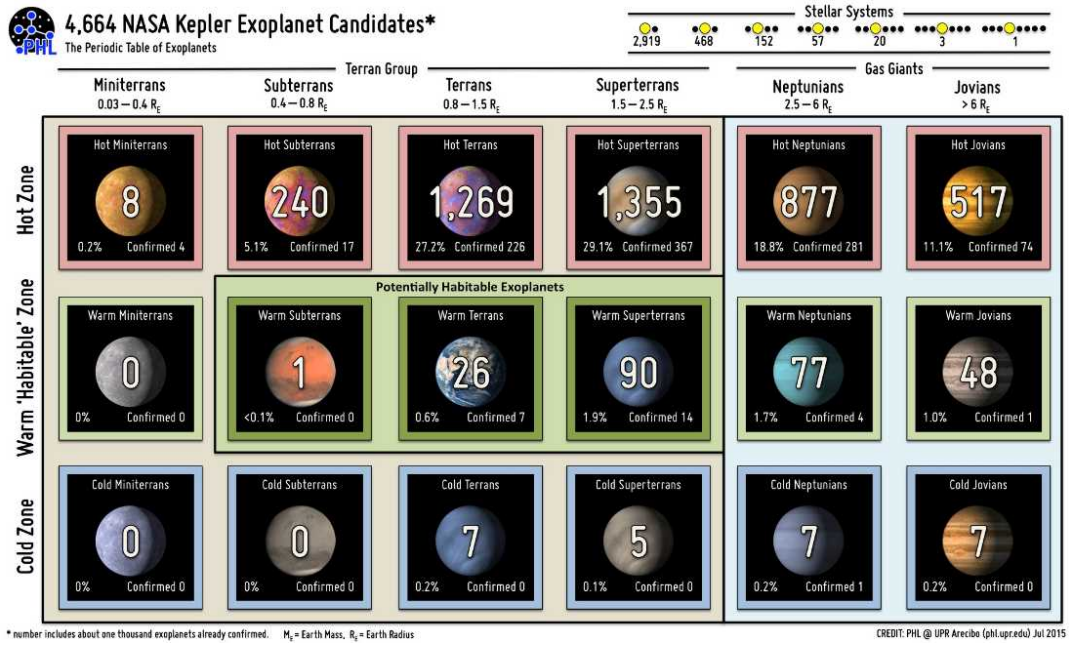

Figure B.5: The periodic table of *Kepler* exoplanets. Planet radius increases from *left* to *right*. The distance from the host star increases from *top* to *bottom*.

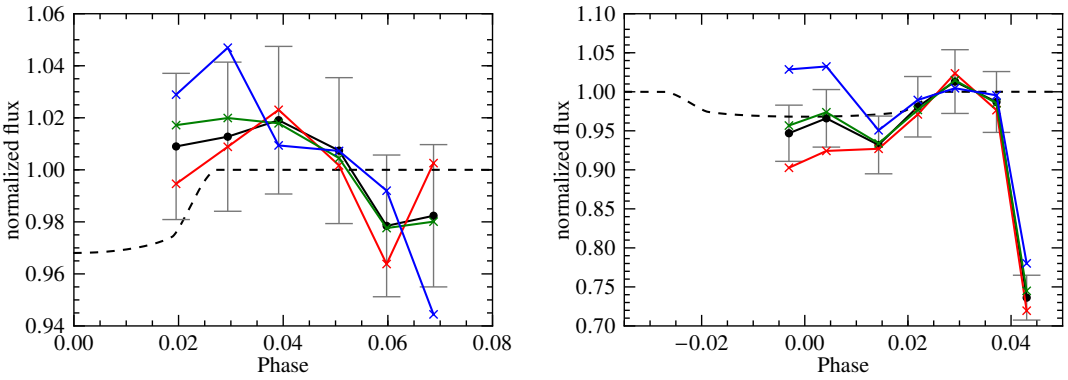

Figure B.6: Normalized PPak light curves of CoRoT-2A in four color bands (*red*: 6975 Å - 8050 Å, *green*: 5895 Å - 6975 Å, *blue*: 4815 Å - 5895 Å, *black*: 4815 Å - 8050 Å). The error bars indicate the 1σ uncertainties of the black dots, others are not shown for clarity. *Dashed lines*: Transit model of CoRoT-2b. *Left*: First observing night *Right*: Second observing night.

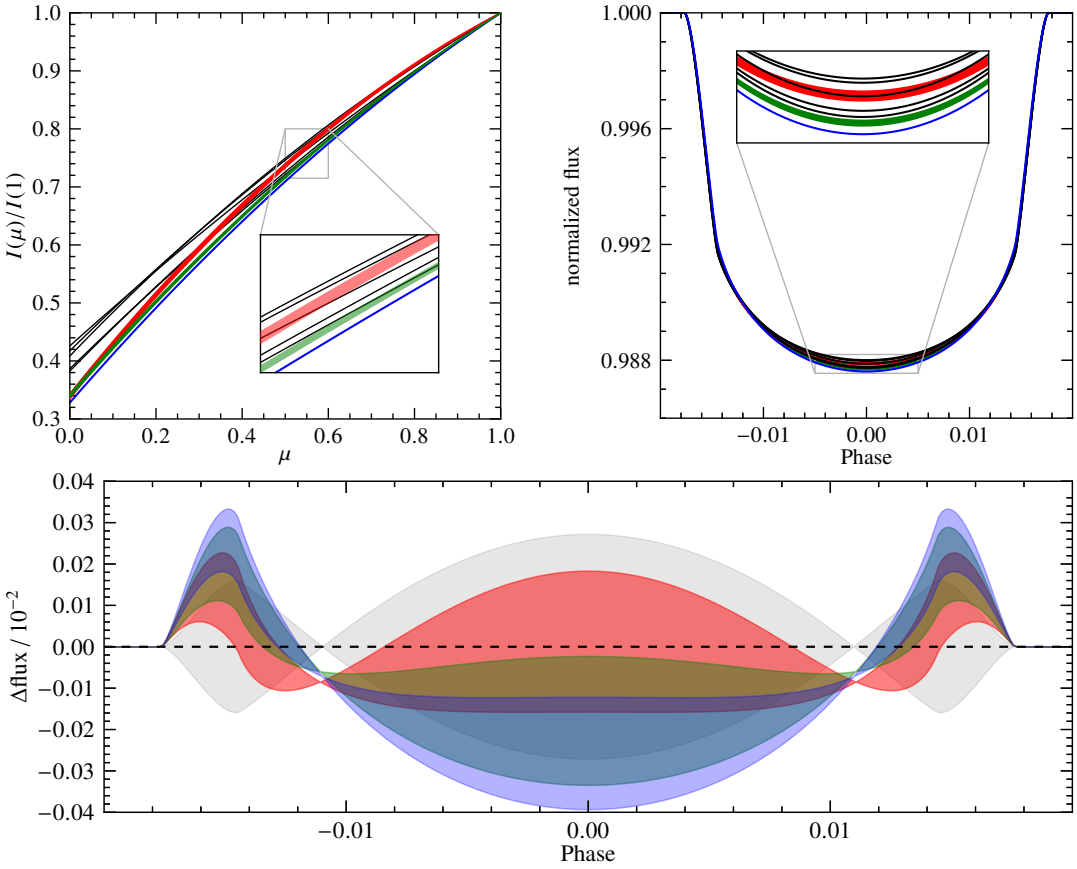

Figure B.7: *Left*: Limb-intensity profiles of five solar-like *Kepler* targets (*black*) together with predicted profiles using ATLAS (*red*), PHOENIX 1D (*green*), and PHOENIX qs (*blue*) for the temperature interval of 5750 K to 5850 K. See Chapter 4 for references. *Right*: Simulated transits using the shown limb intensities of the left panel, and a planet-to-star radii ratio of $p = 0.1$. *Bottom panel*: Maximum and minimum transit residuals determined by subtracting model transit of my *Kepler* measurements from transits created using model predictions. Colors are chosen as above. Additionally, the *gray* area indicates the difference between the transits with the strongest and the weakest measured limb darkening in that temperature range.

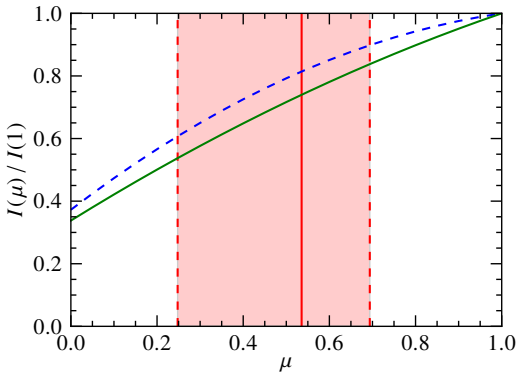

Figure B.8: Planet coverage of the stellar limb intensity during transit center of TrES-2b. *Red* area indicates the μ-values simultaneously covered by the planetary disk during transit center, where the *vertical solid* line marks the center of the planetary disk at $\mu_{\max}$. Theoretical distribution using model LDCs (*green solid*) and result of transit modeling of this highly inclined system (*blue dashed*) are shown for comparison.

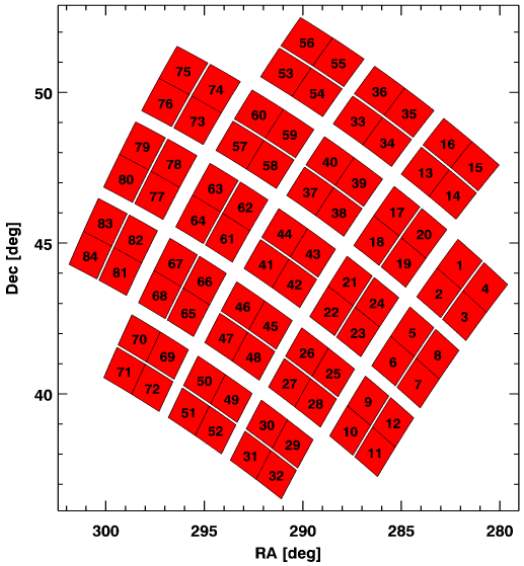

© [MAST, 2012]

Figure B.9: Display of *Kepler* Full Frame Images with corresponding CCD channels.

© [NASA, 2008]

Figure B.10: *Kepler*'s main camera CCD array during assembly. The curved structure needed for a Schmidt-type telescope is clearly visible.

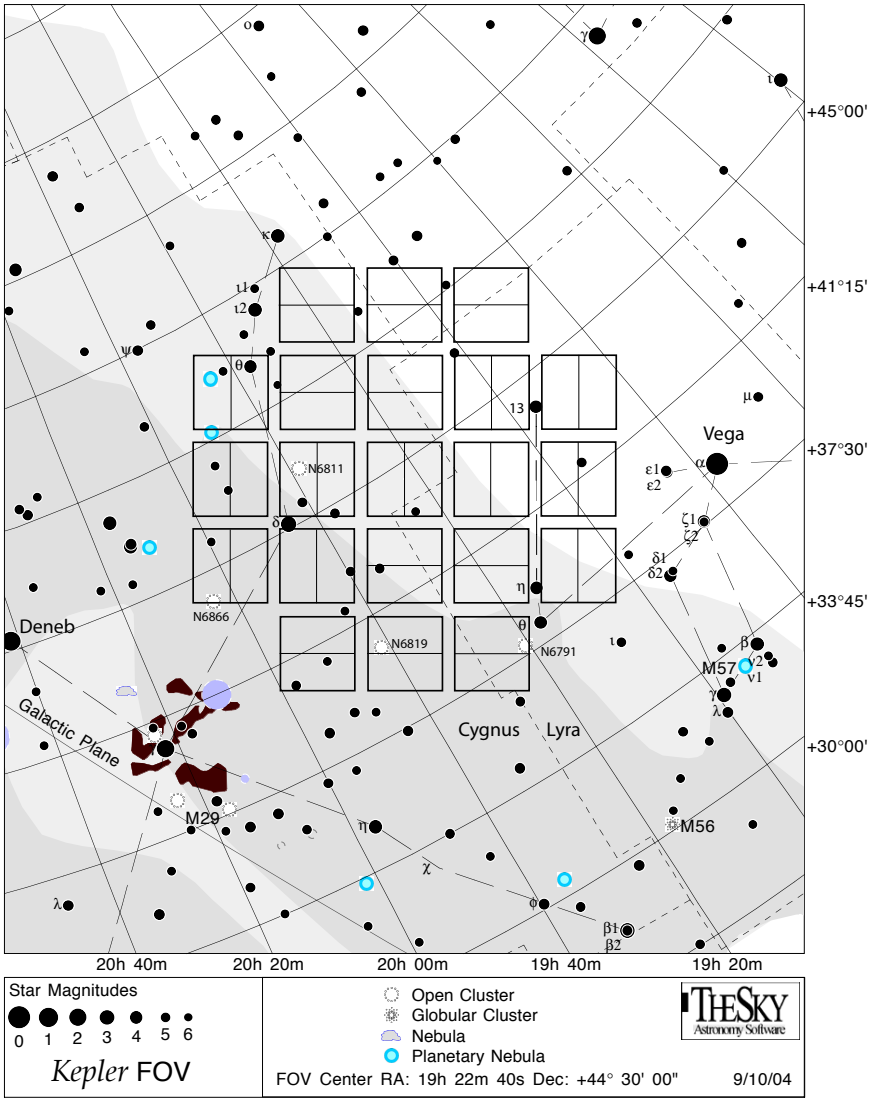

Figure B.11: Sky-projected *Kepler* field-of-view in the Cygnus-Lyra region. The four open star clusters covered by the CCDs are also visible. (Cf. Fig. 3.3).

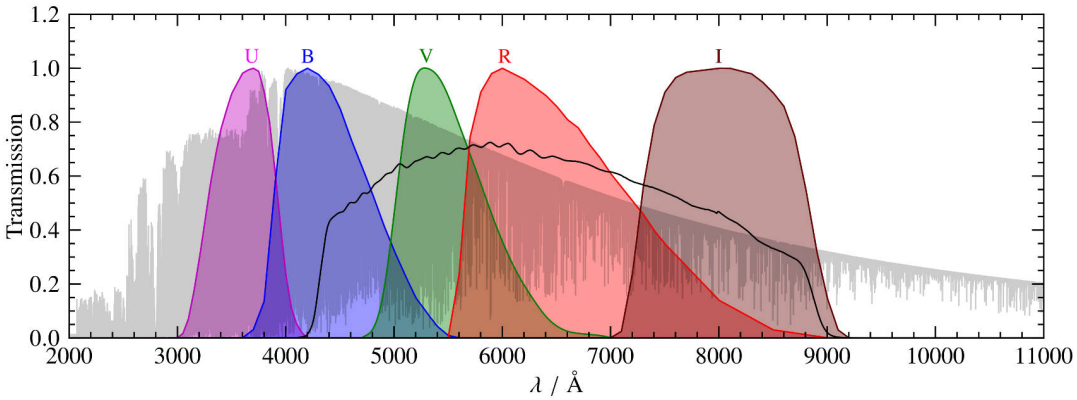

Figure B.12: Johnson- (*labels*) and *Kepler* filter (*black*) transmission curves. The Johnson transmission coefficients are taken from Bessell (1990, Table 2), while the response function of the *Kepler* instrument is given in the supplement of Van Cleve & Caldwell (2009). In the background a PHOENIX-ACES spectrum of a $T_{\mathrm{eff}} = 5800\,\mathrm{K}$ star is shown.

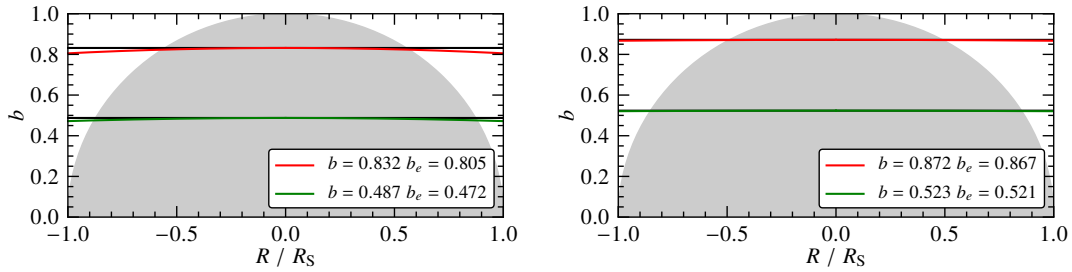

Figure B.13: Comparison of simulated transit paths (*colored* lines) with straight lines (*black*). The stellar disk is shown in *gray*. The *left* panel shows simulated orbits for a semimajor axis of $4\,R_{\mathrm{S}}$. The *right* panel shows orbits with a semimajor axis of $10\,R_{\mathrm{S}}$. The used impact parameters b are given as labels, where b_e denotes the impact parameter at the edge of this plot, which are slightly smaller caused by the curvature. For the simulated planetary traces Eq. 1.26 was used.

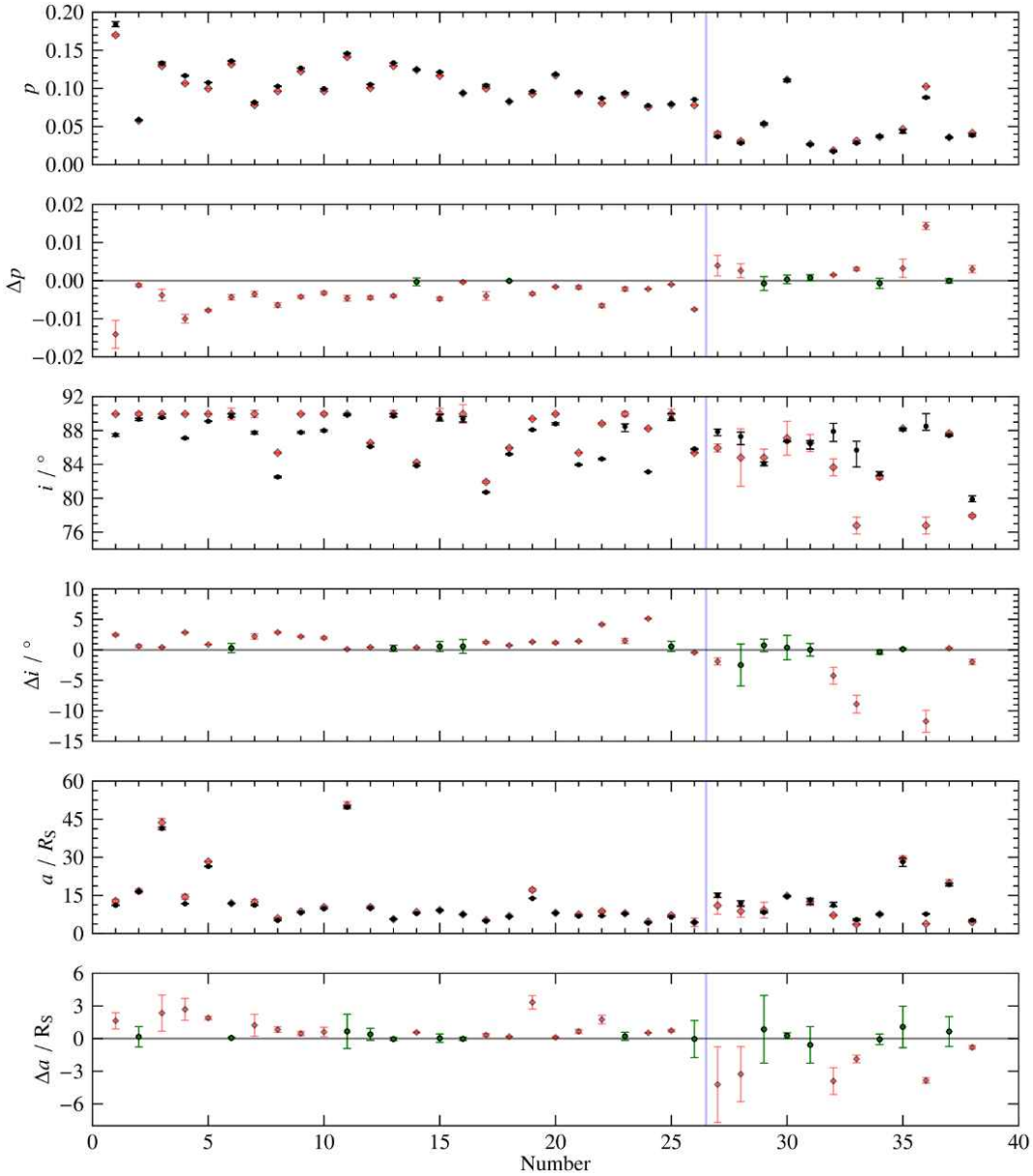

Figure B.14: Comparison of measured transit parameters of my short cadence target sample. Parameters: *Black dots* show results of my MCMC sampling, and the *red diamonds* the public *Kepler* data (NASA, 2014). Residuals: *Green dots* indicate objects, where the parameters deviate not significantly from each other. 1σ error bars in the residuals result from error propagation.

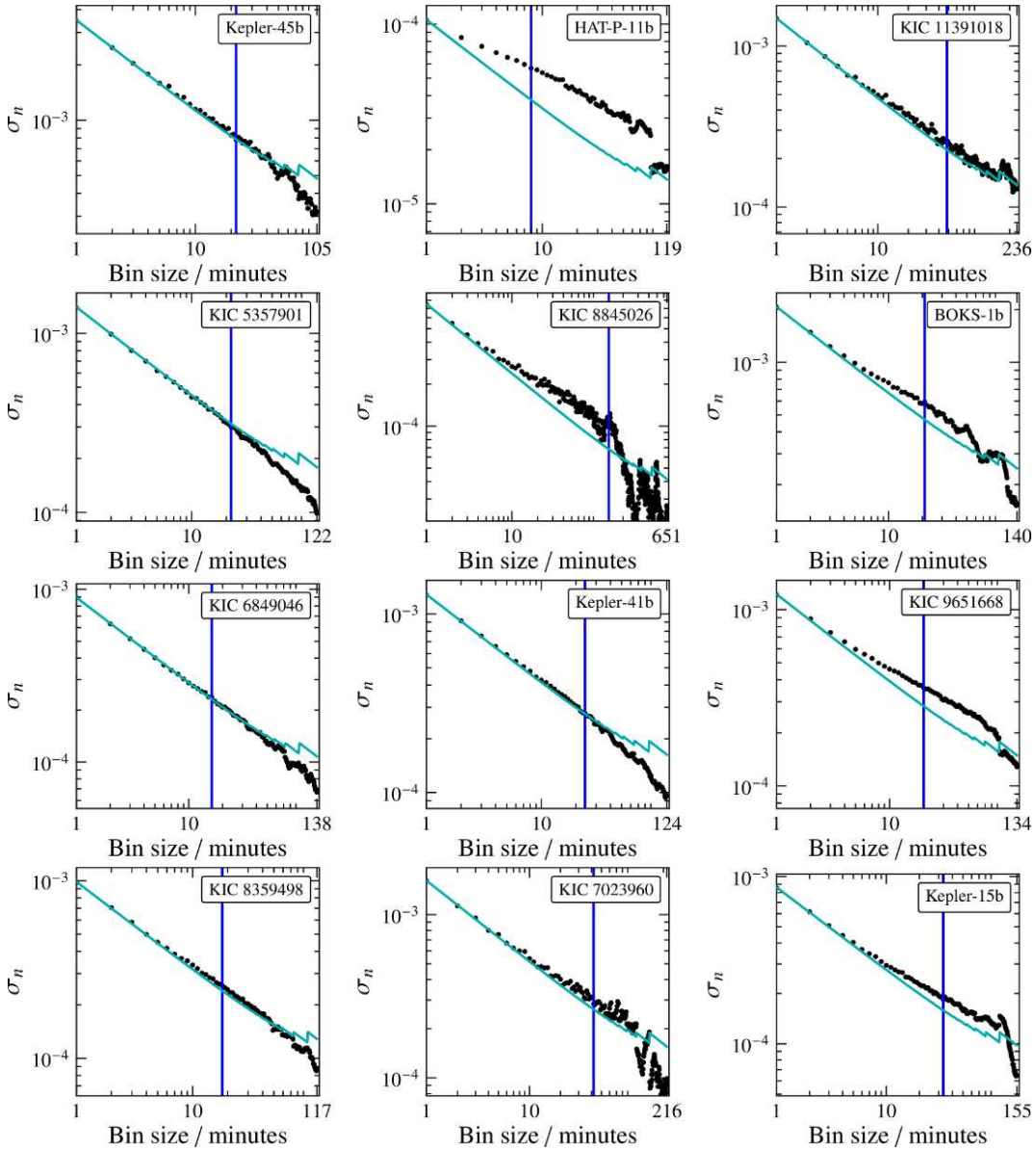

Figure B.15: Measured σ_n curves (*dots*) of the correlated noise analysis made for objects of my high S/N target sample. Transit ingress or egress durations are marked by *blue vertical* lines. *Cyan* lines indicate the white noise prediction corresponding to Eq. 4.15. In the labels the specific target name can be found. Objects sorted by $T_{\rm eff}$, from the upper left (coolest) to the lower right corner.

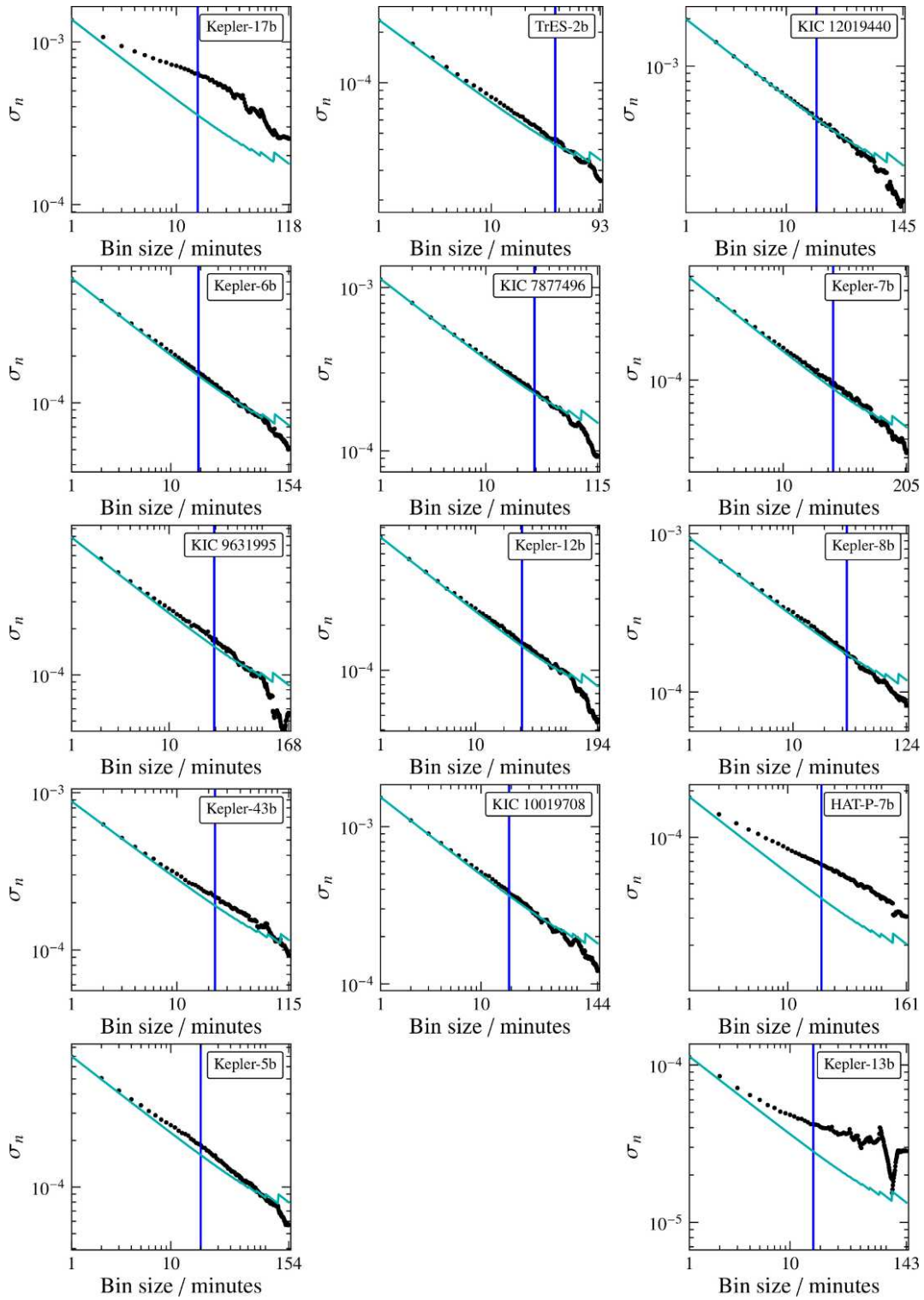

Figure B.15 (continued)

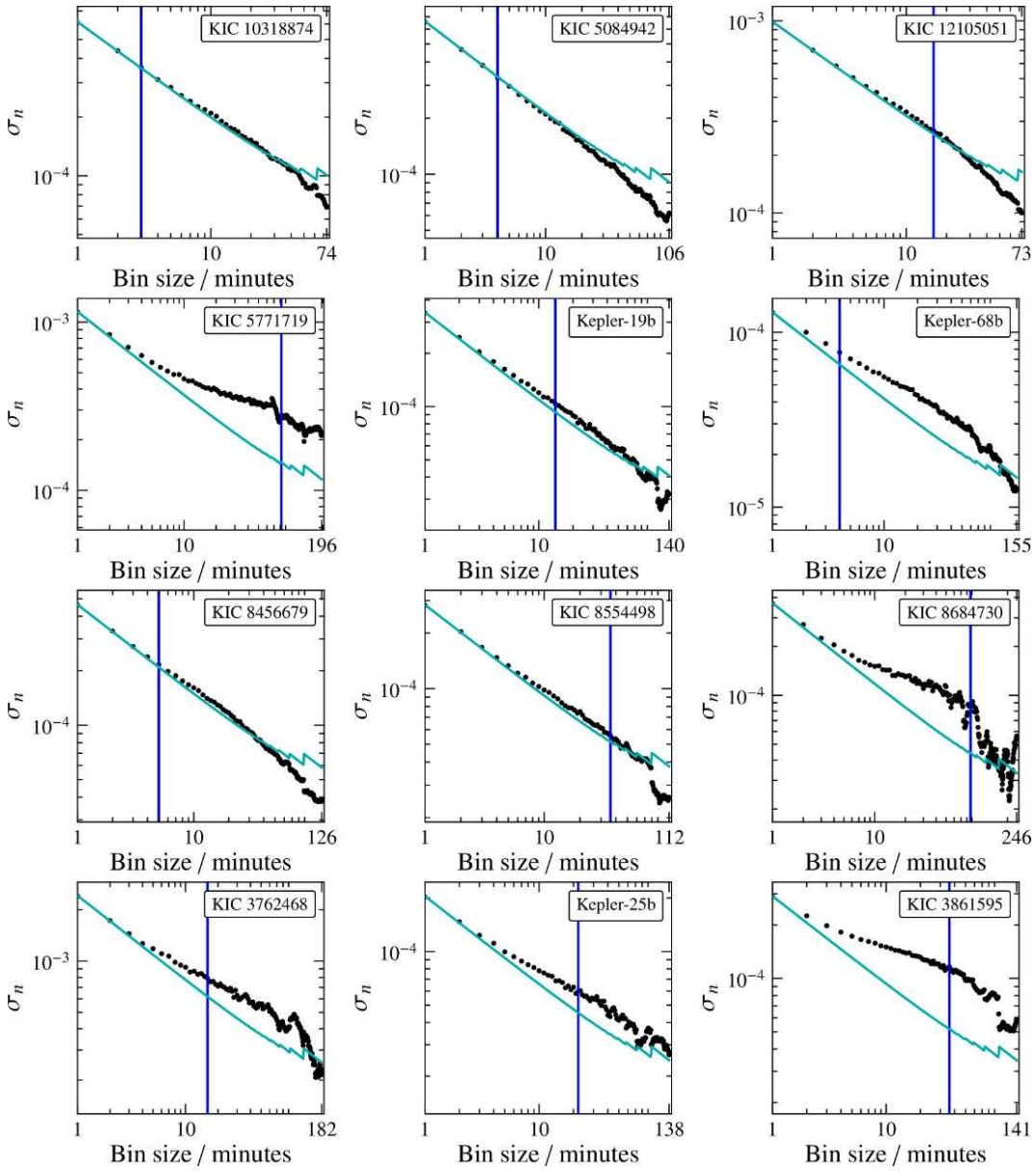

Figure B.16: Measured σ_n curves (*dots*) of the correlated noise analysis made for objects of my high impact parameter ($b \geq 0.8$) target sample.

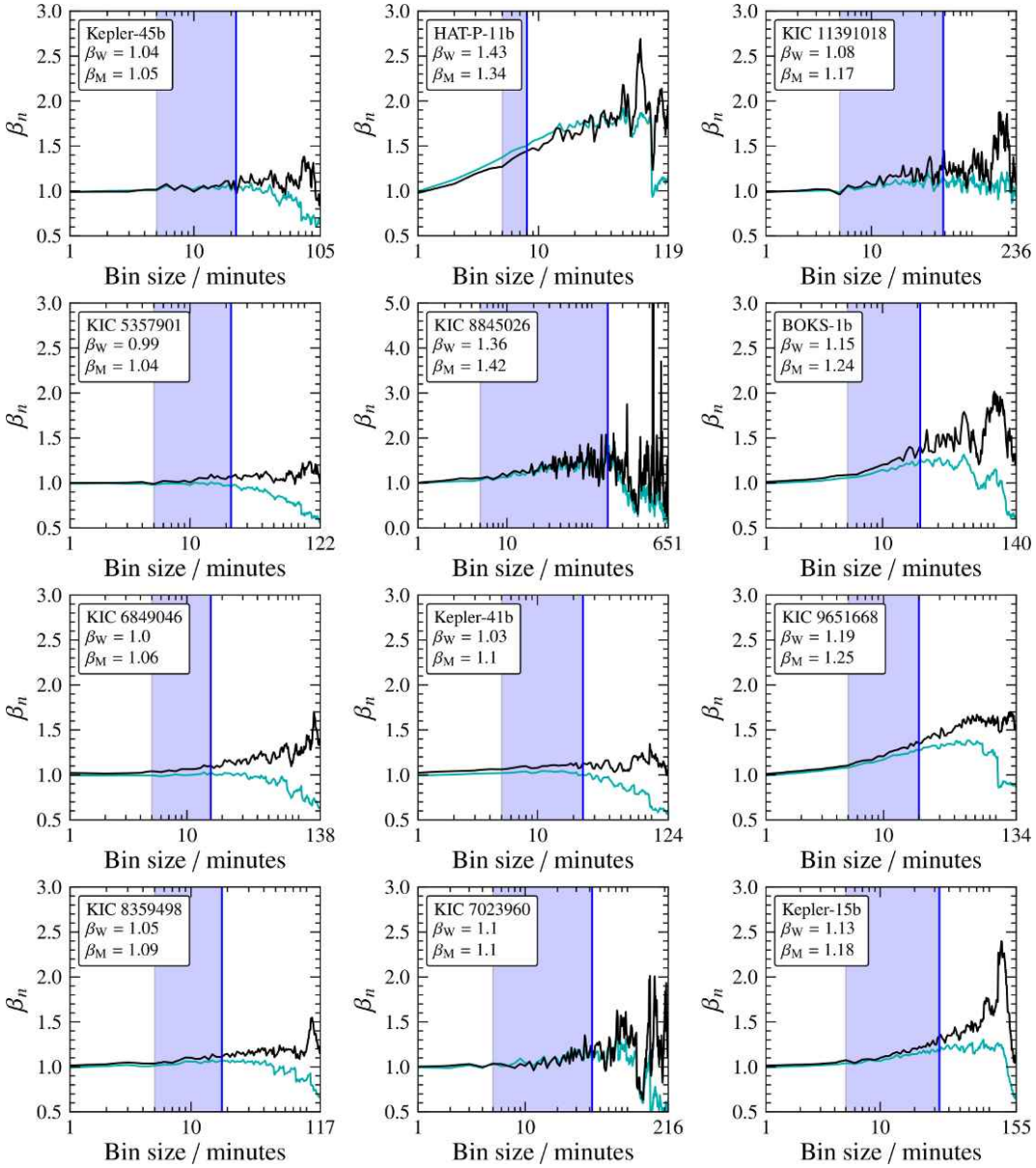

Figure B.17: Determined β_n graphs for all objects of my high S/N target sample. *Cyan lines*: ratios of measured σ_n to Eq. 4.15. *Black lines*: ratios of measured σ_n to measured σ_n of simulations. The *blue areas* marking the bin sizes used for determination of β_W and β_M. See Section 4.4.2 for more information.

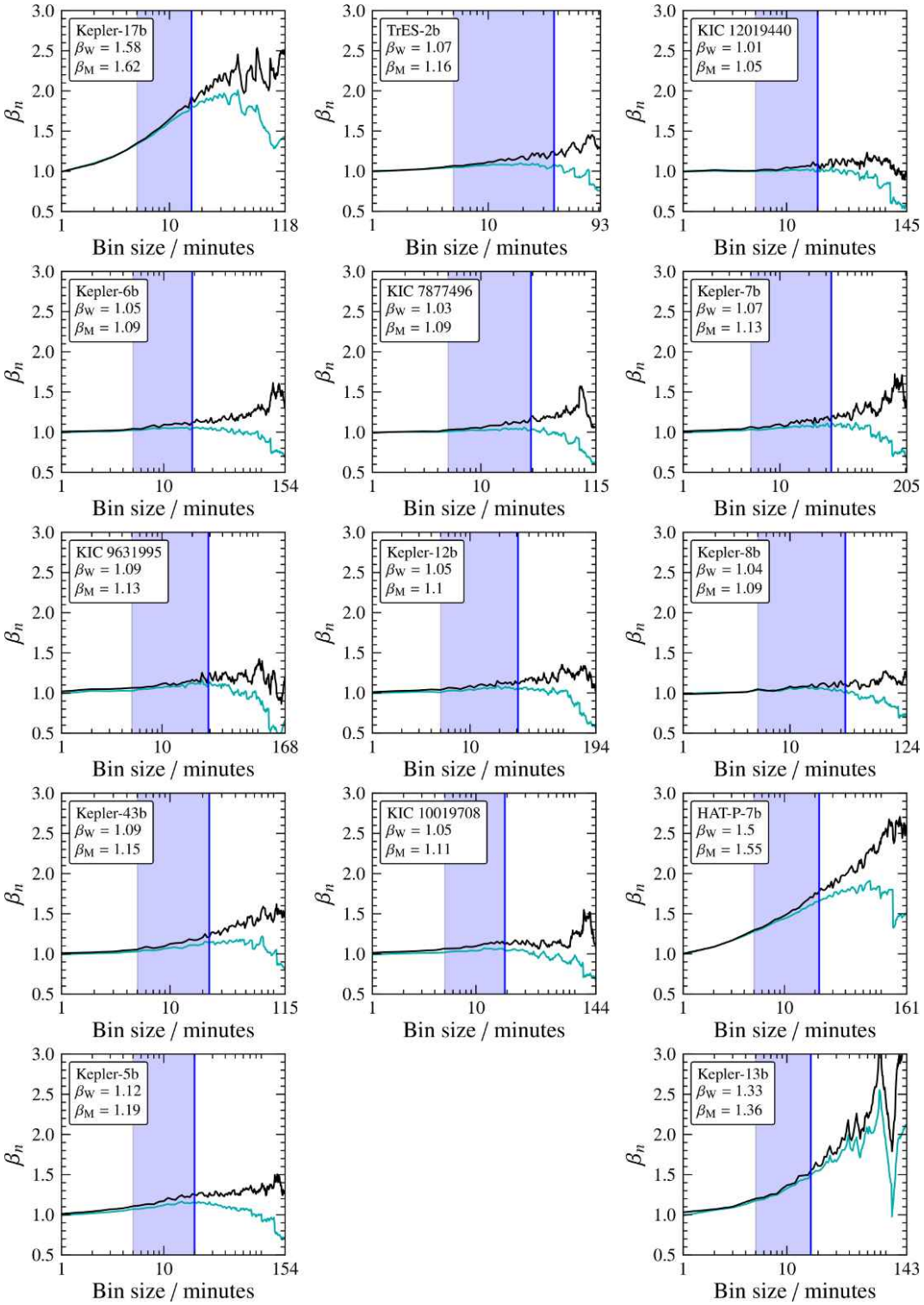

Figure B.17 (continued)

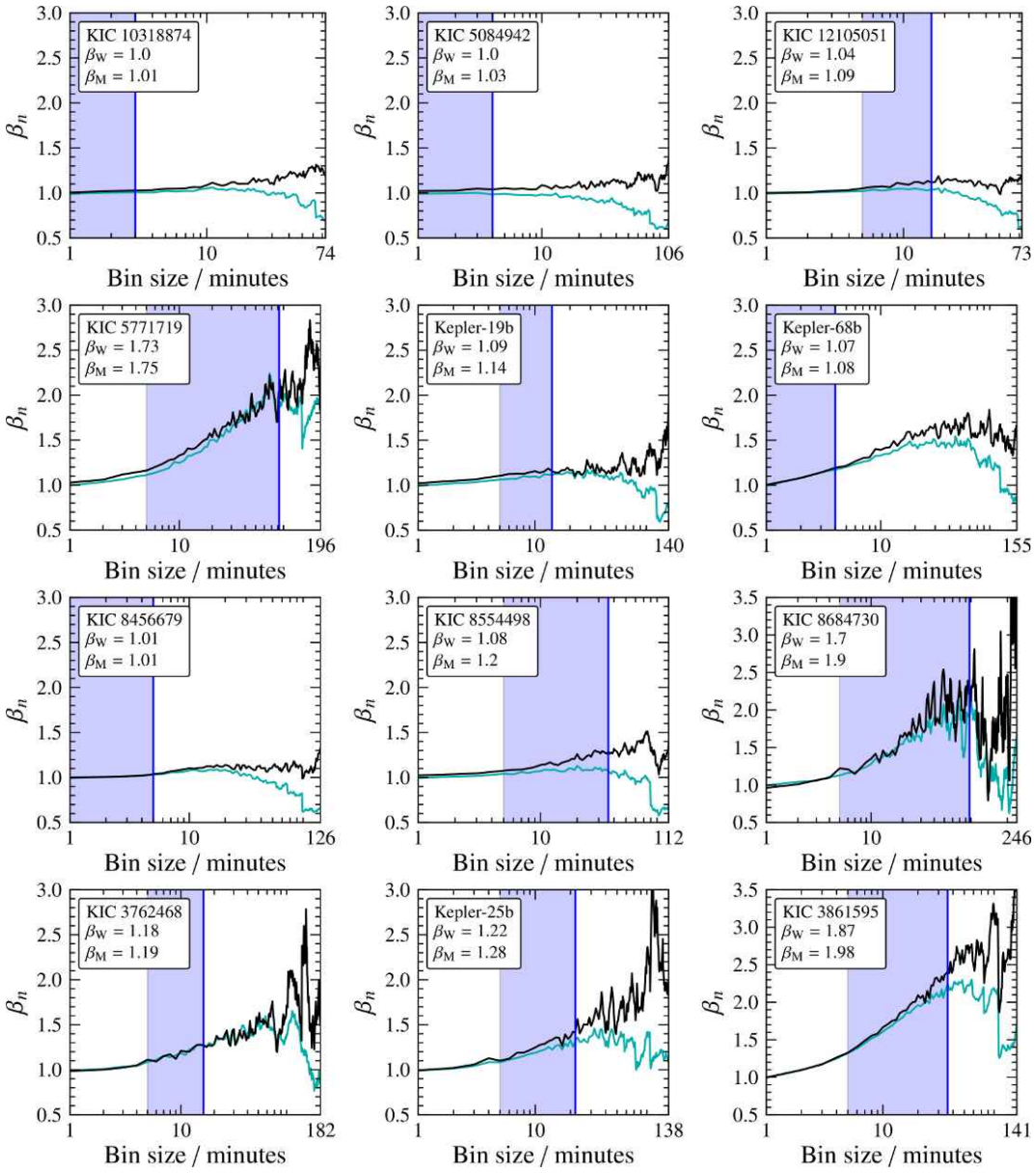

Figure B.18: Determined β_n graphs for all objects of my high impact parameter ($b \geq 0.8$) target sample.

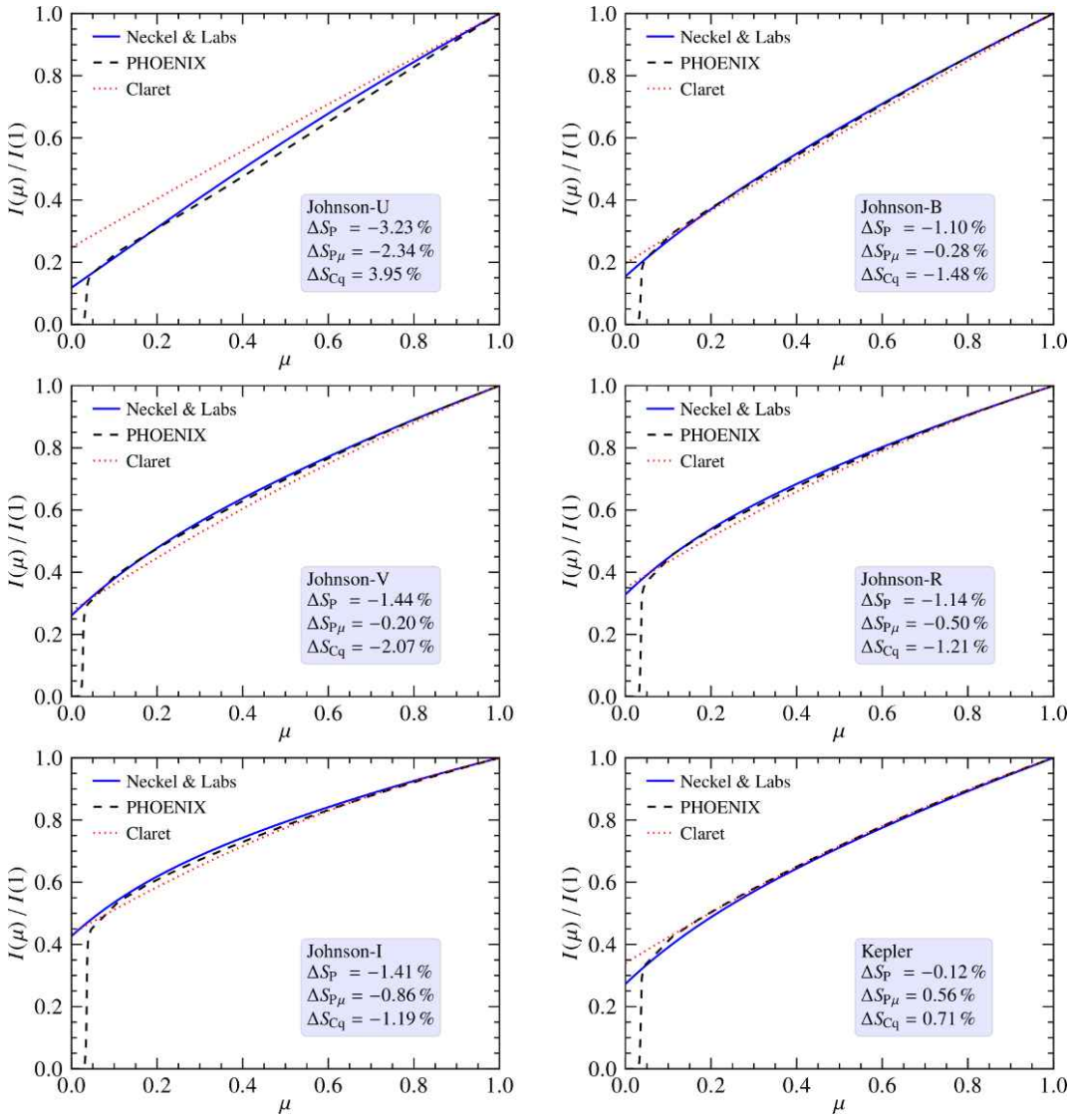

Figure B.19: Comparison between the solar LD as calculated from observations (Neckel & Labs, 1994) using Eq. 5.3 and model predictions. Each panel represents a different filter band. The Claret models are calculated using a quadratic LD law with LDCs taken from Claret & Bloemen (2011). Relative deviations in disk-integrated flux ($\Delta S_x = (S_x/S_N) - 1$) with respect to the measurements of the Sun (*blue*) given in percent for both predictions shown here ($S_{P\mu}$: PHOENIX model with rescaled μ-axis (*dashed*), S_{Cq}: quadratic LD with Claret LDCs). Additionally, the value for the unscaled PHOENIX model is given (S_P).

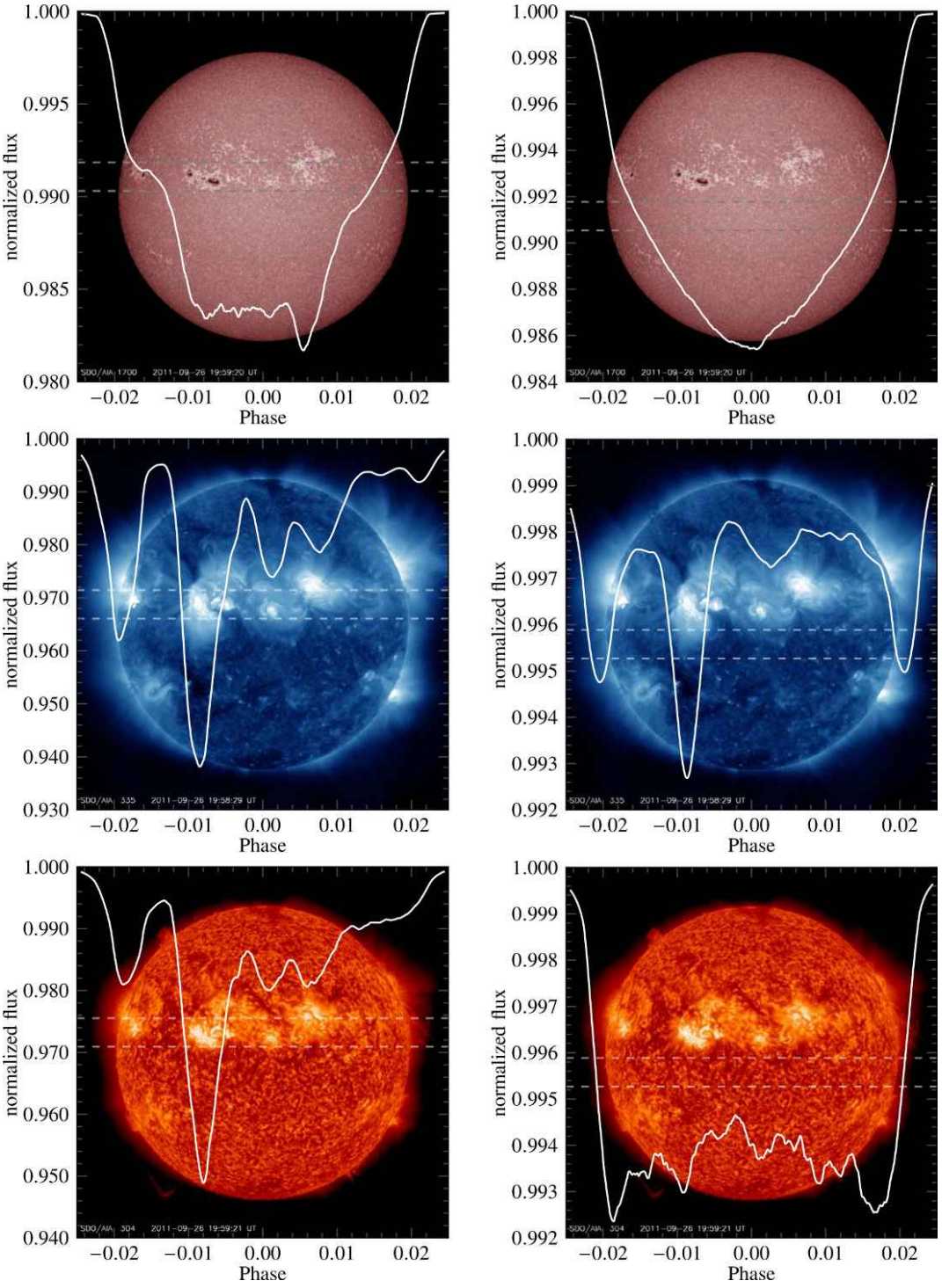

Figure B.20: Numerical transit light curves using different SDO/AIA channels. *Left* column: Transit in front of active regions, *right* column: Transit in front of almost inactive regions. Channels from *top*: 1700 Å continuum, 335 Å Fe XVI corona, 304 Å He II chromosphere.

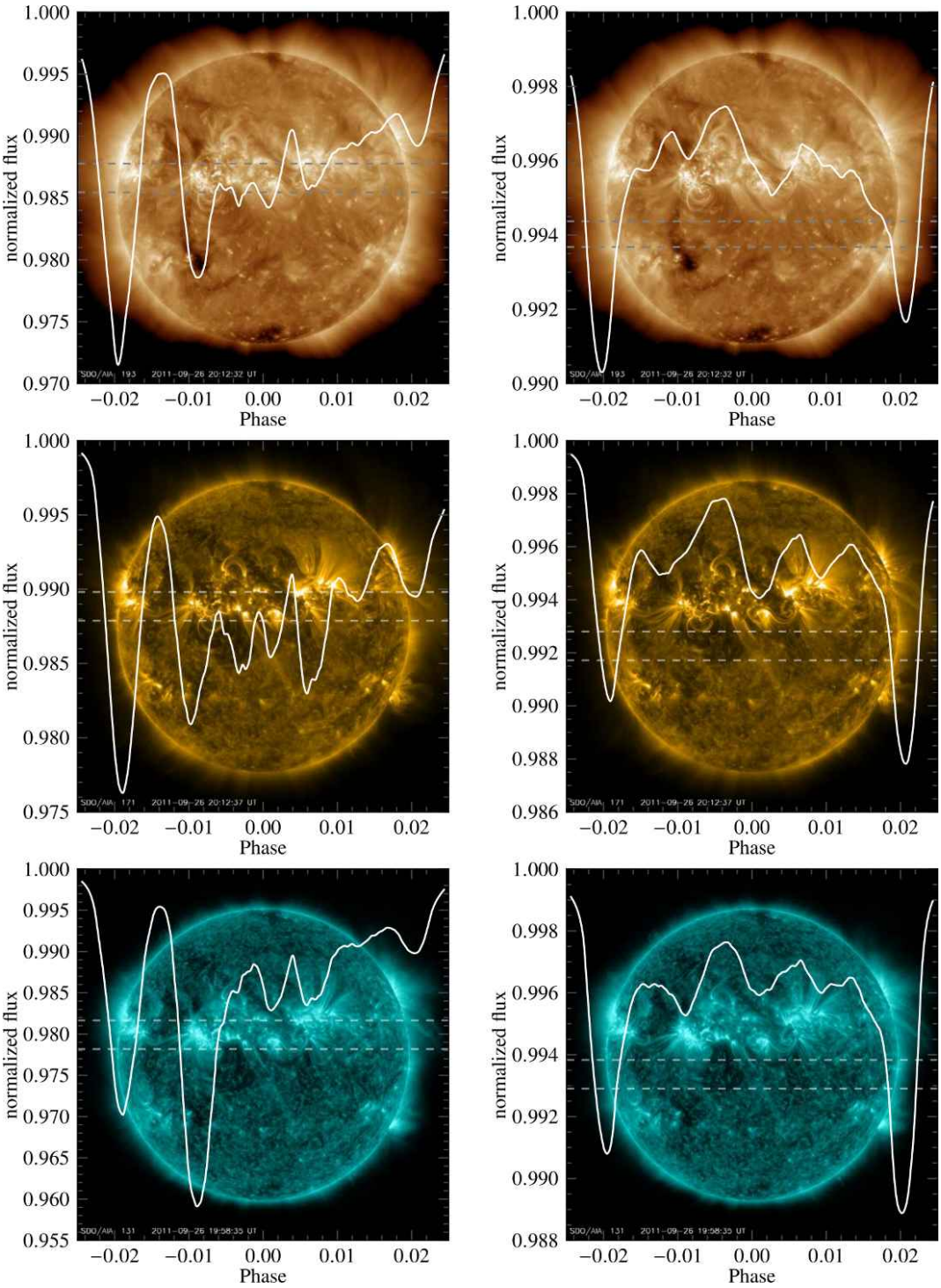

Figure B.20 (continued): 193 Å Fe XII corona, 171 Å Fe IX corona, and 131 Å Fe VIII corona (see Lemen et al., 2012).

Bibliography

References

[Aerts et al., 2010] C. Aerts, J. Christensen-Dalsgaard, and D. W. Kurtz. *Asteroseismology*. Astronomy and astrophysics library. Springer, 2010. ISBN: 978-1-4020-5178-4.

[Alonso et al., 2008] R. Alonso et al. "Transiting exoplanets from the CoRoT space mission. II. CoRoT-Exo-2b: a transiting planet around an active G star". In: A&A 482 (May 2008), pp. L21–L24. DOI: 10.1051/0004-6361:200809431. arXiv: 0803.3207.

[Ammler-von Eiff et al., 2009] M. Ammler-von Eiff et al. "A homogeneous spectroscopic analysis of host stars of transiting planets". In: A&A 507 (Nov. 2009), pp. 523–530. DOI: 10.1051/0004-6361/200912360. arXiv: 0909.0285 [astro-ph.SR].

[Auvergne et al., 2009] M. Auvergne et al. "The CoRoT satellite in flight: description and performance". In: A&A 506 (Oct. 2009), pp. 411–424. DOI: 10.1051/0004-6361/200810860. arXiv: 0901.2206 [astro-ph.SR].

[Avrett & Loeser, 1992] E. Avrett and R. Loeser. "The PANDORA Atmosphere Program (Invited Review)". In: *Cool Stars, Stellar Systems, and the Sun*. Ed. by M. Giampapa and J. Bookbinder. Vol. 26. Astronomical Society of the Pacific Conference Series. 1992, p. 489.

[Baglin & COROT Team, 1998] A. Baglin and COROT Team. "Asteroseismology from space - The COROT experiment". In: *New Eyes to See Inside the Sun and Stars*. Ed. by F.-L. Deubner, J. Christensen-Dalsgaard, and D. Kurtz. Vol. 185. IAU Symposium. 1998, p. 301.

[Barban et al., 2003] C. Barban et al. "New grids of ATLAS9 atmospheres. II. Limb-darkening coefficients for the Strömgren photometric system for A-F stars". In: A&A 405 (July 2003), pp. 1095–1105. DOI: 10.1051/0004-6361:20030619.

[J. A. Barnes & Allan, 1966] J. A. Barnes and D. W. Allan. "A Statistical Model of Flicker Noise". In: *Frequency Stability*. Ed. by A. R. Chi et al. Vol. 54. Proceedings of the IEEE. 1966, pp. 176–178. DOI: 10.1109/PROC.1966.4630.

[J. W. Barnes & Fortney, 2003] J. W. Barnes and J. J. Fortney. "Measuring the Oblateness and Rotation of Transiting Extrasolar Giant Planets". In: ApJ 588 (May 2003), pp. 545–556. DOI: 10.1086/373893. eprint: astro-ph/0301156.

[J. W. Barnes & Fortney, 2004] J. W. Barnes and J. J. Fortney. "Transit Detectability of Ring Systems around Extrasolar Giant Planets". In: ApJ 616 (Dec. 2004), pp. 1193–1203. DOI: 10.1086/425067. eprint: astro-ph/0409506.

[Basri & M. E. Brown, 2006] G. Basri and M. E. Brown. "Planetesimals to Brown Dwarfs: What is a Planet?" In: *Annual Review of Earth and Planetary Sciences* 34 (May 2006), pp. 193–216. DOI: 10.1146/annurev.earth.34.031405.125058. eprint: astro-ph/0608417.

[Batalha et al., 2013] N. M. Batalha et al. "Planetary Candidates Observed by Kepler. III. Analysis of the First 16 Months of Data". In: ApJS 204, 24 (Feb. 2013), p. 24. DOI: 10.1088/0067-0049/204/2/24. arXiv: 1202.5852 [astro-ph.EP].

[Beran et al., 2013] J. Beran, Y. Feng, S. Ghosh, and R. Kulik. *Long-Memory Processes. Probabilistic Properties and Statistical Methods*. Springer, 2013. ISBN: 978-3-642-35512-7.

[Bernardo, 2003] J. M. Bernardo. "Bayesian Statistics." In: *Encyclopedia of Life Support Systems (EOLSS). Probability and Statistics.* Ed. by R. Viertl. Oxford, UK: UNESCO, 2003.

[Bessell, 1990] M. S. Bessell. "UBVRI passbands". In: PASP 102 (Oct. 1990), pp. 1181–1199. DOI: 10.1086/132749.

[Borucki & Summers, 1984] W. J. Borucki and A. L. Summers. "The photometric method of detecting other planetary systems". In: Icarus 58 (Apr. 1984), pp. 121–134. DOI: 10.1016/0019-1035(84)90102-7.

[Borucki et al., 2010] W. J. Borucki et al. "Kepler Planet-Detection Mission: Introduction and First Results". In: *Science* 327 (Feb. 2010), pp. 977–. DOI: 10.1126/science.1185402.

[Borucki et al., 2011] W. J. Borucki et al. "Characteristics of Planetary Candidates Observed by Kepler. II. Analysis of the First Four Months of Data". In: ApJ 736, 19 (July 2011), p. 19. DOI: 10.1088/0004-637X/736/1/19. arXiv: 1102.0541 [astro-ph.EP].

[Bouchy et al., 2008] F. Bouchy et al. "Transiting exoplanets from the CoRoT space mission. III. The spectroscopic transit of CoRoT-Exo-2b with SOPHIE and HARPS". In: A&A 482 (May 2008), pp. L25–L28. DOI: 10.1051/0004-6361:200809433. arXiv: 0803.3209.

[Bouguer, 1760] P. Bouguer. *Traité d'optique sur la gradation de la lumière. Ouvrage posthume de M. Bouguer, de l'Académie Royale des Siences*. Ed. by impr. de H.-L. Guérin (Paris). 1760, p. 91. URL: http://gallica.bnf.fr/ark:/12148/bpt6k948469.

[Brigham, 1974] E. O. Brigham. *The Fast Fourier Transform*. Prentice-Hall, 1974. ISBN: 0-13-307496-X.

[T. M. Brown et al., 2011] T. M. Brown, D. W. Latham, M. E. Everett, and G. A. Esquerdo. "Kepler Input Catalog: Photometric Calibration and Stellar Classification". In: AJ 142, 112 (Oct. 2011), p. 112. DOI: 10.1088/0004-6256/142/4/112. arXiv: 1102.0342 [astro-ph.SR].

[Bryson et al., 2010a] S. T. Bryson et al. "Selecting pixels for Kepler downlink". In: *Society of Photo-Optical Instrumentation Engineers (SPIE) Conference Series*. Vol. 7740. Society of Photo-Optical Instrumentation Engineers (SPIE) Conference Series. July 2010. DOI: 10.1117/12.857625.

[Bryson et al., 2010b] S. T. Bryson et al. "The Kepler Pixel Response Function". In: ApJ 713 (Apr. 2010), pp. L97–L102. DOI: 10.1088/2041-8205/713/2/L97. arXiv: 1001.0331 [astro-ph.EP].

[Butz, 2012] T. Butz. *Fouriertransformation für Fußgänger*. 7th ed. engl. title: Fourier Transformation for Pedestrians. Springer, 2012. ISBN: 978-3-8348-8295-0.

[Campo et al., 2011] C. J. Campo et al. "On the Orbit of Exoplanet WASP-12b". In: ApJ 727, 125 (Feb. 2011), p. 125. DOI: 10.1088/0004-637X/727/2/125. arXiv: 1003.2763 [astro-ph.EP].

[Carlsson, 1992] M. Carlsson. "The MULTI Non-LTE Program (Invited Review)". In: *Cool Stars, Stellar Systems, and the Sun*. Ed. by M. Giampapa and J. Bookbinder. Vol. 26. Astronomical Society of the Pacific Conference Series. 1992, p. 499.

[Carter & Winn, 2009] J. A. Carter and J. N. Winn. "Parameter Estimation from Time-series Data with Correlated Errors: A Wavelet-based Method and its Application to Transit Light Curves". In: ApJ 704 (Oct. 2009), pp. 51–67. DOI: 10.1088/0004-637X/704/1/51. arXiv: 0909.0747 [astro-ph.EP].

[Casagrande et al., 2011] L. Casagrande et al. "New constraints on the chemical evolution of the solar neighbourhood and Galactic disc(s). Improved astrophysical parameters for the Geneva-Copenhagen Survey". In: A&A 530, A138 (June 2011), A138. DOI: 10.1051/0004-6361/201016276. arXiv: 1103.4651 [astro-ph.GA].

[Chalonge & Kourganoff, 1946] D. Chalonge and V. Kourganoff. "Recherches sur le spectre continu du Soleil. I: L'ion négatif hydrogène dans la photosphère solaire". In: *Annales d'Astrophysique* 9 (Jan. 1946), p. 69.

[Charbonneau et al., 2000] D. Charbonneau, T. M. Brown, D. W. Latham, and M. Mayor. "Detection of Planetary Transits Across a Sun-like Star". In: ApJ 529 (Jan. 2000), pp. L45–L48. DOI: 10.1086/312457. eprint: astro-ph/9911436.

[Claret, 2000] A. Claret. "A new non-linear limb-darkening law for LTE stellar atmosphere models. Calculations for -5.0 $\leq$ log[M/H] $\leq$ +1, 2000 K $\leq T_{\rm eff} \leq$ 50000 K at several surface gravities". In: A&A 363 (Nov. 2000), pp. 1081–1190.

[Claret, 2008] A. Claret. "Testing the limb-darkening coefficients measured from eclipsing binaries". In: A&A 482 (Apr. 2008), pp. 259–266. DOI: 10.1051/0004-6361:200809370.

[Claret & Bloemen, 2011] A. Claret and S. Bloemen. "Gravity and limb-darkening coefficients for the Kepler, CoRoT, Spitzer, uvby, UBVRIJHK, and Sloan photometric systems". In: A&A 529 (May 2011), A75. DOI: 10.1051/0004-6361/201116451.

[Claret & Hauschildt, 2003] A. Claret and P. H. Hauschildt. "The limb-darkening for spherically symmetric NextGen model atmospheres: A-G main-sequence and sub-giant stars". In: A&A 412 (Dec. 2003), pp. 241–248. DOI: 10.1051/0004-6361:20031405.

[Claret et al., 2012] A. Claret, P. H. Hauschildt, and S. Witte. "New limb-darkening coefficients for PHOENIX/1D model atmospheres. I. Calculations for 1500 K $\leq T_{\rm eff} \leq$ 4800 K Kepler, CoRot, Spitzer, uvby, UBVRIJHK, Sloan, and 2MASS photometric systems". In: A&A 546, A14 (Oct. 2012), A14. DOI: 10.1051/0004-6361/201219849.

[Claret et al., 2013] A. Claret, P. H. Hauschildt, and S. Witte. "New limb-darkening coefficients for Phoenix/1d model atmospheres. II. Calculations for 5000 K $\leq T_{\rm eff} \leq$ 10 000 K Kepler, CoRot, Spitzer, uvby, UBVRIJHK, Sloan, and 2MASS photometric systems". In: A&A 552, A16 (Apr. 2013), A16. DOI: 10.1051/0004-6361/201220942.

[CNES, 2013] CNES. *CoRoT Astronomy mission. From stars to habitable planets.* Oct. 12, 2013. URL: http://smsc.cnes.fr/COROT/index.htm (visited on Oct. 31, 2013).

[Cooley & Tukey, 1965] J. Cooley and J. Tukey. "An Algorithm for the Machine Calculation of Complex Fourier Series". In: *Mathematics of Computation* 19 (1965), pp. 297–301.

[Cubillos et al., 2013] P. Cubillos et al. "WASP-8b: Characterization of a Cool and Eccentric Exoplanet with Spitzer". In: ApJ 768, 42 (May 2013), p. 42. DOI: 10.1088/0004-637X/768/1/42. arXiv: 1303.5468 [astro-ph.EP].

[Czesla et al., 2009] S. Czesla, K. F. Huber, U. Wolter, S. Schröter, and J. H. M. M. Schmitt. "How stellar activity affects the size estimates of extrasolar planets". In: A&A 505 (Oct. 2009), pp. 1277–1282. DOI: 10.1051/0004-6361/200912454. arXiv: 0906.3604 [astro-ph.SR].

[Deleuil et al., 1997] M. Deleuil, P. Barge, A. Leger, and J. Schneider. "Detection of Earth-Sized Planets with the COROT Space Mission". In: *Planets Beyond the Solar System and the Next Generation of Space Missions*. Ed. by D. Soderblom. Vol. 119. Astronomical Society of the Pacific Conference Series. 1997, p. 259.

[Deserno, 2002] M. Deserno. *How to generate exponentially correlated Gaussian random numbers*. Department of Chemistry and Biochemistry, UCLA, USA, Aug. 26, 2002.

[Diaz-Cordoves & Gimenez, 1992] J. Diaz-Cordoves and A. Gimenez. "A new nonlinear approximation to the limb-darkening of hot stars". In: A&A 259 (June 1992), pp. 227–231.

[DLR, 2013] DLR. *Institut für Planetenforschung - Zusammenstellung der CoRoT-Planeten*. Sept. 1, 2013. URL: http://www.dlr.de/pf/desktopdefault.aspx/tabid-327/1154_read-2072/ (visited on Oct. 30, 2013).

[Doğan et al., 2013] G. Doğan et al. "Characterizing Two Solar-type Kepler Subgiants with Asteroseismology: KIC 10920273 and KIC 11395018". In: ApJ 763, 49 (Jan. 2013), p. 49. DOI: 10.1088/0004-637X/763/1/49. arXiv: 1211.6650 [astro-ph.SR].

[Eddington, 1926] A. S. Eddington. *The Internal Constitution of the Stars*. Cambridge University Press, 1926.

[Fressin et al., 2013] F. Fressin et al. "The False Positive Rate of Kepler and the Occurrence of Planets". In: ApJ 766, 81 (Apr. 2013), p. 81. DOI: 10.1088/0004-637X/766/2/81. arXiv: 1301.0842 [astro-ph.EP].

[Frisch, 1975] H. Frisch. "Finite eddy-size effects on centre-to-limb variations - an alternative to anisotropic microturbulence". In: A&A 40 (May 1975), pp. 267–276.

[Fuhrmann, 2004] K. Fuhrmann. "Nearby stars of the Galactic disk and halo. III." In: *Astronomische Nachrichten* 325 (Jan. 2004), pp. 3–80. DOI: 10.1002/asna.200310173.

[Ghacornac, 1859] M. Ghacornac. *Comptes rendus hebdomadaires des séances de l'Académie des sciences.* Vol. t.49 (1859). Paris :publiés avec le concours du Centre national de la recherche scientifique par MM. les secrétaires perpétuels, 1859, p. 806. URL: http://www.biodiversitylibrary.org/item/17147.

[Gilliland et al., 2010] R. L. Gilliland et al. "Initial Characteristics of Kepler Short Cadence Data". In: ApJ 713 (Apr. 2010), pp. L160–L163. DOI: 10.1088/2041-8205/713/2/L160. arXiv: 1001.0142 [astro-ph.SR].

[Gonzalez et al., 2010] G. Gonzalez, M. K. Carlson, and R. W. Tobin. "VizieR Online Data Catalog: Li abundances vsini for star-planet systems (Gonzalez+, 2010)". In: *VizieR Online Data Catalog* 740 (Oct. 2010), p. 31368.

[Gray, 1976] D. F. Gray. *The Observation and Analysis of Stellar Photospheres. Einführung in die Astronomie und Astrophysik*. John Wiley & Sons, 1976. ISBN: 0-471-32380-2.

[Haario et al., 2001] H. Haario, E. Saksman, and J. Tamminen. "An adaptive Metropolis algorithm". In: *Bernoulli* 7.2 (Apr. 2001), pp. 223–242. URL: http://projecteuclid.org/euclid.bj/1080222083.

[Hampel, 1974] F. R. Hampel. "The Influence Curve and Its Role in Robust Estimation". English. In: *Journal of the American Statistical Association* 69.346 (1974), pages. ISSN: 01621459. URL: http://www.jstor.org/stable/2285666.

[Haubois et al., 2009] X. Haubois et al. "Imaging the spotty surface of Betelgeuse in the H band". In: A&A 508 (Dec. 2009), pp. 923–932. DOI: 10.1051/0004-6361/200912927. arXiv: 0910.4167 [astro-ph.SR].

[Hauschildt & Baron, 2010] P. H. Hauschildt and E. Baron. "A 3D radiative transfer framework. VI. PHOENIX/3D example applications". In: A&A 509, A36 (Jan. 2010), A36. DOI: 10.1051/0004-6361/200913064. arXiv: 0911.3285 [astro-ph.SR].

[Hopf, 1934] E. Hopf. *Mathematical Problems Of Radiative Equilibrium*. Cambridge University Press, 1934.

[Howarth, 2011] I. D. Howarth. "On stellar limb darkening and exoplanetary transits". In: MNRAS 418 (Dec. 2011), pp. 1165–1175. DOI: 10.1111/j.1365-2966.2011.19568.x. arXiv: 1106.4659 [astro-ph.SR].

[Howell et al., 2014] S. B. Howell et al. "The K2 Mission: Characterization and Early Results". In: PASP 126 (Apr. 2014), pp. 398–408. DOI: 10.1086/676406. arXiv: 1402.5163 [astro-ph.IM].

[Hubeny & Mihalas, 2014] I. Hubeny and D. Mihalas. *Theory of Stellar Atmospheres. An Introduction to Astrophysical Non-equilibrium Quantitative Spectroscopic Analysis*. Princeton University Press, 2014. ISBN: 978-0-691-16329-1.

[Huber et al., 2009] K. F. Huber, S. Czesla, U. Wolter, and J. H. M. M. Schmitt. "A planetary eclipse map of CoRoT-2a. Comprehensive lightcurve modeling combining rotational-modulation and transits". In: A&A 508 (Dec. 2009), pp. 901–907. DOI: 10.1051/0004-6361/200912867. arXiv: 0909.3256 [astro-ph.SR].

[Huber et al., 2010] K. F. Huber, S. Czesla, U. Wolter, and J. H. M. M. Schmitt. "Planetary eclipse mapping of CoRoT-2a. Evolution, differential rotation, and spot migration". In: A&A 514, A39 (May 2010), A39. DOI: 10.1051/0004-6361/200913914. arXiv: 1002.4113 [astro-ph.SR].

[IAU, 2006]. *International Astronomical Union 2006 General Assembly: Result of the IAU Resolution votes*. .IAU0603. 2006. URL: http://www.iau.org/static/archives/releases/pdf/iau0603.pdf.

[IAU & USGS, 2014] IAU and USGS. *The Gazetteer of Planetary Nomenclature - Ring and Ring Gap Nomenclature*. International Astronomical Union, Astrogeology Science Center. Aug. 5, 2014. URL: http://planetarynames.wr.usgs.gov/Page/Rings (visited on Aug. 5, 2014).

[Jones et al., 2001] E. Jones, T. Oliphant, P. Peterson, et al. *SciPy: Open source scientific tools for Python*. http://www.scipy.org. 2001. URL: http://www.scipy.org/.

[Kane et al., 2011] S. R. Kane et al. "Revised Orbit and Transit Exclusion for HD 114762b". In: ApJ 735, L41 (July 2011), p. L41. DOI: 10.1088/2041-8205/735/2/L41. arXiv: 1106.1434 [astro-ph.EP].

[Kelz et al., 2006] A. Kelz et al. "PMAS: The Potsdam Multi-Aperture Spectrophotometer. II. The Wide Integral Field Unit PPak". In: PASP 118 (Jan. 2006), pp. 129–145. DOI: 10.1086/497455. eprint: astro-ph/0512557.

[Kenney & Keeping, 1951] J. Kenney and E. Keeping. *7.8 The distribution of the standard deviation*. Vol. 2.2. D. Van Nostrand Company, Incorporated, 1951, pp. 170–173.

[Kepler & Caspar, 1929] J. Kepler and M. Caspar. *Neue astronomie*. German translation of Astronomia Nova, J. Kepler 1609. 1929.

[Kim & Casper, 2013] S. Kim and R. Casper. *Applications of Convolution in Image Processing with MATLAB*. University of Washington, Aug. 20, 2013.

[Kipping, 2010] D. M. Kipping. "Binning is sinning: morphological light-curve distortions due to finite integration time". In: MNRAS 408 (Nov. 2010), pp. 1758–1769. DOI: 10.1111/j.1365-2966.2010.17242.x. arXiv: 1004.3741 [astro-ph.EP].

[Kipping, 2013] D. M. Kipping. "Efficient, uninformative sampling of limb darkening coefficients for two-parameter laws". In: MNRAS 435 (Nov. 2013), pp. 2152–2160. DOI: 10.1093/mnras/stt1435. arXiv: 1308.0009 [astro-ph.SR].

[Kipping & Bakos, 2011] D. M. Kipping and G. Bakos. "Analysis of Kepler's Short-cadence Photometry for TrES-2b". In: ApJ 733, 36 (May 2011), p. 36. DOI: 10.1088/0004-637X/733/1/36. arXiv: 1006.5680 [astro-ph.EP].

[Klinglesmith & Sobieski, 1970] D. A. Klinglesmith and S. Sobieski. "Nonlinear Limb Darkening for Early-Type Stars". In: AJ 75 (Mar. 1970), p. 175. DOI: 10.1086/110960.

[Knutson et al., 2007] H. A. Knutson, D. Charbonneau, R. W. Noyes, T. M. Brown, and R. L. Gilliland. "Using Stellar Limb-Darkening to Refine the Properties of HD 209458b". In: ApJ 655 (Jan. 2007), pp. 564–575. DOI: 10.1086/510111. eprint: astro-ph/0603542.

[Komm et al., 2013] R. Komm, I. De Moortel, Y. Fan, S. Ilonidis, and O. Steiner. "Sub-photosphere to Solar Atmosphere Connection". In: Space Sci. Rev. (Oct. 2013). DOI: 10.1007/s11214-013-0023-5.

[Kopal, 1950] Z. Kopal. "Detailed effects of limb darkening upon light and velocity curves of close binary systems". In: *Harvard College Observatory Circular* 454 (1950), pp. 1–12.

[Kurucz, 2005] R. L. Kurucz. "ATLAS12, SYNTHE, ATLAS9, WIDTH9, et cetera". In: *Memorie della Societa Astronomica Italiana Supplementi* 8 (2005), p. 14.

[Lemen et al., 2012] J. R. Lemen et al. "The Atmospheric Imaging Assembly (AIA) on the Solar Dynamics Observatory (SDO)". In: Sol. Phys. 275 (Jan. 2012), pp. 17–40. DOI: 10.1007/s11207-011-9776-8.

[Llama & Shkolnik, 2015] J. Llama and E. Shkolnik. "Transiting the Sun: the Impact of Stellar Activity on X-Ray and Ultraviolet Transits". In: ApJ 802, 41 (Mar. 2015), p. 41. DOI: 10.1088/0004-637X/802/1/41. arXiv: 1501.04963 [astro-ph.EP].

[Loredo, 1992] T. J. Loredo. "Promise of Bayesian inference for astrophysics." In: *Statistical Challenges in Modern Astronomy*. Ed. by E. D. Feigelson and G. J. Babu. 1992, pp. 275–297.

[Mandel & Agol, 2002] K. Mandel and E. Agol. "Analytic Light Curves for Planetary Transit Searches". In: ApJ 580 (Dec. 2002), pp. L171–L175. DOI: 10.1086/345520. eprint: arXiv:astro-ph/0210099.

[Mathews & Kurtis, 2004] J. H. Mathews and K. F. Kurtis. *Numerical Methods Using Matlab*. 4th ed. Prentice-Hall Inc., 2004. ISBN: 0-13-065248-2. URL: http://mathfaculty.fullerton.edu/mathews//n2003/simpsonsrule/SimpsonsRuleProof.pdf (visited on June 5, 2014).

[Mayor & Queloz, 1995] M. Mayor and D. Queloz. "A Jupiter-mass companion to a solar-type star". In: Nature 378 (Nov. 1995), pp. 355–359. DOI: 10.1038/378355a0.

[Mayor et al., 2003] M. Mayor et al. "Setting New Standards with HARPS". In: *The Messenger* 114 (Dec. 2003), pp. 20–24.

[McCrea, 1931] W. H. McCrea. "Model stellar atmospheres". In: MNRAS 91 (June 1931), p. 836.

[Metropolis et al., 1953] N. Metropolis, A. W. Rosenbluth, M. N. Rosenbluth, A. H. Teller, and E. Teller. "Equation of State Calculations by Fast Computing Machines". In: *The Journal of Chemical Physics* 21.6 (June 1, 1953), pp. 1087–1092. ISSN: 0021-9606. DOI: 10.1063/1.1699114. URL: http://dx.doi.org/10.1063/1.1699114.

[Mislis et al., 2010] D. Mislis, S. Schröter, J. H. M. M. Schmitt, O. Cordes, and K. Reif. "Multi-band transit observations of the TrES-2b exoplanet". In: A&A 510, A107 (Feb. 2010), A107. DOI: 10.1051/0004-6361/200912910. arXiv: 0912.4428 [astro-ph.EP].

[Morton, 2003] D. C. Morton. "Atomic Data for Resonance Absorption Lines. III. Wavelengths Longward of the Lyman Limit for the Elements Hydrogen to Gallium". In: ApJS 149 (Nov. 2003), pp. 205–238. DOI: 10.1086/377639.

[Moutou et al., 2013] C. Moutou et al. "CoRoT: Harvest of the exoplanet program". In: Icarus 226 (Nov. 2013), pp. 1625–1634. DOI: 10.1016/j.icarus.2013.03.022. arXiv: 1306.0578 [astro-ph.EP].

[G. Müller, 1897] G. Müller. *Die Photometrie der Gestirne*. Verlag von Wilhelm Engelmann, 1897.

[Müller et al., 2013] H. M. Müller, K. F. Huber, S. Czesla, U. Wolter, and J. H. M. M. Schmitt. "High-precision stellar limb-darkening measurements. A transit study of 38 Kepler planetary candidates". In: A&A 560, A112 (Dec. 2013), A112. DOI: 10.1051/0004-6361/201322079.

[NASA, 2005] NASA. *Photometer Cross-section (labeled)*. June 21, 2005. URL: http://kepler.nasa.gov/multimedia/artwork/hardware/?ImageID=244 (visited on June 19, 2013).

[NASA, 2009] NASA. *Kepler: NASA's First Mission Capable of Finding Earth-Size Planets*. Press Kit. Feb. 2009. URL: http://www.nasa.gov/pdf/314125main_Kepler_presskit_2-19_smfile.pdf (visited on June 20, 2013).

[NASA, 2013a] NASA. *Kepler Launch*. May 15, 2013. URL: http://www.nasa.gov/mission_pages/kepler/launch/index.html (visited on June 20, 2013).

[NASA, 2013b] NASA. *Kepler News and Media Resources*. Sept. 13, 2013. URL: http://www.nasa.gov/mission_pages/kepler/news/index.html (visited on Sept. 26, 2013).

[NASA, 2013c] NASA. *Table of Confirmed Planets*. Oct. 18, 2013. URL: http://kepler.nasa.gov/Mission/discoveries/ (visited on Aug. 26, 2015).

[NASA, 2014] NASA. *Kepler Objects of Interest*. NASA Exoplanet Archive. Feb. 13, 2014. URL: http://exoplanetarchive.ipac.caltech.edu/cgi-bin/ExoTables/nph-exotbls?dataset=cumulative (visited on Mar. 28, 2014).

[Neckel, 2003] H. Neckel. "On the sun's absolute disk-center and mean disk intensities, its limb darkening, and its 'limb temperature' ($\lambda\lambda$330 to 1099 nm)". In: Sol. Phys. 212 (Feb. 2003), pp. 239–250. DOI: 10.1023/A:1022929504779.

[Neckel, 2005] H. Neckel. "Analytical Reference Functions F(λ) for the Sun's Limb Darkening and Its Absolute Continuum Intensities ($\lambda\lambda$ 300 to 1100 m)". In: Sol. Phys. 229 (June 2005), pp. 13–33. DOI: 10.1007/s11207-005-4081-z.

[Neckel & Labs, 1994] H. Neckel and D. Labs. "Solar limb darkening 1986-1990 ($\lambda\lambda$303 to 1099 nm)". In: Sol. Phys. 153 (Aug. 1994), pp. 91–114. DOI: 10.1007/BF00712494.

[Neilson & Lester, 2012] H. R. Neilson and J. B. Lester. "Using limb darkening to measure fundamental parameters of stars". In: A&A 544, A117 (Aug. 2012), A117. DOI: 10.1051/0004-6361/201117244. arXiv: 1207.7087 [astro-ph.SR].

[Nesvacil et al., 2012] N. Nesvacil et al. "Multi-element Doppler imaging of the CP2 star HD 3980". In: A&A 537, A151 (Jan. 2012), A151. DOI: 10.1051/0004-6361/201117097.

[Niemi, 2013] J. Niemi. *STAT 544 - Bayesian Statistics*. Jan. 2013. URL: http://www.jarad.me/courses/stat544/ (visited on June 19, 2015).

[O'Donovan et al., 2006] F. T. O'Donovan et al. "TrES-2: The First Transiting Planet in the Kepler Field". In: ApJ 651 (Nov. 2006), pp. L61–L64. DOI: 10.1086/509123. eprint: arXiv:astro-ph/0609335.

[Ohta et al., 2005] Y. Ohta, A. Taruya, and Y. Suto. "The Rossiter-McLaughlin Effect and Analytic Radial Velocity Curves for Transiting Extrasolar Planetary Systems". In: ApJ 622 (Apr. 2005), pp. 1118–1135. DOI: 10.1086/428344. eprint: arXiv:astro-ph/0410499.

[Ohta et al., 2009] Y. Ohta, A. Taruya, and Y. Suto. "Predicting Photometric and Spectroscopic Signatures of Rings Around Transiting Extrasolar Planets". In: ApJ 690 (Jan. 2009), pp. 1–12. DOI: 10.1088/0004-637X/690/1/1. eprint: astro-ph/0611466.

[Orosz & Hauschildt, 2000] J. A. Orosz and P. H. Hauschildt. "The use of the NextGen model atmospheres for cool giants in a light curve synthesis code". In: A&A 364 (Dec. 2000), pp. 265–281. eprint: astro-ph/0010114.

[Pál, 2008] A. Pál. "Properties of analytic transit light-curve models". In: MNRAS 390 (Oct. 2008), pp. 281–288. DOI: 10.1111/j.1365-2966.2008.13723.x. arXiv: 0805.2157.

[Patil et al., 2010] A. Patil, D. Huard, and C. J. Fonnesbeck. "PyMC: Bayesian Stochastic Modelling in Python". In: *Journal of Statistical Software* 35.4 (July 2010), pp. 1–81. ISSN: 1548-7660. URL: http://www.jstatsoft.org/v35/i04.

[Perryman, 2014] M. Perryman. "Resource Letter Exo-1: Exoplanets". In: *American Journal of Physics* 82 (June 2014), pp. 552–563. DOI: 10.1119/1.4830455. arXiv: 1311.2521 [astro-ph.EP].

[Pesnell et al., 2012] W. D. Pesnell, B. J. Thompson, and P. C. Chamberlin. "The Solar Dynamics Observatory (SDO)". In: Sol. Phys. 275 (Jan. 2012), pp. 3–15. DOI: 10.1007/s11207-011-9841-3.

[PHL, 2013] PHL. *Data of Potential Habitable Worlds*. Oct. 12, 2013. URL: http://phl.upr.edu/projects/habitable-exoplanets-catalog/data (visited on Oct. 23, 2013).

[Pierce & Slaughter, 1977] A. K. Pierce and C. D. Slaughter. "Solar limb darkening. I - At wavelengths of 3033-7297". In: Sol. Phys. 51 (Feb. 1977), pp. 25–41. DOI: 10.1007/BF00240442.

[Pierce et al., 1977] A. K. Pierce, C. D. Slaughter, and D. Weinberger. "Solar limb darkening in the interval 7404-24 018 A. II". In: Sol. Phys. 52 (Apr. 1977), pp. 179–189. DOI: 10.1007/BF00935800.

[Piskunov et al., 1995] N. Piskunov, F. Kupka, T. A. Ryabchikova, W. W. Weiss, and C. S. Jeffery. "VALD: The Vienna Atomic Line Data Base." In: A&AS 112 (Sept. 1995), p. 525.

[Podlozhnyuk, 2007] V. Podlozhnyuk. *Image Convolution with CUDA*. NVIDIA Corporation, June 2007.

[Pont et al., 2006] F. Pont, S. Zucker, and D. Queloz. "The effect of red noise on planetary transit detection". In: MNRAS 373 (Nov. 2006), pp. 231–242. DOI: 10.1111/j.1365-2966.2006.11012.x. eprint: astro-ph/0608597.

[Pont et al., 2007] F. Pont et al. "Hubble Space Telescope time-series photometry of the planetary transit of HD 189733: no moon, no rings, starspots". In: A&A 476 (Dec. 2007), pp. 1347–1355. DOI: 10.1051/0004-6361:20078269. arXiv: 0707.1940.

[Poppenhaeger et al., 2013] K. Poppenhaeger, J. H. M. M. Schmitt, and S. J. Wolk. "Transit Observations of the Hot Jupiter HD 189733b at X-Ray Wavelengths". In: ApJ 773, 62 (Aug. 2013), p. 62. DOI: 10.1088/0004-637X/773/1/62. arXiv: 1306.2311 [astro-ph.SR].

[Press, 1978] W. H. Press. "Flicker noises in astronomy and elsewhere". In: *Comments on Astrophysics* 7 (1978), pp. 103–119.

[Press et al., 2002] W. H. Press, S. A. Teukolsky, W. T. Vetterling, and B. P. Flannery. *Numerical recipes in C++ : the art of scientific computing*. 2002.

[Raetz et al., 2014] S. Raetz et al. "Transit timing of TrES-2: a combined analysis of ground- and space-based photometry". In: MNRAS 444 (Oct. 2014), pp. 1351–1368. DOI: 10.1093/mnras/stu1505. arXiv: 1408.7022 [astro-ph.SR].

[Roesslein et al., 2007] M. Roesslein, M. Wolf, B. Wampfler, and W. Wegscheider. "A forgotten fact about the standard deviation". English. In: *Accreditation and Quality Assurance* 12.9 (2007), pp. 495–496. ISSN: 0949-1775. DOI: 10.1007/s00769-007-0285-2. URL: http://dx.doi.org/10.1007/s00769-007-0285-2.

[Rosenblatt, 1971] F. Rosenblatt. "A Two-Color Photometric Method for Detection of Extra solar Planetary Systems". In: Icarus 14 (Feb. 1971), pp. 71–93. DOI: 10.1016/0019-1035(71)90103-5.

[Roth et al., 2005] M. M. Roth et al. "PMAS: The Potsdam Multi-Aperture Spectrophotometer. I. Design, Manufacture, and Performance". In: PASP 117 (June 2005), pp. 620–642. DOI: 10.1086/429877. eprint: astro-ph/0502581.

[Saar & Osten, 1997] S. H. Saar and R. A. Osten. "Rotation, turbulence and evidence for magnetic fields in southern dwarfs". In: MNRAS 284 (Feb. 1997), pp. 803–810.

[Sánchez, 2004] S. F. Sánchez. "E3D, the Euro3D visualization tool I: Description of the program and its capabilities". In: *Astronomische Nachrichten* 325 (Mar. 2004), pp. 167–170. DOI: 10.1002/asna.200310202. eprint: astro-ph/0310677.

[Sánchez, 2006] S. F. Sánchez. "Techniques for reducing fiber-fed and integral-field spectroscopy data: An implementation on R3D". In: *Astronomische Nachrichten* 327 (Nov. 2006), p. 850. DOI: 10.1002/asna.200610643. eprint: astro-ph/0606263.

[Sanchis-Ojeda & Winn, 2011] R. Sanchis-Ojeda and J. N. Winn. "Starspots, Spin-Orbit Misalignment, and Active Latitudes in the HAT-P-11 Exoplanetary System". In: ApJ 743, 61 (Dec. 2011), p. 61. DOI: 10.1088/0004-637X/743/1/61. arXiv: 1107.2920 [astro-ph.EP].

[Schmidt, 1938] B. Schmidt. "Ein lichtstarkes komafreies Spiegelsystem". In: *Mitteilungen der Hamburger Sternwarte in Bergedorf* 7 (1938), pp. 15–17.

[Schröter et al., 2012] S. Schröter, J. H. M. M. Schmitt, and H. M. Müller. "A consistent analysis of three years of ground- and space-based photometry of TrES-2". In: A&A 539, A97 (Mar. 2012), A97. DOI: 10.1051/0004-6361/201118536. arXiv: 1205.0969 [astro-ph.EP].

[Schröter et al., 2011] S. Schröter et al. "The corona and companion of CoRoT-2a. Insights from X-rays and optical spectroscopy". In: A&A 532, A3 (Aug. 2011), A3. DOI: 10.1051/0004-6361/201116961. arXiv: 1106.1522 [astro-ph.SR].

[Schwarzschild, 1906] K. Schwarzschild. "Ueber das Gleichgewicht der Sonnenatmosphäre". ger. In: *Nachrichten von der Gesellschaft der Wissenschaften zu Göttingen, Mathematisch-Physikalische Klasse* 1906 (1906), pp. 41–53. URL: http://eudml.org/doc/58631.

[Silva, 2003] A. V. R. Silva. "Method for Spot Detection on Solar-like Stars". In: ApJ 585 (Mar. 2003), pp. L147–L150. DOI: 10.1086/374324.

[Sing et al., 2009] D. K. Sing et al. "Transit spectrophotometry of the exoplanet HD 189733b. I. Searching for water but finding haze with HST NICMOS". In: A&A 505 (Oct. 2009), pp. 891–899. DOI: 10.1051/0004-6361/200912776. arXiv: 0907.4991 [astro-ph.EP].

[Smith, 1997] S. W. Smith. *The Scientist and Engineer's Guide to Digital Signal Processing*. Electronically available. 1997. ISBN: 0-9660176-3-3. URL: http://www.dspguide.com/.

[Snellen et al., 2014] I. A. G. Snellen et al. "Fast spin of the young extrasolar planet β Pictoris b". In: Nature 509 (May 2014), pp. 63–65. DOI: 10.1038/nature13253.

[Sousa et al., 2010] S. G. Sousa, A. Alapini, G. Israelian, and N. C. Santos. "An effective temperature calibration for solar type stars using equivalent width ratios. A fast and easy spectroscopic temperature estimation". In: A&A 512, A13 (Mar. 2010), A13. DOI: 10.1051/0004-6361/200913388. arXiv: 0912.2651 [astro-ph.IM].

[Struve, 1952] O. Struve. "Proposal for a project of high-precision stellar radial velocity work". In: *The Observatory* 72 (Oct. 1952), pp. 199–200.

[STScI, 2012] STScI. *Released Kepler Planetary Candidates*. Space Telescope Science Institute. Feb. 27, 2012. URL: http://archive.stsci.edu/kepler/planet_candidates.html (visited on Mar. 28, 2014).

[Sykes, 1953] J. B. Sykes. "The integral equation of limb-darkening". In: MNRAS 113 (1953), p. 198.

[Torres et al., 2012] G. Torres et al. "Improved Spectroscopic Parameters for Transiting Planet Hosts". In: ApJ 757, 161 (Oct. 2012), p. 161. DOI: 10.1088/0004-637X/757/2/161. arXiv: 1208.1268 [astro-ph.SR].

[Tsantaki et al., 2013] M. Tsantaki et al. "Deriving precise parameters for cool solar-type stars. Optimizing the iron line list". In: A&A 555, A150 (July 2013), A150. DOI: 10.1051/0004-6361/201321103. arXiv: 1304.6639 [astro-ph.SR].

[Tusnski & Valio, 2011] L. R. M. Tusnski and A. Valio. "Transit Model of Planets with Moon and Ring Systems". In: ApJ 743, 97 (Dec. 2011), p. 97. DOI: 10.1088/0004-637X/743/1/97. arXiv: 1111.5599 [astro-ph.EP].

[Unsöld & Bascheck, 2005] A. Unsöld and B. Bascheck. *Der Neue Kosmos. Einführung in die Astronomie und Astrophysik*. 7th ed. 1st corr. reprint. Springer, 2005. ISBN: 3-540-42177-7.

[Valenti & Fischer, 2005a] J. A. Valenti and D. A. Fischer. "Spectroscopic Properties of Cool Stars (SPOCS). I. 1040 F, G, and K Dwarfs from Keck, Lick, and AAT Planet Search Programs". In: ApJS 159 (July 2005), pp. 141–166. DOI: 10.1086/430500.

[Valenti & Fischer, 2005b] J. A. Valenti and D. A. Fischer. "VizieR Online Data Catalog: Spectroscopic properties of cool stars. I. (Valenti+, 2005)". In: *VizieR Online Data Catalog* 215 (Nov. 2005), p. 90141.

[Valenti & Piskunov, 1996] J. A. Valenti and N. Piskunov. "Spectroscopy made easy: A new tool for fitting observations with synthetic spectra." In: A&AS 118 (Sept. 1996), pp. 595–603.

[Valenti et al., 2012] J. A. Valenti, N. E. Piskunov, and U. Heiter. *Spectroscopy Made Easy (SME) User Handbook*. Space Telescope Science Institute, May 21, 2012. URL: http://www.stsci.edu/~valenti/sme/SME-Manual.pdf.

[Van Cleve & Caldwell, 2009] J. E. Van Cleve and D. A. Caldwell. *Kepler Instrument Handbook*. KSCI-19033. NASA Ames Research Center, Moffett Field, CA. 94035, July 15, 2009.

[van't Veer, 1960] F. van't Veer. *L'assombrissement centre-bord des étoiles*. Recherches astronomiques. Drukkerij Schotanus & Jens, 1960.

[Vogel, 1877] H. C. Vogel. *Monatsberichte der Königlichen Preussische Akademie des Wissenschaften zu Berlin*. Buchdruckerei der Kgl. Akademie d. Wiss. (G.VOGT), 1877, p. 104. URL: http://www.biodiversitylibrary.org/item/110478.

[von Essen et al., 2013] C. von Essen, S. Schröter, E. Agol, and J. H. M. M. Schmitt. "Qatar-1: indications for possible transit timing variations". In: A&A 555, A92 (July 2013), A92. DOI: 10.1051/0004-6361/201321407. arXiv: 1309.1457 [astro-ph.EP].

[Winn, 2009] J. N. Winn. "Measuring accurate transit parameters". In: *IAU Symposium*. Ed. by F. Pont, D. Sasselov, and M. J. Holman. Vol. 253. IAU Symposium. Feb. 2009, pp. 99–109. DOI: 10.1017/S174392130802629X. arXiv: 0807.4929.

[Winn, 2010] J. N. Winn. "Transits and Occultations". In: *ArXiv e-prints* (Jan. 2010). arXiv: 1001.2010 [astro-ph.EP].

[Winn et al., 2007] J. N. Winn et al. "The Transit Light Curve Project. VII. The Not-So-Bloated Exoplanet HAT-P-1b". In: AJ 134 (Oct. 2007), pp. 1707–1712. DOI: 10.1086/521599. arXiv: 0707.1908.

[Winn et al., 2008] J. N. Winn et al. "The Transit Light Curve Project. IX. Evidence for a Smaller Radius of the Exoplanet XO-3b". In: ApJ 683 (Aug. 2008), pp. 1076–1084. DOI: 10.1086/589737. arXiv: 0804.4475.

[Wolszczan & Frail, 1992] A. Wolszczan and D. A. Frail. "A planetary system around the millisecond pulsar PSR1257 + 12". In: Nature 355 (Jan. 1992), pp. 145–147. DOI: 10.1038/355145a0.

[Wolter et al., 2009] U. Wolter et al. "Transit mapping of a starspot on CoRoT-2. Probing a stellar surface with planetary transits". In: A&A 504 (Sept. 2009), pp. 561–564. DOI: 10.1051/0004-6361/200912329. arXiv: 0906.4140 [astro-ph.SR].

[Zub et al., 2011] M. Zub et al. "Limb-darkening measurements for a cool red giant in microlensing event OGLE 2004-BLG-482". In: A&A 525, A15 (Jan. 2011), A15. DOI: 10.1051/0004-6361/200912007. arXiv: 0912.2312 [astro-ph.SR].

Image References

[Chauvin et al., 2004] G. Chauvin et al. "A giant planet candidate near a young brown dwarf. Direct VLT/NACO observations using IR wavefront sensing". In: A&A 425 (Oct. 2004), pp. L29–L32. DOI: 10.1051/0004-6361:200400056. eprint: astro-ph/0409323.

[Eddy, 1979] J. A. Eddy. *A New Sun: The Solar Results from Skylab*. Edited by Rein Ise. Prepared by: George C. Marshall Space Flight Center. National Aeronautics and Space Administration, Washington, D.C., 1979. URL: http://history.nasa.gov/SP-402/contents.htm.

[ESA & NASA, 2003] ESA and NASA. *SOHO-Gallery: Best Of SOHO*. Oct. 28, 2003. URL: http://sohowww.nascom.nasa.gov/gallery/images/mdi20031028.html (visited on June 24, 2015).

[ESO, 2007] ESO. *The Radial Velocity Method (artist's impression)*. Apr. 25, 2007. URL: http://www.eso.org/public/images/eso0722e/ (visited on Aug. 31, 2015).

[ESO/J. Rameau, 2013] ESO/J. Rameau. *VLT image of exoplanet HD 95086 b*. June 3, 2013. URL: http://www.eso.org/public/images/eso1324a/ (visited on Aug. 31, 2015).

[Hetlage, 2012] C. Hetlage. *2012 Venus transit*. June 6, 2012. URL: http://hetlage.com/Gallery/Astrophotography/index.html (visited on Aug. 31, 2015).

[Kuzuhara et al., 2013] M. Kuzuhara et al. "Direct Imaging of a Cold Jovian Exoplanet in Orbit around the Sun-like Star GJ 504". In: ApJ 774, 11 (Sept. 2013), p. 11. DOI: 10.1088/0004-637X/774/1/11. arXiv: 1307.2886 [astro-ph.EP].

[MAST, 2012] MAST. *MAST Kepler Images*. Oct. 18, 2012. URL: http://archive.stsci.edu/kepler/images.html (visited on July 9, 2013).

[NASA, 2006] NASA. *Photometer Cross-section (unlabeled)*. June 19, 2006. URL: http://kepler.nasa.gov/multimedia/artwork/hardware/?ImageID=243 (visited on June 19, 2013).

[NASA, 2008] NASA. *Kepler focal plane assembly*. Nov. 18, 2008. URL: http://kepler.nasa.gov/multimedia/photos/imagesofkepler/?ImageID=152 (visited on July 9, 2013).

[NASA, 2010] NASA. *Kepler field of view for each season*. Mar. 24, 2010. URL: http://kepler.nasa.gov/multimedia/photos/?ImageID=103 (visited on June 19, 2013).

[NASA & Ball Aerospace, 2008] NASA and Ball Aerospace. *Kepler Flight Segment - Labeled (version 2)*. Dec. 1, 2008. URL: http://kepler.nasa.gov/multimedia/artwork/hardware/?ImageID=241 (visited on June 19, 2013).

[NASA & DGK, 2008] NASA and DGK. *Kepler's Earth Trailing Orbit Around The Sun*. Nov. 2008. URL: http://www.nasa.gov/mission_pages/kepler/multimedia/images/kepler-orbit-graph.html (visited on June 19, 2013).

[PHL @ UPR Arecibo, 2015] Planetary Habitability Laboratory @ UPR Arecibo. *HEC: Periodic Table of Exoplanets – NASA Kepler exoplanets candidates*. July 2015. URL: http://phl.upr.edu/projects/habitable-exoplanets-catalog/media/pte (visited on July 23, 2015).

[Software Bisque, 2009] Software Bisque. *Kepler Field of View Star Chart*. Dec. 18, 2009. URL: http://kepler.nasa.gov/multimedia/photos/?ImageID=12 (visited on July 9, 2013).

Further Reading

[A&A Editorial Office, 2013] A&A Editorial Office. *Astronomy & Astrophysics - Author's guide*. July 2013. URL: http://www.aanda.org/doc_journal/instructions/aa_instructions.pdf (visited on Dec. 13, 2013).

[Adams et al., 2011] J. Adams, C. Halliday, A. Peter, and M. Usdin. "Guide to the English Editing at Astronomy & Astrophysics". In: *EAS Publications Series*. Ed. by C. Sterken. Vol. 49. EAS Publications Series. July 2011, pp. 85–105. DOI: 10.1051/eas/1149006.

[Bartsch, 2001] H.-J. Bartsch. *Taschenbuch Mathematischer Formeln*. Fachbuchverlag Leipzig, 2001. ISBN: 3-446-21792-4.

[Czesla, 2012] S. Czesla. *MCMC–Hands on workshop*. Hamburger Sternwarte, Oct. 2012.

[Davenport & Root, 1958] W. B. Davenport and W. L. Root. *An introduction to the Theory of Random Signals and Noise*. New York: McGraw-Hill, 1958.

[dict.cc GmbH, 2014] dict.cc GmbH. *dict.cc | Wörterbuch Englisch-Deutsch*. 2014. URL: http://www.dict.cc/ (visited on Jan. 1, 2014).

[Hunter, 2007] J. D. Hunter. "Matplotlib: A 2D graphics environment". In: *Computing In Science & Engineering* 9.3 (May 2007), pp. 90–95.

[Lehman et al., 2014] P. Lehman, P. Kime, A. Boruvka, and J. Wright. *The Biblatex Package. Programmable Bibliographies and Citations*. Comprehensive TeX Archive Network (CTAN), June 24, 2014. URL: http://www.ctan.org/pkg/biblatex.

[LEO GmbH, 2014] LEO GmbH. *Englisch - Deutsch Wörterbuch - leo.org*. 2014. URL: http://dict.leo.org/ (visited on Jan. 1, 2014).

[Linguee GmbH, 2014] Linguee GmbH. *Linguee | Deutsch-Englisch Wörterbuch (und weitere Sprachen)*. 2014. URL: http://www.linguee.de/ (visited on Jan. 1, 2014).

[Nadler, 2012] M. Nadler. *ISO-31-konformer Formelsatz in LaTeX*. Nov. 11, 2012. URL: http://moritz-nadler.de/formelsatz.pdf (visited on July 13, 2013).

[Neckel & Labs, 1984] H. Neckel and D. Labs. "The solar radiation between 3300 and 12500 Å". In: Sol. Phys. 90 (Feb. 1984), pp. 205–258. DOI: 10.1007/BF00173953.

[Neckel & Labs, 1987] H. Neckel and D. Labs. "Asymmetry and variations of solar limb darkening along the diameter defined by diurnal motion in April 1981". In: Sol. Phys. 110 (Mar. 1987), pp. 139–170. DOI: 10.1007/BF00148209.

[Toennies, 2013] K. Toennies. *Grundladen der Bildverarbeitung. 4. 2-D Fouriertransformation*. Univerität Magdeburg. Jan. 7, 2013. URL: http://wwwisg.cs.uni-magdeburg.de/bv/index.php?article_id=10&clang=0 (visited on Oct. 24, 2014).

[Ward & Greenwood, 2007] L. M. Ward and P. E. Greenwood. "1/f noise". In: *Scholarpedia* 2.12 (2007), p. 1537.

Acknowledgements

First of all I would like to thank *Astronomy & Astrophysics* for the kind permission to reproduce my paper Müller et al. (2013).

For the financial support during my thesis I thank the "Deutsche Forschungsgemeinschaft" (DFG). I was supported in the framework of the DFG-funded Research Training Group *Extrasolar Planets and their Host Stars* (DFG 1351/2). I also acknowledge support by the "Deutsches Zentrum für Luft- und Raumfahrt e. V." (DLR) under project number DLR 50 OR 1002.

This thesis has made use of data collected by NASA's *Kepler* mission. The observations were obtained from the NASA Mikulski Archive for Space Telescopes (MAST). Furthermore, the SIMBAD database and the VizieR catalogue access tool were used, both operated at CDS, Strasbourg, France.

Es gibt viele die mich während meiner Doktorarbeit begleitet haben und bei denen ich mich bedanken möchte. Allen voran bei meinen Eltern, die mich immer bei allem was ich tue unterstüzen und aufbauen. Ohne sie wäre mein Studium und diese Doktorarbeit nicht möglich gewesen. Danke für eure Geduld und eure Unterstützung.

Ich bedanke mich bei meinem Doktorvater Professor Jürgen Schmitt, der mir die Gelegenheit gegeben hat meine Doktorarbeit in seiner Arbeitsgruppe anzufertigen. Danke für das Vertrauen und den fachlichen Rat.

Ich möchte mich auch bei Sebastian Schröter bedanken, der insbesondere in der Anfangszeit meiner Doktorarbeit eine große Hilfe war. Danke für die Anregungen und Diskussionen.

Meinen Bürokollegen Michael Petersen, Alexander Müller und Tereza Klocová gilt besonderer Dank. Ihr habt mit eurer Art meine Arbeit hier zu einer unvergesslichen Zeit werden lassen. Danke für die humorvolle Atmosphäre, die Aufmunterungen, die fachlichen Gespräche und die Hilfe bei sämtlichen Fragen die ich hatte.

Fabian Pfeifer, Stefan Dahmke, Natascha Rudolf und allen die sonst noch zu Besuch an meinen Platz gekommen sind, sowie den lieben Kollegen hier oben "unterm Dach", sei selbstverständlich auch für ihren Beitrag zu dieser Arbeitsatmospäre gedankt.

Natürlich bedanke ich mich auch bei meinen Freunden, die für die nötige Ablenkung gesorgt haben und es immer geschafft haben mich aufzuheitern.

Schlussendlich bedanke ich mich auch bei den Mitarbeitern der Hamburger Sternwarte, die hinter den Kulissen für einen reibungslosen Ablauf sorgen. Danke euch allen für diese Zeit.